



Université
de Toulouse

THÈSE

En vue de l'obtention du

DOCTORAT DE L'UNIVERSITÉ DE TOULOUSE

Délivré par :

Institut National Polytechnique de Toulouse (INP Toulouse)

Discipline ou spécialité :

Génie Electrique

Présentée et soutenue par :

M. JOSE IOAV RAMOS CHAVEZ

le lundi 21 novembre 2016

Titre :

DESIGN OF HIGH FREQUENCY OPERATING MECHATRONIC
SYSTEMS: TOOLS AND METHODS OF CHARACTERIZATION OF
ELECTROMAGNETIC COUPLINGS BETWEEN ELECTROMECHANIC
CONVERTERS AND POWER ELECTRONICS CONVERTERS

Ecole doctorale :

Génie Electrique, Electronique, Télécommunications (GEET)

Unité de recherche :

Laboratoire de Génie de Productions de l'ENIT (E.N.I.T-L.G.P.)

Directeur(s) de Thèse :

M. JEAN MARC DIENOT

M. PAUL-ETIENNE VIDAL

Rapporteurs :

M. CHRISTIAN VOLLAIRE, ECOLE CENTRALE DE LYON

M. DANIEL ROGER, UNIVERSITE D'ARTOIS

Membre(s) du jury :

M. FRANÇOIS COSTA, UNIVERSITE PARIS 12, Président

M. CHRISTOPHE VIGUIER, SOCIETE NOVATEM, Membre

M. FARID MEIBODY-TABAR, UNIVERSITE DE LORRAINE, Membre

M. JEAN MARC DIENOT, IUT TARBES, Membre

M. PAUL-ETIENNE VIDAL, ECOLE NATIONALE D'INGENIEUR DE TARBES, Membre

A mi má, a mi bro y a Pancha. A mi Padrino Gustavo.

A la memoria de los que importan. A Fernanda, a Roberto, a Po, a Buabuelo.

Remerciements

Le travail présenté ici est le fruit d'une étroite collaboration entre la société toulousaine Novatem et le Laboratoire Génie de Production de l'ENI de Tarbes. Novatem conçoit des systèmes mécatroniques de puissance à hautes performances visant des applications embarquées. Dans un effort de rationalisation des procédures de design et de fabrication, Novatem a sollicité les compétences de l'équipe de recherche DIDS du Laboratoire de Génie de Production et des plateformes de recherche Labceem de l'IUT de Tarbes et PRIMES de l'ENIT pour mener à terme ces travaux de recherche. Le résultat de cette collaboration est ici présenté.

Je tiens à remercier le Professeur François COSTA d'avoir présidé le jury de ma soutenance de Thèse, et surtout, un grand merci pour l'échange intense et extrêmement intéressant que nous avons pu avoir à cette occasion, je vous souhaite du succès dans vos recherches sur le sujet. Je remercie aussi mes rapporteurs les Professeurs Daniel ROGER et Christian VOLLAIRE pour leur effort d'évaluation et de critique constructive et intéressante de mon travail. Je souhaite aussi remercier le professeur Farid MEIBODY-TABAR et M. Pascal IZZO d'avoir pu assister à ma soutenance et d'avoir porté un intérêt à mes travaux. Et surtout, merci à Christophe pour ton accompagnement et ton soutien, pour la bonne humeur et le travail intense que nous avons fourni ensemble.

Mes directeurs de thèse m'ont vu grandir avec ce travail. Et je leur dois beaucoup. Merci à Jean-Marc pour les débats politiques mais surtout pour votre aide technique et la confiance. Merci à Paul-Etienne pour la confiance, pour les bons moments, et pour l'appui moral et technique. Je me rappellerai toujours de mon premier entretien Skype devant vous où la vidéo ne marchait pas et vous avez parlé à mon avatar, un lama très très moche...

J'aimerais aussi remercier le Professeur Bertrand Nogarède qui a été depuis le début, un mentor et une inspiration. L'élève n'a pas dépassé le maître mais il me reste toute une vie pour essayer. Merci pour votre confiance, et votre encouragement. Merci aussi à Novatem et à son équipe : Nico, Arnaud, Mounir et Maxime. Nous avons beaucoup appris ensemble.

Je remercie aussi Dr. Pommerenke de l'EMClab de Missouri Science and Technology pour l'opportunité de faire un séjour à l'EMClab ainsi qu'à Satyajeet Shinde et Abhisek Patniak de leur accueil et du travail que nous avons fourni ensemble.

Je n'aurai jamais assez de place pour citer toutes les personnes qui ont compté pour moi tout le long de cette aventure...

Mais je veux particulièrement remercier Patrick *Patxi* parce qu'il m'a fait confiance depuis le début, et que sans ton aide, je ne serais jamais arrivé jusqu'ici.

Je remercie toute ma famille pour leur support moral. Je remercie Ale pour l'exemple, ma mère et mon frère pour leur soutien inconditionnel et Pancha pour sa complicité à toute épreuve. Emilio et Angélica, Ana, Cris et Jorge, Astrid, Eduardo, Jenn, los primos... Vous avez tous participé d'une manière ou d'une autre à cette réussite.

Je suis vraiment reconnaissant envers Françoise et Charles (et les Vernes en général) pour ces moments où votre support (surtout moral) a été important. Merci à Annie et Jano (et aux chasseurs basques), pour votre soutien dès le début de cette histoire. Merci aussi à Mathieu, Norhis et Lorenzo, car vous avez été une partie fondamentale pour ma réussite, et je ne vous serai jamais assez reconnaissant, vous êtes une part importante de ma vie. Merci aux parents Romero avec qui j'ai commencé une belle amitié très chère pour moi il y a déjà quelques années. Merci à Jeff et Letty, qui ont une place très spéciale dans ma vie et qui ne cessent de perdre à la pétanque ! Merci à Olmo qui a subi le même sort que moi, et je l'en félicite.

Gracias aux *Porcs et Porches* mexicains qui m'ont aussi encouragé, particulièrement à Vero et Fernando. Gracias a mi grupo (Gustavo, Paulo, Rafa, Dulce, Carlos, Victor...), que sin él no lo hubiera logrado.

Merci aux différentes personnes des labos de Tarbes qui m'ont aussi porté un coup de main quand il le fallait. Merci à Karima pour la super bonne humeur et les délires à longueur de journée mais aussi des voyages en conférence et des journées de travail. Merci à tous les doctorants de Tarbes. Merci à José Gonzalo pour cette nouvelle amitié inattendue.

Je veux particulièrement dire à toute l'équipe de bras cassés (toulousains et autres) qu'ils ont fait que ces années aient été une série d'histoires les unes plus folles que les autres. Une mention spéciale à Manu (le grand maître du n'importe quoi !), Matthieu et Camille, Alex, Navisse, Thomas, Sam, Flopette, Loïc, Casa, Rudy, Julien, Bapt (oye guey !), Brubru, Gohu, Pedro, Maël, Léon, Antoine Orth, Nico Meunier, David VM, *l'Equipe d'Hautacam*... Des gens qui me sont chers... Les gars, vous avez tellement envoyé du rêve ! Sans oublier surtout Alexia, ma fillotte, car notre amitié improbable depuis cette mythique soirée parrainage tient toujours et reste toujours très spéciale, nous avons vécu des années inoubliables !

Je ne pourrai jamais assez te remercier, Julie, car tu n'as pas hésité à me soutenir dans les moments les plus difficiles de ce voyage. Merci Ju, de m'avoir supporté avec mes énervements et mauvaises humeurs, mes angoisses et mes nuits blanches. Mais aussi d'avoir partagé la joie de cet accomplissement. On forme une belle équipe !

Merci à vous, avec qui j'ai parcouru un bout de chemin.

Serenidad, Valor, Sabiduría.

Résumé du rapport de thèse en français

Titre de la Thèse :

« Conception d'ensembles mécatroniques à haute fréquence de fonctionnement : outils et méthodes de caractérisation des couplages électromagnétiques entre convertisseur électromécanique et électronique de puissance »

1 CONTRAINTES D'INTEGRATION DANS LES SYSTEMES MECATRONIQUES DE PUISSANCE ET CONSEQUENCES DE COMPATIBILITE ELECTROMAGNETIQUE (CEM)

Les systèmes mécatroniques peuvent être définis comme des systèmes électromécaniques hautement intégrés. Ils sont particulièrement adaptés pour des applications embarquées comme les avions, les véhicules électriques ou hybrides, la robotique ou les implants corporels humains.

Les systèmes mécatroniques permettent de transformer la puissance électrique en puissance mécanique avec un faible impact en termes de volume et de masse sur l'ensemble des systèmes les intégrant.

La **Fig. i** présente une vue générale décrivant l'architecture de base d'un ensemble mécatronique comme assumé dans ce travail.

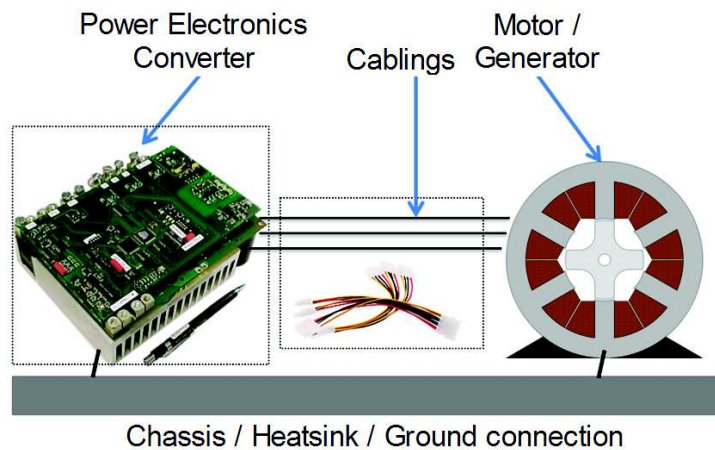


Fig. i - Architecture des systèmes mécatroniques

Les architectures des systèmes mécatroniques dépendent d'un large éventail de facteurs tels que l'application visée, les performances nominales, l'adaptation aux interfaces mécaniques, les exigences de refroidissement, le poids et le volume et les facteurs environnementaux comme la température.

Les contraintes de compacité et de légèreté des ensembles mécatroniques pour les applications embarquées ont été intensifiées au cours des dernières décennies. Par conséquent, diverses stratégies visant à réduire l'impact du volume et de la masse de ces ensembles ont été récemment développées.

En effet, les vitesses de rotation élevées ont été un vecteur important pour l'augmentation de la densité de puissance pour les moteurs électriques. Dans les convertisseurs de puissance utilisés dans les ensembles mécatroniques, l'augmentation de la fréquence et la réduction des temps de commutation ont permis de réduire considérablement la masse et le volume des éléments de filtrage et de refroidissement.

En termes d'intégration, des matériaux plus efficaces et des mécanismes mécaniques et électriques plus rapides, ont apporté de grands avantages en termes de densité de puissance dans les systèmes mécatroniques. Mais ces stratégies ont également favorisé des problèmes complexes comme des

difficultés d'extraction de chaleur ou de compatibilité électromagnétique (CEM). Dans ce travail, nous nous concentrons sur des conséquences relatives aux problèmes de CEM.

1.1 STRATEGIES D'INTEGRATION DANS LES MOTEURS ELECTRIQUES

Pour augmenter la densité de puissance dans les moteurs électriques, les développements dans les matériaux ont été fondamentaux. Pour les machines électriques à aimants, l'augmentation de la polarisation des aimants permanents joue un rôle déterminant dans la réduction du volume du rotor tout en conservant un couple constant.

De la même manière, les fortes densités de courant ont un impact sur la réduction du volume des moteurs. Mais les densités de courant plus élevées induisent des pertes Joule plus élevées, augmentant ainsi la température des conducteurs et la création d'un vieillissement accéléré de polymères d'isolation entre autres.

Néanmoins, la méthode la plus efficace pour augmenter la densité de puissance des moteurs a été l'augmentation de la vitesse rotor. En effet, la puissance mécanique P_m (W) est délivré en tant que produit de la vitesse de rotation Ω (rad / s) et le couple T (Nm). Or, le couple est linéairement relié au volume du rotor et donc à sa masse. Ainsi, des couples réduits à puissance égale permettent de diminuer la masse et le volume de l'actionneur.

Par conséquent, pour augmenter la compacité des moteurs, la vitesse est devenue un vecteur majeur de la réduction de l'encombrement des systèmes mécatroniques, améliorant ainsi la densité de puissance.

Pour illustrer ces propos, dans le **Tableau i** sont présentés quelques moteurs conçus par Novatem®, illustrant l'importance de la vitesse dans la réduction de la masse des systèmes mécatroniques. Les masses correspondent uniquement aux composants électromécaniques actifs, sans convertisseurs de puissance ni carter mécanique.

Tableau i – Exemples de motorisations conçues par Novatem® et impact de la vitesse dans la densité de puissance

Motor type	Application domain	Peak power	Max speed	Mass of active components	Power density
Permanent magnet synchronous motor	Aeronautical	1.5 kW	1.5 krpm	1.8 kg	0.8 kW/kg
Switch reluctance motor	Automotive (traction)	20 kW	12 krpm	17 kg	1.2 kW/kg
Switch reluctance motor	Aeronautical	2.3 kW	60 krpm	0.9 kg	2.4 kW/kg
Asynchronous motor	Aeronautical	80 kW	50 krpm	25 kg	4 kW/kg
Permanent magnet synchronous motor	Automotive (exhaust recovery system)	120 kW	80 krpm	13 kg	9.2 kW/kg

1.2 STRATEGIES D'INTEGRATION DANS LES CONVERTISSEURS DE PUISSANCE

Les convertisseurs de puissance sont des transformateurs d'énergie basés sur des interrupteurs semi-conducteurs de puissance. Leur but est d'adapter les niveaux et les formes d'ondes

électriques entre deux sources, ou bien entre une source et une charge, avec le rendement le plus élevé possible (**Fig. ii**).

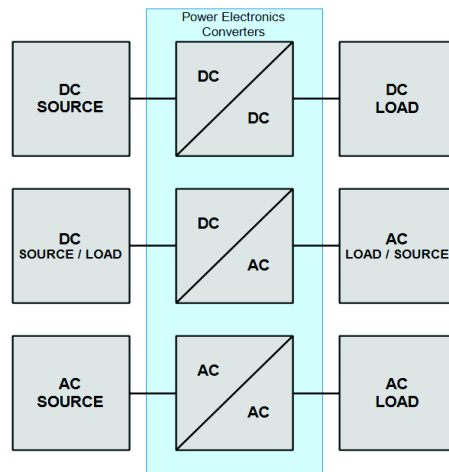


Fig. ii - Définition générale des convertisseurs statiques de puissance

Contrairement à l'électronique de faible puissance, où les processus dissipatifs pour réguler les tensions et les courants ne sont pas une préoccupation fondamentale, le rendement de l'électronique de puissance est une préoccupation majeure de la conception.

Une vue schématique d'un convertisseur de puissance est présenté sur la **Fig. iii**.

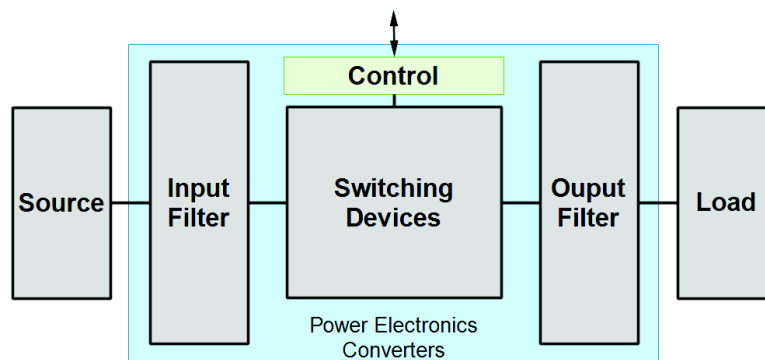


Fig. iii - Description schématique d'un convertisseur statique

Pour les systèmes mécatroniques, l'architecture typique se compose d'un convertisseur DC / AC alimenté par une source de courant continu et la source est un moteur / générateur avec éventuellement, des câbles d'interconnexion entre les deux (**Fig. iv**).

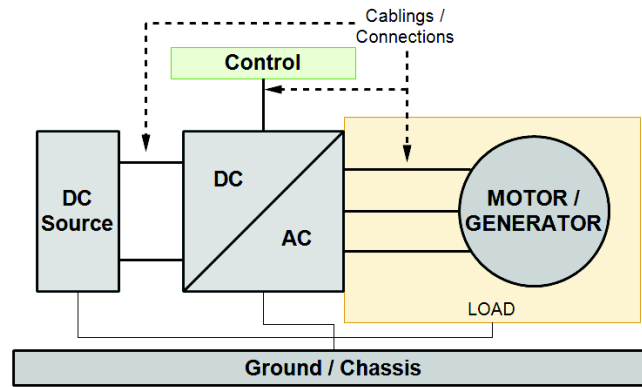


Fig. iv – Architecture détaillée d'un convertisseur alimentant un moteur

Les convertisseurs de puissance ont généralement des fréquences de commutation allant de quelques kilohertz à même quelques mégahertz. Et, bien que les fréquences de commutation des convertisseurs statiques soient encore nettement plus faibles que pour les composants numériques comme pour les circuits intégrés, une augmentation des vitesses de commutation a contribué à réduire le volume de l'électronique de puissance.

Effectivement, en augmentant la fréquence de commutation, les éléments de filtrage, qui constituent des composantes essentielles des convertisseurs de puissance, deviennent plus compacts. Les éléments inductifs, utilisés pour le filtrage par exemple, sont beaucoup plus efficaces pour filtrer les courants à des fréquences élevées, réduisant ainsi leur volume et leur masse. De même, les condensateurs sont plus efficaces pour filtrer des tensions à haute fréquence.

Le concept de densité de puissance est un outil rationnel pour comparer les performances des convertisseurs. Elle est définie comme suit:

$$\rho = \frac{P}{V} \text{ [kW/dm}^3\text{]}$$

La densité de puissance est équivalente aux critères de l'industrie de la microélectronique en ce sens que, c'est une mesure des progrès relatifs à l'intégration des transistors dans un volume donné [5] mieux connu comme la loi de Moore. D'une manière analogue, une augmentation régulière de la densité de puissance a été observée, comme indiqué sur la **Fig. v** Au cours des dernières décennies, la densité de puissance a doublé tous les dix ans.

Mais, pour augmenter la densité de puissance, la technique la plus courante a été l'augmentation de la fréquence de commutation. Pour doubler la densité de puissance d'un convertisseur de puissance, des recherches récentes montrent qu'une augmentation de la fréquence de commutation par un facteur de 10 est nécessaire.

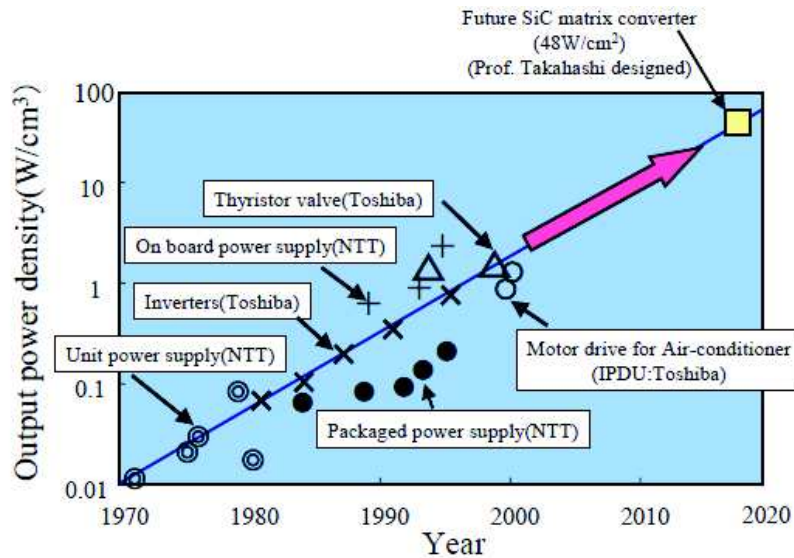


Fig. v – Evolution de la densité de puissance des convertisseurs

Cependant, les fréquences de commutation ne sont pas la seule technique permettant une augmentation de la densité de puissance. La réduction des temps de commutation a un impact significatif sur la réduction des pertes par commutation et par conséquent, dans la réduction de volume des systèmes de refroidissement. Néanmoins, la diminution des temps de montée et de descente conduisent aussi à enrichir les spectres de fréquence équivalents émis induits par la commutation.

En outre, la réduction du volume a été obtenue en réduisant les pertes thermiques et par conséquent, réduisant la taille des composants de refroidissement dans les systèmes embarqués. Mais la réduction des pertes thermiques est principalement réalisée en réduisant les temps de commutation des interrupteurs d'électroniques de puissance, aggravant d'avantage les problèmes d'émissions.

En outre, les semi-conducteurs à grand gap tels que Nitrure de Gallium (GaN) ou Carbure de Silicium (SiC), ont introduit la possibilité d'augmenter les performances de l'électronique de puissance. Ils permettent une tension de fonctionnement, une température et une puissance admissible plus élevées améliorant ainsi la densité de puissance. La **Fig. vi** montre la limite de vitesse théorique de la technologie (Si) par rapport aux composants grand gap.

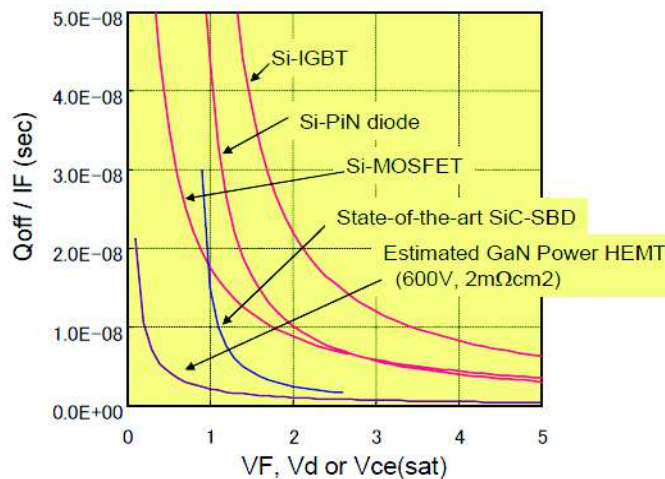


Fig. vi - Vitesse de commutation théorique pour les deux technologies Si et SiC

Ainsi, les interférences électromagnétiques (EMI) induites par la commutation sont devenues des éléments essentiels à prendre en compte lors de la conception de systèmes électriques. Effectivement, une conséquence directe des améliorations dans les performances fonctionnelles des alimentations commutées est une augmentation de la signature électromagnétique de l'ensemble du système. Les émissions conduites (EC) et rayonnées (ER), et les interférences électromagnétiques sont une préoccupation croissante dans les processus de design des systèmes mécatroniques.

1.3 ASSOCIATION CONVERTISSEUR-MACHINE

La nécessité d'une modélisation large bande de moteurs / générateurs dérive du problème plus général de la modélisation des machines alimentés par des convertisseurs statiques, et plus particulièrement, la caractérisation du comportement EMC / EMI de ces ensembles.

La présence d'éléments parasites (boucles inductives, couplages capacitifs et d'amortissement à travers les phénomènes dissipatifs) dans la structure du moteur / générateur contribuent à sa signature en basse et haute fréquence (large bande) et plus précisément, à ses courants et tensions de mode commun (CM) et le mode différentiel (DM). En retour, les courants circulant à travers le système électrique transmettent fatalement la signature du comportement du moteur.

Comme indiqué dans le paragraphe précédent, l'augmentation des valeurs de dV / dt et di / dt ainsi que des environnements électromagnétiques sévères, doivent être intégrés dans la logique de conception des moteurs et des générateurs d'ensembles mécatroniques. Ainsi, de nouvelles perturbations potentielles modifient les méthodes classiques de modélisation EMC / EMI de la totalité de l'ensemble mécatronique, et par conséquent, la machine elle-même.

La plupart des méthodes de modélisation de la machine a été axée sur les questions d'émissions conduites (CE), principalement en raison des normes obsolètes régissant les systèmes de puissance que dans la zone d'émissions conduites, comme le fait la norme DO-160 pour l'aviation civile. En conséquence, peu de travaux de modélisation ont été effectués au-dessus de 30 MHz. Dans certains cas particuliers, cependant, comme présenté dans des analyses ont été faites jusqu'à 100 MHz.

Bien que très peu d'études soient disponibles, d'importantes interférences rayonnées à des fréquences au-delà de 100 MHz dans les variateurs AC ont été bien documentées. Ces études entre autres symptômes devraient pousser le développement de modèles à des gammes de fréquences où le rayonnement efficace des câblages et des structures des systèmes électriques métalliques longues peuvent potentiellement apparaître. Les capacités parasites des enroulements jouent un rôle fondamental dans ce problème. Les capacités entre les spires et les noyaux magnétiques du moteur contribuent à des fuites de courant HF en mode commun provoquant l'apparition des courants de mode d'antenne à l'origine des émissions rayonnées.

L'analyse d'impédance en mode commun et en mode différentiel des enroulements des actionneurs est une manière habituelle et efficace d'avoir une bonne prédiction de la compatibilité électromagnétique de la machine.

Actuellement, les modèles existants utilisent des mesures d'impédance sur des actionneurs existants pour adapter les modèles d'impédance. Ainsi, il semble très difficile de prédire le

comportement EMC entre l'onduleur et la machine, à partir de la phase de conception, lorsque la machine et l'onduleur sont co-conçus à des fins mécatroniques avec des techniques de modélisation du comportement.

Dans le deuxième chapitre, des modèles complètement prédictifs d'impédance en mode commun et différentiel sont établis, permettant ainsi de se passer des modèles nécessitant des mesures expérimentales.

2 MODELISATION LARGE BANDE DES MOTEURS ELECTRIQUES ET IMPLEMENTATION CIRCUIT POUR SIMULATION HAUTE FREQUENCE

Les moteurs et générateurs électromécaniques sont des structures électromagnétiques très complexes combinant une large gamme de matériaux et architectures. L'agencement complexe des enroulements dans les culasses ferromagnétiques de la machine rend très difficile de paramétrer sa géométrie et de calculer les couplages parasites. En outre, la dépendance des différents matériaux à une grande variété de paramètres physiques ajoute un défi complémentaire pour la modélisation sur une large gamme de fréquences de telles structures électromagnétiques.

Dans ce chapitre, un effort pour modéliser le comportement large bande de machines d'enroulement concentré est effectué. L'objectif est de contribuer à l'élaboration d'une méthode de modélisation de la machine électrique dans le domaine des hautes fréquences en tenant compte des paramètres physiques et géométriques des enroulements. En prenant en compte les paramètres physiques, ainsi que l'architecture des enroulements, tels que le fil et la classe d'isolation, l'arrangement des fils, les matériaux ferromagnétiques ou le nombre de tours par couche, un outil rationnel et prédictif est créé. Cet effort est fait, afin de prévenir et de prédire les niveaux de susceptibilité et d'émissions à partir d'une vue d'ensemble du système global.

Puisqu'une solution globale complète du mode commun équivalent et le mode différentiel est très difficile à trouver, l'étude est divisée en plusieurs parties.

Dans le premier paragraphe, la modélisation analytique des différentes impédances concernées est réalisée comme suit:

- Hypothèses et considérations générales
- Modélisation du comportement capacitif et diélectrique de la structure des enroulements
- Modélisation de l'impédance des conducteurs en cuivre modifiée par les courants de Foucault
- Modélisation du comportement inductif avec le noyau ferromagnétique

Puis, afin de mettre en œuvre un outil de simulation de circuit, une synthèse de réseaux est effectuée pour reproduire des comportements dépendants de la fréquence dans une simulation circuit.

Enfin, une comparaison entre les modèles analytiques implémentés dans des simulations circuit et des résultats expérimentaux est faite dans les domaines temporels et fréquentiels.

A des fins de simplification, tous les calculs analytiques seront réalisés dans le cadre d'une hypothèse de section transversale circulaire. Ainsi, il est admis que dans ce développement, la géométrie cylindrique des pôles stator sont assujetties à un système de coordonnées cylindriques (r , ϕ , z). Les effets de ces approximations sont discutés dans le cœur du travail.

D'autre part, une hypothèse forte concernant la longueur de la bobine est également intégrée dans la modélisation. En effet, dans les moteurs électriques, les enroulements sur les pôles stator sont de courte longueur. Dans l'analyse, on considère que les longueurs de bobine sont assez longues pour ne pas tenir compte des effets de bord. Cette hypothèse impacte particulièrement la modélisation des effets des courants de Foucault sur les fils de cuivre et la modélisation d'inductance des spires.

Tous les modèles analytiques sont synthétisés dans l'Approximation des Etats Quasi Stationnaires, ce qui signifie que les termes dérivés de temps dans les équations de Maxwell et leurs conséquences sont négligés. En ce qui concerne les matériaux, l'hypothèse concernant la linéarité et isotropie à un niveau macroscopique sont traités dans leurs sections respectives.

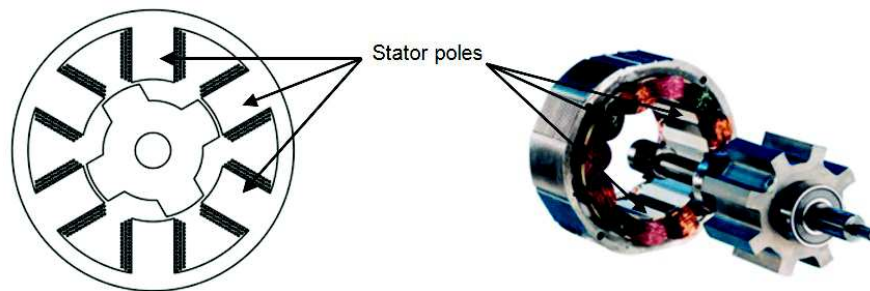


Fig. vii - Vue générale des plots statoriques de moteurs à bobinage concentré

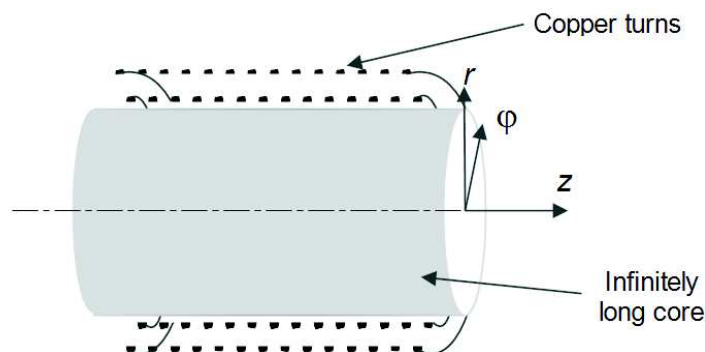


Fig. viii - Géométrie assumée pour la modélisation des plots stator

Ainsi dans ce chapitre, des modèles analytiques d'impédance interne des spires ainsi que des capacités inter-spire et spire-noyau ont été synthétisés, adaptés ou repris de sources diverses.

La modélisation des différents phénomènes est visée sur une plage allant de 0 Hz jusqu'à 300 MHz.

2.1 CALCUL DES CAPACITES PARASITES DANS LES BOBINAGES CONCENTRES

Tout d’abord, les calculs des capacités inter-spire et spire-noyau ont été menés. Ces modèles se basent sur le calcul d’énergie électrostatique dans les régions entre deux conducteurs du bobinage et entre les conducteurs et le noyau. La géométrie considérée est présentée dans la **Fig. ix**.

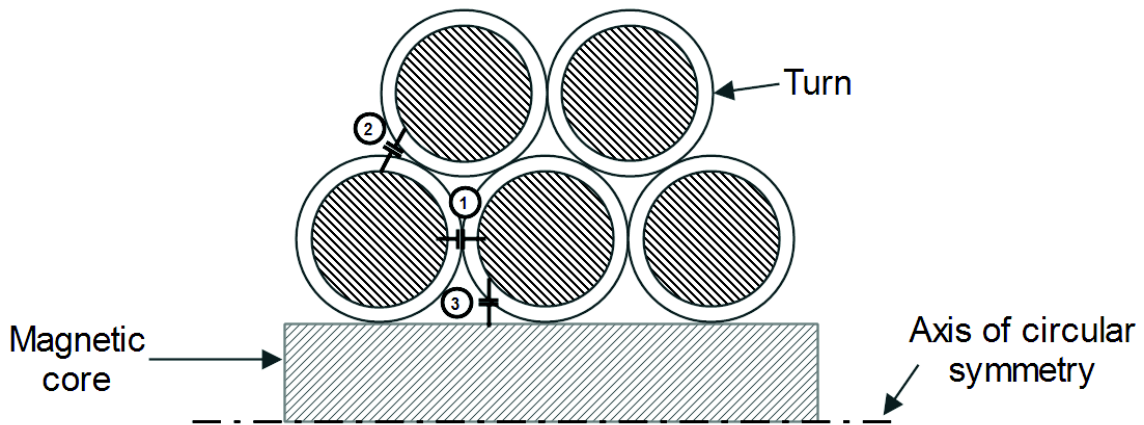


Fig. ix - Vue en coupe de la géométrie assumée pour les calculs analytiques des capacités

L’étude s’est divisée en 8 cas. Les quatre premiers correspondent aux bobinages sans imprégnation d’époxy. Les quatre derniers correspondent à des bobinages imprégnés.

Les résultats issus des calculs analytiques ont été confrontés à des simulations numériques électrostatiques en 2D. Les écarts constatés sont résumés dans le **Tableau ii**.

Tableau ii – Résumé des résultats de comparaison entre calculs analytiques et simulations éléments finis en 2D

Film thickness	Sans imprégnation		Avec imprégnation	
	Grade 1 average error %	Grade 2 average error %	Grade 1 average error %	Grade 2 average error %
50 μm	7.44	13.5	1.9	1
100 μm	9.44	16.3	12.3	12.5
200 μm	20.2	23.7	32.5	29.7

Les conclusions sur ces écarts sont vastes. Mais globalement, compte tenu des fortes hypothèses, le modèle semble se comporter tout à fait acceptablement par rapport à l’analyse éléments finis (FEA) pour des épaisseurs de film entre 50 et 200 μm , qui sont des standards pour des moteurs de moyenne tension. Et, en raison des irrégularités inhérentes à l’enroulement des fils et des déformations des matériaux diélectriques avec les contraintes mécaniques, les dimensions indiquées ici peuvent varier fortement. Ainsi, dans le pire des cas, ce qui est la configuration de grade 1 avec une épaisseur de 200 μm à 32,5%, les modèles analytiques sont convergents avec les résultats de simulation FEA.

2.2 IMPEDANCE INTERNE DES SPIRES DU BOBINAGE ET EFFET DES COURANTS INDUITS

Dans un deuxième temps, ce chapitre traite les modélisations possibles de l'impédance interne des fils de cuivre formant le bobinage. Les courants de Foucault sont susceptibles d'apparaître dans tout matériau conducteur soumis à des champs magnétiques variant dans le temps.

Pour un conducteur de conductivité σ , un champ électromagnétique alternatif pénètre et produit un champ électromagnétique induit, entraînant l'apparition de courants dits courants induits ou courants de Foucault. L'effet des courants de Foucault sur les conducteurs de cuivre de l'enroulement est la distribution non uniforme de la densité de courant dans une section transversale donnée. Ceci est directement traduit par une dissipation plus forte sous la forme de pertes par effet Joule.

Le premier objectif de cette analyse est de comparer plusieurs expressions de modèles d'impédance tenant compte des effets des courants de Foucault dans les conducteurs afin d'adapter les modèles au mieux nos applications. Ensuite, les approximations sélectionnées sont soigneusement analysées et mises en œuvre. Enfin, le but final est de créer des modèles de réseaux de circuits afin de reproduire le comportement des impédances dans le domaine temporel et fréquentiel.

Ainsi, le modèle d'impédance interne par spire adopté prend en compte les effets de proximité ainsi que les effets de peau. De plus, contrairement aux autres modèles, il prend en compte la courbure des conducteurs autour du noyau. Cependant ce modèle est adapté pour des conducteurs de géométrie carrée. Or, les enroulements considérés dans cette étude sont à base de fils à section circulaire. Malgré cette hypothèse forte, ce modèle a été conservé. Ainsi, dans la **Fig. x** l'impédance interne de conducteurs appartenant à différentes couches est illustrée.

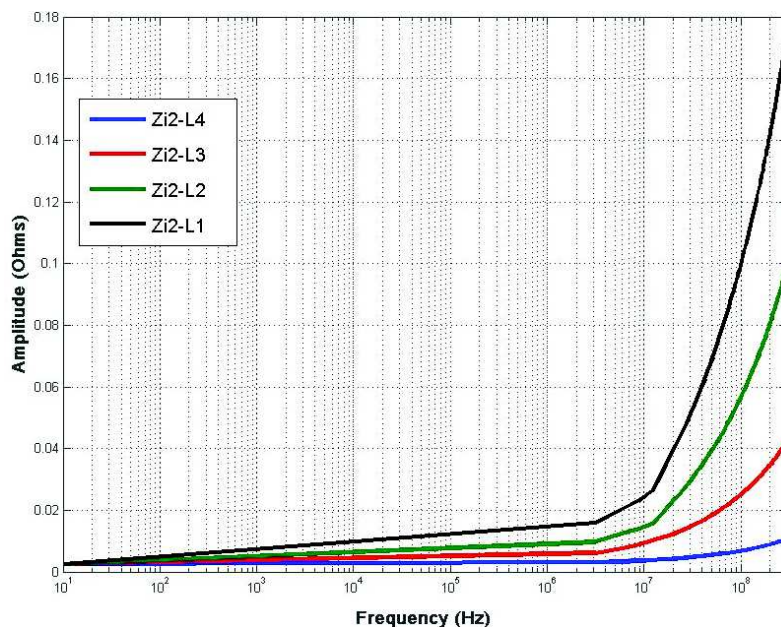


Fig. x - Impédance interne de spires appartenant à des couches différentes d'un bobinage

On peut clairement noter l'évolution de l'impédance avec la position de la couche sur la bobine. Pour les couches externes (couche 4), l'impédance augmente plus lentement que pour les couches internes (couche 1).

2.3 CALCUL DES INDUCTANCES PARTIELLES DANS LES BOBINAGES CONCENTRES

Dans ce deuxième chapitre, le troisième aspect traité est celui des inductances partielles.

Une partie essentielle de la modélisation à haute fréquence pour les enroulements de moteurs est la représentation du comportement inductif. Afin de modéliser avec précision le comportement inductif de la structure, plusieurs considérations doivent être prises en compte.

Pour les matériaux ferromagnétiques communs, la perméabilité relative diminue rapidement à 1 en raison de la dynamique des parois de Bloch et les phénomènes d'inertie à l'échelle mésoscopique (à savoir des moments magnétiques). En d'autres termes, la dépendance en fréquence de la perméabilité magnétique se produit lorsque les moments magnétiques ne peuvent plus se réaligner parallèle au champ externe avant que celui-ci ne change de direction. Cette dispersion de perméabilité se produit à une fréquence appelée de relaxation.

Dans des matériaux ferromagnétiques à base de fer classiques, la relaxation apparaît à des fréquences aussi basses que quelques kilohertz et pour les matériaux composites à base de matériaux ferromagnétiques doux (SMC) à un 10 kHz et jusqu'à plusieurs centaines de kilohertz.

La profondeur de pénétration du champ électromagnétique dans des matériaux joue aussi un rôle fondamental dans les effets de perméabilité sur le comportement magnétique. Pour un matériau donné, la profondeur de pénétration du champ électromagnétique dépend non seulement de la fréquence d'une conductivité donnée, mais également de la dispersion de la perméabilité lors de l'intégration du modèle de relaxation dans l'expression de la profondeur de pénétration.

Ainsi, une expression des inductances mutuelles a été adoptée en tenant compte de différents cas possibles trouvés dans les matériaux et la fréquence d'excitation. L'expression adoptée est aussi présentée dans des applications de très haute fréquence par exemple, où la pénétration du champ est nulle. Aussi, cette expression adoptée de la littérature est dérivée sous sa forme de noyau non ferromagnétique. A titre d'illustration du phénomène de dispersion magnétique, un exemple d'inductance mutuelle est présenté dans la *Fig. xi*.

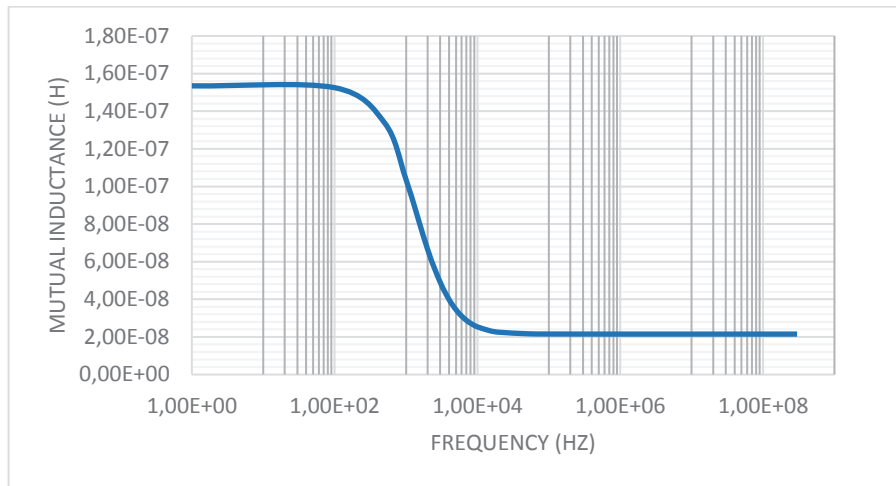


Fig. xi - Evolution de la mutuelle inductance avec la fréquence

A basse fréquence, l'inductance mutuelle entre deux spires de l'enroulement a une valeur élevée. Lors du phénomène de relaxation, autour de 1.5 kHz, la mutuelle inductance diminue de valeur fortement jusqu'à atteindre sa valeur finale proche de celle de l'air.

L'expression de la mutuelle inductance permet ainsi de prendre en compte de manière analytique le phénomène de dispersion de la perméabilité magnétique, et nous permet d'effectuer la modélisation des phénomènes inductifs au sein des bobinages concentrés dans les moteurs électriques.

Cependant, contrairement au cas purement inductif, les pertes du noyau pourraient être analysées dans le contexte des hypothèses:

- hypothèse des niveaux d'excitation faible

Comme indiqué dans le chapitre I, le modèle large bande dans ce travail concerne excitations seulement de bas niveau. Les courants induits dans le noyau sont fonction du champ inducteur, qui est directement lié à l'excitation. Par conséquent, compte tenu des niveaux d'excitation faible, les courants de Foucault sont ici considérés comme inexistant.

- la réalité technologique

Les noyaux en empilement de tôles ainsi que les SMC sont utilisés pour réduire considérablement l'intensité des courants induits. Les tôles isolées forcent les chemins de courant à être considérablement réduits, réduisant ainsi les pertes. Dans le cas de SMC, les grains isolés de matériaux ferromagnétiques ont le même effet que dans les laminations, mais dans toutes les directions et pour des tailles de grain très faibles. Par conséquent, avec les hypothèses ci-dessus, les courants induits par les pertes sont négligés.

En tenant compte des pertes de fer, les niveaux sont également tributaires de l'intensité de champ et, par conséquent, les pertes de noyau ne sont pas prises en compte dans le cadre de bas niveau d'excitation du signal.

2.4 REPRESENTATION DE TYPE CIRCUIT DES MODELES ANALYTIQUES

Les calculs analytiques effectués dans les paragraphes ci-dessus, sont nécessaires pour la modélisation du comportement de l'impédance en mode commun et mode différentiel dans les enroulements. Mais, afin de construire un modèle complet plus convivial pour représenter les impédances calculées ci-dessus dans le domaine de fréquence et de temps, des simulateurs de circuits peuvent être utiles. Par conséquent, la mise en œuvre d'un modèle de circuit des enroulements permet des simulations au niveau du système à prendre en compte le comportement HF de l'actionneur.

La synthèse de réseaux permet de déterminer des comportements précis pour les phénomènes décrits auparavant. Donc, aussi bien pour les couplages capacitifs que résistifs et inductifs, des réseaux d'impédance ont été synthétisés et implémentés dans un simulateur circuit.

Seul un problème considérable a été rencontré. La dispersion de la perméabilité n'a pas pu être prise en compte. Ainsi, les simulations d'impédance globale ne sont valables qu'à des fréquences proches de celle où les mutuelles inductances et les coefficients de couplage ont été calculés. D'autre part, la dispersion de la permittivité diélectrique est considérée comme constante et par conséquent, elle n'est pas incluse dans les réseaux synthétisés.

Finalement, à partir des réseaux synthétisés, un modèle circuit global d'un enroulement a pu être construit. Les valeurs des composants insérés dans ce modèle, sont directement issus des

2.5 COMPARAISON AUX RESULTATS EXPERIMENTAUX

Afin de comparer les résultats des simulations en fréquence et dans le domaine temporel avec des mesures expérimentales, plusieurs structures bobinées ont été conçues. Les échantillons sont conçus pour tester des configurations représentatives des enroulements concentrés présents dans plusieurs types de moteurs électriques. Les échantillons et les matériaux utilisés sont soumis à un ensemble de mesures afin d'en extraire les informations nécessaires à la modélisation. Puis, des mesures d'impédance en mode commun et mode différentiel sont effectuées.

Deux instruments de mesure sont utilisés dans ce processus:

- Keysight analyseur d'impédance de précision (PIA) E4990A pour des fréquences allant de 20 Hz à 1 MHz,
- Keysight analyseur de réseau vectoriel (VNA) E6051B pour des fréquences de 1 MHz à 300 MHz

La raison de l'utilisation de deux différents équipements est qu'un seul instrument ne peut pas gérer la mesure pour la gamme de fréquences de 20 Hz à 300 MHz.

En fait, bien que la limite supérieure de la PIA soit de 120 MHz, les adaptateurs de test qui ont été utilisés n'étaient pas tous utilisables jusqu'à 120 MHz.

D'autre part, le VNA peut manipuler des fréquences comprises entre 5 Hz et 3 GHz. Toutefois, en raison de la protection contre les décharges électrostatiques sur les ports et les protections du bloc courant continu, la limite inférieure de la VNA réduit à 300 kHz. Il a été décidé que, pour de bonnes

mesures de qualité sur la gamme de fréquences, les deux équipements doit être utilisé. Le **Tableau iii** résume les caractéristiques des éprouvettes utilisées.

Tableau iii - Description des éprouvettes utilisées pour la validation expérimentale

Specimen	Name	Core material	Core insulation	Impregnation
A	Delrin	Delrin (polymer)	-	-
B	Bare Core	Soft Magnetic Compound	-	-
C	Insulated Core	Soft Magnetic Compound	Kapton® 50 μm	-
D	Impregnated	Soft Magnetic Compound	-	Araldite F®

Des mesures différentielles et mode commun ont été effectuées sur les quatre spécimens. Dans la **Fig. xiii** l'arrangement des éprouvettes est décrit.

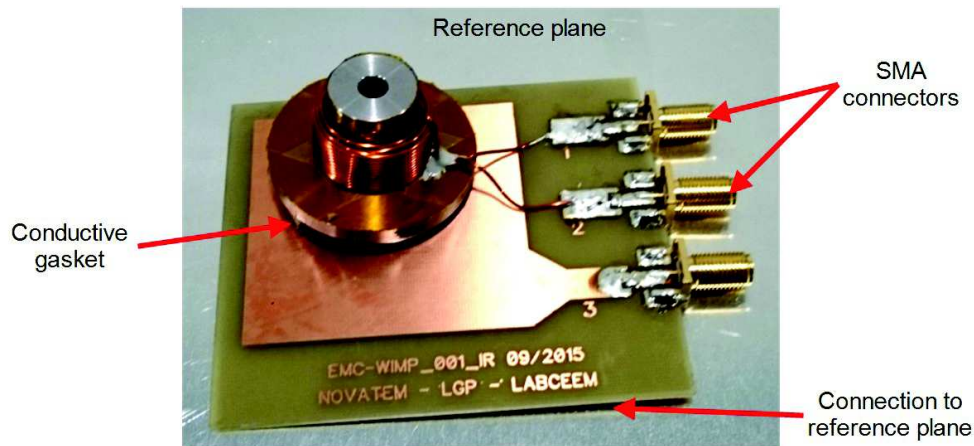


Fig. xii - Vue du support pour la mesure de paramètres d'impédance

Les résultats sont présentés pour les différentes éprouvettes.

Par-dessus tout, il doit être considéré que la gamme de fréquence ciblée de la modélisation est très grande. Et à la lumière des observations ci-dessus, les résultats sont convaincants d'un point de vue du processus de modélisation. Les résultats de simulation ont été confrontés à des mesures expérimentales bien que plusieurs points doivent être relevés.

Premièrement, les tendances de l'impédance de mode différentiel et de mode commun sont décrites de façon très précise par le modèle de circuit analytiquement construit. Toutes les résonances présentes dans les impédances mesurées apparaissent dans les dans les impédances simulées, à la fois en amplitude et en phase.

Alors, même si la tendance des impédances est prédite avec précision, les modèles sont très sensibles aux valeurs analytiques attribués aux paramètres du circuit. Par conséquent, plus la précision est élevée sur les calculs analytiques, plus le modèle se comportera de manière précise. Le problème

avec cette caractéristique, est que, des hypothèses telles que permittivité constante et les pertes diélectriques ont un impact énorme sur impédances simulées.

Par ailleurs, le modèle de circuit ne tient pas compte de la perméabilité dépendant de la fréquence, ce qui oblige l'analyse en termes de cadrage de l'impédance à l'intérieur des valeurs extrêmes, mais pour améliorer la précision, une analyse plus approfondie à bande étroite est tout à fait possible d'atteindre des fréquences autour de celle de l'inductance calculée.

Gardez à l'esprit que, bien que les géométries testées ne soient pas celles des enroulements de machines, le modèle se comporte remarquablement bien pour les enroulements testés. Dans le dernier chapitre de ce rapport, une application sur un moteur réel est réalisée avec d'excellents résultats.

3 EXTRACTION DES PARAMETRES PARASITES DANS LES CARTES DE CIRCUITS IMPRIMES DE PUISSANCE

Les cartes de circuits imprimés (PCB) sont des composants essentiels de convertisseurs de puissance, qui permettent l'intégration compacte de fonctions autour des convertisseurs de puissance. Un large éventail d'architectures de convertisseurs de puissance peut être trouvé dans l'industrie. Ces architectures dépendent fortement des paramètres tels que la densité de puissance et du type d'application. Mais comme une tendance générale, les PCB de convertisseurs de puissance sont de grandes structures avec de grands plans d'alimentation et de masse en raison des densités de courant actuellement nécessaires pour les applications de puissance. Ces grands conducteurs ont tendance à induire des problèmes EMI.

Par exemple, les chutes de tension sur des conducteurs de signaux peuvent se traduire par un rayonnement en mode commun. En outre, de grands plans de PCB peuvent former des structures de type antenne dipôle avec leurs câbles d'alimentation connectés aux sources RF créés par la commutation des composants de puissance. Une partie de l'antenne est typiquement un câble fixé à un châssis métallique ou de grands plans du PCB.

Dans ce chapitre, le but est d'étudier la réponse des gros plans des PCB multicouches de convertisseurs de puissance industriels et complexes. L'objectif est d'analyser la réponse et les couplages de bus de puissance et d'autres plans de signaux dans une approche rationnelle et générique afin de les intégrer dans une plus grande analyse des circuits à grande échelle.

Pour cette question, un procédé d'extraction et de simulation intégral est utilisé. En outre, la technique décrite ci-dessous permet d'inclure des structures conductrices entourant le PCB ce qui est utile pour prédire les chemins de couplage CM et DM en tenant compte des mécanismes de couplage inductifs et capacitifs parasites à partir des couches de PCB vers les parties environnantes.

Le but de cette étude est d'extraire un modèle de circuit équivalent d'un PCB multicouches utilisé dans des applications mécatroniques industrielles. Le modèle circuit doit être valable aussi bien dans domaine temporel et fréquentiel. La plage de fréquences recherchée dans cette analyse, est du continu jusqu'à à 300 MHz.

Le processus d'extraction est schématisé dans la **Fig. xiv**. Une fois le processus de routage effectué, une extraction du modèle 3D est réalisée en utilisant un format ODB+. Ensuite, le fichier ODB+ est converti en format STEP afin d'être importé dans un modèleur 3D pour d'autres modifications.

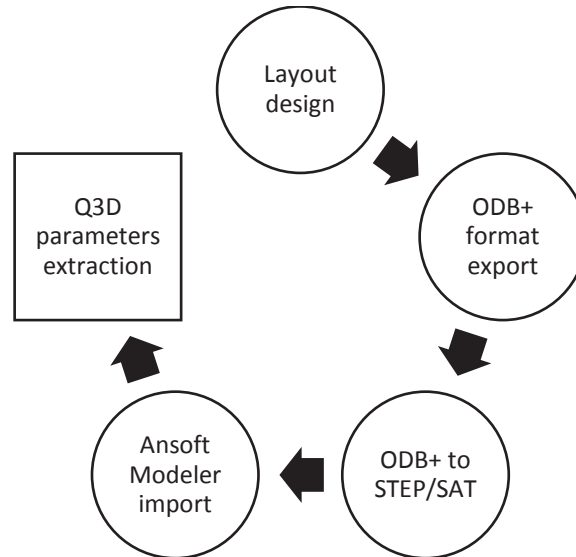


Fig. xiii - Processus d'extraction des paramètres dans les PCB

Ansoft Q3D® est un logiciel de calcul électromagnétique sur la base d'une méthode hybride de Méthode des Moments (MoM) et Méthode des Eléments Finis (FEM). Q3D® est un logiciel complet d'analyse multi-matériaux en tenant compte de la disposition géométrique et électrique d'une structure. Les solutions électromagnétiques d'un problème donné sont interprétées en termes de distribution de courant ou la charge de surface et, et puis, en termes d'éléments partiels.

Pour un problème donné, un ensemble de conducteurs est défini comme un système de réseaux. Chaque réseau est affecté à une entrée et une surface de sortie pour le courant d'excitation harmonique. Pour un système de conducteurs, les inconnues sont alors la densité de courant J dans les conducteurs et la densité des charges q sur la surface de ces conducteurs. Afin de résoudre le système d'équations dérivé du problème donné, les densités de courant sont discrétisées en cellules volumiques, en donnant l'intensité du courant global pour chacun des volumes des réseaux, dans les trois directions dimensionnelles. En ce qui concerne la densité de charges, elles sont définies sur la surface du conducteur. Ensuite, des solutions du problème sont donc interprétées en termes de chutes de tensions capacitive, inductive et de tension résistive, et donc, comme des éléments partiels d'impédance du circuit.

Une fois que le modèle 3D a pu être modifié dans le modèleur de Ansoft Q3D, une extraction de paramètres des éléments partiels RLC du PCB peut être effectuée. La **Fig. xv** montre le modèle du PCB modifié et prêt pour l'extraction des paramètres partiels.

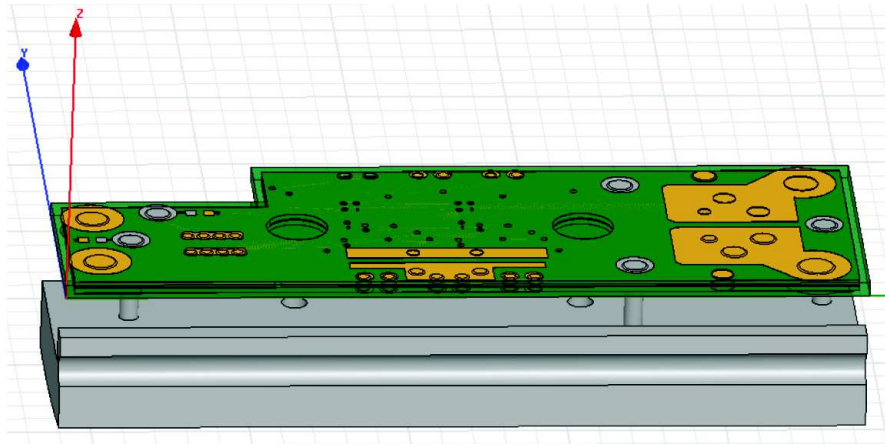


Fig. xiv - Modèle final utilisé pour le calcul électromagnétique

Finalement, une fois que la simulation a été faite, les résultats de la simulation circuit extraits à partir avec Q3D ont été comparés à des mesures expérimentales.

Un bon accord entre les résultats de simulation et les données mesurées sont concluantes en ce qui concerne l'extraction de circuit équivalent de PCB de puissance multicouche, en particulier d'un point de vue prédictif. L'extraction des éléments de circuit partiels de simulations électromagnétiques s'est avéré être un moyen efficace d'expérimentation virtuelle pour les PCB de puissance multicouches.

Dans ce chapitre, une méthode rationnelle permettant de caractériser un PCB de puissance multicouche à partir du routage assisté par ordinateur a été présentée. La méthode montre la procédure standard pour obtenir des données 3D à partir des fichiers de routage, en important des fichiers dans un logiciel électromagnétique permettant l'extraction de circuits équivalents et exportant les circuits dans un simulateur circuit. Plusieurs adaptations de la géométrie 3D doivent être prises en compte dans le but de réduire les géométries complexes.

Les circuits extraits résultants sont une image du PCB conçu. En effet, la simulation pour l'analyse EMC / EMI peut être utilisé pour prédire les émissions sans avoir recours à la fabrication de la carte électronique. Si un comportement inacceptable est alors détecté, des modifications au routage des PCB et de l'architecture de manière générale peuvent donc être effectuées avant le prototypage.

4 METHODE D'INVESTIGATION EMC POUR LES SYSTEMES MECATRONIQUES ET EXPERIMENTATION VIRTUELLE

Ce chapitre est divisé en deux études différentes. La première étude porte sur l'analyse EMC / EMI d'une partie d'un système moto convertisseur commercial. La deuxième étude porte sur la mise en œuvre des techniques et des méthodes développées dans ce travail pour compléter la première étude.

La première étude, qui est désigné comme le "analyse Flyback", aborde le problème de la compatibilité électromagnétique d'un point de vue de la modélisation. L'analyse Flyback établit une procédure standard pour l'évaluation du rayonnement induit par les courants de mode commun sur

le câble d'alimentation du convertisseur. Une méthode complète, à partir de la simulation circuit jusqu'à la prévision des émissions rayonnées est construite.

Bien que le convertisseur Flyback ne soit pas considéré comme un système mécatronique, la procédure établie ici peut aider à l'évaluation des émissions rayonnées pour tout système mécatronique.

En ce qui concerne le processus de modélisation du convertisseur Flyback, lors de la modélisation de composants fonctionnels constituant le convertisseur, un PCB adapté avec des caractéristiques très spécifiques et bien connues est fabriqué et le transformateur modélisé en mesurant ses paramètres S. Ainsi, le changeant le remplacement d'un de ces composants invaliderait les conclusions établies par l'analyse.

La deuxième étude, appelée analyse de EMOD, vise à inclure les techniques de modélisation abordées dans les travaux présentés dans le chapitre II et III dans la procédure présentée dans l'étude Flyback. Il est appliqué à un module d'un moteur de 20 kW conçu par Novatem, utilisé pour la traction de véhicules électriques. Dans l'analyse de EMOD, les modèles prédictifs du PCB et des bobines sont effectués. Au lieu de construire les modèles à base de mesures, les modèles analytiques pour modéliser les enroulements et l'extraction de paramètres pour le PCB sont utilisés pour compléter la simulation globale du système mécatronique.

Par conséquent, les deux techniques sont décidément complémentaires. L'analyse de EMOD, montre que les courants de mode commun générés dans le système sont accessibles sans qu'il soit nécessaire de les mesurer et, par conséquent, de prototyper. Ainsi, le procédé entier devient complètement prédictif.

Le processus d'analyse global CEM est présenté dans la figure suivante.

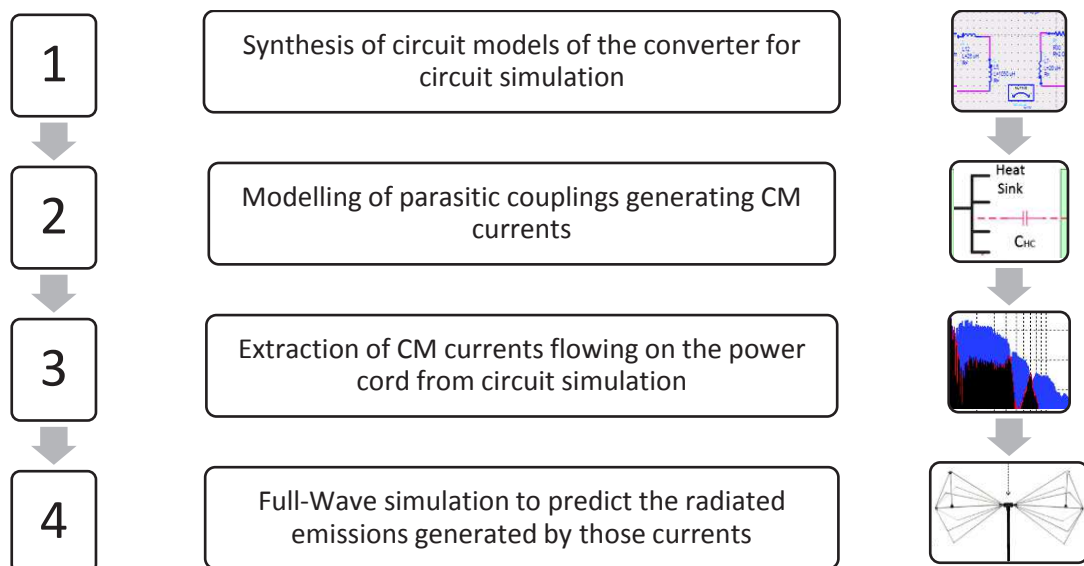


Fig. xv - Schéma général d'investigation d'émissions rayonnées de mode commun

Les conclusions de ce chapitre sont variées.

L'analyse d'un convertisseur Flyback a aidé à établir les techniques qui peuvent aider à prédire les émissions rayonnées à partir de la connaissance des courants de mode commun circulant dans le câble d'alimentation entre la source de courant continu et le convertisseur. L'acquisition des courants de mode commun dans le convertisseur Flyback a été faite par la fabrication d'un PCB très spécifique avec une structure simplifiée, et en mesurant les paramètres du transformateur et en les incluant dans une Netlist à des fins de simulation circuit. De très bons résultats ont été obtenus, et les émissions rayonnées pourraient être validées jusqu'à 120 MHz.

Dans la deuxième partie de ce travail, une contribution pour la prédiction des courants de mode commun dans une perspective prédictive est présentée. Une simulation globale a été établie avec des modèles purement physiques et donc, prédictifs. Cette technique permet une expérimentation virtuelle qui a montré comment un grand nombre de paramètres peuvent être explorés. L'impact d'éléments simples, comme le capteur de courant LEM et l'influence de l'impédance du PCB a été observée.

Peut-être l'aspect le plus important qui peut être exploré avec ces outils prédictifs du point de vue de la conception du moteur, sont les courants de mode commun qui sont générés entre les spires et le noyau. Cela montre, comment chaque composant inséré dans un système mécatronique modifie son comportement à haute fréquence. Les courants de mode commun circulant directement à partir des enroulements, en fin de compte vont traverser jusqu'au cordon d'alimentation pour revenir à la source de courant continu. L'impact de ces courants sur les émissions rayonnées portent fatalement la signature du PCB, et vice-versa. Ignorer un composant sur la chaîne peut conduire à des erreurs de prédiction et le rejet de la certification normative.

5 CONCLUSION ET PERSPECTIVES

Donc, pour conclure, beaucoup de travail doit encore être mené. Tous les moteurs n'ont pas des bobinages concentrés, et la modélisation des enroulements telle que présentée ici peut s'avérer très difficile à effectuer. En outre, des aspects importants de la modélisation d'enroulements doivent encore être détaillés. En effet, les paramètres importants tels que les pertes du noyau ne sont pas encore incluses dans cette modélisation, et bien que les modèles soient utilisés pour des petits signaux, la simulation avec des signaux plus réalistes peuvent être envisagée. Ensuite, bien que ce travail soit très généralisable, la construction de modèles physiques peut parfois être un processus de longue haleine. Mais les modèles mathématiques utilisés ici peuvent facilement être intégrés dans un seul code mathématique ou d'une matrice.

D'autres aspects qui doivent être explorés sont l'influence paramètres des matériaux et d'autres variables telles que les aspects géométriques. Une connaissance approfondie des paramètres physiques est essentielle pour la construction de modèles soignés.

Enfin, une validation expérimentale globale des émissions rayonnées du système comme analysé dans le chapitre IV serait extrêmement rassurante depuis une perspective d'ingénierie. Ce travail est décidément seulement un très petit pas dans la contribution pour comprendre les effets des contraintes difficiles auxquelles les systèmes mécatroniques de puissance devront faire face à

l'avenir. Mais, les modèles basés sur la physique peuvent être une réponse définitive à la nécessité de designers pour mieux comprendre les choix technologiques auxquels ils sont confrontés.

Ce travail a été construit avec l'objectif de se rapprocher des méthodes rationnelles et généralisables qui aident à ce que les processus de conception technique soient plus efficaces et fiables.

Abstract

From the more electrically operated aircraft, to the hybridization of motor vehicles, all the way to electromechanic cardiac implants, compactness has become the holy grail of modern embedded electrical engineering. Indeed, the power-to-weight ratio demands for electromechanical systems has greatly increased. To meet these high integration needs, power electronic converters find a vector of development by increasing their temperature and operating frequencies but also by reducing the switching time of power switches, thus enabling them to reduce their power losses and thereby reducing their cooling requirements. Electric motors and generators operate with various innovative topologies that meet integration, robustness and reliability needs. Motor windings, particularly, are the first motor components on the battle front. It is at the heart of the winding that occur the exchanges between motor and converter. In terms of electromagnetic compatibility (EMC) for embedded systems, the increased frequency and transient stresses in the form of current and voltage edges from the power electronic assemblies are considered steep challenges.

The work presented herein is the result of a close cooperation between the company Novatem and the laboratory Génie de Production of ENIT de Tarbes, through CIFRE funding, in combination with the Labceem platform of IUT of Tarbes. Its aim is to develop predictive models that will serve to determine the consequences of such integration constraints in power mechatronic systems that are in the early stages of design. Conducted disturbances whose HF source is located at the inverter power switches are shaped by the impedances characterizing the coupling path of which the electrical machine is an integral part. This work proposes to develop methods and tools to support the predictive study of electromagnetic compatibility (EMC) of mechatronic assemblies, by attempting to cover a modeling frequency range that goes from 0 to 300 MHz's

In the first chapter of this work, a literature review is detailed for the definition of the context and boundaries of the study. A second chapter focuses on the analytical modeling of concentrated windings in electric motors. The analytical models that are established allow determination of circuit networks settings to perform time- and frequency- domain simulations. Unlike the widespread behavioral models of electrical machine in the literature, the models that are synthesized here take into account the physical parameters of the coils. The user of such models is offered the opportunity to account for the different winding architectures, by changing core parameters such as geometry, insulation materials or permeability. A third chapter describes the establishment of a rational method for extraction of functional and parasitic parameters in multilayer Power PCBs. This method being of a generic and predictive logic aims to account for physical parameters. Finally, in the last chapter, the previously established tools and methods are applied to the study of a real electric vehicle drive system developed by the company Novatem. The physical and predictive value of these tools allows for execution of virtual experimentations on the motor-converter assembly without the need for prototypes. This chapter illustrates the value of a physical approach to modeling the electromagnetic compatibility of mechatronic systems.

Key words: High frequency, Power Mechatronic, Concentrated Windings, EMC, Multilayer PPCB, Conducted Emissions

General Table of Contents

GENERAL TABLE OF CONTENTS

- General Introduction..... 1

- Chapter I: Severe Integration Constraints in Power Mechatronics Systems and Induced Electromagnetic Compatibility (EMC) Consequences..... 7

- Chapter II: Wide Band Analytical Modelling of Actuators with Concentrated Windings and Circuit Implementation for High Frequency Analysis 39

- Chapter III: Extraction of Parasitic Parameters for Power Printed Circuit Boards 131

- Chapter IV: EMC Investigation Method for Power Mechatronic Assemblies and Virtual Experimentation..... 161

- General Conclusions and Perspectives 205

General Introduction

Increasing pressure on compactness and lightness for embedded applications has constantly been put on mechatronic assemblies in the last decades. Mechatronic assemblies are considered as highly integrated electromechanical systems containing a motor fed by a power converter.

Several strategies to reduce the volume and mass impact of mechatronic assemblies have been developed throughout the last decades. In power converters used in mechatronic assemblies, the increase of frequency and switching rates have allowed to dramatically reduce weight too. They have enabled electrical-to-mechanical power to be transformed with low volume and mass impact on the larger system containing it.

In terms of integration, more efficient materials and faster mechanisms (mechanical and electrical) have brought great benefits in terms of power densities in mechatronic systems. But these strategies have also fostered complex problems as heat extraction difficulties and electromagnetic compatibility (EMC) issues.

The presence of parasitic elements as inductive loops, capacitive couplings and damping through dissipative phenomena within the motor/generator's structure contribute to its wide band signature and more specifically, to its Common Mode (CM) and Differential Mode (DM) currents and voltages. In return, the currents flowing throughout the whole electrical system fatally convey the motor and converter signature behaviors. Therefore, EMC and EMI is becoming an increasing concern since high frequency voltages and currents flowing in electrical systems can easily interfere with surrounding sensitive equipment. From a functional and point of view, the integrity of electrical systems, especially in embedded applications must be guaranteed. From a regulatory point of view perspective, the commercialization of mechatronic products depend on the EMC certification.

The leading idea of this work is that increasing power densities of power applications is leading to higher and higher compactness, higher temperature, higher equivalent frequencies of switching and slew rates with more and more integrated functions and different technologies as with RF and digital applications a few decades ago. Available techniques already exist to analyze the impact of such integrated electronics structures. Power electronics behave a lot more like high power fast switching structures as they did several decades ago and techniques used for digital and RF applications might be useful for the study of power applications.

The work presented here is the result of a collaboration between Novatem, a mechatronic system designer and manufacturer, and the Laboratoire Génie de Production of the ENIT engineering school, part of the Institut National Polytechnique de Toulouse and the Labceem platform of the IUT de Tarbes. A temporary collaboration was also made with the Electromagnetic Compatibility Laboratory of the Missouri Science and Technology University in Rolla, Missouri, USA. The expertise of all the partners that supported this work has made possible the achievement of useful models for designing compatible mechatronic systems for industry and embedded applications.

In this contribution, fully predictive tools and methods are synthesized in order to help designers to meet the functional and regulatory demands by virtually experimenting on the electrical behavior of the designed system, drawing conclusions to better handle the prototyping phase.

In the first chapter a literature review is detailed. It allows to put into context the techniques available to adapt to power mechatronics high frequency analysis and to identify the missing methods that need to be integrated into the modeling process.

Based on the conclusions drawn from the literature review, the second chapter features an effort to model the wide band behavior of concentrated winding in electrical machines. The objective is to contribute to the development of a modeling methodology of the electrical machine in the high frequency domain taking into account the physical and geometrical parameters of windings. By taking into account physical parameters, as well as structural layout of the windings and the machine, a rational and predictive tool is synthesized.

In the third chapter the purpose is to investigate the response of large plane structures in complex multilayered PCBs of state-of-the-art power switched converters. The aim is to analyze the response and couplings of power buses and other signal planes in a rational and generic approach in order to integrate them into a larger scale circuit analysis. For this matter, an integral extraction and simulation process is used. Besides, the following described technique allows for including conductive structures surrounding the PCB which is helpful in predicting CM and DM coupling paths and taking into account parasitic inductive and capacitive coupling mechanisms from the PCB layers to conducting surrounding parts.

Finally, in the last chapter, a system-level analysis is overtaken to implement the established models in state-of-the-art power systems for EMC and EMI analysis. Two different applications are used to implement complementary modeling techniques. In the first application a Flyback converter is used to show how the common-mode-induced radiated emissions can be estimated from a circuit simulation provided all components of the converter are properly modelled. In the second application, a Novatem-designed motor is used as a support to illustrate how the common-mode currents can be extracted by using the modelling techniques presented in the second and third chapter.

Chapter I
Severe Integration Constraints in Power
Mechatronics Systems and Induced
Electromagnetic Compatibility (EMC)
Consequences

CONTENTS

Table of figures.....	10
Table index.....	10
1 Introduction.....	11
2 Integration strategies in motor design	12
3 Integration strategies for power converters.....	15
3.1 General structure of power electronics converters	15
3.2 Power density as a measure of compactness	17
4 The association of power converters and motor	20
4.1 State of the art in modelling.....	20
4.2 Emission Bands of power mechatronic systems	23
5 EMC techniques and tools for wide band modeling and analysis.....	24
5.1 General definitions of EMC.....	24
5.1.1 Compatibility and Interference.....	24
5.1.2 Coupling mode and path.....	26
5.1.3 Differential- and Common- conducted Mode.....	26
5.1.4 Fundamental EMI mechanisms inducing common-mode currents and voltages	28
5.2 Circuit simulation for common- and differential-mode impedance	31
5.2.1 Impedance synthesis for analysis.....	31
5.2.2 Scattering parameters	32
6 Conclusion	33
7 References.....	34

TABLE OF FIGURES

Fig. I. 1 – Generalized constitution of mechatronic assemblies	11
Fig. I. 2 - Electrical motor / generator constitution	12
Fig. I. 3 - Implications of high speed / high torque at rated power	13
Fig. I. 4 - Rotational speed impact on peripheral rotor speed as a function of rated power	13
Fig. I. 5 - Function of power electronics converters between two different sources or loads.....	15
Fig. I. 6 - Power converters functional structure	16
Fig. I. 7 - The role of power converters in a mechatronic system.....	16
Fig. I. 8 - Power density of power electronics converters by year and forecast [7]	17
Fig. I. 9 - Power density predictions by type of application [5].....	18
Fig. I. 10 - Soft switching principle [8]	18
Fig. I. 11 - Switching energy decrease with newer IGBT technology	19
Fig. I. 12 - Theoretical speeds attainable with wide bandgap technology [7].....	20
Fig. I. 13 - Cable, Motor and total absorbed common-mode current spectra of a MS	21
Fig. I. 14 - Transient DM voltage at motor leads (red) and at converter's output (blue).....	21
Fig. I. 15 - Measured typical behavior (CM, DM) – Novatem ©	23
Fig. I. 16 - EMC limits, margins and compatibility zones in emissions and susceptibility.....	25
Fig. I. 17 - Aggression and susceptibility scheme in EMI.....	25
Fig. I. 18 - Two conductors carrying currents I1 and I2.....	26
Fig. I. 19 – Differential-mode path	27
Fig. I. 20 – Common-mode path	27
Fig. I. 21 - Signal level vs. time and switching times	28
Fig. I. 22 - Current-induced CM path and EMI	29
Fig. I. 23 - Assymmetrically fed load and circuit loop modelling [32]	30
Fig. I. 24 - Current-induced CM path and EMI	30
Fig. I. 25 - Electromagnetic system of two conductors separated by a dielectric.....	31
Fig. I. 26 – One type of circuit modelling of the two-conductor system.....	32
Fig. I. 27 - Equivalent transformations between impedance and scattering parameters	33

TABLE INDEX

Table I. 1 - Impact of pair poles in currents frequencies	14
Table I. 2 - Examples of realizations by Novatem® and their power-to-weight ratio	15
Table I. 3 - Identified emission bands of mechatronic assemblies components.....	24
Table I. 4 - Maximum equivalent frequency at switching by technology	29

1 INTRODUCTION

Power mechatronic systems can be broadly defined as highly integrated electromechanical systems. They are especially adapted for embedded applications as in airplanes, vehicles, robotics or human body implants.

Mechatronic systems allow for electrical-to-mechanical power to be transformed with low volume and mass impact on the larger system containing it. The core components of mechatronic assemblies are the actuator, which accomplishes the main task of transforming electrical power into mechanical power (motor) or vice versa (generator), its converter which ensure the actuators' current feeding, control components cooling systems and the mechanical interface. In Fig. I. 1, a fragmented view of a mechatronic assembly as assumed in this work is presented. The fundamental architecture of a mechatronic assembly is there described. The DC source feeding the power converter is not a part of the analysis.

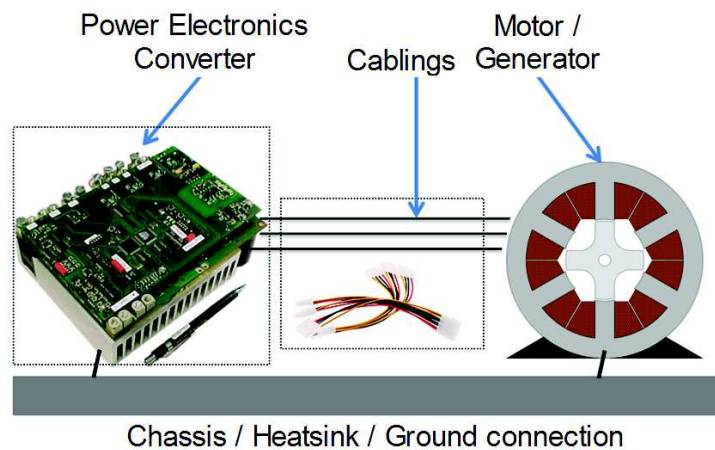


Fig. I. 1 – Generalized constitution of mechatronic assemblies

The layouts of different mechatronic systems depend on a wide range of factors such as application, rated performances, adaptation to mechanical interfaces, cooling requirements, weight and volume and environmental factors as humidity and temperature.

Increasing pressure on compactness and lightness for embedded applications has constantly been put on mechatronic assemblies in recent years. Several strategies to reduce the volume and mass impact of mechatronic assemblies have been developed throughout the last decades. Indeed, high rotational speeds have been an important vector for increase in power density for electrical motors. In power converters used in mechatronic assemblies, the increase of frequency and switching rates have allowed to dramatically reduce weight too.

In terms of integration, more efficient materials and faster mechanisms (mechanical and electrical) have brought great benefits in terms of power densities in mechatronic systems. But these strategies have also fostered complex problems as heat extraction difficulties an electromagnetic compatibility (EMC) issues.

2 INTEGRATION STRATEGIES IN MOTOR DESIGN

An electric motor can be defined as an organ transforming electrical into mechanical power. An electric motor is often reversible, meaning the input mechanical power can be transformed into electrical power and is called a generator. A motor is composed of a moving part called rotor and a static part called the stator. Windings are located in the stator and are responsible for the transformation of a varying magnetic field into electrocinetic currents and vice versa. Fig. I. 2 shows a description of the component parts of an electrical motor or generator.

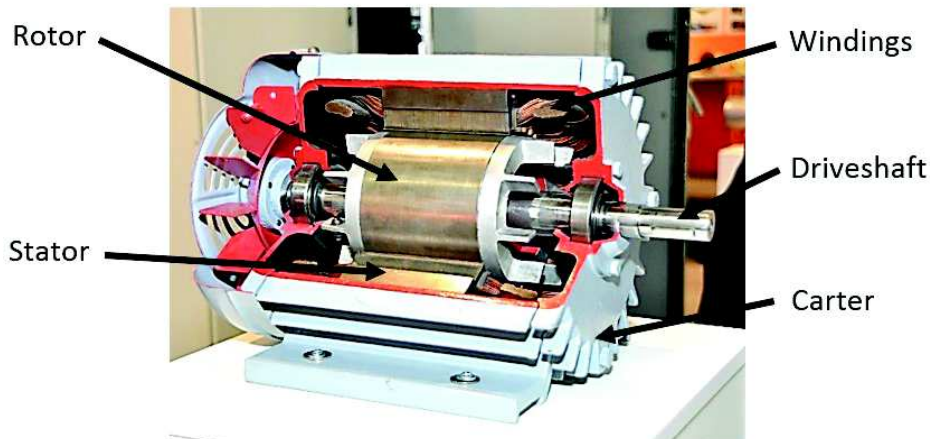


Fig. I. 2 - Electrical motor / generator constitution

To increase power density, improvements in materials has been fundamental. Polarization of permanent magnets is fundamentally related to volume reduction as higher polarization helps decrease rotor volume for a constant torque.

In the same manner, higher current densities have an impact on reducing volumes. But higher current densities induce higher Joule losses, thus raising the temperature of conductors and creating accelerated aging on insulation polymers and other materials.

Besides, an increasing pole pairs in motors, brings benefits concerning ferromagnetic yokes' volumes. The number of pole pairs p has a direct impact on the frequency of the magnetic field producing the torque and therefore, in the reduction of the yokes' volume [1].

Nonetheless, the most efficient way that power density has been increased in recent decades, is definitely higher rotor speed. Mechanical power P_m (W) is delivered as the product of rotational speed Ω (rad/s) and torque T in (Nm) as described in Fig. I. 3. Torque is linearly related to the actuator's volume. For lower torques, lower masses for given rated powers can be achieved.

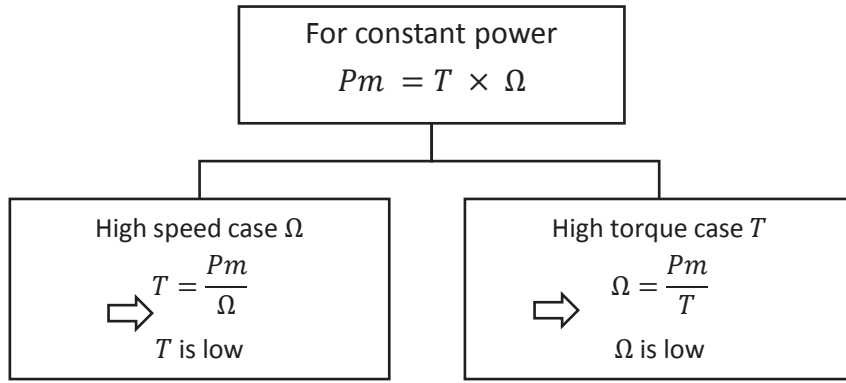


Fig. I. 3 - Implications of high speed / high torque at rated power

In the case of the permanent magnet synchronous motor (PMSM) the maximum moment of the torque deliverable by the motor while fed by a current density charge K (A/m) and having permanent magnets of remnant polarization J_p (T) and α being a constant can be approximated by [1]:

$$T \approx \alpha \cdot V_{rot} \cdot J_p \cdot K$$

V_{rot} is the motor's rotor volume. Therefore, torque is a major contributor of the motors' volume and consequently, mass. Indeed, to reduce volume, speed has become a major vector for mechatronic systems' volume and mass reduction, thus improving power density [1]–[3].

Furthermore, materials improvements have allowed this progress in terms of speed to be achieved. Carbon-fiber or titanium-vanadium (TA6V) sleeves around the rotor allow to preserve the integrity of permanent magnets in the rotor for high-speed permanent magnet machines with peripheral speeds reaching very high speeds [1], [2].

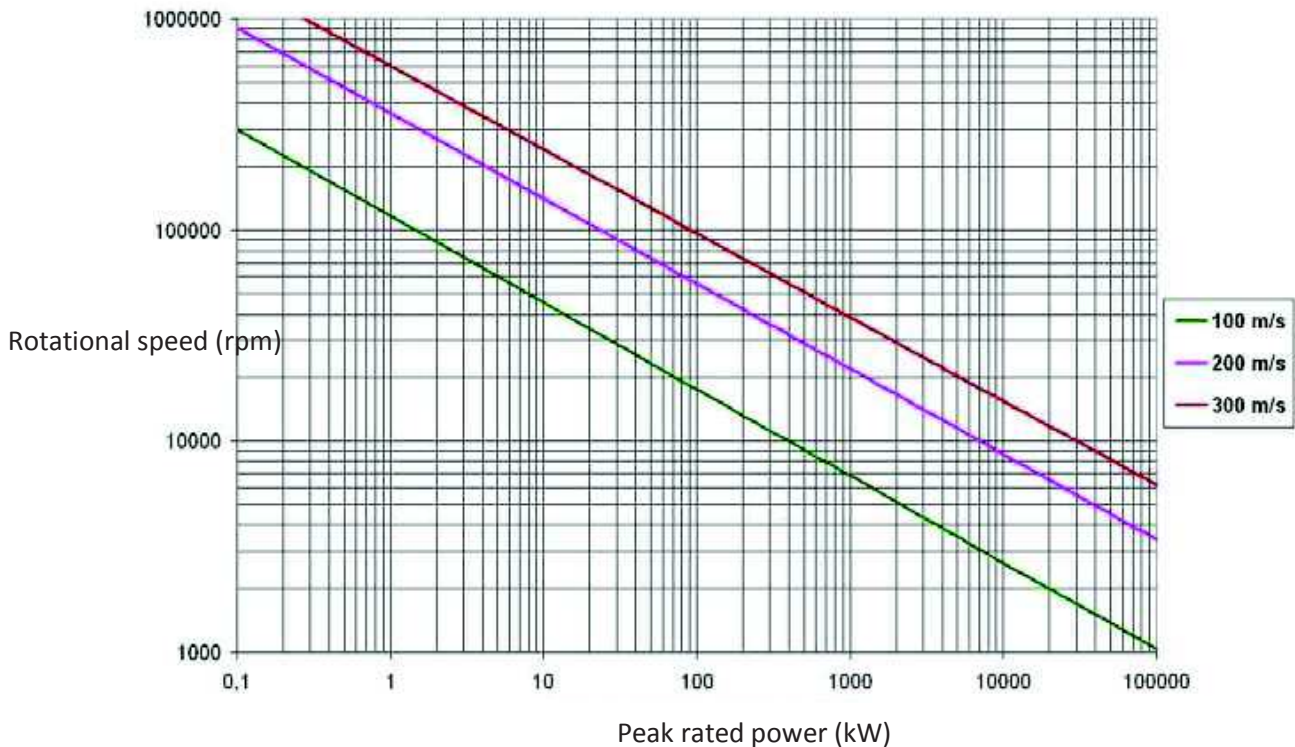


Fig. I. 4 - Rotational speed impact on peripheral rotor speed as a function of peak power

In Fig. I. 4 is shown the feasibility barriers of high speed motors in terms of peripheral rotor speed against power density and rotational speed with state of the art technologies and materials.

Peripheral speed accounts for the “destructive” parameter which has to be taken into account for the design. Improvements in materials can increase the peripheral capabilities of such structures. But today, limits are around 300 m/s. High rotational speeds that are useful for reducing mass and volume, cannot exceed certain limits with state-of-the-art technology. The larger the rotor diameter, the higher its peripheral speed for constant rotational speed. Today, design has to take into account feasibility limits in order to maximize the rotational speed capabilities for increasing power densities.

But, even when fostered by materials achievements, increased rotational speeds induce increased fundamental current frequencies.

Rotating fields in electric motors of all kinds are created by currents. And, in a condition called the *synchronism condition*, (even for asynchronous motors), the frequency of the currents in the stator ω_s and the rotor speed Ω must verify the condition:

$$p\Omega = \omega_s - \omega_r$$

Where, ω_r is the electrical frequency of the currents at the rotor in the case of the asynchronous motor, and is **strictly zero** for the other cases including “DC motors”, and p is the number of pair of poles of the machine.

Therefore, increasing rotor speeds to increase power density induces higher current frequencies to the motor. Typical examples of current frequencies for different synchronous ($\omega_r = 0$) motors is found in Table I. 1.

Table I. 1 - Impact of pair poles in currents frequencies

Rotor speed Ω	Pole pairs p	Currents frequency ω_s
1.5 krpm	2	50 Hz
12 krpm	2	800 Hz
50 krpm	1	833 Hz
60 krpm	2	2 kHz
80 krpm	1	1.33 kHz

In Table I.2 are resumed some of the motors designed by Novatem®, illustrating the importance of speed in the mass reduction of mechatronic systems. The masses correspond only to active electromechanical components, without power converters nor housing.

Table I. 2 - Examples of realizations by Novatem® and their power-to-weight ratio

Motor type	Application domain	Peak power	Max speed	Mass of active components	Power density
Permanent magnet synchronous motor	Aeronautical	1.5 kW	1.5 krpm	1.8 kg	0.8 kW/kg
Switch reluctance motor	Automotive (traction)	20 kW	12 krpm	17 kg	1.2 kW/kg
Switch reluctance motor	Aeronautical	2.3 kW	60 krpm	0.9 kg	2.4 kW/kg
Asynchronous motor	Aeronautical	80 kW	50 krpm	25 kg	4 kW/kg
Permanent magnet synchronous motor	Automotive (exhaust recovery system)	120 kW	80 krpm	13 kg	9.2 kW/kg

3 INTEGRATION STRATEGIES FOR POWER CONVERTERS

3.1 GENERAL STRUCTURE OF POWER ELECTRONICS CONVERTERS

Power converters are static energy transformers that are based on power semiconductor switches. Their purpose is to adapt the electrical levels and waveforms between two sources or a source and a load with the highest possible efficiency (cf. Fig. I. 5).

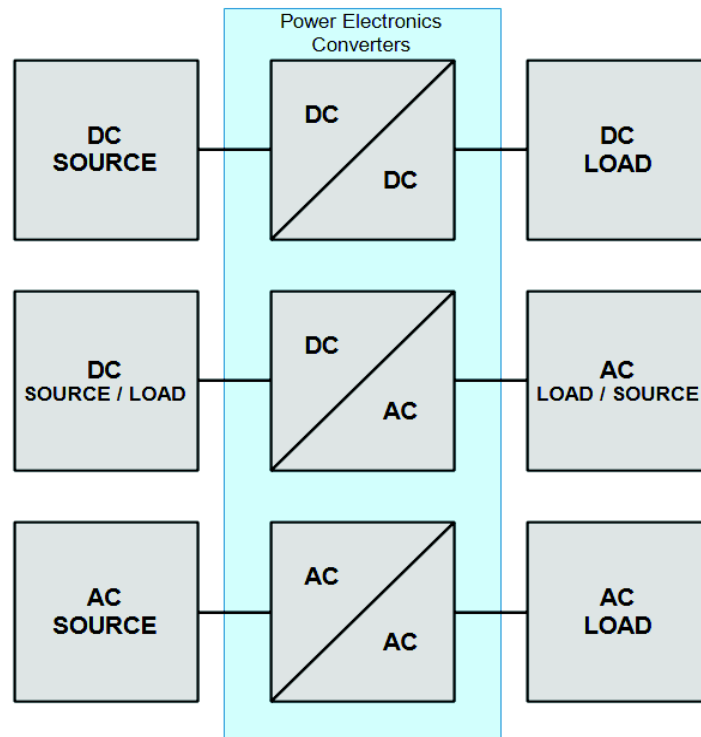


Fig. I. 5 - Function of power electronics converters between two different sources or loads

Contrary to low-power electronics, where dissipative processes for regulating voltages and currents are not a fundamental concern, in power electronics efficiency is a major vector of design. For example, regulation of voltages in low-power electronics can be performed by modulating the base current in a transistor junction thus creating a voltage drop across the junction that is an image of the

modulated base current. However, for power applications, dissipative process are replaced by switching processes to avoid losses.

A schematic view of a power converter is presented in Fig. I. 6.

By chopping input voltage and current, the controlled switching power semiconductor switches can transform them into voltage or current with defined characteristics feeding the load.

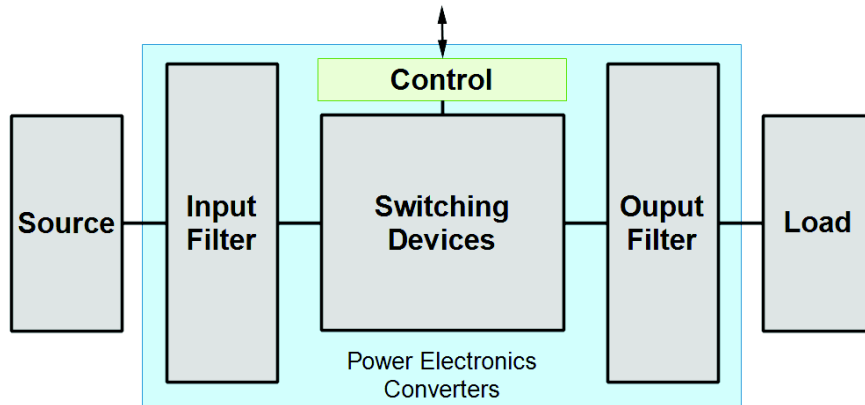


Fig. I. 6 - Power converters functional structure

For mechatronic systems, the typical architecture is composed of a DC/AC converter fed by a DC source and the source is a motor/generator with eventually, cablings in between (Fig. I. 7).

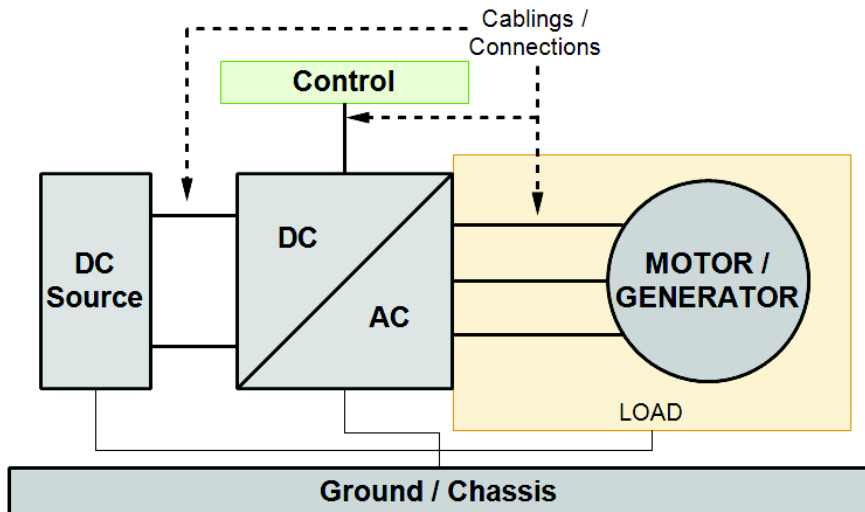


Fig. I. 7 - The role of power converters in a mechatronic system

Power converters typically have switching frequencies ranging from few kilohertz to even few megahertz [4]. And, although switching frequencies of static converters are still significantly lower than for digital components as clocks and ICs, an increase of switching rates has helped to reduce the embedded volume of power electronics.

By increasing the switching frequency, filtering elements that constitute core components of the switching converters become smaller. Inductance elements used for filtering for example, are much

more efficient at filtering currents at high frequencies, thus reducing its volume and mass. Capacitors are more efficient at filtering high frequency voltages also.

3.2 POWER DENSITY AS A MEASURE OF COMPACTNESS

The concept of power density is a rational tool to compare converters performance. It is defined as:

$$\rho = \frac{P}{V} \text{ [kW/dm}^3\text{]}$$

Power density is equivalent to the microelectronic industry criteria as a measure of progress related to the integration of greater number of transistors within a given volume [5] better known as Moore’s Law. In this context, in [6], the author shows the increasing power density of converters of the last decades.

In an analog manner as for the microelectronic industry, a steady increase in power density has been observed as shown in Fig. I. 8. Over the last few decades, power density has doubled every ten years. More recent research shows the same overall trend as shown in Fig. I. 9 where predictions of power density for 2020 are assumed given the demonstrated trend.

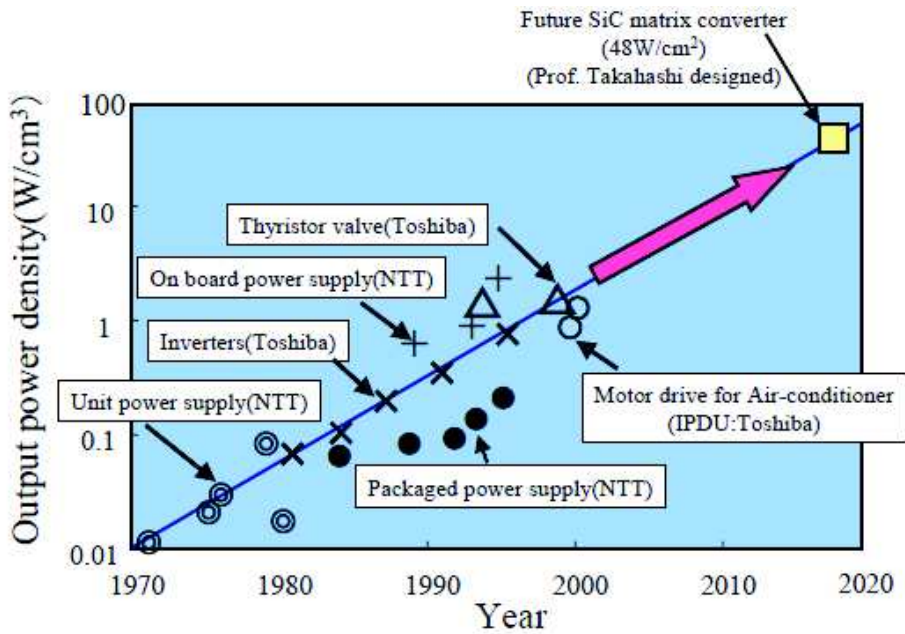


Fig. I. 8 - Power density of power electronics converters by year and forecast [7]

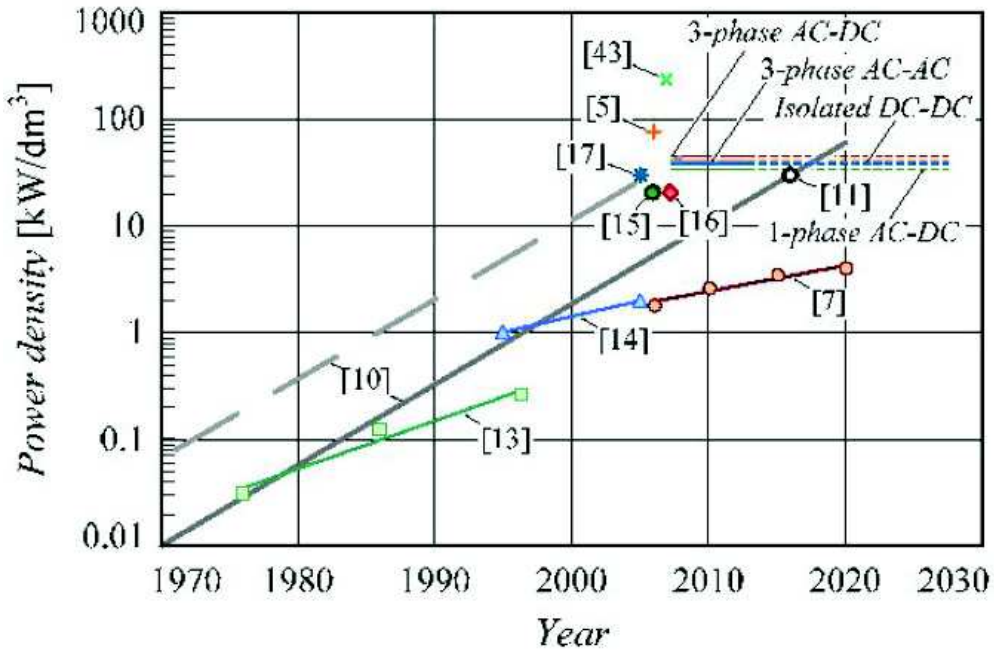


Fig. I. 9 - Power density predictions by type of application [5]

But, to increase compactness in power supplies and other converters, few available options are offered. Traditionally, the most common technique has been the increase of switching frequency. For doubling the power density of a power converter, recent research show that an increase of switching frequency by a factor of 10 is needed [4], [5].

An increase of switching frequencies is expected in the next years and in extreme cases for low-to-medium power supplies, switching frequencies have already been increased to the VHF band [4]. However, switching frequencies are not the only substantial technique for power density increase. Reduction in turn-off and turn-on times has a significant impact in switching losses reduction and therefore, in cooling systems volume reduction. Nonetheless, decreasing turn-off and turn-on times lead to richer equivalent frequency spectra since shorter rise and fall times are equivalent to harmonic-rich squared signal transitions.

But, soft switching techniques however, have been introduced mainly to avoid shorter and shorter rise and fall times and thus, avoiding high dV/dt and dI/dt which translates to lower emissions [8]. Soft switching allows lower losses for larger rise and fall times, since turn-on or turn-off is made at zero voltage or zero current transitions. The soft switching principle is illustrated in Fig. I. 10.

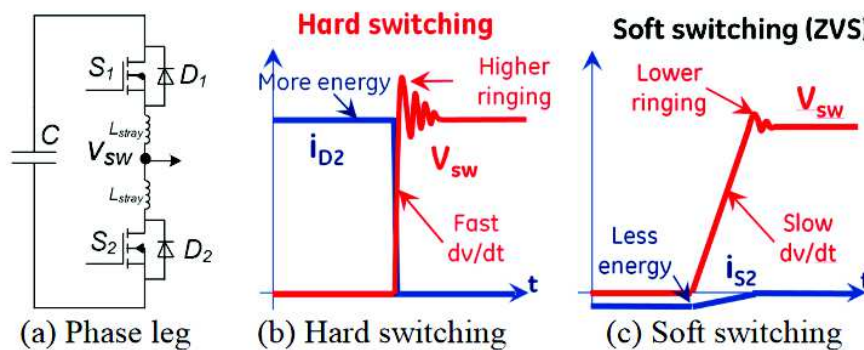


Figure 1. Noise reduction through soft switching

Fig. I. 10 - Soft switching principle [8]

However, complex soft switching techniques are not always available as they involve complex, more expensive layouts and is not suited for all modulation techniques [9].

Although an increasing pressure is put on switching frequency and lower switching losses, a decrease in switching energy has also been observed first in classic Si components as shown in Fig. I. 11 thus lowering the needs of faster switching times [10].

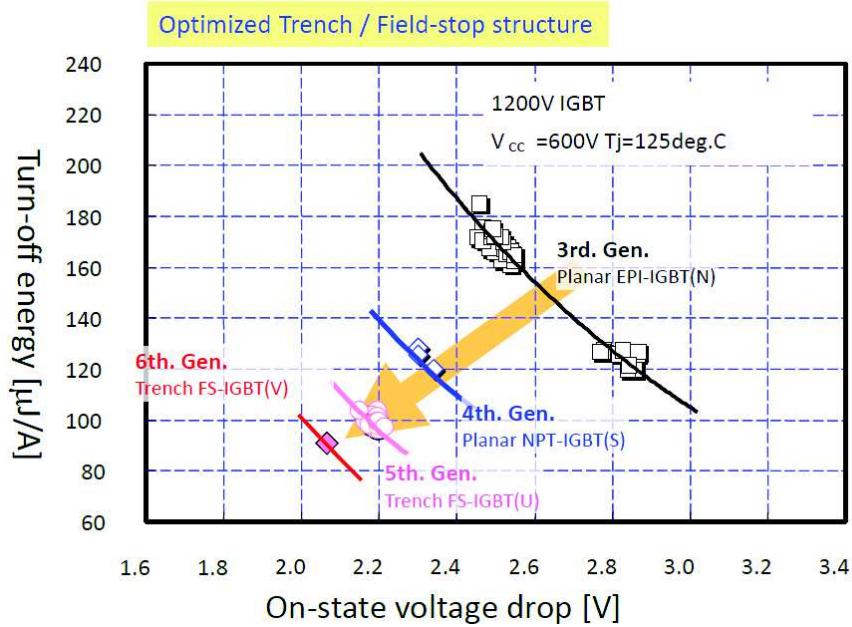


Fig. I. 11 - Switching energy decrease with newer IGBT technology

Also, reduction of volumes has been achieved by reducing thermal losses thus reducing cooling components in embedded assemblies. But thermal losses reduction is mostly achieved by reducing the turn-on and turn-off intervals of power electronic switches.

Furthermore, compound semiconductors or wide bandgap semiconductors such as Gallium Nitride (GaN) or Silicon Carbide (SiC) devices, have introduced a leap in the possibilities to increase the performance in power electronics. They allow higher voltage, temperature and power handling thus improving power density [11]. Higher frequency performance of such devices is illustrated in [7]. Fig. I. 12 shows the theoretical speed limit of state of the art Si technology compared with compound devices in terms of turn-off charge and forward voltage.

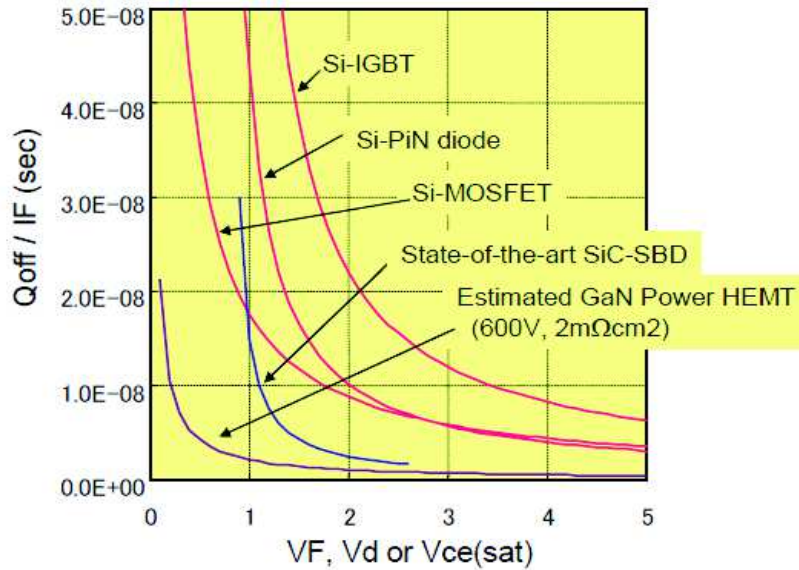


Fig. I. 12 - Theoretical speeds attainable with wide bandgap technology [7]

Better temperature withstanding of such components is also a vector of power density increase. Higher operation temperature decreases the need of lower losses which can be translated into slower rise and fall times for switching components.

So, a clear trend of faster turn-on and turn-off can't be established especially since Electromagnetic Interference (EMI) has become an essential part of electrical systems design. But increasing frequency induces increasing switching losses regardless of the commutation performances, and reducing switching losses can, among others, be achieved by reducing turn-on and turn-off times. New wideband gap components have increased frequency performance and temperatures allowing for yet higher power densities.

A direct consequence of such improvements in functional performances of switched power supplies is a rise in electromagnetic signature of the whole system. The increasing conducted and radiated emissions CE and RE, EMI in conducted and radiated mode (Radio Frequency Interference or RFI) are an increasing concern in nowadays design processes.

4 THE ASSOCIATION OF POWER CONVERTERS AND MOTOR

4.1 STATE OF THE ART IN MODELLING

The need for wide band modelling of motor/generators derives from the more general problem of modelling inverter-fed drives and systems for several purposes, one of which is characterizing the EMC/EMI behavior of these assemblies.

The presence of parasitic elements (inductive loops, capacitive couplings and damping through dissipative phenomena) into the motor/generator's structure contribute to its low and high frequency (wide band) signature and more specifically, to its Common Mode (CM) and Differential Mode (DM) currents and voltages [12]–[14]. In return, the currents flowing throughout the electrical system fatally convey the motor signature behavior.

As stated in the previous paragraph, increasing values of dV/dt and dI/dt and electrical architecture specifications in embedded systems along with severe electromagnetic environments, are

to be integrated into the design of motors and generators for mechatronic assemblies. Thus, new and increasing potential perturbations modify the conventional state-of-the-art methods of modelling the entire mechatronic assembly for EMC/EMI purposes, and consequently, the machine itself.

In Fig. I. 13 a typical mechatronic system spectra of CM currents is illustrated. It has been measured in a design made by Novatem. In some configurations, long length cables between the inverter and the electrical machine, may cause the CM currents to be higher than the limit given by standards (as DO160 in aeronautical applications), and overvoltage (up to 2 times the rated voltage) to occur in machines' input as shown in Fig. I. 16.

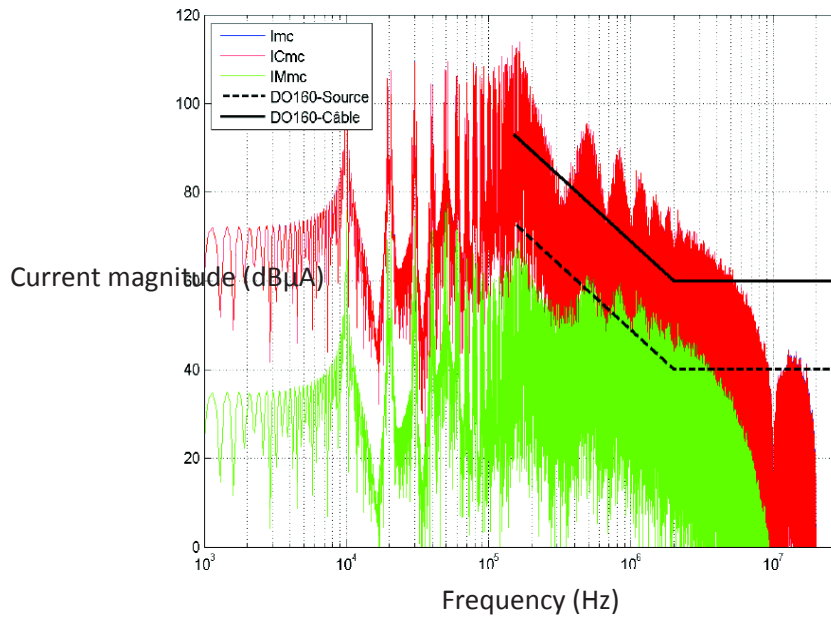


Fig. I. 13 - Cable, Motor and total absorbed common-mode current spectra of a mechatronic system and DO-160 limits – Novatem©

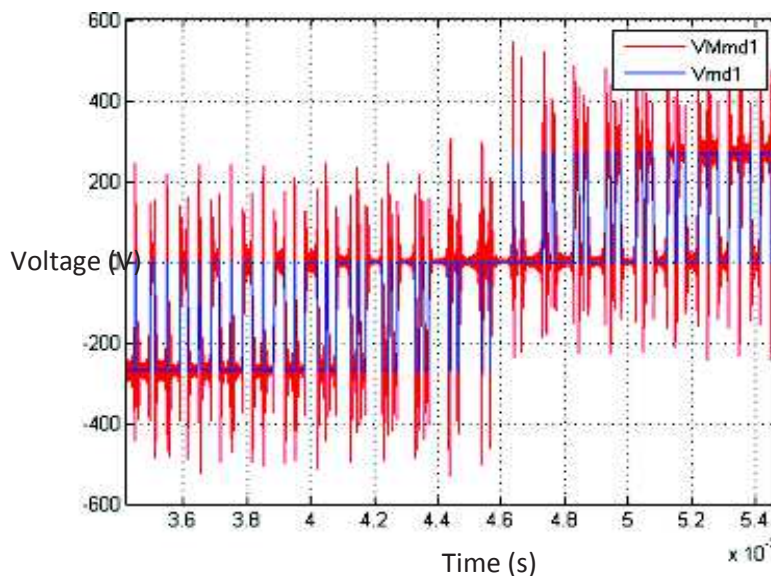


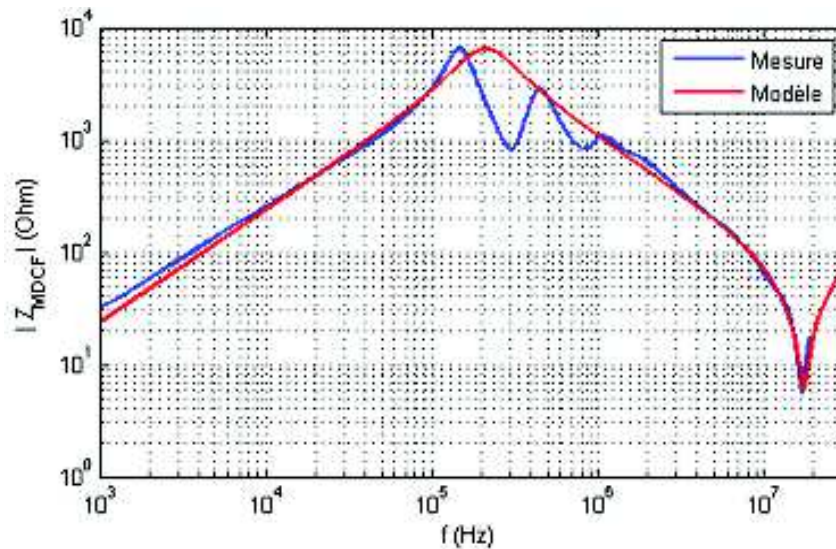
Fig. I. 14 - Transient DM voltage at motor leads (red) and at converter's output (blue) – Novatem ©

Most of the machine modelling has been focused on conducted emissions (CE) issues [12]–[15], mainly because of outdated norms regulating power assemblies only into the conducted emissions zone, as does the DO-160 norm for civil aviation. As a consequence, few modelling efforts have been carried out above 30 MHz. In some special cases however, as presented in [13] up to 100 MHz analysis has been done or in [16] where modelling seems to be carried out for frequencies up to 1GHz.

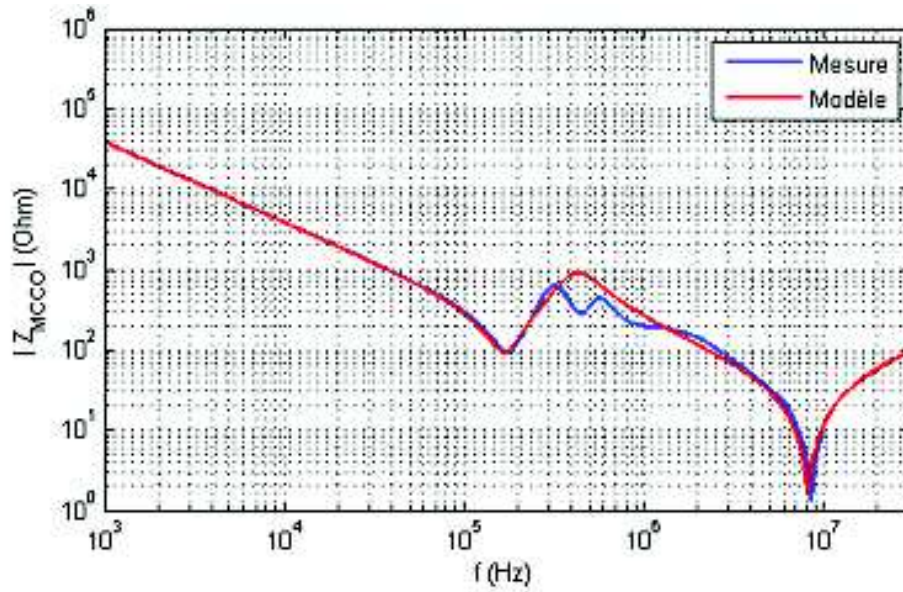
Although very few studies are available, significant radiated interferences above 100 MHz in inverter-fed AC drives have been well documented [17], [18]. This acknowledgement among other symptoms should push the development of models up to frequency ranges where efficient radiation of cablings and long metallic structures of the electrical systems may potentially appear. The parasitic capacitances of the windings play a fundamental role in this EMI issue. Turn-to-turn and turn-to-core capacitances within the very heart of the motor contribute to HF current leaks to the grounding network and CM antenna mode currents leading to radiated emissions potentially exceeding regulations [19].

Furthermore, functional aspects of inverter-fed drives and mechatronic assemblies for embedded applications are at the very basis of the need for accurate modelling of the wide band behavior of the structures. Safety, availability and robustness of these assemblies, especially in embedded applications justify such an effort. For instance, high switching rates induce over-voltages that appear at the electrical machine level, which can be destructive for the winding insulation (premature aging of insulation, partial discharge in dielectric materials...) [20], [21].

Common mode and differential mode impedance analysis of the actuators and windings is a usual and efficient way to have good prediction of the EMC behavior of the machine. Experimental impedance measures in DM and CM are carried out to characterize the overall machine behavior. These results are currently used to fit behavioral models with good results as shown in Fig. I. 15.



(a) Differential Mode



(b) Common Mode

Fig. I. 15 - Measured typical behavior (CM, DM) – Novatem ©

The frequency domain modelling is widely used for modeling purposes because of high simulation speeds especially for large systems. It is noted that the approach hasn't been able to deal with inherent nonlinear phenomena of couplings [14], [22]. On the other hand, other methods combine a simple time domain and frequency domain model whose accuracy is fairly useful for modeling the Common Mode (CM) and Differential Mode (DM) behavior. Based on identification process, measurements of common mode and differential mode impedance of synchronous and induction machines allow the parameterization for time and frequency domain simulations where models are fitted to measurements by identifying significant points in the impedance plot and relating them, when possible, to actual winding parameters [15], [23]. Unfortunately, the optimal model tuning is obtained when some parameters not directly related with winding parameters are introduced. Moreover, these same parameters, for different machines, do not correlate to general trends of increasing rated power nor size [13].

Thus, it seems very difficult to predict EMC behavior between the inverter and the machine, starting from the design phase, when both machine and inverter are co-designed for mechatronic purposes with behavioral modelling techniques.

4.2 EMISSION BANDS OF POWER MECHATRONIC SYSTEMS

The latter developments leads to optimize the efficiency of electromechanical actuators associated to their power electronics and cabling. Consequently, the power-to-weight ratio constraints, the increasing nominal and switching frequencies and the integration challenges on geometrical dimensions contribute to new severe Electromagnetic Interferences (EMI) within the mechatronic assemblies. These cases of new potential perturbations modify the conventional state-of-the-art methods of driving and monitoring of coupling modes of the system, for Electromagnetic Compatibility (EMC) issues. To put into context, the complexity of the EMC analysis of such structures comes from the various ranges of emissions found to be present. Very different and wide emission bands for several subparts of mechatronic assemblies have been recorded in the above literature. These emission bands are summarized in Table I. 3.

Table I. 3 - Identified emission bands of mechatronic assemblies components

Bands	0-9kHz	9-150kHz	150kHz-30MHz	30-300MHz	300MHz-3GHz
Coupling modes	-Conducted, Very Low Freq.	-Conducted, Low Freq.	-Conducted HF -Near Field Radiated	- Conducted HF -Near Field Radiated -Far Field Radiated (RF)	-Far Field Radiated (RF, μ waves)
Emission zones	Electromechanical actuators			Power Electronics Converters	
		Analog and Digital control circuits			

5 EMC TECHNIQUES AND TOOLS FOR WIDE BAND MODELING AND ANALYSIS

As can be seen, in power applications, compactness and severe integration constraints have important implications.

By reducing the distance between power converters and actuators, parasitic impedances and coupling paths are drastically reduced. Therefore, from an emissions point of view, lower emissions related to antenna mode currents are present. But for embedded systems, cablings and other large metallic conductors can represent efficient radiating parasitic antennas. Furthermore, control components are closely installed to power converters, rendering them susceptible switching-generated pollution.

To properly model the high frequency and wide band behavior of such structures, a thorough analysis of each subcomponent of mechatronic assemblies must be carried out. A description of main inducing mechanisms of high frequency behavior and their modeling is presented here after.

The leading idea of this work is that increasing power densities of power applications is leading to higher and higher compactness, higher temperature, higher equivalent frequencies of switching and slew rates with more and more integrated functions and different technologies as with RF and digital applications a few decades ago. Available techniques already exist to analyze the impact of such integrated electronics structures. Power electronics behave a lot more like high power fast switching structures as they did several decades ago and techniques used for digital and RF applications might be useful for the study of power applications.

5.1 GENERAL DEFINITIONS OF EMC

5.1.1 Compatibility and Interference

An electrical system in a certain environment is electromagnetically compatible if its emission levels are low enough to stay not surpass the emission limit and its susceptibility levels high enough to stay above the immunity limit (cf. Fig. I. 16). The immunity and emission levels are, for most cases determined by normative authorities. These limits are stated in standards that account for the emission and susceptibility levels that a system should be able to be commercialized. If the system complies with the standard, the system is certified to be compatible. The standards state the test environment where the immunity and emission test should be carried out, the aggression levels and instruments for measurement.

The immunity margin and emission margin are statistically determined zones that give a certain safety margin to compatibility in order to account for uncertainties in the certification process or for

emission or susceptibility mechanisms in the tested system that couldn't be predicted by the standards. A compatible system will **probably** not interfere with another compatible system.

Since immunity and emission limits are mostly empirical and statistically established, in some cases, systems can interfere with each other regardless of being certified. EMI can appear among compatible systems.

But definitions of immunity and emission limits can be given from a functional point of view. Compatibility zone limits can then be given for safety purposes, and in a non-certification process, especially when the systems are not for commercialization nor industrial applications.

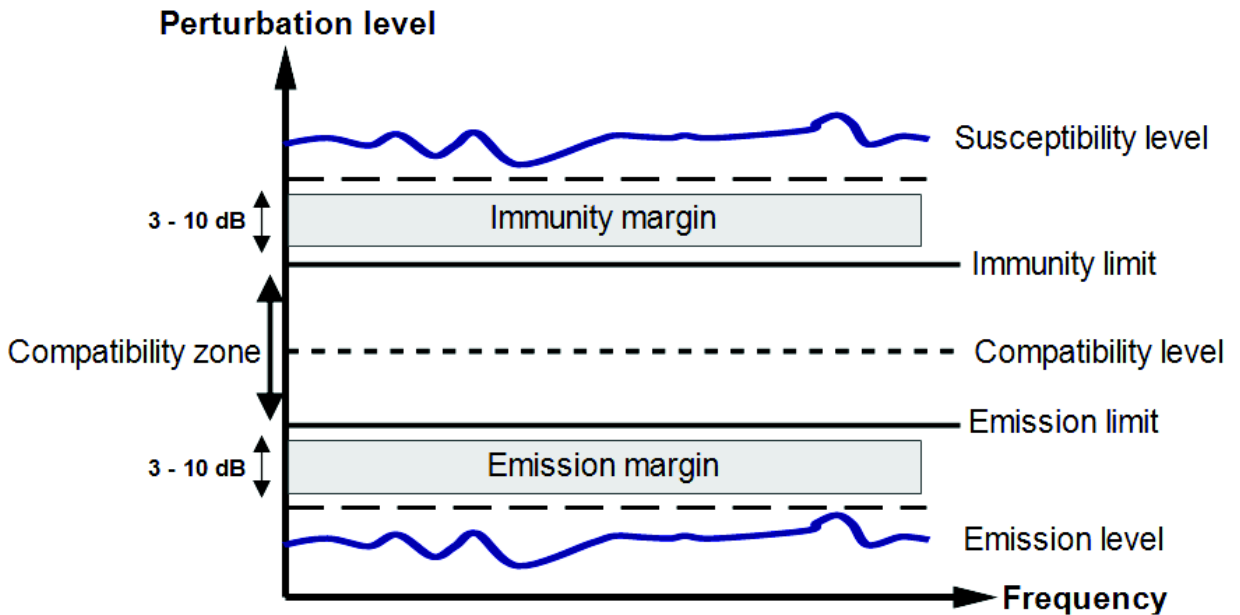


Fig. I. 16 - EMC limits, margins and compatibility zones in emissions and susceptibility

When interference appears, a source interferes with a victim through a coupling path in a certain coupling mode. Fig. I. 17 shows the perturbation mechanism and the areas of investigation according to the nature of the coupled element of the scheme.

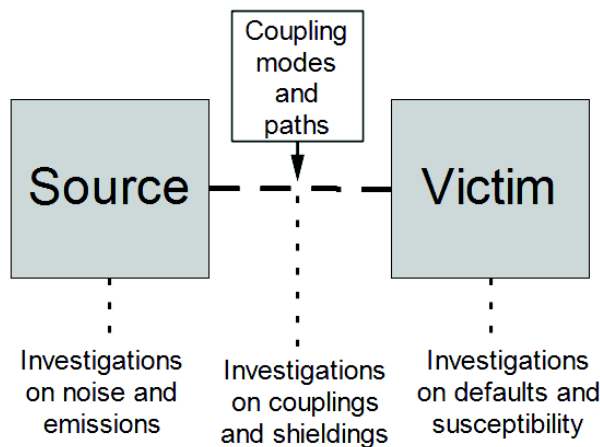


Fig. I. 17 - Aggression and susceptibility scheme in EMI

5.1.2 Coupling mode and path

A coupling mode is the mechanism from an electromagnetic point of view in which a source of perturbation interferes with a victim of perturbation. There are two types of coupling modes [24], [25]:

- Radiated mode

Radiated mode can still be divided into two subcategories:

- Far field radiated mode

For distances larger than the near-far-field-frontier (NFF) calculated from the wavelength of the field λ as $NFF = \lambda/2\pi$ in meters, the electromagnetic can be analyzed by taking only one of its component, either magnetic or electric, since linearity between the two components, the linearity coefficient is called wave impedance, exists depending on the media of propagation. The coupling path is generally the air, but can be any media defined by its permittivity and permeability.

- Near field radiated mode

For distances close to the electromagnetic source, and inferior to NFF, the two components of the electromagnetic field are considered to be decoupled.

- Conducted mode

Conducted mode can be divided into two subcategories as will be detailed presented later:

- Common-mode
- Differential-mode

This is the mode that will be thoroughly analyzed in this work. The coupling paths are common impedances i.e. capacitances, inductances and resistances.

5.1.3 Differential- and Common- conducted Mode

Conducted and radiated EMI can be produced both by Differential-Mode DM and Common-Mode CM currents and voltages. For this matter, DM and CM currents and voltages (driving currents through impedances) are essential parameters to analyze the potential emissions of an electrical system [26]–[28].

Let us consider two conductors carrying a current I_1 and I_2 respectively as shown in Fig. I. 18 [26]:

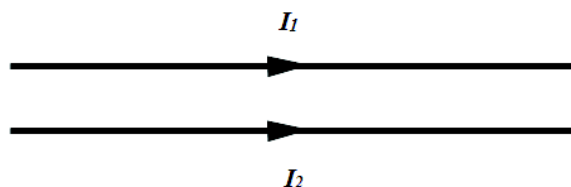


Fig. I. 18 - Two conductors carrying currents I_1 and I_2

The DM current I_D can be assumed to be the functional current driving a load through the two wires. At the same cross section of the two wires, DM currents in wire 1 are the same as in wire 2 but out of phase by 180° (or in opposite direction). The CM currents I_C , at the same cross section of the wires, have the same magnitude and phase (they have the same direction).

At the same cross section of normal vector pointing to the right for the two wires, it can be thus written that:

$$I_1 = I_C + I_D$$

$$I_2 = I_C - I_D$$

And therefore:

$$I_D = \frac{I_1 - I_2}{2}$$

$$I_C = \frac{I_1 + I_2}{2}$$

CM currents are easily generated by couplings to surrounding metal objects through which return paths can appear. An example of common- and differential- mode current is presented in Fig. I. 19 and Fig. I. 20.

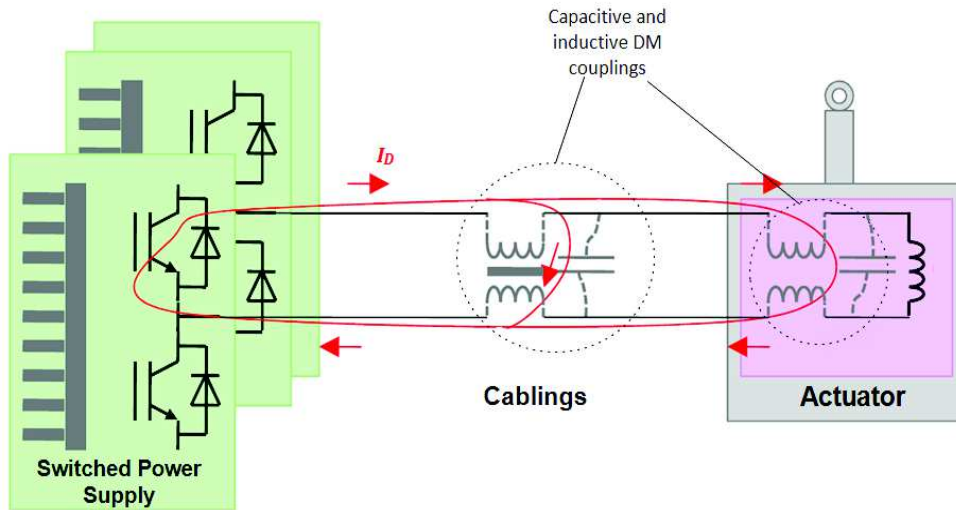


Fig. I. 19 – Differential-mode path

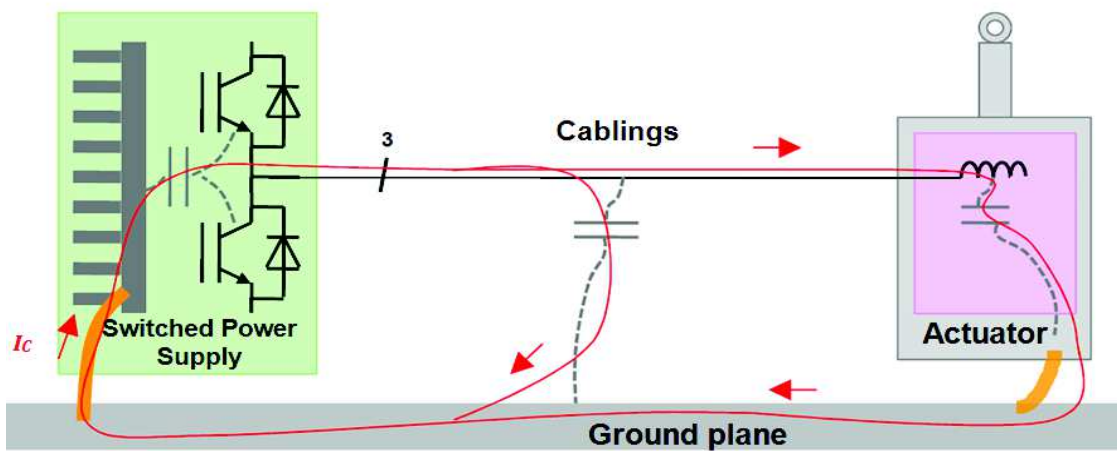


Fig. I. 20 – Common-mode path

CM and DM voltages are the voltage potential differences created by CM and DM currents through respective conductors.

Common-mode currents and voltages however have a wide variety of inducing mechanisms. In [24] and [26], C. R. Paul demonstrates the need to properly consider and model CM currents to adequately predict radiation from printed circuit boards and attached elements.

5.1.4 Fundamental EMI mechanisms inducing common-mode currents and voltages

5.1.4.1 EMI sources in switched power supplies

For a given signal or electromagnetic perturbation, an equivalence between time-domain and frequency-domain can be mathematically demonstrated with Fourier transform and its inverse. In the particular case of the switched power supplies, a simple relationship can be used to link the rise time of a signal to its equivalent maximum frequency in the spectrum. Fig. I. 21 represents a switched voltage or current as a function of time.

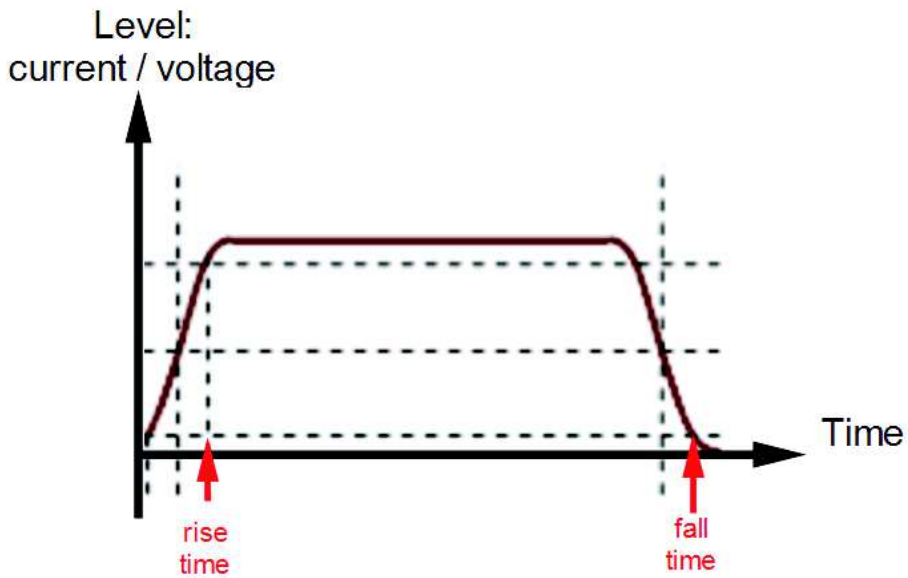


Fig. I. 21 - Signal level vs. time and switching times

The maximum significant frequency equivalent to the switching times t_{switch} (rise and fall) of a current or voltage can be approximated to [29]:

$$f_M \sim \frac{0.35}{t_{switch}}$$

Above that frequency, a rapid attenuation of the spectrum appears.

In Table I. 4 are illustrated some typical examples of switching devices and their usual switching times and equivalent frequencies [30].

Table I. 4 - Maximum equivalent frequency at switching by technology

Switching device	Maximum Voltage / Current handling	Maximum switching frequency	Minimum Switching times	Maximum Equivalent frequency
Bipolar transistor	1.2 kV / 800 A	10 kHz	450 ns	< 800 kHz
Thyristor	6 kV / 3.5 kA	500 Hz	10 μ s	< 35 kHz
GTO	4.5 kV / 3 kA	2 kHz	3 μ s	< 120 kHz
Mosfet	500 V / 50 A	1 MHz	5 ns	< 70 MHz
IGBT	1.2 kV / 400 A	50 kHz	50 ns	< 7 MHz

These equivalent spectra can become efficient EMI sources which through coupling paths, can become efficient source of EMI.

5.1.4.2 Current Driven Mechanisms

In Fig. I. 22 is depicted a very simple topology of a circuit portion allowing to explain the current-driven mechanism [28], [31].

The time-varying differential-mode current (I_{DM}) induces a flux potentially coupling with conductors, including a common-mode current path. The electromotive force *emf* driving the current in the common-mode path is a current-driven EMI source. As a consequence, the two extended parts of the reference plane drive a voltage difference across L_{return} against each other.

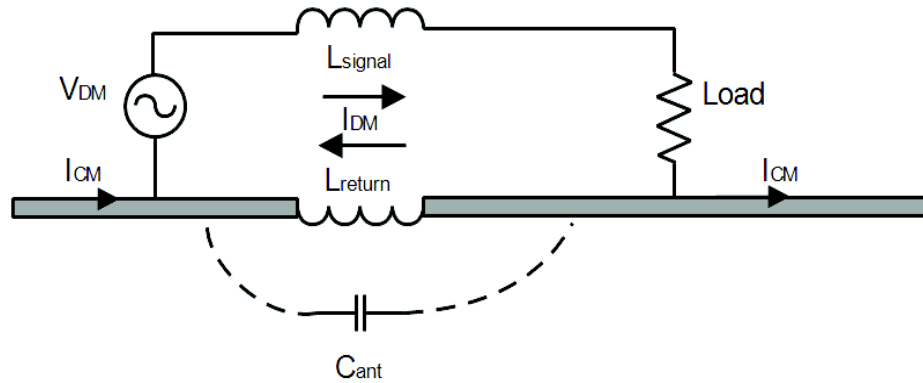


Fig. I. 22 - Current-induced CM path and EMI

The potential *dipole-type* antenna created by the reference plane’s two portions is thus driven by the voltage difference induced by the current flowing in the center portion of the plane.

An example of this inducing mechanism is the asymmetries in circuit topologies as illustrated In Fig. I. 23. The authors in [32] examine a power bus composed of one power and one ground planes of a PCB is symmetrically fed by an external power source. Symmetrically-fed means that the feeding points in the planes are strictly at the same *x* and *y* coordinates. An asymmetrically connected load is represented by the integrated circuit. The coordinates of the power connection differ from those of ground connection.

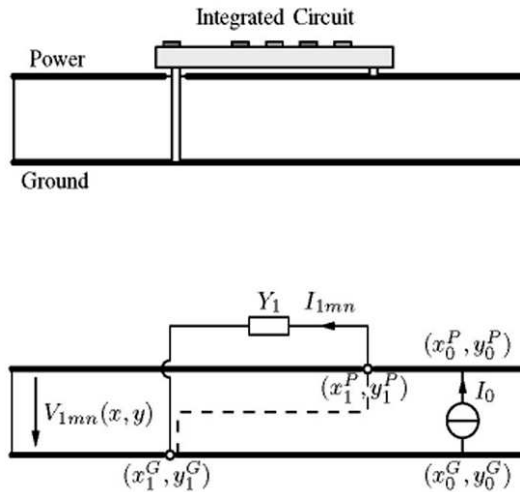


Fig. I. 23 - Assymmetrically fed load and circuit loop modelling [32]

The impact of the connection asymmetry is one responsible of generation of CM currents on the power bus since the surface crossed through the inducing flux is larger than for symmetrically connected ICs [31]–[34]. Analytical modelling of these CM currents was performed in [34].

Now, for power applications, where rise and fall times of switching devices and control circuits are larger than for digital devices, this asymmetries have a lower impact on common-mode currents. Regardless, as addressed in §I.3.2, a strong reduction of switching intervals has been seen in recent years. Therefore, asymmetries in printed circuit boards should be an increasing concern for EMI in power applications.

5.1.4.3 Voltage induced mechanisms

In Fig. I. 24 is schematized a simple case showing a simple case of voltage-driven mechanism.

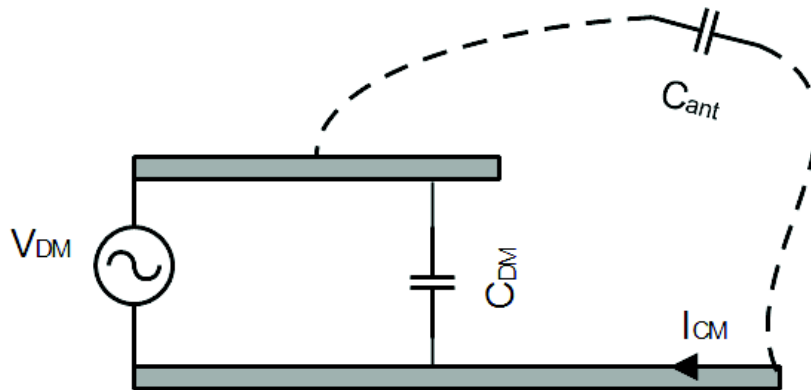


Fig. I. 24 - Current-induced CM path and EMI

A voltage-driven (through V_{DM}) differential-mode current path is formed between the reference conductor and the upper segment through a capacitive coupling. The extension of the reference conductor far from the DM current location, couples then to the upper conductor through a parasitic capacitance C_{ant} inducing common-mode currents. The dipole formed by the upper conductor and the extended far-away portion of the reference conductor is driven by the voltage source across the parasitic capacitance linking them [28].

A common example of voltage-driven mechanisms is the MOSFET Drain's against radiator through parasitic capacitive couplings.

5.2 CIRCUIT SIMULATION FOR COMMON- AND DIFFERENTIAL-MODE IMPEDANCE

5.2.1 Impedance synthesis for analysis

Circuit simulation for the analysis of both functional and parasitic behaviors of electrical systems can be an efficient method.

The impedance modeling of electrical systems is based on the description of the behavior of currents and voltages. Impedance models are constructed from the ratio of voltage and current when a resistive, inductive or capacitive dipole is fed by a source. But also, impedance can be an equivalent mathematical tool to describe the propagation of electromagnetic fields since it can account for the component of the electromagnetic field that is predominantly manifested (electric or magnetic component) and the characterization of the media where that component dwells (permeability, conductivity and permittivity) [35].

Therefore, to define the electromagnetic state of a given system (circuit) it is helpful to use the impedance concept applied to certain delimited portions of the system and its interactions with the adjacent portions. The delimitation of portions may be overcome by using geometrical or physical characteristics.

In the case of windings for example, each copper turn might be considered as an independent portion. The insulation portion covering the copper turn can therefore be considered as a second portion of the electromagnetic system. By introducing a second turn and its insulation, two more portions can be integrated into the system. Their electromagnetic interactions can be accounted for by analyzing their impedances and couplings among each other.

In Fig. I. 25, an electromagnetic system composed of two conductors A and B separated by a dielectric material is presented. This two-conductor system carries a Transverse Electromagnetic (TEM) wave, where magnetic field \vec{H} and electric field \vec{E} components are always orthogonal to each other and orthogonal to the propagation direction. The propagation of waves is not dealt with in this work. This is an example of field-impedance equivalence.

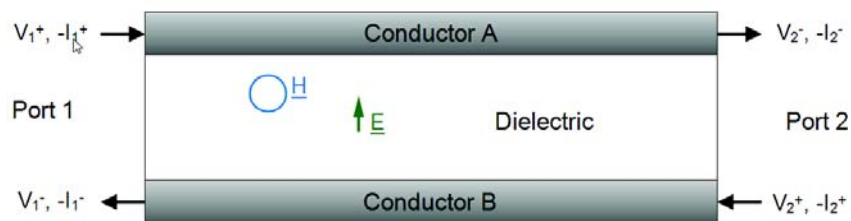


Fig. I. 25 - Electromagnetic system of two conductors separated by a dielectric

Each two-pair terminals are called Ports.

Impedances then, can be determined according to the physical reality of the network. An example of circuit representation of the two-conductor system is shown in Fig. I. 26 provided no propagation effect is taken into account.

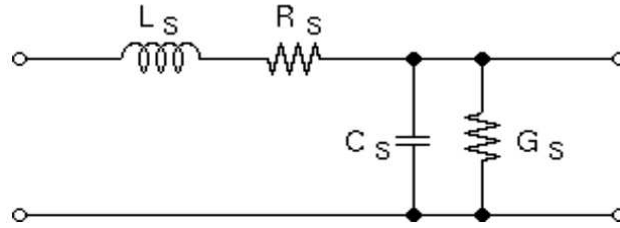


Fig. I. 26 – One type of circuit modelling of the two-conductor system

Whenever identification of circuit parameters is feasible, directly constructing the circuit model is useful. This will be the case for the modelling of motor windings in this work. By analyzing the geometry and physical characteristics of the electromagnetic systems, impedances of each turn are synthesized. However, in some cases, because of the complexity of the network, impedances might be difficult to assimilate. In those cases, other techniques exist.

5.2.2 Scattering parameters

According to Fig. I. 26, an impedance matrix corresponding to the two-port network can be synthesized. The impedance matrix is related to the complex currents and voltages carried by the conductors as:

$$Z = \begin{bmatrix} Z_{11} & Z_{12} \\ Z_{21} & Z_{22} \end{bmatrix}$$

$$\begin{bmatrix} V_1 \\ V_2 \end{bmatrix} = \begin{bmatrix} Z_{11} & Z_{12} \\ Z_{21} & Z_{22} \end{bmatrix} \begin{bmatrix} I_1 \\ I_2 \end{bmatrix}$$

$$\begin{bmatrix} V_1 \\ V_2 \end{bmatrix} = \begin{bmatrix} V_1^+ + V_1^- \\ V_2^+ + V_2^- \end{bmatrix}$$

$$\begin{bmatrix} I_1 \\ I_2 \end{bmatrix} = \begin{bmatrix} I_1^+ - I_1^- \\ I_2^+ - I_2^- \end{bmatrix}$$

But, since voltages and currents might be difficult to calculate or measure, especially for high frequency applications, an equivalent to the matrix impedance called Scattering matrix can be used since both give a complete description of the network. The scattering matrix is composed of complex scattering parameters which are measured with a Network analyzer or Vector Network Analyzer (VNA). These are equivalent to impedance parameters but instead of calculating or measuring currents and voltages, they are obtained by measuring the power balance of the electromagnetic waves travelling through each port [35].

An equivalent representation of the network can therefore be presented as:

$$S = \begin{bmatrix} S_{11} & S_{12} \\ S_{21} & S_{22} \end{bmatrix}$$

$$\begin{bmatrix} V_1^- \\ V_2^- \end{bmatrix} = \begin{bmatrix} S_{11} & S_{12} \\ S_{21} & S_{22} \end{bmatrix} \begin{bmatrix} V_1^+ \\ V_2^+ \end{bmatrix}$$

Equivalent relationships of Z and S can be found since both are equivalent representations of the circuit network. In Fig. I. 27 is presented a partial equivalence table between S and Z parameters for a 2-port system extracted from [35]:

	S	Z
s_{11}	s_{11}	$\frac{(Z_{11} - Z_0)(Z_{22} + Z_0) - Z_{12}Z_{21}}{\Delta Z}$
s_{12}	s_{12}	$\frac{2Z_{12}Z_0}{\Delta Z}$
s_{21}	s_{21}	$\frac{2Z_{21}Z_0}{\Delta Z}$
s_{22}	s_{22}	$\frac{(Z_{11} + Z_0)(Z_{22} - Z_0) - Z_{12}Z_{21}}{\Delta Z}$
Z_{11}	$Z_0 \frac{(1 + s_{11})(1 - s_{22}) + s_{12}s_{21}}{(1 - s_{11})(1 - s_{22}) - s_{12}s_{21}}$	Z_{11}
Z_{12}	$Z_0 \frac{2s_{12}}{(1 - s_{11})(1 - s_{22}) - s_{12}s_{21}}$	Z_{12}
Z_{21}	$Z_0 \frac{2s_{21}}{(1 - s_{11})(1 - s_{22}) - s_{12}s_{21}}$	Z_{21}
Z_{22}	$Z_0 \frac{(1 - s_{11})(1 + s_{22}) + s_{12}s_{21}}{(1 - s_{11})(1 - s_{22}) - s_{12}s_{21}}$	Z_{22}

Fig. I. 27 - Equivalent transformations between impedance and scattering parameters

With impedance and scattering parameters, the analysis of the behavior of a given network, can be performed by simulating currents and voltages at any given port of the modelled network.

The impedance analysis of common-mode and differential-mode of a system thus can give an enormous amount of information on its behavior, especially in high frequency simulations and time-domain simulations.

By examining the impedance of a system, conclusions on its compatibility can therefore be drawn.

6 CONCLUSION

Power mechatronic systems are highly integrated electromechanical assemblies. By pursuing the objective of mass and volume reduction in embedded applications, severe pressure is put on compactness by increasing the frequency of fundamental working mechanisms of the constitutive parts of these systems.

Moreover, the increasing switching frequency of power converters as well as the introduction of wide band gap semiconductors, allowing the increase of switching rates, induces an unprecedented constraint in the high frequency behavior of mechatronic systems. Furthermore, EMC constraints are also an increasing concern from a normative and security points of view.

The equivalence between switching mechanisms and frequency spectra associated with it, allows to analyze the high frequency signature of mechatronic assemblies in both frequency- and time-domain.

An enormous amount of information is needed to properly characterize the high frequency behavior of mechatronic systems. But circuit simulation of common- and differential-mode impedances of such systems can be a valuable tool to contribute to the study of their high frequency and EMC behavior. Direct modelling of the impedance of a system can be done by analyzing its physical and geometrical properties. If a complex system is under analysis, scattering parameters containing the same amount of information can be used.

7 REFERENCES

- [1] B. Nogarède and D. V. den Bossche, *Electrodynamique appliquée : Fondements et principes physiques de l'électrotechnique Cours et exercices corrigés*. Paris: Dunod, 2005.
- [2] M. Couderc, "Contribution à l'élaboration d'une méthodologie générale de conception des machines à aimants permanents à haute vitesse", Thèse de Doctorat, INP Toulouse, France, 2011.
- [3] M. Leroy, "Etude et mise au point de motoventilateurs à hautes performances pour l'aéronautique," Thèse de Doctorat, INP Toulouse, Toulouse, France, 2006.
- [4] A. Knott, T. M. Andersen, P. Kamby, J. A. Pedersen, M. P. Madsen, M. Kovacevic, and M. A. E. Andersen, "Evolution of Very High Frequency Power Supplies," *IEEE J. Emerg. Sel. Top. Power Electron.*, vol. 2, no. 3, pp. 386–394, Sep. 2014.
- [5] J. W. Kolar, U. Drofenik, J. Biela, M. L. Heldwein, H. Ertl, T. Friedli, and S. D. Round, "PWM converter power density barriers," in *Power Conversion Conference-Nagoya, 2007. PCC'07, 2007*, p. P–9.
- [6] H. Ohashi, "Research Activities of the Power Electronics Research Centre with Special Focus on Wide Band Gap Materials," in *Integrated Power Systems (CIPS), 2006 4th International Conference on, 2006*, pp. 1–4.
- [7] I. Omura, W. Saito, T. Domon, and K. Tsuda, "Gallium nitride power HEMT for high switching frequency power electronics," in *Physics of Semiconductor Devices, 2007. IWPSD 2007. International Workshop on, 2007*, pp. 781–786.
- [8] R. Wang, J. Sabate, Y. Mei, J. Xiao, and S. Chi, "Phase-shift soft-switching power amplifier with lower EMI noise," in *2014 IEEE Energy Conversion Congress and Exposition (ECCE), 2014*, pp. 2767–2772.
- [9] N. Rathi, A. Ahmed, and R. Kumar, "Comparative Study of Soft Switching and Hard Switching For Brushless DC Motor," *ResearchGate*, Jun. 2016.
- [10] N. Satheesh, "Advanced T-type NPC-3 level modules: A new possibility with RB-IGBT's," presented at the APEC 2014, Beijing, China, 2014.
- [11] S. Coffa, M. Saggio, and A. Patti, "SiC-and GaN-based power devices: Technologies, products and applications," in *2015 IEEE International Electron Devices Meeting (IEDM), 2015*, pp. 16–8.
- [12] E. Zhong and T. A. Lipo, "Improvements in EMC performance of inverter-fed motor drives," *IEEE Trans. Ind. Appl.*, vol. 31, no. 6, pp. 1247–1256, Nov. 1995.
- [13] S.-P. Weber, E. Hoene, S. Guttowski, W. John, and H. Reichl, "Modeling induction machines for EMC-Analysis," in *Power Electronics Specialists Conference, 2004. PESC 04. 2004 IEEE 35th Annual, 2004*, vol. 1, pp. 94–98 Vol.1.
- [14] M. Schinkel, S. Weber, S. Guttowski, W. John, and H. Reichl, "Efficient HF modeling and model parameterization of induction machines for time and frequency domain simulations," in *Twenty-First Annual IEEE Applied Power Electronics Conference and Exposition, 2006. APEC '06, 2006*, p. 6 pp.–.
- [15] F. Costa, C. Vollaïre, and R. Meuret, "Modeling of Conducted Common Mode Perturbations in Variable-Speed Drive Systems," *IEEE Trans. Electromagn. Compat.*, vol. 47, no. 4, pp. 1012–1021, Nov. 2005.
- [16] M. Beltramini, "Contribution à l'optimisation de l'ensemble convertisseur/filtres de sortie vis à vis des contraintes CEM avion", Thèse de Doctorat, Institut National Polytechnique de Toulouse-INPT, 2011.

- [17] E. T. Arntzen, R. F. Kubichek, J. W. Pierre, and S. Ula, "Initial findings in electromagnetic emissions above 30 MHz from power inverters and variable speed motor controllers," in *IEEE 1997 International Symposium on Electromagnetic Compatibility, 1997*, 1997, pp. 106–108.
- [18] A. F. Moreira, T. A. Lipo, G. Venkataramanan, and S. Bernet, "High-frequency modeling for cable and induction motor overvoltage studies in long cable drives," *IEEE Trans. Ind. Appl.*, vol. 38, no. 5, pp. 1297–1306, Sep. 2002.
- [19] U. R. G Grandi, "High-Frequency Behavior of Three-Phase Induction Motor Windings," 2001.
- [20] R. G. Rhudy, E. L. Owen, and D. K. Sharma, "Voltage Distribution Among the Coils and Turns of a Form Wound AC Rotating Machine Exposed to Impulse Voltage," *IEEE Power Eng. Rev.*, vol. PER-6, no. 6, pp. 40–41, Jun. 1986.
- [21] V. Mihaila, "Nouvelle conception des bobinages statoriques des machines à courant alternatif pour réduire les effets négatifs des dv/dt ," Artois, 2011.
- [22] G. Skibinski, R. Kerkman, D. Leggate, J. Pankau, and D. Schlegel, "Reflected wave modeling techniques for PWM AC motor drives," in *Applied Power Electronics Conference and Exposition, 1998. APEC '98. Conference Proceedings 1998., Thirteenth Annual, 1998*, vol. 2, pp. 1021–1029 vol.2.
- [23] G. Grandi, D. Casadei, and U. Reggiani, "Common- and differential-mode HF current components in AC motors supplied by voltage source inverters," *IEEE Trans. Power Electron.*, vol. 19, no. 1, pp. 16–24, Jan. 2004.
- [24] C. R. Paul, *Introduction to Electromagnetic Compatibility*. John Wiley & Sons, 2006.
- [25] G. Lourdel, "Méthodologie et outils de calcul numérique pour la prise en compte de la compatibilité électromagnétique des nouveaux prototypes de circuits intégrés de puissance," Toulouse 3, 2005.
- [26] C. R. Paul, "A comparison of the contributions of common-mode and differential-mode currents in radiated emissions," *IEEE Trans. Electromagn. Compat.*, vol. 31, no. 2, pp. 189–193, May 1989.
- [27] A. Guena, F. Costa, and C. Labarre, "Hybrid Modeling Techniques for Multilayered Printed Circuit Board in Power Electronics: Association of Electromagnetic Methods," *IEEE Trans. Electromagn. Compat.*, vol. 46, no. 4, pp. 559–570, Nov. 2004.
- [28] D. M. Hockanson, J. L. Drewniak, T. H. Hubing, T. P. V. Doren, F. Sha, and M. J. Wilhelm, "Investigation of fundamental EMI source mechanisms driving common-mode radiation from printed circuit boards with attached cables," *IEEE Trans. Electromagn. Compat.*, vol. 38, no. 4, pp. 557–566, Nov. 1996.
- [29] E. Batista, "Nouvelles structures électroniques pour le transport électrique : impacts des nouvelles contraintes d'intégration sur les interférences électromagnétiques et moyens de prévision de la compatibilité électromagnétique," Thèse de Doctorat, Université de Toulouse, Université Toulouse III - Paul Sabatier, 2009.
- [30] M. Rashid, *POWER ELECTRONICS HANDBOOK*. Elsevier, 2011.
- [31] J. L. Drewniak, T. H. Hubing, and T. P. V. Doren, "Investigation of fundamental mechanisms of common-mode radiation from printed circuit boards with attached cables," in *IEEE International Symposium on Electromagnetic Compatibility, 1994. Symposium Record. Compatibility in the Loop, 1994*, pp. 110–115.
- [32] M. Hampe and S. Dickmann, "Double and single summation expression for the impedance of populated PCB power-bus structures including asymmetrically connected

- components,” in *Electromagnetic Compatibility, 2006. EMC-Zurich 2006. 17th International Zurich Symposium on, 2006*, vol. 2006, pp. 375–378.
- [33] R. W. Dockey and R. F. German, “New techniques for reducing printed circuit board common-mode radiation,” in *, 1993 IEEE International Symposium on Electromagnetic Compatibility, 1993. Symposium Record, 1993*, pp. 334–339.
- [34] M. Hampe and S. Dickmann, “Generation of common-mode currents on PCB power-bus structures,” in *Electromagnetic Compatibility, 2006. EMC-Zurich 2006. 17th International Zurich Symposium on, 2006*, pp. 320–323.
- [35] D. M. Pozar, *Microwave Engineering, 4th Edition*. Wiley, 2011.

Chapter II
Wide Band Analytical Modelling of
Actuators with Concentrated windings
and Circuit Implementation for High
Frequency Analysis

CONTENTS

Contents	41
Table of Figures	43
List of tables	45
1 Overview of power actuator models and simulation	46
2 General hypotheses and considerations for high frequency impedance modelling	46
3 Calculation of parasitic capacitances in concentric winding structures	48
3.1 Introduction	48
3.2 Theoretical basis	48
3.3 Overview of common dielectric materials and wires for industrial design	51
3.3.1 Round enameled winding copper wire for industrial applications	52
3.3.2 Dielectric films	52
3.3.3 Epoxy Resin Casting (impregnation)	53
3.4 General considerations	53
3.5 Analytical modeling process	55
3.5.1 Winding over a conducting bare magnetic core	55
3.5.2 Introduction of a dielectric film over the core and between two different windings ...	59
3.5.3 Turn-to-turn capacitance calculation in the presence of a dielectric insulating	61
3.5.4 Case of impregnated windings	64
3.5.5 Summary of analytical expressions of partial capacitances	66
3.6 2-D Finite Element Analysis modeling and comparison to analytical modeling	68
3.6.1 Hypothesis and setup	68
3.6.2 Per-meter values as function of the case, wire diameter and grade	70
3.6.3 Comparative analysis and results	71
3.6.4 Discussion	74
4 Calculation of induced currents in the winding turns	75
4.1 The skin and proximity effects	75
4.1.1 Overview	75
4.1.2 Summary of analyzed expressions of eddy-current-modified impedance	76
4.2 Implementation for concentrated windings in electrical motors	79
4.2.1 Hypotheses	79
4.2.2 Comparison of skin-effect impedance modules	79
4.2.3 Analytical formulations	81
4.3 Implementation for a specific case of concentrated windings	82
5 Calculation of partial inductances in wound structures	83

5.1	Relative Permeability Dispersion	83
5.2	Inductance calculation methods.....	86
5.3	Derivation of useful formulas	87
5.3.1	General case: mutual impedance of two coaxial circular turns over an iron core	88
5.3.2	Special Case 1: Air-cored inductor	89
5.3.3	Special case 2: Zero penetration flux into the core.....	89
5.4	Analysis of a specific case of concentrated winding	90
5.5	The problem of core losses.....	92
6	Circuit representation of the analytical models	93
6.1	Capacitance and dielectric losses implementation	94
6.2	Copper skin and proximity effect.....	100
6.2.1	Foster series Network Synthesis	100
6.2.2	Number of network cells for simulation	102
6.3	Inductances and core model	104
6.4	Global circuit model of a complete winding	105
6.4.1	One-turn circuit model	105
6.4.2	Two turns of adjacent layers.....	106
6.4.3	Coupling to the core	107
6.4.4	Full model for a 4 layer cored winding (4 turns per layer)	108
7	Experimental and simulation results and analysis.....	109
7.1	Specimens used for model validation purposes	109
7.2	Frequency-domain simulation and experimental data comparison	110
7.2.1	Experimental protocol for measurements	110
7.2.2	Experimental and simulation results comparison	113
7.3	Conclusions on experimental validations	124
8	Conclusion	125
9	References.....	126

TABLE OF FIGURES

Fig. II. 1 - Common stator poles geometry for concentrated winding motors.....47

Fig. II. 2 - Stator poles' assumed modelling geometry with a circular cross-section infinitely long core and attached coordinates system.47

Fig. II. 3 - Debye relaxation patterns ($\epsilon DC = \epsilon S$) [3]50

Fig. II. 4 - Dielectric constant of Araldite F® (epoxide resin) at 50 Hz for different resin/hardener mix ratios and temperatures53

Fig. II. 5 - Power dissipation factor of Araldite F® (epoxide resin) at 50 Hz for different resin/hardener mix ratios and temperatures53

Fig. II. 6 - Partial concentric winding around a magnetic core and insulating materials54

Fig. II. 7 - Dimensions of the structures under consideration54

Fig. II. 8 - Representation of capacitive couplings between turns and core55

Fig. II. 9 - Coupling mechanism for the inner turns of the winding.....56

Fig. II. 10 - Assumed path x for field lines between adjacent conductors for $-\pi/6 \leq \theta \leq \pi/6$ 57

Fig. II. 11 - Dimensions of the structure under consideration58

Fig. II. 12 - Capacitance arrangement for a multilayer winding59

Fig. II. 13 - Diagram of the wound structure with a dielectric film over the core60

Fig. II. 14 - Overall capacitance arrangement for the inner layer turns61

Fig. II. 15 - Two-winding structure separated by a dielectric film62

Fig. II. 16 - Assumed three-cell elementary coupling mechanism62

Fig. II. 17 – Field lines through the 4 different paths63

Fig. II. 18 - Discretization of the area between an inner turn and the bare core.....65

Fig. II. 19 - FEA setup and segmentations for electrostatic energy calculations68

Fig. II. 20 - Segmentation and field lines contained in the specified regions for energy calculation69

Fig. II. 21 – Comparison of results for turn-to-turn capacitance for Grade 1.....72

Fig. II. 22 – Comparison of results for turn-to-turn capacitance for Grade 2.....72

Fig. II. 23 - Comparison of results for turn-to-core capacitance for Grade 173

Fig. II. 24 - Comparison of results for turn-to-core capacitance for Grade 273

Fig. II. 25 - Two different Litz wire arrangement for modelling76

Fig. II. 26 - Squared-cross-section closely packed conductors arrangement78

Fig. II. 27 - Circular torrent Litz wire78

Fig. II. 28 - Comparison of three different internal impedance approximations80

Fig. II. 29 - Internal impedance of curved conductors for 4 different layers.....82

Fig. II. 30 - Complex permeability of different rolled and laminated iron alloy materials [21]85

Fig. II. 31 – Physical characteristics of different ferromagnetic materials: sample R - amorphous ribbon milled for 6 hours, consolidated at 500°C for 5 min, annealed at 540°C for 60 min.; sample L - amorphous ribbon cryo-milled for 6 hours, consolidated at 500°C for 5 min., annealed at 540°C; Iron powders (S) and flakes of Fe73Cu1Nb3Si16B7 (VPM) with the different content (0, 5, 30, 50 wt% of Fe73Cu1Nb3Si16B7) [21]85

Fig. II. 32 - Dependence of the penetration depth with permeability and frequency (**in mm**).....86

Fig. II. 33 –Turns and core arrangement for mutual impedance calculations.....87

Fig. II. 34 – Layout of a particular winding for a case study90

Fig. II. 35 – Mean value of the per-turn self-inductance against frequency91

Fig. II. 36 - Mean value of the per-turn mutual inductances against frequency91

Fig. II. 37 - Mean value of the coupling coefficients against frequency92

Fig. II. 38 - LTSpice screenshot.....93

Fig. II. 39 - Common model for lossy dielectric materials.....94

Fig. II. 40 - Several parallel branches model for lossy dielectrics modelling	94
Fig. II. 41 – Impedance module of the dielectric network	98
Fig. II. 42 – Absolute value of the phase of the impedance of the dielectric network.....	98
Fig. II. 43 - Dielectric loss factor of the modelled dielectric.....	99
Fig. II. 44 - Foster series network.....	100
Fig. II. 45 - Foster series model for internal impedance compared to original impedance expression	102
Fig. II. 46 - Foster model for different layers and $N_c = 25$	103
Fig. II. 47 - Single-turn circuit model.....	105
Fig. II. 48 - Foster network for copper skin effect.....	106
Fig. II. 49 - Dielectric network.....	106
Fig. II. 50 - Couplings between turns of two adjacent layers	107
Fig. II. 51 - Couplings to the core	107
Fig. II. 52 – Circuit structure of a complete winding	108
Fig. II. 53 - Schematic representation of the specimens for experimental comparison.....	109
Fig. II. 54 - Different specimens for experimentation	110
Fig. II. 55 - DM and CM connections on the DUTs	111
Fig. II. 56 - Specific fixturing of the samples for VNA measurements	111
Fig. II. 57 - Test setup for S-parameters measurements on the samples.....	112
Fig. II. 58 - Impedance comparison with PIA and VNA measurements between 1 MHz and 120 MHz	112
Fig. II. 59 - Resulting measured and simulated impedance module of the non-ferromagnetic core specimen	114
Fig. II. 60 – Simulated impedance magnitude with inductive parameters calculated at different frequencies.....	117
Fig. II. 61 - Simulated impedance phase with inductive parameters calculated at different frequencies	117
Fig. II. 62 – Measured DM impedance magnitude on Specimen (B) and comparison with extreme values up to 1 MHz (PIA measurement)	118
Fig. II. 63 - Measured DM impedance phase on Specimen (B) and comparison with extreme values up to 1 MHz (PIA measurement)	119
Fig. II. 64 - Measured DM impedance magnitude on Specimen (B) and comparison with extreme values up to 300 MHz (VNA measurement)	119
Fig. II. 65 – Measured DM impedance magnitude on Specimen (B) and comparison with extreme values up to 300 MHz (VNA measurement)	120
Fig. II. 66 - Resonances comparison between measured and simulated DM impedance	121
Fig. II. 67 - Common-mode impedance magnitude analysis on specimen (B)	122
Fig. II. 68 - Common-mode impedance phase analysis on specimen (B)	123
Fig. II. 69 - DM impedance comparison for specimens (B), (C) and (D) and resonance analysis.....	124
Fig. II. 70 - Flow chart of the modelling process presented here and Virtual Experimentation capabilities	126

LIST OF TABLES

Table II. 1 - Extract from IEC 06317 standard for grade specifications	52
Table II. 2 - Grade specifications and usual material examples	52
Table II. 3 - Kapton® dielectric film properties	52
Table II. 4 - Geometrical parameters for modelling.....	55
Table II. 5 - Summary of the partial capacitance expressions for non-impregnated windings	66
Table II. 6 - Summary of the partial capacitance expressions for impregnated windings.....	67
Table II. 7 - Equipotential conditions for energy calculations.....	68
Table II. 8 - Wire specifications used in the analysis.....	70
Table II. 9 - Materials properties used in the analysis	70
Table II. 10 - Turn-to-core capacitance for different film thickness.....	74
Table II. 11 - Different internal impedance models and hypotheses for eddy current effects on copper turns.....	76
Table II. 12 - Dimensional orders of coils in electromagnetic structures.....	79
Table II. 13 - Winding characteristics for illustration	80
Table II. 14 - Winding dimensions for example implementation.....	82
Table II. 15 – Physical properties and parameters for mutual inductance modelling.....	87
Table II. 16 – Winding characteristics.....	90
Table II. 17 –Core physical properties	90
Table II. 18 - Resulting error for a given N_{cap} number of cells and maximum modelling frequency ..	96
Table II. 19 - Resistance values calculated for a network of 13 branches.....	97
Table II. 20 - Resulting error at certain frequencies for different number of cells N_c	103
Table II. 21 - Elements composing the turn structure	106
Table II. 22 - Geometrical parameters of the samples.....	109
Table II. 23 - Specimens' materials and layout	109
Table II. 24 - Calculated vs. measured value of self-inductance of the non-ferromagnetic sample ...	113
Table II. 25 - Calculation of self-inductance and capacitance at different resonance points.....	116

1 OVERVIEW OF POWER ACTUATOR MODELS AND SIMULATION

Motors and generators are very complex electromagnetic structures combining a wide range of materials and architectures. The complex arrangement of the windings into the ferromagnetic yokes of the machine makes it very difficult to parameterize its geometry and to calculate the parasitic couplings prohibitive. Moreover, the dependence of the different materials on a large variety of elements adds a complementary challenge for the modelling over a wide range of frequencies of such electromagnetic structures.

In this chapter, an effort to model the wide band behavior of concentrated winding machines is carried out. The objective is to contribute to the development of a modeling methodology of the electrical machine in the high frequency domain taking into account the physical and geometrical parameters of windings. By taking into account physical parameters, as well as structural layout of the windings, such as wire and insulation class, wires arrangement, ferromagnetic materials or number of turns per layer, a rational and predictive tool is created to help including the machine model into a larger model of the whole power system. This effort is done, in order to prevent and predict susceptibility and emission levels from a comprehensive view of the global system.

Since a global comprehensive solution of the equivalent common mode and differential mode is very difficult to synthesize, the study is divided in several parts:

In the first paragraph, analytical modelling of the different concerned impedances is achieved as follows:

- General hypotheses and considerations
- Modelling of the capacitive and dielectric behavior of winding structure
- Modelling of the copper conductors impedance modified by eddy currents
- Modelling of the inductive behavior along with the core

Then, in order to implement a circuit simulation tool, a network synthesis is performed to reproduce frequency-dependent behaviors.

And finally, a comparison between analytical models implemented in circuit simulations and experimental results is carried out in frequency and time domain.

2 GENERAL HYPOTHESES AND CONSIDERATIONS FOR HIGH FREQUENCY IMPEDANCE MODELLING

Motors with concentrated winding structures (straight cored coils) generally have rectangular cross-section wound stator poles as described in Fig. II. 1. However, for simplification purposes, all the subsequent analytical calculations will be carried out in the context of a circular cross-sectional hypothesis. Thus, it is accepted in this development that a cylindrical geometry of the stator poles are subjected to a cylindrical coordinate system (r, φ, z) (Fig. II. 2). The effects of this approximation will be discussed in subsequent sections.

Besides, a strong hypothesis concerning the coil length is also integrated into the modelling. Indeed, in electrical motors, windings over the stator poles are short in length. In the analysis, it is considered that the coil lengths are long enough to consider the border effects inexistent. This strong hypothesis especially impacts eddy-current effects on copper wires and per-turn inductance

modelling, because for capacitive modelling, the coupling mechanisms are localized between the turns and the core.

Furthermore, the coils are supposed to be rotation-invariant with respect to their axis since copper turns' generator curves are considered to be circles contained into planes perpendicular to the winding axis Oz . Thus, the length of the turns l_t are assimilated to their perimeter. Consequently, the subsequent analysis can be carried out considering a 2-dimension problem into a reference plane containing the axis Oz of the coil. Currents and electromotive fields are perpendicular to the reference plane of analysis whereas magnetic field is contained into the reference plane of study.

All the analytical models are synthesized in the quasistatic approximation of states, meaning that time derivative terms in the Maxwell's equations and their consequences are neglected.

Concerning the materials, the hypothesis concerning linearity and isotropy at a macroscopic level are dealt with in their respective sections.

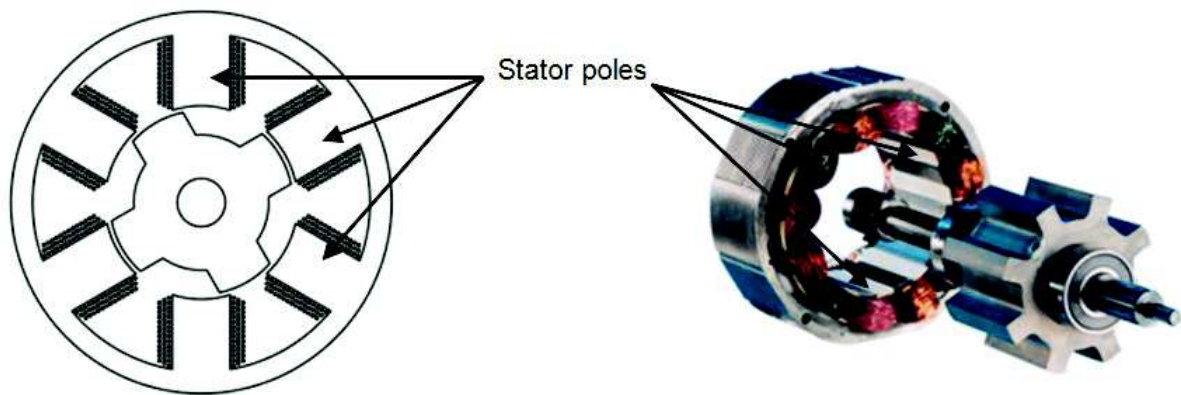


Fig. II. 1 - Common stator poles geometry for concentrated winding motors

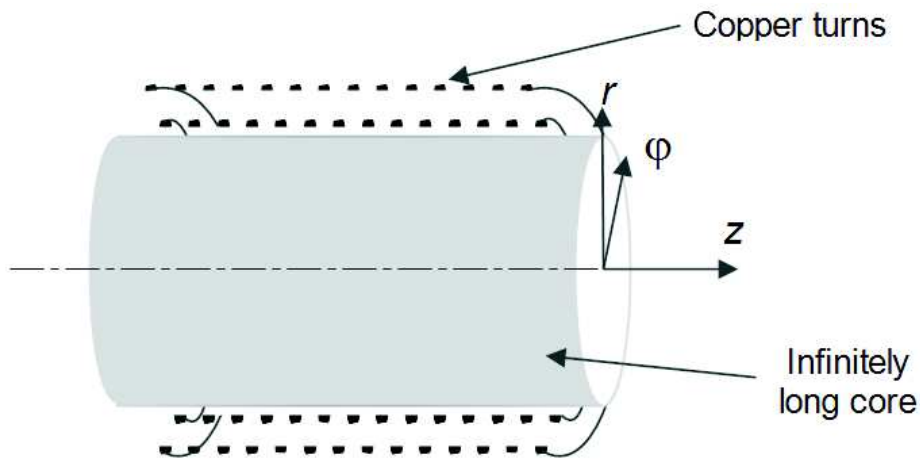


Fig. II. 2 - Stator poles' assumed modelling geometry with a circular cross-section infinitely long core and attached coordinates system.

3 CALCULATION OF PARASITIC CAPACITANCES IN CONCENTRIC WINDING STRUCTURES

3.1 INTRODUCTION

An essential part of the high frequency modeling of the actuator is the modeling of the capacitive couplings created within the motor/generator. A particular effort is granted to parasitic capacitance modelling since this coupling is a main contributor to the generation of HF antenna mode currents.

In this section, modeling of the turn-to turn and turn-to core capacitive couplings in different configurations is carried out for concentric winding topologies. The inclusion of insulating coatings around the copper turns, dielectric films over the core or potential impregnations of resins for mechanical purposes lead to specific capacitive behaviors of the actuator.

In an effort to understand the impact of such behaviors, the partial capacitances deduced from analysis of the layout and electrical configuration of concentrated windings can be used to build complex circuit models for circuit simulation.

3.2 THEORETICAL BASIS

By their electrical properties, all bodies can be divided into two categories: conductors and dielectrics. The essential property of perfect dielectric media is that no continuous current can dwell within. Thus, contrary to conductors, the magnitude of a constant electric field is not necessary equal to zero within the considered body. In this sub-paragraph, it is sought to clearly establish the mechanisms that define the dielectric properties of the materials used, but only for the conditions of our concern.

By expressing the neutrality of a dielectric body in terms of its total charge ρ_T , for a given volume V , one can write that $\int \rho_T dV = 0$, which directly yields $\rho_T = -\nabla \cdot \vec{P}$.

\vec{P} ($\vec{P} = 0$ outside the body) is called the electric polarization of the dielectric material.

For a polarized dielectric body, a distinction has to be observed between the electric field intensity \vec{E} created by the contribution of bound charges and the displacement field \vec{D} created only by the free charges [1]. Bound charges are dipolar moments intimately linked to the polar state of the dielectric matter and thus to the polarization. Free charges are charges whose source is external to the media and is responsible of maintaining the polarization. The difference between these fields thus resides in the bound carriers, also called polarization charges, and it can be shown that

$$\vec{E} = \frac{1}{\epsilon_0} (\vec{D} - \vec{P}) \quad // \text{ 3-1}$$

where, by definition, $\epsilon_0 = 8.854 \dots 10^{-12}$ F/m is the permittivity of the vacuum. It is from this difference between the fields that an analysis concerning the dielectric properties of media can be made.

Most dielectric materials have a behavioral linearity between the electric intensity and its polarization, which is represented by:

$$\vec{E} = \epsilon_0 \chi \vec{P} \quad // \text{ 3-2}$$

χ is called the electric susceptibility. Thus, with (III.3-1) and (III.3-2),

$$\vec{D} = \varepsilon_0 \vec{E} + \varepsilon_0 \chi \vec{E} = \varepsilon_0 (1 + \chi) \vec{E} = \varepsilon \vec{E} \quad \text{II. 3-3}$$

ε being the absolute media permittivity.

A linearity between \vec{E} and \vec{D} appears and therefore, the relative permittivity (or dielectric permeability) can be expressed as:

$$\varepsilon_r = 1 + \chi = \frac{\varepsilon}{\varepsilon_0} \quad \text{II. 3-4}$$

The absolute permittivity of a given media is only described by ε_r , and is a function of its thermodynamic state (temperature, polarization intensity and frequency, molecular state...)[2]. This parameter is very often indicated in technical datasheet and is intimately linked to the application purposes of the material. For example, capacitors are made with high-permittivity materials for increasing capacitance in order to reduce their volume.

In order to introduce a more properties-driven analysis, let's consider the most general relationship between the displacement field $\vec{D}(t)$ and field intensity $\vec{E}(t)$:

$$\vec{D}(t) = \vec{E}(t) + \int_0^\infty f(\tau) \vec{E}(t - \tau) d\tau \quad \text{II. 3-5}$$

f is a function of the material's thermodynamic properties [2].

Now, in a harmonic analysis (by the means of a Fourier series expansion), it can be stated that, the latter formulation linking D and E is given by:

$$\vec{D} = \varepsilon(\omega) \vec{E} \quad \text{II. 3-6}$$

With

$$\varepsilon(\omega) = 1 + \int_0^\infty f(\tau) e^{j\omega\tau} d\tau \quad \text{II. 3-7}$$

The permeability becomes then a complex quantity and depends not only on the properties of the media but also on the frequency, thus having

$$\varepsilon_r^* = \varepsilon_r' - j\varepsilon_r'' \quad \text{II. 3-8}$$

In non-perfect dielectrics, containing impurities and discontinuities in the body for example, several dielectric phenomena appear.

The first phenomenon is that a dielectric conductivity is present in the body. This conductivity which is closely related to the bound and free charges in the media, creates losses and under certain conditions, *partial discharges* (which is not treated here either, see footnote) that may harm the integrity of the material.

For the frequencies in question, i.e. DC to radio frequencies (RF) up to 300 MHz, and ignoring the temperature dependence (which is a very strong hypothesis) the preponderant mechanism accounting for the current absorption of dielectrics, is by far the Debye dipolar absorption (DDA) mechanism. This mechanism is responsible for the *relaxation* of the orientation of the permanent dipoles (bound carriers) with the external field: the orientation is achieved with a certain delay because of viscous resistance and inertia of the dipoles within the matter. Ultimately, when the orientation is no longer efficient because of the fast changing field, the absolute permittivity decreases to the vacuum permittivity value ($\epsilon_r \rightarrow 1$) [3].

This behavior is described by the Debye equation:

$$\epsilon_r^* = \epsilon_\infty + \frac{\epsilon_{DC} - \epsilon_\infty}{1 + j\omega\tau} \quad \text{II. 3-9}$$

The interesting fact about this is that, in a harmonic analysis frame, it can be shown that:

$$\epsilon_r' = \epsilon_\infty + \frac{\epsilon_{DC} - \epsilon_\infty}{1 + \omega^2\tau^2} \quad \text{II. 3-10}$$

$$\epsilon_r'' = \frac{(\epsilon_{DC} - \epsilon_\infty)\omega\tau}{1 + \omega^2\tau^2} \quad \text{II. 3-11}$$

And finally,

$$\tan\delta = \frac{\epsilon_r''}{\epsilon_r'} = \frac{(\epsilon_{DC} - \epsilon_\infty)\omega\tau}{\epsilon_{DC} + \epsilon_\infty\omega^2\tau^2} \quad \text{II. 3-12}$$

ϵ_∞ : Relative permittivity at infinite frequency

ϵ_{DC} : Relative permittivity at zero frequency

τ : Relaxation time, a function of the thermodynamic state of the media

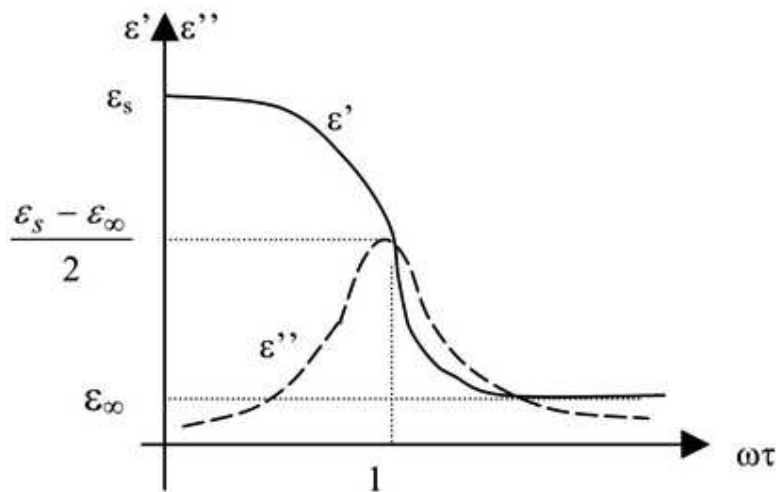


Fig. II. 3 - Debye relaxation patterns ($\epsilon_{DC} = \epsilon_s$) [3]

The dissipation factor or loss tangent, translates the phase shift between the between a purely capacitive current and a purely resistive current dwelling within the dielectric media. It is perhaps the second most important technical parameter defining a dielectric material. In fact, the total current in a polarized dielectric is defined by (in the absence of free carriers):

$$\vec{j}_T = \varepsilon_0 \varepsilon_r \frac{\partial \vec{E}}{\partial t} = \frac{\partial \vec{D}}{\partial t} \quad \text{II. 3-13}$$

and therefore,

$$\vec{j}_T = \varepsilon_0 \varepsilon_r' \frac{\partial \vec{E}}{\partial t} - j \varepsilon_0 \varepsilon_r'' \frac{\partial \vec{E}}{\partial t} \quad \text{II. 3-14}$$

Since,

$$\vec{j}_T = \sigma \vec{E} \quad \text{II. 3-15}$$

σ is the conductivity of the dielectric material, therefore, it can be written that

$$\sigma' = \omega \varepsilon_0 \varepsilon_r'' \quad \text{II. 3-16}$$

$$\sigma'' = \omega \varepsilon_0 \varepsilon_r' \quad \text{II. 3-17}$$

Note that the real part of the conductivity is linked to the imaginary part of the permittivity. This gives rise to the real part of the total current within the material, and therefore, to the losses¹. Inversely, the imaginary part of the conductivity is linked to the real part of the permittivity which in turn gives rise to the capacitive behavior of the material. This is why the loss tangent is an important parameter to take into account when selecting dielectrics.

Finally, from a practical point of view, relaxation phenomena in most solid dielectrics appear at fairly high frequencies (several hundreds of MHz). So basically, for the desired frequencies, this may be unnecessary for most of the cases, but it has to be demonstrated on a case to case basis. However, the dielectric losses appear from very low frequencies and have to be taken into account.

The other untreated phenomena are not dealt with because they do not concern us for this study. More can be found in [2] and [3].

3.3 OVERVIEW OF COMMON DIELECTRIC MATERIALS AND WIRES FOR INDUSTRIAL DESIGN

In this paragraph, some examples of widely used materials in the industry are presented.

¹ In fact, the free carriers also would induce a conduction current. In that case, the imaginary part of the permittivity would have two components $\varepsilon_r'' = \varepsilon_b'' + \varepsilon_f''$, one for the dielectric losses from the polarizing charges, and the other from the free charges but the definition of the real conductivity remains unchanged. Partial discharges are a direct consequence of free carriers' absorption mechanism.

3.3.1 Round enameled winding copper wire for industrial applications

The IEC 60317 norm specifies the standards for winding round-section copper. The main specifications for usual industrial designs concern (among several others):

- The grade which is related to the breakdown voltage as shown in an extract of IEC 60317 standard below (Table II. 1).

Table II. 1 - Extract from IEC 06317 standard for grade specifications

Copper diameter mm	Grade 1			Grade 2			Grade3		
	Diameter with insulation			Diameter with insulation			Diameter with insulation		
	Min	Max	Breakdown voltage	Min	Max	Breakdown voltage	Min	Max	Breakdown voltage
	mm	mm	V	mm	mm	V	mm	mm	V (50-60 Hz)
0.200	0.214	0.226	1800	0.227	0.239	3500	0.240	0.252	5100
0.400	0.421	0.439	2300	0.440	0.459	4400	0.460	0.478	6600
0.500	0.524	0.544	2400	0.545	0.566	4600	0.567	0.587	7000
1.000	1.034	1.063	4600	1.066	1.094	6900	1.095	1.124	8500
2.000	2.031	2.074	6500	2.098	2.112	7700	2.122	2.148	>9kV

- The thermal class (cf. Table II. 2) [4]:

Table II. 2 - Grade specifications and usual material examples

Class *	Maximum continuous operating temperature (rated for 20 000 hours)	Example of coating material used by manufacturers (enameling)	Relative permittivity (Dielectric constant)
F	150 °C	Polyurethane	6.7 to 7.4
H	180 °C	Modified Polyurethane	5.8 to 7
C	200 °C	Polyamide-imide (aka Polyimide or Polymidimde)	3.5 to 5.4

* Non exhaustive list. Materials and dielectric constants are highly dependent on manufacturer’s technology.

3.3.2 Dielectric films

Kapton® is a dielectric insulating film manufactured by Dupont™ widely used in winding applications for its dielectric, thermal and mechanical properties. As for the coating of wires, it is also based on Polyamide-imide compounds. Table II. 3 shows commonly used dielectric film insulations for different thicknesses and their dielectric properties.

Table II. 3 - Kapton® dielectric film properties

Type (thickness)	Dielectric constant	Dissipation factor	Test condition	Temperature operating range
25 µm	3.4	1.8x10 ⁻³	1 kHz	-269 to 400 °C
50 µm	3.4	2.0x10 ⁻³		
125 µm	3.5	2.6x10 ⁻³		

3.3.3 Epoxy Resin Casting (impregnation)

In Fig. II. 4, the dielectric constant of an epoxide resin (Araldite F®) for different mix ratios is presented. Then, Fig. II. 5 exhibits the dissipation factor for the same conditions as for the dielectric constant.

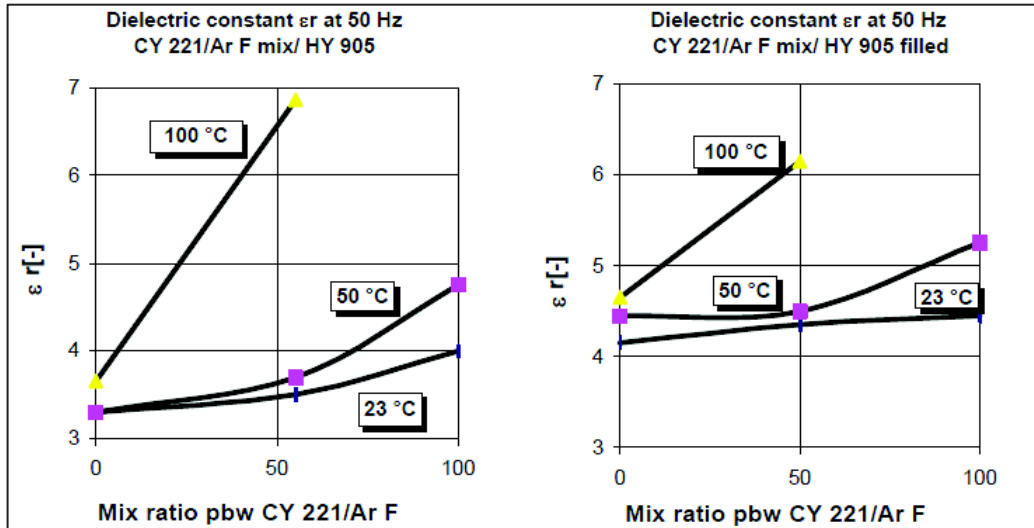


Fig. II. 4 - Dielectric constant of Araldite F® (epoxide resin) at 50 Hz for different resin/hardener mix ratios and temperatures

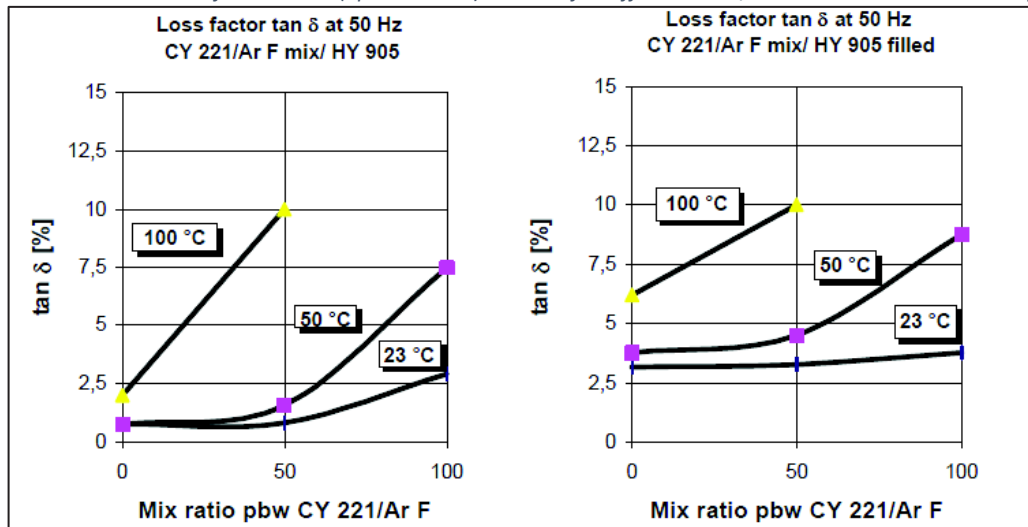


Fig. II. 5 - Power dissipation factor of Araldite F® (epoxide resin) at 50 Hz for different resin/hardener mix ratios and temperatures

As stated in eq. (II.3-12), the loss tangent can be directly calculated from the permittivity data. However, as can be seen, technical datasheets give little information on the dissipation factor (loss tangent) and no information on imaginary part of permittivity whatsoever. It is then impossible to determine the frequency characteristics of a given material over a wideband frequency range from the datasheet information.

3.4 GENERAL CONSIDERATIONS

The analytical formulations here synthesized are for concentrated winding topologies. In Fig. II. 6 is shown schematically a portion of a generic concentric winding structure composed of two windings

around an insulated ferromagnetic core each one isolated from one another by a dielectric film. The turns of both windings are enameled with a thin coating thickness around the copper turn. The axis accounts for the 2D- axisymmetric geometry taken into account for the consolidation of the capacitive coupling models. Dielectric materials are considered to behave linearly with respect to their excitation and, copper turns and ferromagnetic core are considered to be perfect conductors.

Because of symmetries, electric field lines are considered to be equally shared between adjacent conductors of the inner layers.

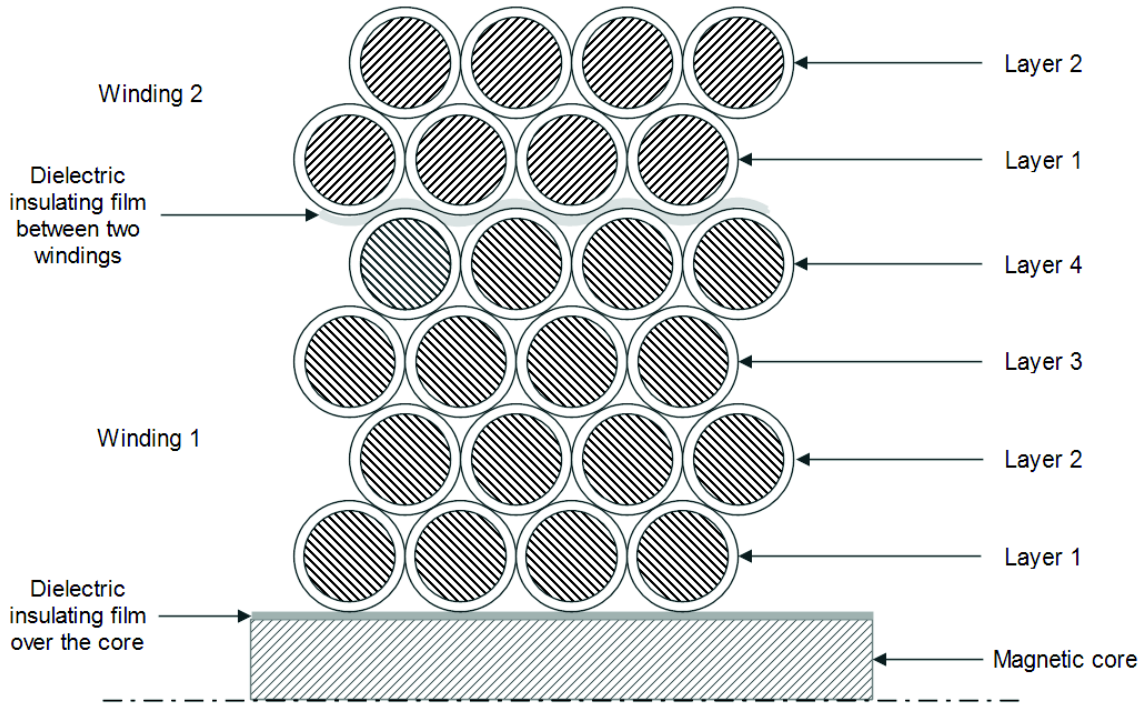


Fig. II. 6 - Partial concentric winding around a magnetic core and insulating materials

In Fig. II. 7, the dimensions and variables taken into account for the modeling are pointed out. Then, in Table II. 4, the materials properties and description of the parameters used in the study described.

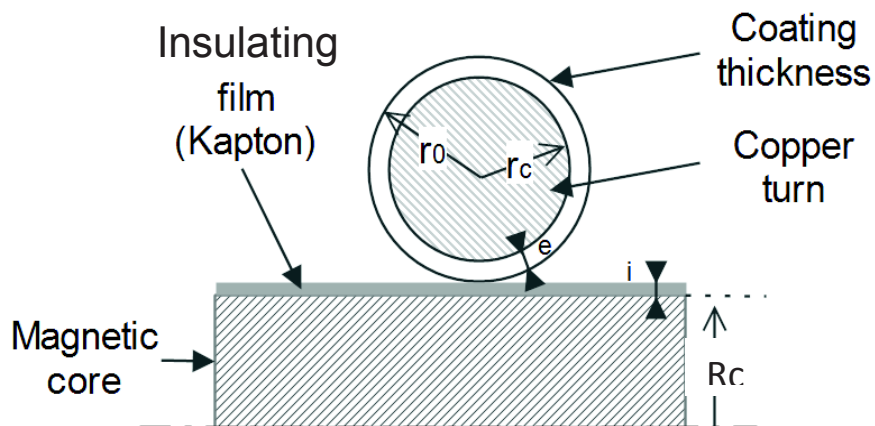


Fig. II. 7 - Dimensions of the structures under consideration

Table II. 4 - Geometrical parameters for modelling

R_c	Iron core radius
l_t	Turn length
r_c	Copper wire radius
r_0	Outer diameter of radius
e	Coating thickness
i	Insulating film thickness

The study will be divided into four cases. Each one of the different cases will treat one particular of the several possible configurations with concentric windings as presented just before. All the four cases should be sufficient to cover a large set of possible configurations with coils with similar characteristics.

The resulting analytical models are then confronted to Finite Element (FE) simulations and measurements on actual windings.

3.5 ANALYTICAL MODELING PROCESS

3.5.1 Winding over a conducting bare magnetic core

3.5.1.1 Considered geometry and problem definition

Fig. II. 8 shows a schematic representation of a cross-section of a portion of a concentric-wound structure. The ferromagnetic core has no insulation over its surface. Only the coating thickness of the turns are ensuring the electrical insulation to the core. This kind of geometry can be found in HF filter coils. Only few turns are represented in the figure for clarity purposes.

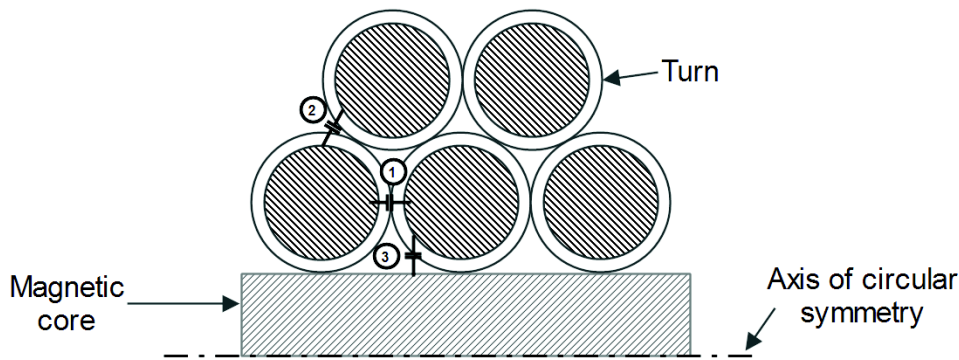


Fig. II. 8 - Representation of capacitive couplings between turns and core

Three types of couplings can be identified:

- 1- Turn-to-turn capacitance of turns in the same layer
- 2- Turn-to-turn capacitance of turns in different layers
- 3- Turn-to-core capacitance

The analytical calculation of the equivalent capacitances accounting for those couplings are described along with the hypotheses stated for the modeling.

3.5.1.2 Calculation of the turn-to-turn capacitance

The turn-to-turn capacitance calculations are an evolution of the work presented in [5].

For the inner layers, the calculation of turn-to-turn capacitance can be reduced to the analysis of the ABCD cell representing the assumed electric field lines mean paths between two turns because of symmetries. In fact, for concentric windings, a single turn from a given layer will share its electric field lines with two other turns from the adjacent layer. Due to symmetries in this kind of winding, for the reasoning can be extended for the same-layer coupling, considering the turns to be in two different but adjacent layers. Fig. II. 9 shows the coupling mechanism for the inner turns of a concentric winding.

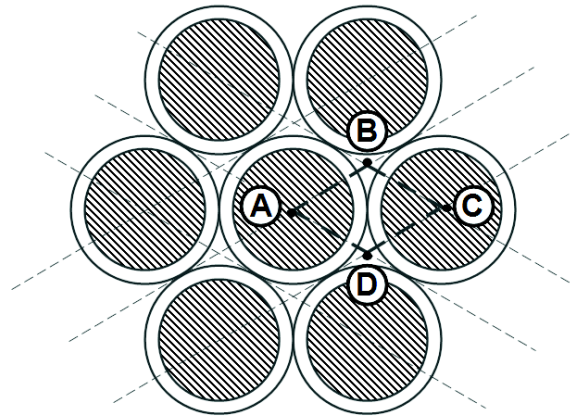


Fig. II. 9 - Coupling mechanism for the inner turns of the winding

The coupling mechanism between one turn and the two turns from the adjacent layer, form a basic cell and E lines shared between these turns form, by symmetries considerations, an ABCD path for E lines. In fact, we assume, by proximity of the turns, that all E lines coming out from a turn, are equally shared between the two adjacent turns.

Then, electric field lines going from one turn to the other, go through:

- coating thickness of the first turn
- the airgap formed by the three adjacent turns
- coating thickness of the second turn

Since conductor surfaces are considered to be perfect equipotentials, electric field lines are orthogonal to the conductor surfaces.

Besides, since the thickness e is small to the copper wire diameter $Dc = 2 \cdot r_c$, lines in the coatings are considered to be orthogonal to the conductor surface as shown in Fig. II. 10.

Furthermore, because of the proximity effect, electric field lines are concentric around the shortest distance between two different equipotentials. Thus, E lines are considered to be parallel and close to small values of θ as shown in Fig. II. 10. It is then assumed that for adjacent turns, the field lines are exclusively directed towards the next immediate conductor. Capacitance for non-adjacent turns is neglected since the E lines are considered to be totally shared only amongst adjacent conductors. Figure 5 shows the path for electric field lines between two adjacent turns, derived from the ABCD path.

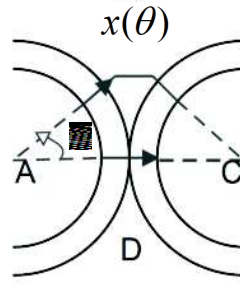


Fig. II. 10 - Assumed path x for field lines between adjacent conductors for $-\pi/6 \leq \theta \leq \pi/6$

- **For the external layer**

A supplementary hypothesis has to be taken for the analytical calculations of the turn-to-turn capacitance for the external layer, where symmetries used before are no longer valid. As a first approximation, for the external layer of the winding it is considered that because of the proximity effect, electric field lines between turns of the layer are shared in the same way that for the turns of the inner layers. This especially means, that no electric field lines travel through greater distances than those mentioned above. And thus, non-adjacent turns have no capacitive coupling whatsoever.

The validity of this strong hypothesis is analyzed in subsequent sections.

- **For the inner layer adjacent to the core**

For the first layer adjacent to the core, the lines between turns are also considered to be shared equally than for the inner layers. The basis of this assumption is again the proximity effect that will make the electric field lines to be concentrated at the closes path between turns. The validity of this hypothesis will also be discussed when comparing simulation and analytical results.

This is not the case however for the turn-to-core capacitance which is discussed in the latter sections.

The turn-to-turn capacitance is then considered to be the same for all adjacent turns of any same or adjacent layer.

Taking these considerations into account, the paths for the E lines can then be calculated.

In general terms, the elementary capacitance dC between the equivalent elementary surfaces dS of two adjacent conductors along a path x can be described as:

$$dC = \epsilon_r \epsilon_0 \frac{dS}{dx} \tag{II. 3-18}$$

The capacitance along the coating of the first turn can then be calculated:

$$dC_c(\theta) = \epsilon_{r_c} \epsilon_0 \frac{r}{dr} d\theta dl \tag{II. 3-19}$$

When integrating over the turn length, (III.3-19) yields:

$$dC_c(\theta) = \epsilon_{r_c} \epsilon_0 \frac{l_t}{\ln\left(\frac{r_0}{r_c}\right)} d\theta \tag{II. 3-20}$$

For the airgap, the capacitance can be calculated considering that in this region

$$x(\theta) = D_0(1 - \cos\theta) \quad \text{II. 3-21}$$

This gives:

$$dC_g(\theta) = \varepsilon_0 \frac{l_t}{2(1 - \cos\theta)} d\theta \quad \text{II. 3-22}$$

Finally, for the third segment concerning E lines entering the coating of the second conductor, the capacitance is the same as in (II.3-19), as for the first coating.

Thus, the total turn-to-turn capacitance can be written as **the series combination** of the calculated capacitances:

$$C_{tt} = \frac{C_c * C_g}{2C_g + C_c} \quad \text{II. 3-23}$$

From hypotheses stated in the above paragraph and as depicted in Fig. II. 10 the integration of the element $d\theta$ has to be taken from $\theta = -\frac{\pi}{6}$ to $\theta = \frac{\pi}{6}$.

Thus, the resulting total capacitance is given by:

$$C_{tt} = \frac{\varepsilon_0 l_t}{2} \int_{-\pi/6}^{\pi/6} \frac{1}{1 + \frac{1}{\varepsilon_{rc}} \ln\left(\frac{r_0}{r_c}\right) - \cos\theta} d\theta \quad \text{II. 3-24}$$

3.5.1.3 Turn-to-core capacitance calculations

For the inner layer, the turn-to core capacitance can easily be calculated with the same expressions.

Considering the iron core surface as a perfect equipotential, electric field lines are orthogonal to the surface of the core. This is in the very specific case of a non-insulated core. In that case, turn-to-core electric field lines go through half of the path compared to the turn-to-turn lines [6] as shown in Fig. II. 11.

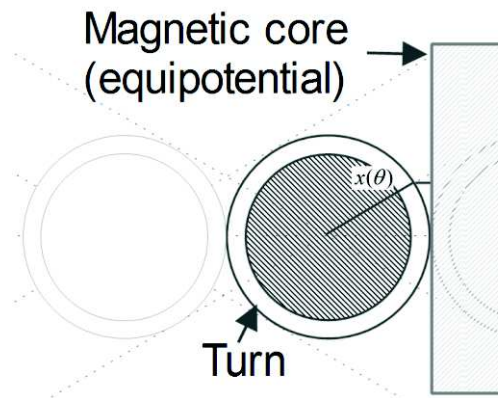


Fig. II. 11 - Dimensions of the structure under consideration

Then, the path taken by the E lines is described as:

$$x(\theta) = r_0(1 - \cos\theta) \quad \text{II. 3-25}$$

Contrary to what the author in [5] predicted, which is integrating over the same angle aperture as the turn-to-turn mechanism, i.e. $\theta = -\frac{\pi}{6}$ to $\theta = \frac{\pi}{6}$, the observation that for geometry reasons, the surface through which electric field lines are shared between the inner turns and the core, is larger than that for the turn-to-turn mechanism from $\theta = -\frac{\pi}{3}$ to $\theta = \frac{\pi}{3}$. However, the short distance from the inner turns to the core increases the proximity effect, and thus, the effective exchange surface is considered to be narrowed to an angle aperture of $\theta = -\frac{\pi}{4}$ to $\theta = \frac{\pi}{4}$. And finally, the resulting turn-to-core capacitance can be modelled similarly as for the turn-to-turn capacitance for half the path and integrated over $\theta = -\frac{\pi}{4}$ to $\frac{\pi}{4}$:

$$C_{tc} = \epsilon_0 l_t \int_{-\pi/4}^{\pi/4} \frac{1}{1 + \frac{1}{\epsilon_{rc}} \ln\left(\frac{r_0}{r_c}\right) - \cos\theta} d\theta \quad \text{II. 3-26}$$

To illustrate the arrangement of the resulting capacitance network, the diagram in Fig. II. 12 shows several turns of adjacent layers virtually separated to show the equivalent capacitances calculated.

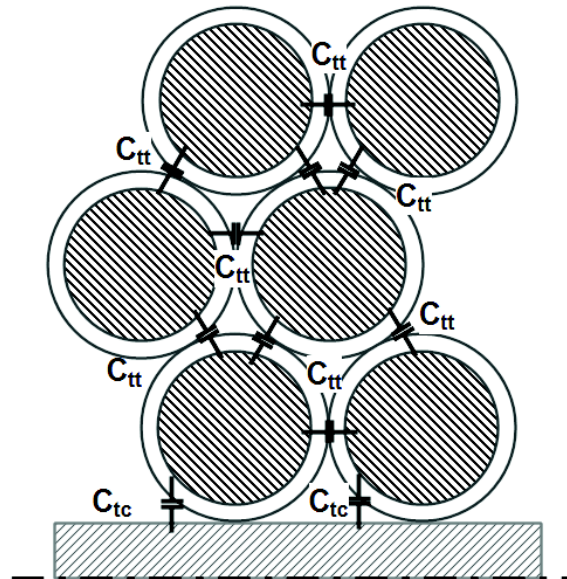


Fig. II. 12 - Capacitance arrangement for a multilayer winding

3.5.2 Introduction of a dielectric film over the core and between two different windings

3.5.2.1 Considered geometry and problem definition

In this complementary model, a thin dielectric film is introduced between the core and the winding. Figure III.16 shows the schematic structure.

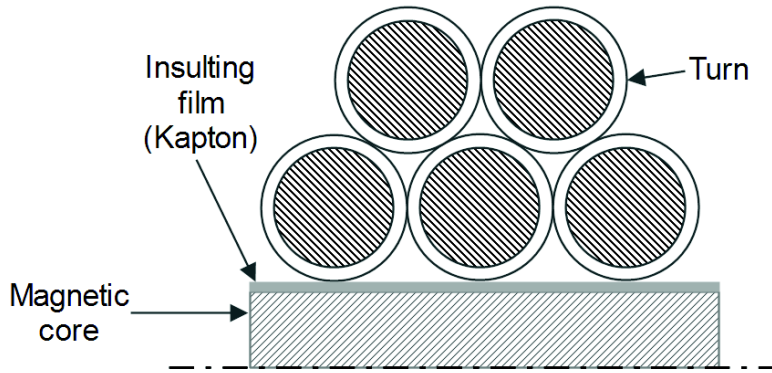


Fig. II. 13 - Diagram of the wound structure with a dielectric film over the core

The introduction of a dielectric medium modifies the above considered path of the electric field lines. The electric field lines are not actually orthogonal to the core in the dielectric film region. However, if the thickness of the film is assumed to be very small compared with the distance between the two conductors (core and copper turn), some assumptions can be made but must be verified.

It can be assumed, that the thickness i of the dielectric film being very small, the electric field lines can still be considered to be orthogonal to the surface of the core in the dielectric film region as for the E lines in the coating thickness of the copper as mentioned before.

For the airgap region, the electric field lines are concentrated between two dielectric materials and the distance between the two equipotentials is larger than in the case of no dielectric film on the core. In fact, by adding media of high relative permittivity, the electric field lines can travel more effectively than in vacuum or air.

3.5.2.2 Turn-to-core capacitance calculation in the presence of a dielectric insulating film

- **Coating and airgap**

As for the turn-to-core capacitance for the case without dielectric film, the coating capacitance can be described as:

$$dC_c(\theta) = \epsilon_r \epsilon_0 \frac{r}{dr} d\theta dl \quad \text{II. 3-27}$$

For the airgap, the conclusions are also the same as for the turn-to-core case with no dielectric film:

$$x(\theta) = r_0(1 - \cos\theta) \quad \text{II. 3-28}$$

Thus, the final expression of the airgap equivalent elementary capacitance is calculated by:

$$dC_g(\theta) = \frac{\epsilon_0 l_t}{x(\theta)} d\theta \quad \text{II. 3-29}$$

It is evident that the expression of the coating and airgap capacitance in this case is the same as for the turn-to-core capacitance in formulation (II.3-26) without dielectric insulating film.

- **Insulating dielectric film over the core**

Electric field lines are orthogonal to the surface of the core, and since the insulating dielectric film is considered to have a small thickness i , as for the coating thickness over the copper turns. E lines are still considered to be orthogonal to the surface of the core.

Thus, the path for the electric field lines in the coating thickness is reduced to only $x(\theta) = i$. The equivalent surface however, is considered to be the projection of the turn on the dielectric thickness over the core:

$$dS_f(\theta) = r_0 l_t \cos(\theta) d\theta \quad \text{II. 3-30}$$

The equivalent capacitance of the dielectric film is then:

$$dC_f(\theta) = \frac{\epsilon_0 \epsilon_{rf} l_t r_0}{i} \cos(\theta) d\theta \quad \text{II. 3-31}$$

The overall capacitance between the inner layer turns and the insulated core, is the series combination of the coating capacitance, the airgap capacitances, and the dielectric film capacitance. Arrangement is presented in Fig. II. 14.

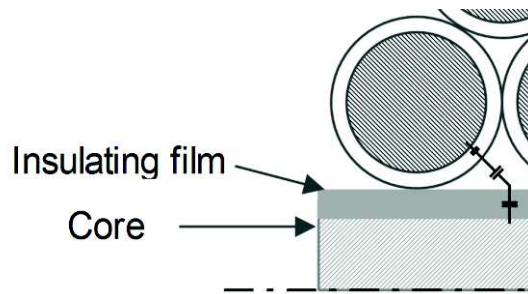


Fig. II. 14 - Overall capacitance arrangement for the inner layer turns

The final expression of the turn-to-core capacitance in presence of a dielectric film is given by:

$$C_{tcf} = \frac{C_{tc} * C_f}{C_{tc} + C_f} = \epsilon_0 \cdot \epsilon_{rf} \cdot l_t \cdot r_0 \int_{-\pi/4}^{\pi/4} \frac{1}{\left(1 + \frac{1}{\epsilon_{rc}} \ln\left(\frac{r_0}{r_c}\right) - \cos\theta\right) \cdot \epsilon_{rf} \cdot r_0 \cdot \cos\theta + i} d\theta \quad \text{II. 3-32}$$

3.5.3 Turn-to-turn capacitance calculation in the presence of a dielectric insulating

The last interesting case to analyze is the insulating film between two different windings with the same turn wire gauge.

Fig. II. 15 describes two windings isolated from each other by a dielectric deformable film. This is a common transformer setup.

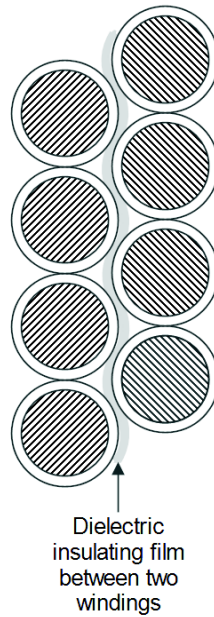


Fig. II. 15 - Two-winding structure separated by a dielectric film

The concerned coupling mechanism, is the turn-to-turn capacitance of the two layers adjacent to the dielectric film. Fig. II. 16 shows the elementary cell, in a similar manner than that for the simple turn-to-turn capacitance.

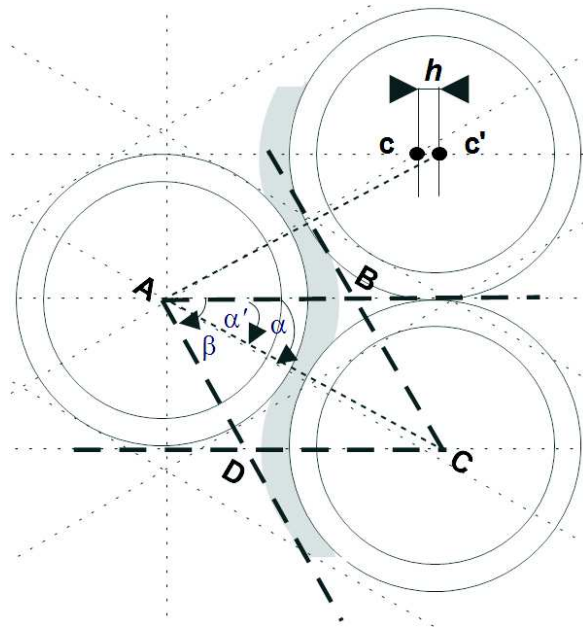


Fig. II. 16 - Assumed three-cell elementary coupling mechanism

The dielectric film being deformable, the geometric configuration is different. However, with several to-validate hypotheses, the problem can again be narrowed to a two-turn elementary configuration such as for the simple turn-to-turn capacitance in the first case.

First, the implantation of a dielectric film causes a translation along the horizontal of a distance h according to Fig. II. 16. As long as the condition $i \ll r_0$, the distance h can be linked to the dielectric thickness i by the approximation:

$$h = i * \cos(\alpha) \quad \text{with } \alpha = \pi/6$$

The turn-to-turn capacitance calculation can be narrowed to the ABC cell. Since $i \ll r_0$ then $\alpha \approx \alpha'$ and thus, by a rotation of an angle of π rad. the cell ABC is the same as ADC. The capacitance calculated over ABC will have to be doubled.

The thickness of the dielectric film is not negligible compared to the coating thickness of the turn.

• **Calculation of the equivalent capacitance**

Four paths are identified:

- Paths (1) and (4): coating thicknesses
- Path (2): airgap
- Path (3): dielectric thickness

The path length through the airgap is considered to be small enough compared with the turn radius so the E lines follow a similar behavior as for the simple turn-to-turn case. The electric field lines are considered to be perpendicular to the common tangent line to the circle formed by the left turn of radius r_0 and the right turn including the dielectric film of radius $r_0 + i$ as shown in Fig. II. 16.

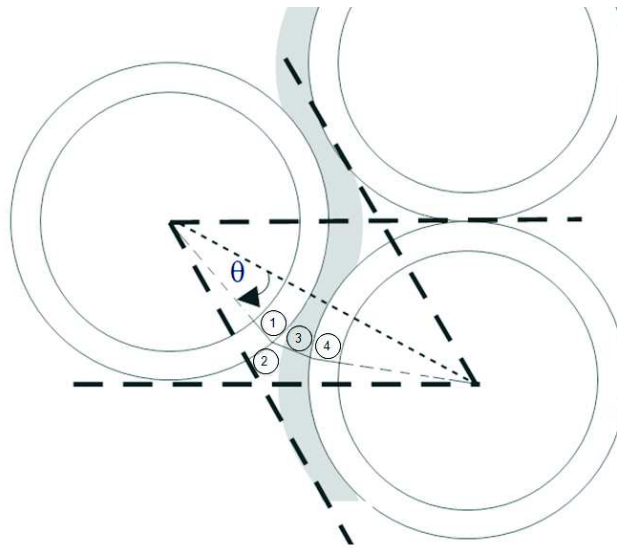


Fig. II. 17 – Field lines through the 4 different paths

Under that assumption, the equivalent capacitance is quickly calculated by noticing that it is the same case that for the simple case of the turn-to-turn capacitance over approximately half the distance as for the normal case.

Then, again, the film being very thin compared to the turn radius, it can be considered that the E lines in the dielectric film are orthogonal to the equipotential surface (copper) of the turn bearing the film.

From this analysis, it is obvious that, taking the symmetry axis of the turn-to-turn mechanism, the calculations are exactly the same as for the turn-to-core with insulating film case but only over $\theta =$

$-\frac{\pi}{6}$ to $\theta = \frac{\pi}{6}$. Thus, the overall turn-to-turn capacitance with the insulating film **involves double the distance** as in the turn-to-core case.

Therefore, the final expression of the turn-to-turn capacitance with an insulating film is obtained by dividing by 2 the value of the capacitances obtained for the turn-to-core capacitance with half the thickness of the insulating film ($i/2$) and integrating only for $\theta = -\frac{\pi}{6}$ to $\theta = \frac{\pi}{6}$:

$$C_{ttf} = \frac{\varepsilon_0 \cdot \varepsilon_{rf} \cdot l_t \cdot r_0}{2} \int_{-\pi/6}^{\pi/6} \frac{1}{\left(1 + \frac{1}{\varepsilon_{rc}} \ln\left(\frac{r_0}{r_c}\right) - \cos\theta\right) \cdot \varepsilon_{rf} \cdot r_0 \cdot \cos\theta + i/2} d\theta \quad \text{II. 3-34}$$

3.5.4 Case of impregnated windings

For the same difference of voltage potential between two given conductors, the electric field intensity $|\vec{E}|$ is formally ε_r times less important in the presence of a dielectric media than in the vacuum [2].

Therefore, all the partial capacitances of the airgaps calculated here before, will see its value increased by a factor equal to the value of the relative permittivity of the dielectric material (epoxide resin in this case) it was replaced with.

In the case of the turn-to-turn mechanism, symmetries force the electric flux lines to be equally shared between turns, so the surface aperture is the same as for the air case even with the presence of the resin impregnation. Thus, the only change in the turn-to-turn capacitance for an impregnated winding is the increase in the partial “airgap” capacitance as follows:

$$dC_g(\theta) = \varepsilon_{rR} \varepsilon_0 \frac{l_t}{2(1 - \cos\theta)} d\theta \quad \text{II. 3-35}$$

Consequently, the overall turn-to-turn capacitance in an impregnated winding is (refer to eq. (7)):

$$C_{ttimp} = \frac{\varepsilon_0 \cdot \varepsilon_{rR} \cdot \varepsilon_{rc} \cdot l_t}{2} \int_{-\pi/6}^{\pi/6} \frac{1}{\varepsilon_{rR} \cdot \ln\left(\frac{r_0}{r_c}\right) + \varepsilon_{rc} \cdot (1 - \cos\theta)} d\theta \quad \text{II. 3-36}$$

Furthermore, for the turn-to-core mechanism, an increase of the permittivity is equally taken into account. But, apart from that increase in relative permittivity of the airgap, the presence of a dielectric body eases the exchange of electric field lines between the core and the inner turns over a wider surface. So the angle aperture is larger than in the case of air-filled airgap.

In Fig. II. 18 is diagrammed the discretized space available between the inner turns and the core. The discretization takes into account the remaining area left from the aforementioned symmetries for the turn-to-turn couplings ($\theta = \frac{\pi}{3}$ to $\theta = \frac{\pi}{2}$ in this figure) and the symmetries concerning the inner turns and the core (blue zone).

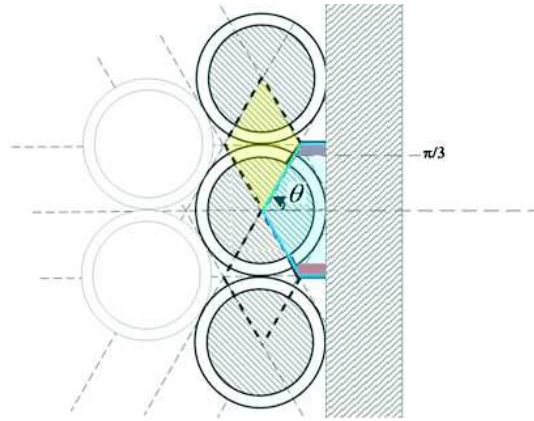


Fig. II. 18 - Discretization of the area between an inner turn and the bare core

To take a bigger surface of exchange into account, the angle aperture will be taken from $\theta = -\frac{\pi}{3}$ to $\theta = \frac{\pi}{3}$ and up to the tangent line between two inner turns (blue zone). However, taking the expression of the path through the airgap as in eq. (II.3-28), a small amount of electric field lines wouldn't be taken into account (red zone). Although this area would be ignored, the proximity of the turns to the core is still a major factor for the field lines to concentrate close to the core rather than the adjacent turns. So the hypothesis taken here is that all the field lines are concentrated in the clear blue zone minus the red zones. It is again obvious that this hypothesis has to be validated.

The turn-to core mechanism thus becomes (refer to the development of eq. (II.3-26) integrated between $\theta = -\frac{\pi}{3}$ to $\theta = \frac{\pi}{3}$:

$$C_{tc_{imp}} = \varepsilon_0 \cdot \varepsilon_{rR} \cdot \varepsilon_{rC} \cdot l_t \int_{-\pi/3}^{\pi/3} \frac{1}{\varepsilon_{rR} \cdot \ln\left(\frac{r_0}{r_c}\right) + \varepsilon_{rC} \cdot (1 - \cos\theta)} d\theta \quad II. 3-37$$

For the dielectric film over the core or between windings when an impregnation resin is used, the same hypotheses as before are used: the introduction of the resin changes the equivalent partial capacitance of the filled airgap by a factor of ε_{rR} and the presence of a thin dielectric film. Consequently, the turn-to core capacitance with a dielectric film is expressed as the series combination of the turn-to-core capacitance for an impregnated winding and the partial capacitance yielded by the thin dielectric film:

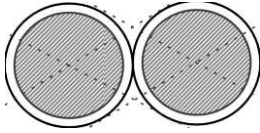
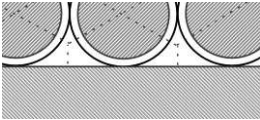
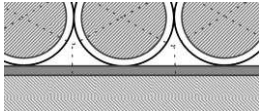
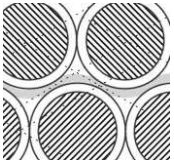
$$C_{tc_{f_{imp}}} = \varepsilon_0 \cdot \varepsilon_{rR} \cdot \varepsilon_{r_f} \cdot \varepsilon_{r_c} \cdot l_t \int_{-\pi/3}^{\pi/3} \frac{\cos\theta}{\varepsilon_{r_f} \cdot \cos\theta \left(\varepsilon_{rR} \cdot \ln\left(\frac{r_0}{r_c}\right) + \varepsilon_{r_c} \cdot (1 - \cos\theta) \right) + \frac{i}{r_0} \varepsilon_{rR} \varepsilon_{r_c}} d\theta \quad II. 3-38$$

For the last case scenario processed in this study, the turn-to-turn capacitance for two insulated windings with a dielectric film inserted in between, the modified airgap partial capacitance is included in eq. (II.36).

$$C_{tt_{f_{imp}}} = \frac{\varepsilon_0 \cdot \varepsilon_{rR} \cdot \varepsilon_{r_f} \cdot \varepsilon_{r_c} \cdot l_t}{2} \int_{-\pi/6}^{\pi/6} \frac{\cos\theta}{\varepsilon_{r_f} \cdot \cos\theta \left(\varepsilon_{rR} \cdot \ln\left(\frac{r_0}{r_c}\right) + \varepsilon_{r_c} \cdot (1 - \cos\theta) \right) + \frac{i}{2 \cdot r_0} \varepsilon_{rR} \varepsilon_{r_c}} d\theta \quad II. 3-39$$

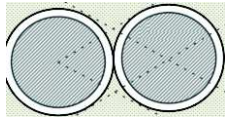
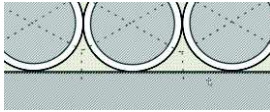
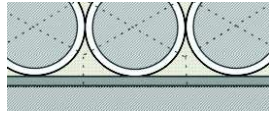
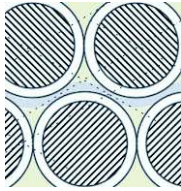
3.5.5 Summary of analytical expressions of partial capacitances

Table II. 5 - Summary of the partial capacitance expressions for non-impregnated windings

Case reference	Coupling mechanism	Desig.	Schematic view	Analytical value of the capacitance for a given turn length
Case 1	Turn-to-turn	C_{tt}		$C_{tt} = \frac{\epsilon_0 l_t}{2} \int_{-\pi/6}^{\pi/6} \frac{1}{1 + \frac{1}{\epsilon_{rc}} \ln\left(\frac{r_0}{r_c}\right) - \cos\theta} d\theta$
Case 2	Turn-to-core	C_{tc}		$C_{tc} = \epsilon_0 l_t \int_{-\pi/4}^{\pi/4} \frac{1}{1 + \frac{1}{\epsilon_{rc}} \ln\left(\frac{r_0}{r_c}\right) - \cos\theta} d\theta$
Case 3	Turn-to-core through insulating dielectric film	C_{tc_f}		$C_{tc_f} = \epsilon_0 \cdot \epsilon_{rf} \cdot l_t \cdot r_0 \int_{-\pi/4}^{\pi/4} \frac{1}{\left(1 + \frac{1}{\epsilon_{rc}} \ln\left(\frac{r_0}{r_c}\right) - \cos\theta\right) \cdot \epsilon_{rf} \cdot r_0 \cdot \cos\theta + i} d\theta$
Case 4	Turn-to-turn through insulating dielectric film	C_{tt_f}		$C_{tt_f} = \frac{\epsilon_0 \cdot \epsilon_{rf} \cdot l_t \cdot r_0}{2} \int_{-\pi/6}^{\pi/6} \frac{1}{\left(1 + \frac{1}{\epsilon_{rc}} \ln\left(\frac{r_0}{r_c}\right) - \cos\theta\right) \cdot \epsilon_{rf} \cdot r_0 \cdot \cos\theta + i} d\theta$

Chapter II: Wide Band Analytical Modelling of Actuators with Concentrated Windings

Table II. 6 - Summary of the partial capacitance expressions for impregnated windings

Case reference	Coupling mechanism	Desig.	Schematic view	Analytical value of the capacitance for a given turn length
Case 5	Impregnated turn-to-turn	C_{ttimp}		$C_{ttimp} = \frac{\epsilon_0 \cdot \epsilon_{rR} \cdot \epsilon_{rc} \cdot l_t}{2} \int_{-\pi/6}^{\pi/6} \frac{1}{\epsilon_{rR} \cdot \ln\left(\frac{r_0}{r_c}\right) + \epsilon_{rc} \cdot (1 - \cos\theta)} d\theta$
Case 6	Impregnated Turn-to-core	C_{tcimp}		$C_{tcimp} = \epsilon_0 \cdot \epsilon_{rR} \cdot \epsilon_{rc} \cdot l_t \int_{-\pi/3}^{\pi/3} \frac{1}{\epsilon_{rR} \cdot \ln\left(\frac{r_0}{r_c}\right) + \epsilon_{rc} \cdot (1 - \cos\theta)} d\theta$
Case 7	Impregnated turn-to-core through insulating dielectric film	C_{tcfimp}		$C_{tcfimp} = \epsilon_0 \cdot \epsilon_{rR} \cdot \epsilon_{rf} \cdot \epsilon_{rc} \cdot l_t \int_{-\pi/3}^{\pi/3} \frac{\cos\theta}{\epsilon_{rR} \cdot \ln\left(\frac{r_0}{r_c}\right) + \epsilon_{rc} \cdot (1 - \cos\theta) + \frac{i}{r_0} \epsilon_{rR} \epsilon_{rc}} d\theta$
Case 8	Impregnated turn-to-turn through insulating dielectric film	C_{ttfimp}		$C_{ttfimp} = \frac{\epsilon_0 \cdot \epsilon_{rR} \cdot \epsilon_{rf} \cdot \epsilon_{rc} \cdot l_t}{2} \int_{-\pi/6}^{\pi/6} \frac{\cos\theta}{\epsilon_{rR} \cdot \ln\left(\frac{r_0}{r_c}\right) + \epsilon_{rc} \cdot (1 - \cos\theta) + \frac{i}{2 \cdot r_0} \epsilon_{rR} \epsilon_{rc}} d\theta$

3.6 2-D FINITE ELEMENT ANALYSIS MODELING AND COMPARISON TO ANALYTICAL MODELING

In order to challenge the validity of the models established in (§II.3.5), a Finite Element Analysis is performed. A two-dimension model such as for the analytical model is built and parameterized to include different materials, coating thickness and insulating layouts. The results sought concern the value of the different capacitances summarized in Table II. 5 and Table II. 6 with different materials and configurations. The validity of the analytical model is therefore tested against numerical calculations. However, the ultimate verification of the model will be performed in later sections with experimental results.

3.6.1 Hypothesis and setup

As for the analytical modeling of capacitive couplings, the problem is considered to be axisymmetric. The axis of the circular geometry is considered to be the axis of the magnetic core. The resulting quantities calculated in the FEA are per/meter quantities.

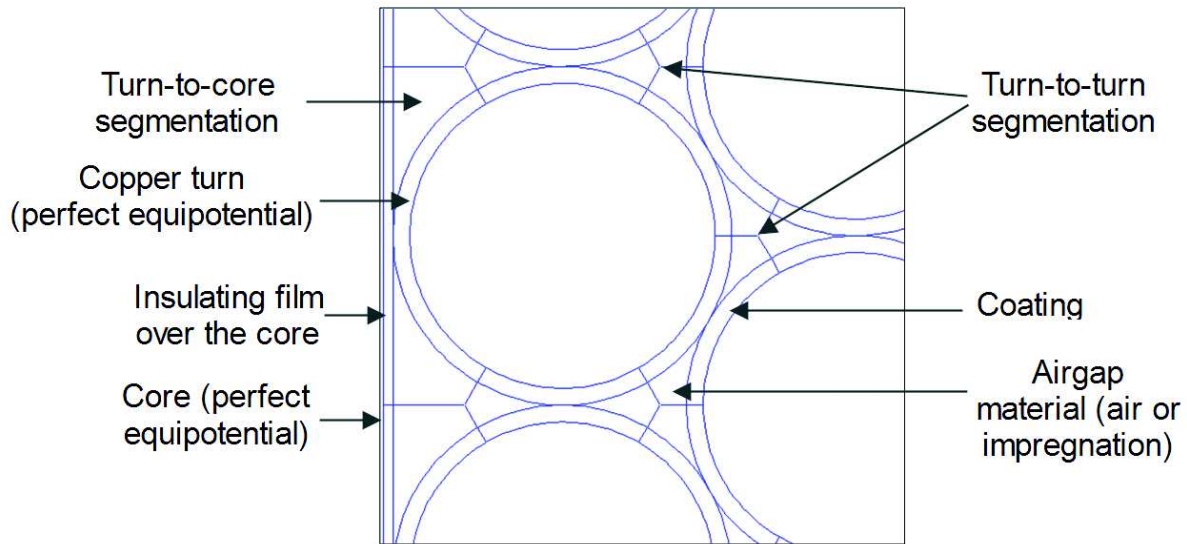


Fig. II. 19 - FEA setup and segmentations for electrostatic energy calculations

In Fig. II. 19 are depicted the conditions of FEA setup and segmentation between turns and turns and core. The software used for the analysis is Finite Element Method Magnetics (FEMM) [2], a magnetostatic and electrostatic FE free software for two-dimensional problem solving.

The equipotentials (copper turns and core) are set to fixed voltages as follows:

Table II. 7 - Equipotential conditions for energy calculations

Equipotential	Voltage
High potential	1 V
Low potential	0 V

The output variable for the analysis is the electrostatic energy stored in the segmented areas circumventing the copper turns (dielectric materials or air) and along the surface of the core.

The energy calculated in each region yields:

$$W_s = \frac{C_s (\Delta V)^2}{2} \quad \text{II. 3-40}$$

Thus, the partial capacitance in the selected area is given by:

$$C_s = \frac{2 \cdot W_s}{(\Delta V)^2} \tag{II. 3-41}$$

The segmentation is made according to the hypothesis stated in the analytical modeling part. As for the turn-to-turn mechanism, it is thus assumed that the couplings outside the segmented areas is negligible compared to the energy stored inside these areas. In Fig. II. 20 is presented a segmented problem solution in which the field lines (arrows) are mainly concentrated into the segmented areas. This hypothesis has yet to be verified by the calculation of the ratio of energy escaping the stated areas against the total energy.

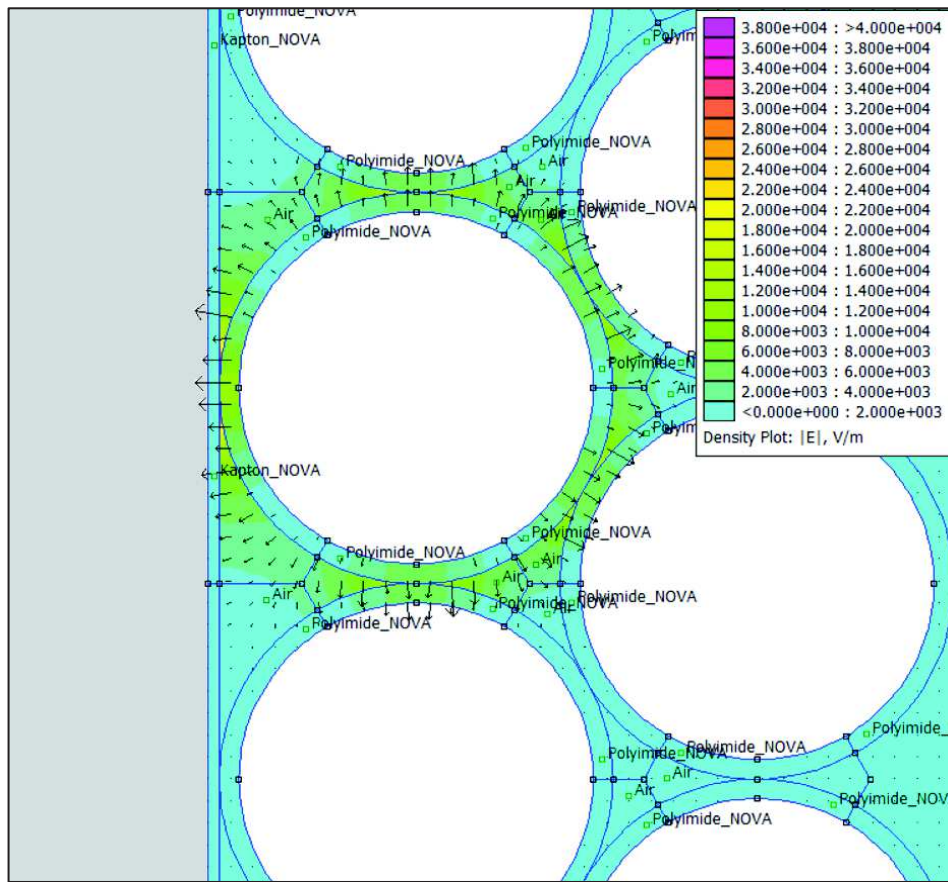


Fig. II. 20 - Segmentation and field lines contained in the specified regions for energy calculation

In order to compare the analytical and FEA model computation results, a set of different IEC 60317 commonly used wires were chosen and resumed in Table II. 8. Because of the time consuming process, only two grades were tested.

Also, only a few set of materials were chosen for the analysis (cf. Table II. 9):

Table II. 8 - Wire specifications used in the analysis

Copper diameter	Grade 1 diameter (average)	Grade 2 diameter (average)
mm	mm	mm
0.200	0.220	0.233
0.250	0.274	0.289
0.315	0.342	0.359
0.400	0.430	0.449
0.500	0.534	0.556
0.630	0.668	0.692
0.710	0.750	0.776
0.800	0.843	0.870
1.000	1.048	1.079
1.250	1.301	1.333
1.600	1.654	1.689
2.000	2.057	2.094

Table II. 9 - Materials properties used in the analysis

Function	Commercial name	Material	Relative permittivity (at frequency)
Dielectric film over the core	Kapton®	Polyamide-imide	3.4 (1 kHz)
Turns coating		Polyamide-imide	3.5 (1 MHz)
Impregnation*	AralditeF® Aradur C121/HY905 mixture at 50% 23 °C	Epoxide Resin	3.7 (50 Hz)

*Airgap filling is analyzed with both epoxide resin and air ($\epsilon_{r_{air}} = 1.00$)

Furthermore, IEC 60317 specifies the properties of *thermo-adhesive* wires for windings. The thermal-adherent coating fuses at lower temperatures than class specifications. For class C wires, the materials used are aromatic polyurethanes or polyurethane nylon sensitive to solvent or temperatures of 130 °C.

Although the dielectric constant of such materials are higher than impregnation materials accounted for, in this study, bondable wires are not taken into account because of the little information on airgap-filling properties of thermal-adherent polyurethanes. For further information on thermos-adhesive behaviors in such windings, please refer to [2] where the author examines a full airgap filling of such materials.

3.6.2 Per-meter values as function of the case, wire diameter and grade

To illustrate the resulting calculations in a per-meter perspective, some values are given for the different cases treated here above. The analytical calculations of per-meter capacitance value are resumed hereafter:

Without insulating dielectric film								
Wire diameter (mm)	Non impregnated				Impregnated			
	Turn-to-turn (pF/m)		Turn-to-core (pF/m)		Turn-to-turn (pF/m)		Turn-to-core (pF/m)	
	Grade 1	Grade 2	Grade 1	Grade 2	Grade 1	Grade 2	Grade 1	Grade 2
0.20	87,9	63,6	195,0	146,4	125,7	86,4	308,6	218,6
0.40	105,0	76,4	230,7	172,9	156,4	107,9	374,3	267,1
0.71	125,0	91,4	271,4	204,3	192,1	133,6	450,0	324,3
1.25	152,1	112,9	326,4	252,1	261,4	175,0	554,3	415,0
2.00	186,4	140,0	397,9	301,4	305,7	221,4	686,4	507,1

With insulating dielectric film (50 µm)								
Wire diameter (mm)	Non impregnated				Impregnated			
	Turn-to-turn (pF/m)		Turn-to-core (pF/m)		Turn-to-turn (pF/m)		Turn-to-core (pF/m)	
	Grade 1	Grade 2	Grade 1	Grade 2	Grade 1	Grade 2	Grade 1	Grade 2
0.20	37,3	33,8	65,0	60,7	44,2	39,2	344,3	250,0
0.40	55,9	48,8	104,3	92,1	72,1	63,2	410,7	300,7
0.71	72,9	65,0	148,6	127,1	105,0	80,0	488,6	360,0
1.25	102,1	87,1	207,9	176,4	151,4	122,9	595,0	452,1
2.00	130,7	110,0	275,0	226,4	206,4	159,3	728,6	545,7

3.6.3 Comparative analysis and results

In Fig. II. 21 and Fig. II. 22, the relative errors between analytical models and FEA models of turn-to-turn cases are presented both for grade 1 and grade 2 wires.

Globally, the relative errors are inferior to 30% except for case 7. The general trends are in the sense of error reduction with increasing wire diameter. In fact, the larger the diameter, the better the hypotheses are respected giving better predictions. A singularity in this general behavior is found with non-impregnated turn-to-turn capacitance when a dielectric film is present as can be seen in Fig. II. 23 and Fig. II. 24. Adding a thickness of dielectric materials seems to have a larger impact on the hypotheses of closeness of equipotentials than expected.

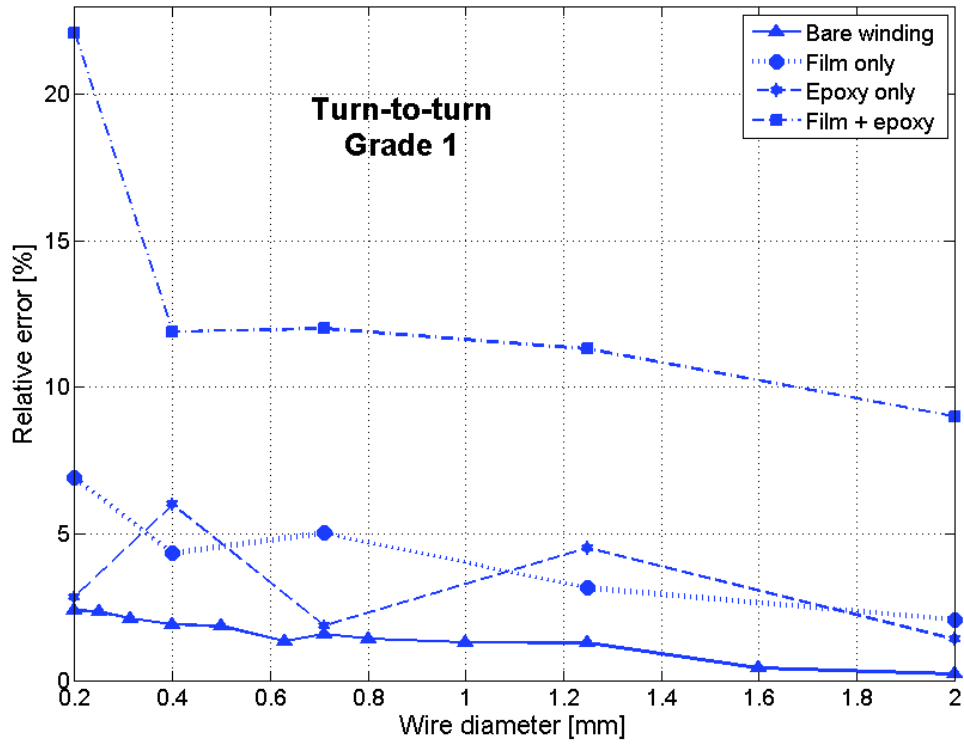


Fig. II. 21 – Comparison of results for turn-to-turn capacitance for Grade 1

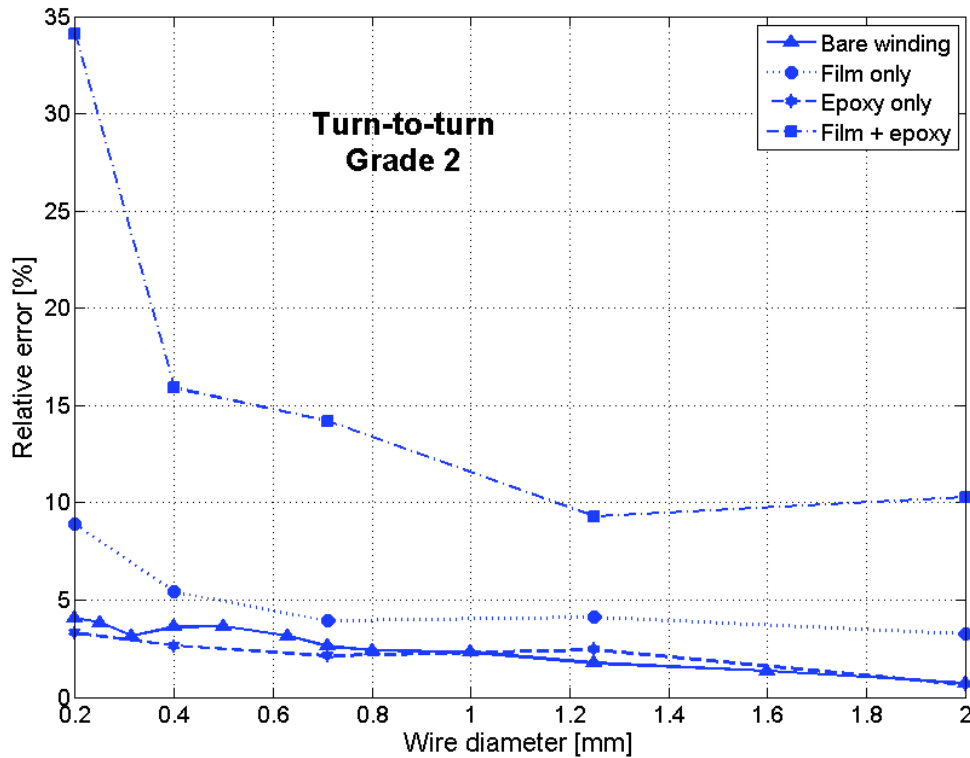


Fig. II. 22 – Comparison of results for turn-to-turn capacitance for Grade 2

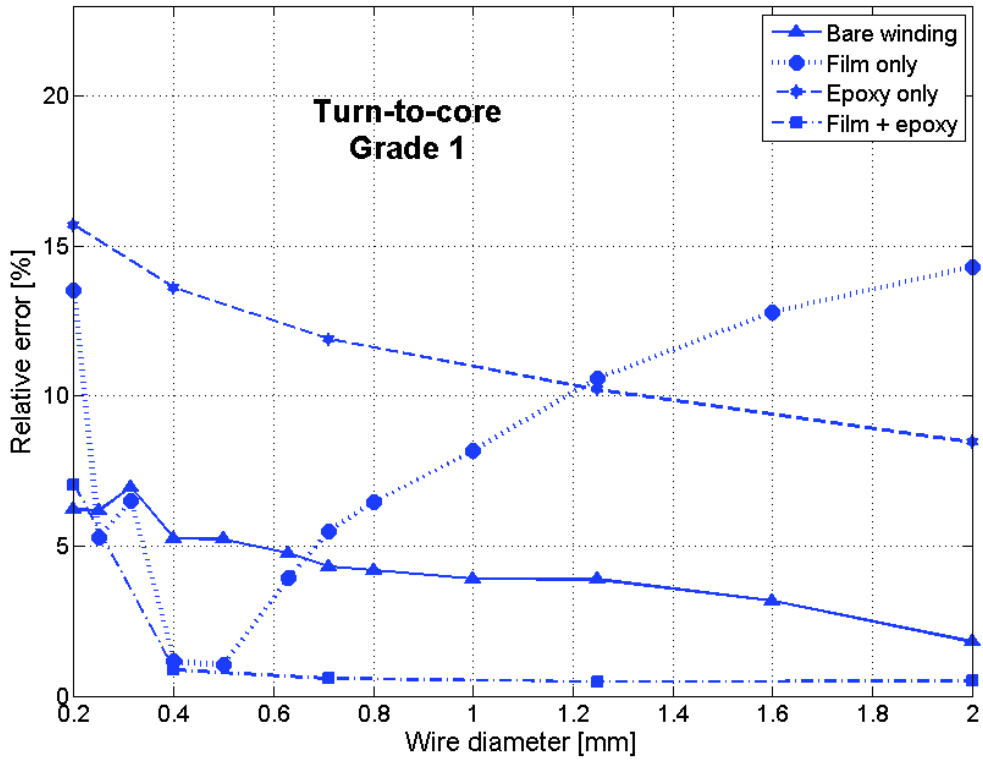


Fig. II. 23 - Comparison of results for turn-to-core capacitance for Grade 1

Finally, concerning the turn-to-core mechanism for the different film thickness, the average relative errors for grade 1 and 2 wire cases are resumed in Table II. 10.

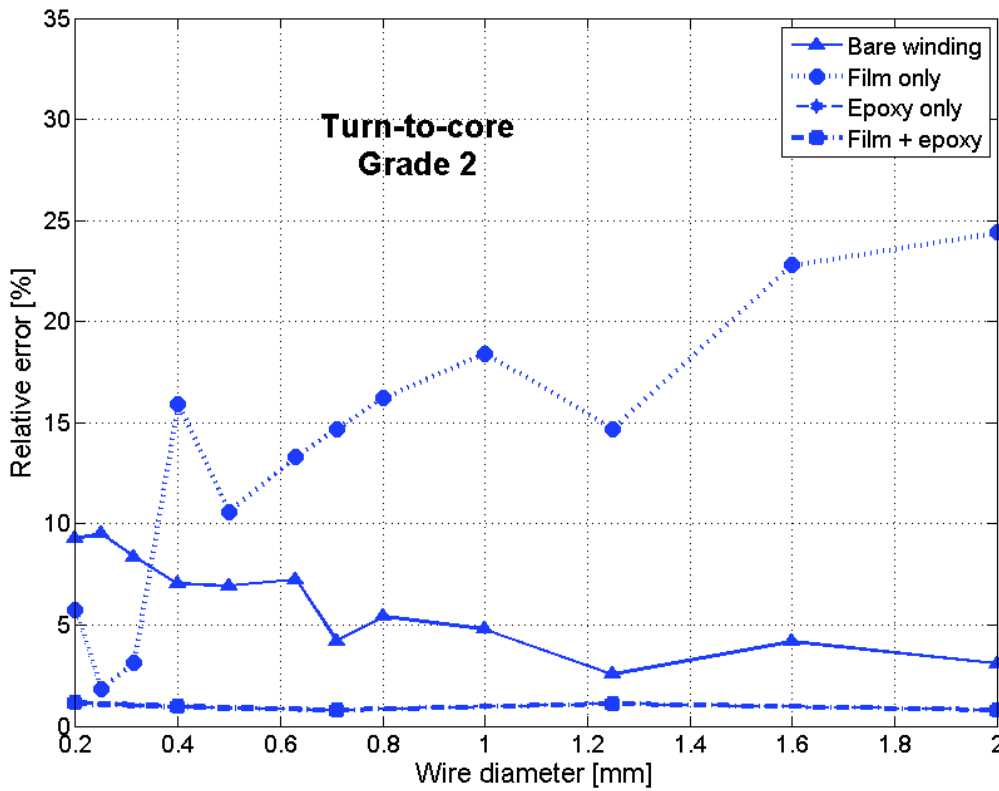


Fig. II. 24 - Comparison of results for turn-to-core capacitance for Grade 2

The same conclusion is drawn for grade 1 vs. grade 2 insulations since results for grade 1, which is a thinner coating insulation than grade 2 are better overall, compared to FEA results.

Table II. 10 - Turn-to-core capacitance for different film thickness

Film thickness	Non-impregnated		Impregnated	
	Grade 1 average error %	Grade 2 average error %	Grade 1 average error %	Grade 2 average error %
50 μm	7.44	13.5	1.9	1
100 μm	9.44	16.3	12.3	12.5
200 μm	20.2	23.7	32.5	29.7

The thicker the insulating film, the bigger the difference between analytical and FEA results. This is especially accentuated by the fact that the model doesn't perform well when an insulating film is included.

However, for most of the cases, especially for bare windings, errors are very small. Besides, the analytical models, even at 30 % error, are useful to estimate the capacitive behavior with very simple formulations.

3.6.4 Discussion

The overall difference between the analytical model and the FE model calculations is slightly larger for the grade 2 case than for the grade 1 case. But still, the models, even for a large variety of conditions are concordant with FEA. Only two cases are divergent which involve the large dielectric insulating films and impregnated windings.

Symmetry reasons make the turn-to-turn case more convergent with the FE analysis inasmuch as the electric field is evenly spread among the adjacent turns. For the turn-to-core, a strong hypothesis was assumed stating that only a major part of the potential region was accounted for in the calculations.

Then, it can be pointed out that for the 50 μm film case, analytical model broadly overestimates the turn-to-core capacitance whereas for the 100 and 200 μm , they are underestimated. The reason for this finding might lie in the fact that 50 μm film is still thin enough to concentrate the field around the $\theta = 0$ area, so integrating over $2\pi/4$ seems to overrate the actual field in the region.

For the other cases, the model seems to badly behave when the hypothesis of small distances separating the two equipotentials is not respected. The growing distance between the copper turn and the core because of the larger dielectric film thickness tends to increase the path $x(\theta)$ for the electric field lines. E lines don't concentrate close to $\theta = 0$ area only. Instead, the larger separation induces a scattering of E lines over a larger angle. It seems that for larger film thicknesses, integrating over $2\pi/4$ wouldn't be enough.

But, given these conclusions about the integrating angle, the model seems to behave quite acceptably compared to FEA for film thicknesses between 50 and 200 μm , which are standard medium voltage motor insulating magnitudes. And, because of the irregularities inherent to winding wire mechanical tensions and deformations of dielectric materials with mechanical stress, dimensions stated here may strongly vary. So in the worst case scenario, which is the Grade 1 configuration with a 200 μm thickness at 32.5 %, the analytical models are convergent with FEA.

4 CALCULATION OF INDUCED CURRENTS IN THE WINDING TURNS

4.1 THE SKIN AND PROXIMITY EFFECTS

4.1.1 Overview

Eddy currents are subject to be found in any conducting material subject to time varying magnetic fields.

For a given conductor of conductivity σ an alternating electromagnetic field penetrates it and produces an induced electromagnetic field, resulting in the occurrence of currents called induced currents or Foucault currents or eddy currents in the conductor [2]. The effects of eddy-currents is the non-uniform distribution of current density in a given cross-section. This is directly translated into higher dissipation in the form of Joule losses.

The field penetrates the conductor to a depth given by:

$$\delta = \sqrt{\frac{2}{\omega\sigma\mu}} \quad \text{II. 4-1}$$

Where, ω is the pulsating frequency, σ the copper conductivity and μ the absolute permeability of copper.

First of all, it is considered that the conductors' physical dimensions are larger than the field penetration depth. Then, in metals and high conductivity bodies, when the penetration depth δ is large compared with the main free path of conduction electrons l_e , the eddy currents can be analyzed in the frame of the quasi-static approximation. In copper, the mean free path of conduction electrons can be approximated by stating that there is 1 conduction electron per atom, which yields, $l_e \sim 20$ nm at ambient temperature. This length corresponds to ultra-high frequencies, which means, that at frequencies pertinent to this analysis, the quasi-static approximation is largely sufficient for desired purposes. For less conductive materials, the mean free path becomes larger but still, the quasi-static approximation is assumed to be valid up to several tens of GHz [2].

For standard ferromagnetic materials, the problem is slightly different. The high permeability at fairly low frequencies (<1 kHz up to 100 kHz) and the reduced conductivity compared with good conductors, facilitates the penetration of the field into the conductive body of ferromagnetic materials.

Similarly, when a conductor carries an alternating current, it is subject to a self-induced electromagnetic field, narrowing the effective cross-section of the conductor carrying the current to a penetration depth. This effect is called the skin effect. Besides, a proximity effect appears for conductors near to each other carrying currents, inducing electromagnetic fields among them and further reducing their effective conductivity. This two phenomena are usually calculated together [7].

In this section, only the induced currents in conductors (copper turns of the winding) are considered. For the ferromagnetic core, a specific paragraph in subsequent sections is provided.

The first objective of this analysis is to compare several expressions of impedance models accounting for the eddy current effects in conductors in order to best fit our applications. Then, the selected approximations are thoroughly analyzed and implemented. Finally, the ultimate aim is to create circuit models of networks to reproduce the behavior of the impedances valid in time and frequency domains.

4.1.2 Summary of analyzed expressions of eddy-current-modified impedance

In [7], the authors calculate the equivalent impedance of round Litz wire windings by calculating the losses resulting from the skin and proximity effects in the copper conductors. However, the spatial arrangement of the Litz strands is assumed to be as shown in Fig. II. 25 which doesn't take into account the interlacing of the strands of adjacent layers to occupy a maximum amount of space.

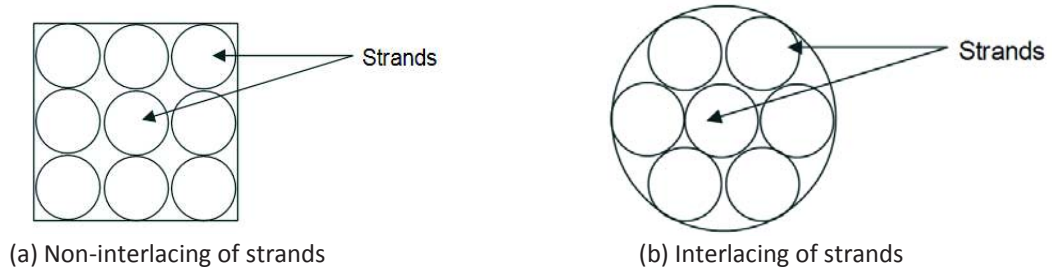


Fig. II. 25 - Two different Litz wire arrangement for modelling

Then, in the work of [8], the author establishes the expression of the resistance of a conductor in a Litz wire in a more general manner, taking into account macroscopic parameters such as the packing factor to improve compactness of the Litz wire (Fig. II. 25 -b). In [9], this expression is applied to a four-strand wire with good results. The main problem with this expression is the assumption that the wire has a straight geometry, which may be disadvantageous for coil geometries with shallow depths.

In [10], the expression of the impedance of rectangular cross-section conductors is derived for both curved-shape turns in long transformer windings and straight conductors. Though this expression doesn't take into account the proximity effect in axial directions because of the assumption of sufficiently long coils compared with their cross-section area, it takes into account the radial distribution of the proximity effect from the center of the core in the \vec{r} direction.

Furthermore, there are several other expressions of the impedance of conductors in coils as presented in [11] (originally developed in [12]), [13] and [14] together with impedance expressions and approximations of single conductors (skin effect only) as in [15] and [16].

In e above models are summarized.

Table II. 11, the hypotheses and assumed geometries used in some of the above models are summarized.

Table II. 11 - Different internal impedance models and hypotheses for eddy current effects on copper turns

Expression name	Modelled effects	Hypotheses	Per-turn or global value
Z_{i_1} as found in [12]	Skin effect only Impedance approximation	<ul style="list-style-type: none"> • Cylindrical conductor • Curved conductor 	Per-turn impedance
Z_{i_2} as found in [10]	Skin + proximity Impedance approximation	<ul style="list-style-type: none"> • Rectangular conductor • Curved conductor 	Per-turn impedance
Z_{i_3}	Skin + proximity Impedance approximation	<ul style="list-style-type: none"> • Rectangular conductor • Straight conductor 	Per-turn impedance

as found in [10]			
R_{iL} as found in [8]	Skin + proximity Resistance approximation	<ul style="list-style-type: none"> • Cylindrical conductor • Curved conductor 	Global resistance
Z_{skinM} as found in [15]	Skin effect impedance approximation	<ul style="list-style-type: none"> • Cylindrical conductor • Straight conductor 	Per-turn impedance

The internal impedance found in [12] concerns an isolated cylindrical conductor of curved shape and corresponds to the exact calculation of the impedance according to Maxwell equations for an isolated (in vacuum – skin effect only -) conductor with a current:

$$Z_{i_1} = R_{dc} \frac{\gamma \cdot r \cdot I_0(\gamma \cdot r_c)}{2 \cdot I_1(\gamma \cdot r_c)} \quad II. 4.2$$

Where I_0 and I_1 are the modified Bessel functions of the first kind of the zero and first order, r is the cylindrical conductor radius and l the length of the straight conductor. R_{dc} is the DC resistance of the wire and γ is a complex quantity given by

$$\gamma = \sqrt{j\omega\sigma\mu} \quad II. 4.3$$

Furthermore, the internal impedances for curved (circular shape around the core) and straight rectangular conductors given by [10] are here specified:

$$Z_{i_2} = R_{dc}\xi[(2k^2 - 2k - 1) \coth(\xi) - 2k(k - 1)\operatorname{csch}(\xi)] \quad II. 4-2$$

$$Z_{i_3} = 2\pi R_{dc}\xi[(k^2 r_k + (k - 1)^2 r_{k-1}) \coth(\xi) - 2k(k - 1)\sqrt{r_k r_{k-1}}\operatorname{csch}(\xi)] \quad II. 4-3$$

where r_k is the radius from the centre of the core to the center of the turns of the k^{th} layer and $\xi = \gamma \cdot d$, d being the width of the rectangular-shaped conductor (Fig. II. 26).

It can be shown as in [8], [10], [12] and [17], that the real part of the impedance modified by the induced currents is preponderant compared with the imaginary part. This is, that the equivalent internal resistance of the wires accounts for the major part of its impedance, the internal inductance having values orders of magnitude lower than the internal resistance. This is why, in several cases, only the resistive part of the impedance is modelled to account for the induced currents effects.

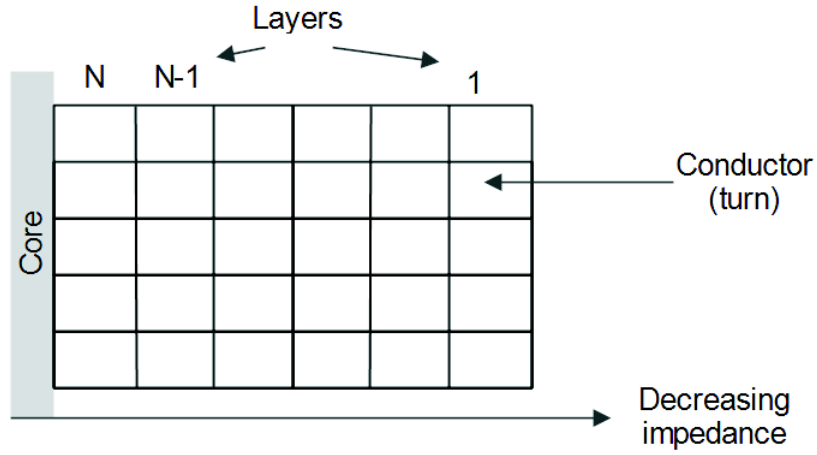


Fig. II. 26 - Squared-cross-section closely packed conductors arrangement

The considered case of the straight Litz wire given by Lammeraner in [8] yields the following expression of the internal resistance of the whole wire:

$$R_{i_3} = R_{dc} + R_{prox} + R_{skin} \quad II. 4-4$$

Where

$$R_{prox} = \frac{l}{2\pi\sigma r_c^2} f\left(\frac{r}{\delta}\right) \quad II. 4-5$$

$$R_{skin} = \frac{l}{N\pi\sigma r_c^2} g\left(\frac{r}{\delta}\right) \quad II. 4-6$$

And for $r_0 < \delta$, r_0 being the outer radius of the Litz wire as shown in Fig. II. 27, and r_c the radius of a single conductor (strand).

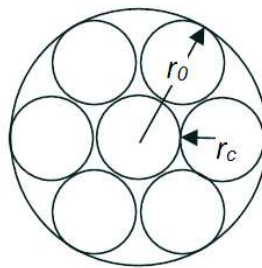


Fig. II. 27 - Circular Litz wire

$$f\left(\frac{r_c}{\delta}\right) = \frac{r_c}{\delta} - \frac{1}{2} \quad II. 4-7$$

$$g\left(\frac{r_c}{\delta}\right) = 1 + \frac{1}{48} \left(\frac{r_c}{\delta}\right)^4 \quad II. 4-8$$

Finally, the approximation in [15] of the impedance taking into account only the skin effect is given by:

$$Z_{skin_M} = \frac{R_{dc}}{2} \sqrt{4 + \frac{j\omega\mu}{\pi R_{dc}}} \quad II. 4-9$$

These expressions are compared and analyzed hereafter in order to select the one that best fits our analysis.

4.2 IMPLEMENTATION FOR CONCENTRATED WINDINGS IN ELECTRICAL MOTORS

4.2.1 Hypotheses

In motor windings of concentrated shape, the assumption of long coils compared to their area is extremely rare because contrary to the transformer topology, the slots are not very long (in the radial direction of the stator) into the stator yoke.

To schematize the dimensional trends of motors against transformers, in Table II. 12 are depicted the dimensional characteristics of coils in these structures:

Table II. 12 - Dimensional orders of coils in electromagnetic structures

Electromagnetic structure	Characteristic length	Dimension	Coil length
Motor	Stator diameter	D	D*0.2 to 0.25
Transformer	Height	H	H*0.7 to 0.9

So for a motor diameter of 50 cm, the coil length would be about 12 cm whereas for the transformer, for a height of 50 cm, the coil length would be about 40 cm.

Consequently, a Litz wire approximation as in [8], might be more accurate as long as the geometry of the winding can be assimilated to a wire with several strands. On the other hand, coils for electrical machines are relatively short in depth (along the machine axle) in general trends, especially for high power-to-weight ratio applications as in aeronautical systems. The straight wire approximation cannot strictly be employed either. Therefore, the curved conductor approximation as in [10] might be a better option since it gives the per-turn impedance depending on the position of the turn and around the core.

The comparison of the methods is done around a specific example. The core material is here irrelevant since the mutual inductances are not considered. Only the internal impedance of the wire is dealt with.

4.2.2 Comparison of skin-effect impedance modules

To begin with, only the skin effect on the impedance module of several methods is tested. For this matter, only one isolated wire is considered. The expressions tested are:

- Z_{i_1} which is based on Maxwell's equations resolution for circular cross-section
- Z_{i_2} adapted for straight rectangular cross section conductors
- Z_{skin_M} simple approximation for circular cross-section conductors

The results of this comparison, allow to determine if the rectangular approximation of the curved conductor can be implemented. If the impedance for a straight rectangular conductor is compatible in terms of skin effect with the reference case of circular conductors, then we assume that the derivation of the same straight impedance into a curved conductor is also valid. This is a strong hypothesis, but since either method is completely adapted to our layouts, it is necessary to integrate it into the analysis.

The difficulty for this part, is that the rectangular cross-section impedance expressions Z_{i_2} cannot be directly implemented without assimilating the perimeters of a circular conductor of radius r_c to a rectangular conductor. For this matter, squared-cross section conductors are assumed to have as the length of their side $d = \frac{\pi r_c}{2}$ to keep their perimeter equivalent to that of the circular conductors.

The numerical calculations for this particular demonstration are based on the dimensions resumed in Table II. 13.

Table II. 13 - Winding characteristics for illustration

Dimension	Value
Core radius	8 mm
Copper wire diameter	0.35 mm
Turn diameter	39.5 mm
Number of turns per layer	12
Number of layers	4
Conductivity of copper	1.6e-8 Ωm
Relative permeability of copper	1

The results are presented in Fig. II. 28. The exact impedance according to Maxwell’s equations is Z_{i_1} . Taking this formula as a reference, we can see that the approximation of Z_{skin_M} is overestimating the skin effect impedance. Assuming that the approximation of the square conductor to round conductors is acceptable, the straight conductor impedance expression proposed in [10] is still larger than the reference, but closer than the above approximation.

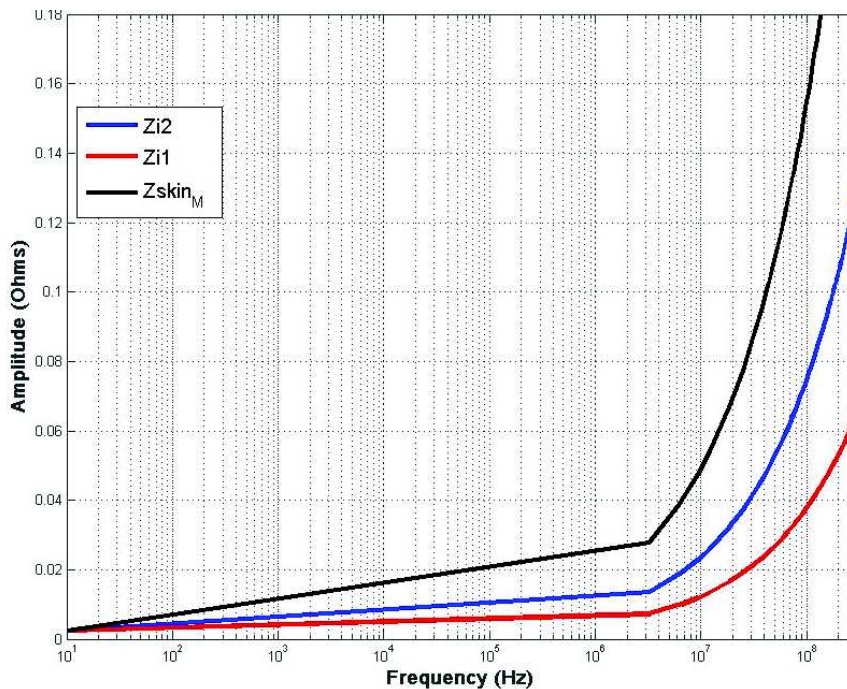


Fig. II. 28 - Comparison of three different internal impedance approximations

Since the curved conductor impedance for rectangular conductors is a direct derivation of the straight case, taking different boundary conditions and using asymptotic expansions for large Bessel arguments, we consequently assume in this analysis, that the squared-section conductor impedance expression gives as close results as the straight squared case. This is, that, since the squared section straight conductor approximation is close to the reference case, then, the derivation of that model for a curved conductor is also close to the reference case. These strong hypotheses might have a large impact on small section cores.

4.2.3 Analytical formulations

In [10], the expression of internal impedance takes into account the arrangement of the conductors as shown in Fig. II. 26 but with a curved conductor around the core.

The formulation is derived from [18] in an axisymmetric approach and yields:

$$Z_i = 2\pi R_{dc} \xi \left[(k^2 r_k + (k-1)^2 r_{k-1}) \coth(\xi) - 2k(k-1) \sqrt{r_k r_{k-1}} \operatorname{csch}(\xi) \right] \quad \text{II. 4-10}$$

where,

$$r_k = R_c + \frac{d}{2} + (N-k)d \quad \text{II. 4-11}$$

$$r_{k-1} = R_c + \frac{d}{2} + (N-k+1)d \quad \text{II. 4-12}$$

r_k is the radius of the k^{th} turn around the core.

In our case as shown in the latter sections, the numbering of the layers is inverted (Fig. II. 26) because of practical arrangements and coherence with the rest of the study, and a simple variable modification of $k = N - t + 1$ yields:

$$Z_i = 2\pi R_{dc} \xi \left[((N-t+1)^2 r_t + (N-t)^2 r_{t-1}) \coth(\xi) - 2(N-t+1)(N-t) \sqrt{r_t r_{t-1}} \operatorname{csch}(\xi) \right] \quad \text{II. 4-13}$$

$$r_t = R_c + \frac{d}{2} + (t-1)d \quad \text{II. 4-14}$$

$$r_{t+1} = R_c + \frac{d}{2} + t.d \quad \text{II. 4-15}$$

As stated before, this expression is only valid for rectangular or squared cross-section. But, in the case under consideration, the windings are composed of circular cross-section wires. This formulation of the internal impedance is thus invalid for our case. In fact, this formula is valid for rectangular conductors because of the boundary conditions in the resolution of the field produced by neighboring conductors carrying a current density.

However, the closely and regularly packed wires in concentrated windings reduces the error of this formulation applied to round wires coils. Therefore, we assume the hypothesis that this formulation is valid for the analysis in question. In order to assimilate the round conductors to square conductors, the distance d is calculated noting that, since each layer of round wires is interlaced with the adjacent

layers because of the shift of length r between them, the layers are considered to have a virtual separation distance of $d = r_c \cdot \sin\left(\frac{2\pi}{3}\right)$.

The potential impact this strong hypothesis can have on the resulting impedance is an overestimation of the module compared to a circular cross-section case, the proximity effect being more acute in the squared cross-section case.

Since this impedance formulation is synthetized considering infinitely long coils in the coil axis direction (which is not the case in our study), all the conductors belonging to the same layer have exactly the same impedance. The proximity effect only modifies the impedance from one layer to the other.

This will have the effect of increasing the overall impedance of the inner layers since normally, the external turns (close to the extremities of the core) wouldn't be affected by neighboring conductors. In this case, these external conductors of the inner layers would be considered as being surrounded by other wires carrying current.

4.3 IMPLEMENTATION FOR A SPECIFIC CASE OF CONCENTRATED WINDINGS

The per-turn and per-layer impedance predicted by the analytical expression in (II.4-13) is plotted in Fig. II. 29 for a winding of 4 layers for the dimensions resumed in Table II. 14 - Winding dimensions for example implementation.

Table II. 14 - Winding dimensions for example implementation

Dimension	Symbol	Value
Core radius	Rc	8 mm
Copper wire diameter	rc	0.35 mm
Separation distance of layers	d	0.303 mm
Number of layers	N	4

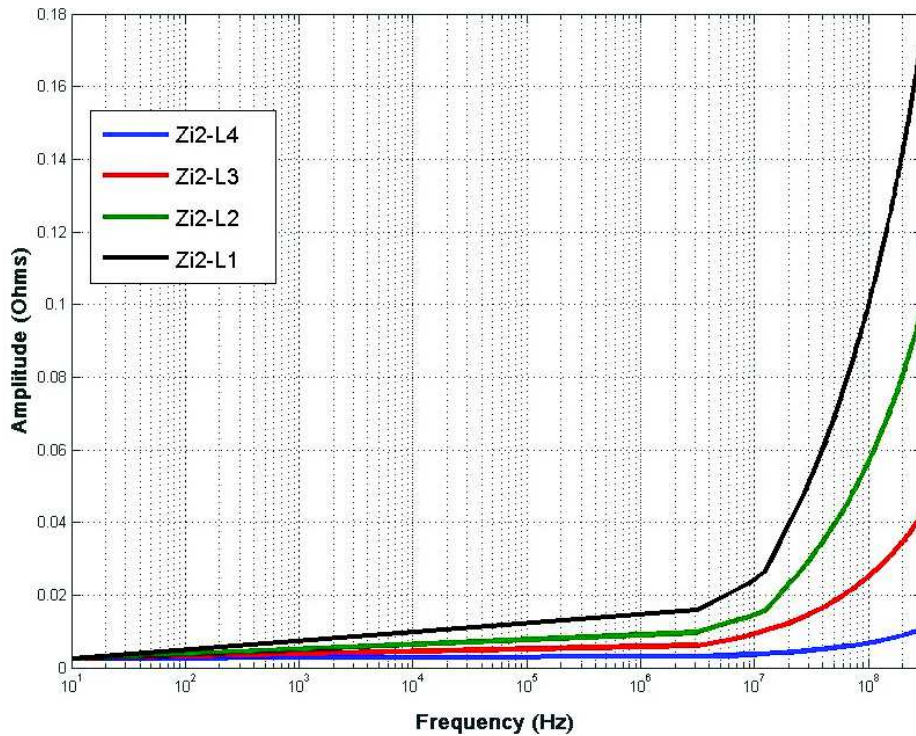


Fig. II. 29 - Internal impedance of curved conductors for 4 different layers

It can clearly be noted the evolution of the impedance with the position of the layer on the coil. For the external layers (layer 4), the impedance increases slower than for the inner layers (layer 1).

5 CALCULATION OF PARTIAL INDUCTANCES IN WOUND STRUCTURES

An essential part of high frequency modelling for motor/generators' windings is the inductive behavior representation. As for the capacitive and resistive models, an elementary approach is sought. In order to accurately model the inductive behavior of the wound structure, several considerations have to be taken into account.

5.1 RELATIVE PERMEABILITY DISPERSION

The first important aspect of the inductance modelling is the ferromagnetic nature of the structure. Ferromagnetic materials' properties have a strong dependence on various parameters such as temperature, frequency, magnetic induction or structural parameters as lamination or grain volume in the case of composites. The presence of a ferromagnetic core inside the winding modifies the inductive behavior and introduces losses and nonlinear behaviors.

First of all, the two-phase frequency behavior of relative permeability is particularly difficult to deal with. In fact, contrary to the dielectric permittivity, the magnetic permeability rapidly loses its physical sense with the increasing frequency. A magnetized body can be represented, in the continuous media approximation, by its magnetizing moments \vec{M} created by the volume density of magnetic dipolar moments. In an analog manner to the dielectric media, for a magnetized body (analog to a polarized dielectric body), a magnetizing moment \vec{M} induced by bound currents or magnetizing currents \vec{J}_m creates a magnetic polarization field $\vec{J} = \mu_0 \vec{M}$ [1]:

$$\vec{J}_m = \vec{\nabla} \times \vec{M} = \frac{1}{\mu_0} \vec{\nabla} \times \vec{J} \quad \text{II. 5-1}$$

μ_0 is defined as the free space magnetic permeability, and is calculated from its relationship with the free space permittivity ϵ_0 and the free space speed of light $c = 2.9975 \times 10^8$ m/s:

$$\mu_0 = \frac{1}{\epsilon_0 c^2} = 4\pi \times 10^{-7} \text{ H/m} \quad \text{II. 5-2}$$

By differentiating its components, a magnetic field density \vec{B} within a magnetized body is decomposed as:

$$\vec{B} = \mu_0 \vec{H} + \vec{J} \quad \text{II. 5-3}$$

\vec{H} is the magnetic field, created by external sources thus from free currents (comparably to free charges in dielectrics) and \vec{J} by the bound or magnetizing currents inextricably linked to the body.

As for dielectrics, a relationship between the magnetization \vec{M} and external magnetic field \vec{H} appears as:

$$\vec{M} = \chi_v \vec{H} \quad \text{II. 5-4}$$

And therefore,

$$\vec{B} = \mu_0(\vec{H} + \vec{M}) = \mu_0(1 + \chi_v)\vec{H} = \mu\vec{H} \quad II. 5-5$$

Again, as studied for the dielectric permittivity, in a harmonic analysis approach the absolute magnetic permeability μ is frequency dependent:

$$\vec{B} = \mu(\omega)\vec{H} \quad II. 5-6$$

Finally, the absolute relative permeability of the media can be defined as:

$$\mu_r^* = \frac{\mu(\omega)}{\mu_0} \quad II. 5-7$$

And therefore:

$$\mu_r^* = \mu_r' - j\mu_r'' \quad II. 5-8$$

For common ferromagnetic materials, the relative permeability decreases rapidly to 1 due to the dynamics of the Bloch walls and inertial phenomena at a mesoscopic scale (i.e. magnetic moments) [19]. In other words, frequency dependence of magnetic permeability occurs when magnetic moments can no longer realign parallel to the external field before it switches direction [20]. This permeability dispersion occurs at a relaxation frequency. Fig. II. 30 shows the relaxation process with frequency in ferromagnetic materials. The dispersion process occurs very quickly, over a small range centered at the relaxation frequency. Thus, a very important hypothesis stated here is that the variation range can be neglected compared to the whole extent of the frequency range modelling. Two behavior zones then appear to be relevant: the low frequency before relaxation, and the high frequency zone, where the relative permeability is considered to be 1.

As for the relaxation phenomena in dielectrics, a Debye relaxation model can be applied to magnetic dispersion:

$$\mu^* = \mu_\infty + \frac{\mu_{DC} - \mu_\infty}{1 + j\omega\tau} \quad II. 5-9$$

And,

$$\mu_r' = \mu_\infty + \frac{\mu_{DC} - \mu_\infty}{1 + \omega^2\tau^2} \quad II. 5-10$$

Finally,

$$\mu_r'' = \frac{(\mu_{DC} - \mu_\infty)\omega\tau}{1 + \omega^2\tau^2} \quad II. 5-11$$

Where μ_∞ and μ_{DC} are the relative permeabilities at infinite and zero frequency, and τ the relaxation time constant calculated for each material which depends on thermodynamic characteristics.

In classic iron-based ferromagnetic materials, relaxation appears at frequencies as low as few kilohertz and for iron-based Soft Magnetic Compounds (SMCs) at a higher 10 kHz and up to several hundreds of kilohertz [21]. SMCs are ferromagnetic materials powders sintered to form solid ferromagnetic structures. The results of the measurement of dispersion and other physical properties of SMCs discussed in the latter reference are described for some materials including iron laminations and SMCs of different grain diameters, different compression pressures and temperatures.

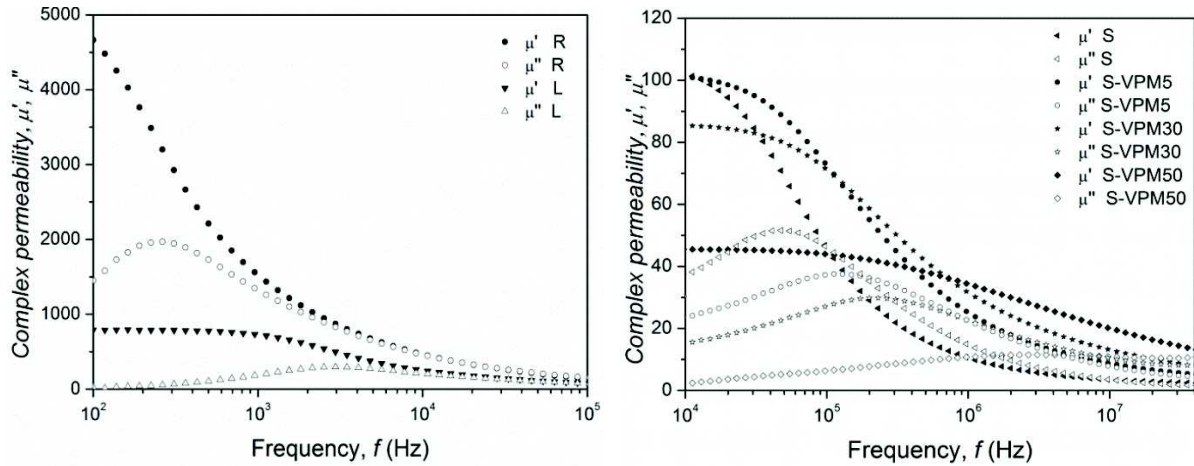


Fig. II. 30 - Complex permeability of different rolled and laminated iron alloy materials [21]

Sample	R	L	S-VPM5	S-VPM30	S-VPM50	S
Total losses [W/kg] (f=20 kHz, B _m =0.1 T)	254	227	140	170	105	205
Specific resistivity [$\mu\Omega \cdot m$]	2.5	2.7	32	105	135	4.5
Relaxation frequency [kHz]	0.2	2.7	150	240	3000	50
Density [kg/m ³]	6709	6730	7080	6770	6100	6570

Fig. II. 31 – Physical characteristics of different ferromagnetic materials: sample R - amorphous ribbon milled for 6 hours, consolidated at 500°C for 5 min, annealed at 540°C for 60 min.; sample L - amorphous ribbon cryo-milled for 6 hours, consolidated at 500°C for 5 min., annealed at 540°C; Iron powders (S) and flakes of Fe73Cu1Nb3Si16B7 (VPM) with the different content (0, 5, 30, 50 wt% of Fe73Cu1Nb3Si16B7) [21]

The interesting fact about these figures, is the wide range of materials’ behaviors. More on the dispersion of permeability can be found in references [22]–[24] and particularly in [25].

The penetration depth of the electromagnetic field into materials plays a fundamental role in the permeability effects on magnetic behavior. Since the penetration depth is fundamentally described by (cf. eq. II.4-1):

$$\delta_m = \sqrt{\frac{2}{\omega\sigma\mu(\omega)}} \tag{II. 5-12}$$

Where δ_m is the penetration depth of the field into the ferromagnetic body, σ_m its conductivity, which is considered to be constant for all frequencies, and $\mu(\omega)$ its absolute permeability.

For a given material then, the penetration depth of the electromagnetic field depends not only on the frequency for a given conductivity, but also on the dispersion of its permeability when integrating

the Debye model into the penetration depth expression. Fig. II. 32 shows the dependence of permeability with frequency and permeability of a SMC material:

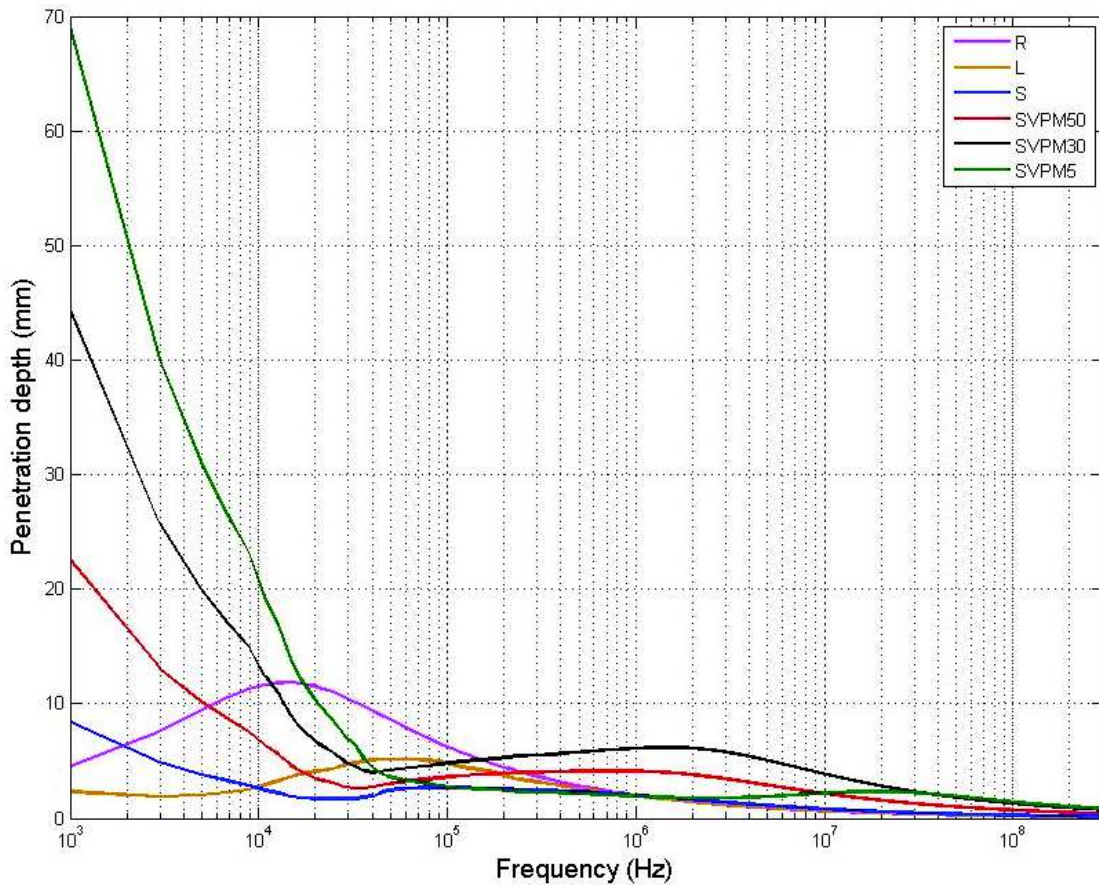


Fig. II. 32 - Dependence of the penetration depth with permeability and frequency (*in mm*)

It can be pointed out that, the penetration depth of ferromagnetic materials vary sensibly over a wide range of frequencies. Furthermore, this is only considering that the resistivity of the material is constant over the full range of frequencies, which is certainly not the case. Besides, it is very difficult to assume a zero-penetration depth of the field even at as high as 100 MHz where the above materials still have a penetration depth of a few mm. An easy method to calculate the inductances cannot be clearly identified. However, the impact of the relaxation frequency and the resistivity can help to delimit zones of validity of certain assumptions and models. It is up to the user of the below formulas to assume the hypotheses that will allow the use of the general case or the special cases formulations.

5.2 INDUCTANCE CALCULATION METHODS

For the high permeability zone, the ferromagnetic nature of the core makes the inductance calculation difficult. In a magnetostatic approach (very low frequency), the work of Durand in [26] is useful for the calculations of interaction energy between two fields in terms of vector potentials (turns) in the presence of a core. The resulting formulation of this approach is frequency independent and based on the resolution of elliptic integrals. Durand also proposes a magnetic induction calculation formulation, but still, frequency independent.

In the zone with dispersed permeability, the inductive behavior of the structure can then be assimilated to a non-ferromagnetic structure. However, the iron losses have to be accounted for. Several authors deal with the non-ferromagnetic inductance modelling. The work presented in [27] is particularly accomplished and deals with the fundamentals of mutual inductances in air-cored inductors. This work includes the Maxwell formulas of inductance and mutual inductance derived from his work in [28]. This latter formulae is useful in achieving fast and accurate calculation of circular-cross section air-cored inductors. In fact, this formula has been proven to yield very accurate results for air-cored inductors.

But, in [29], an outstandingly elegant and thorough analytical formulation of the mutual impedance between two-turns of a wound structure over a magnetic core is developed strictly in accordance with Maxwell's equations. The derivation of a basic mutual impedance formula between two turns of a wound structure is carried out. In this work, this formulation has been chosen because of its simplicity and its accuracy at high frequencies even though the numerical evaluation can suppose very specific techniques. It is based on a quasi-stationary approximation in the frequency domain and the mutual impedance is complex: the imaginary part describes the mutual inductance modified by the presence of a conducting core whereas the real part of the mutual impedance accounts for the dissipation of power in the iron core.

5.3 DERIVATION OF USEFUL FORMULAS

The hypotheses used to the derivation of the formulas are described based on the diagram of the Fig. II. 33.

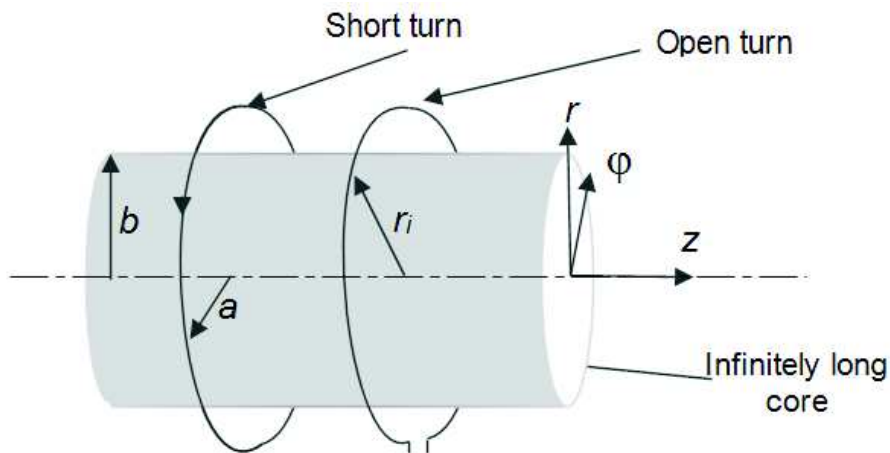


Fig. II. 33 –Turns and core arrangement for mutual impedance calculations

Table II. 15, the physical properties and parameters for modelling are summarized.

Table II. 15 – Physical properties and parameters for mutual inductance modelling

Parameter	Description
z	Relative distance from the energizing turn and the induced turn
φ	Angular coordinate of a cylindrical coordinate system
r_i	Radius of the induced turn
a	Radius of the energizing turn
b	Core radius
μ_1	Permeability of medium 1 (air)
μ_2	Permeability of medium 2 (core, considered isotropic)
σ_2	Conductivity of medium 2

The ferromagnetic core is considered to be infinitely long and of homogeneous conductivity and permeability. A shorted filamentary turn located at $z = 0$ carries a sinusoidal current i_φ , which in the frequency domain at an angular frequency $\omega = 2\pi f$ yields: $i_\varphi(t) \equiv I_\varphi e^{j\omega t}$. A second turn is considered to be open and located at a position z . The resulting electric field intensity is $E_\varphi = E_\varphi(r, z)$. The displacement currents are neglected in the work of Wilcox. However, they are taken into account in this work separately (cf. §II.3.5). And finally, the propagation effects are neglected considering that the dimensions of each turn are shorter than the shortest wavelength of the excitation currents.

The mutual impedance Z between these two elementary turns can then be described as the ratio of the resulting electric field intensity integrated over the open turn and the energizing current I_φ of the short turn as detailed in [29]. Without going through the detailed development², it can be shown that the resulting impedance Z can be written as:

$$Z = -\frac{2\pi r}{I_\varphi} E_\varphi(r, z) = j\omega M_1 + Z_c \quad \text{II. 5-13}$$

The first term of equation (II.5-13) corresponds to the effects of an energizing field completely in air, while the second term corresponds to the effects of the reflected field caused by the induction of the core [29].

5.3.1 General case: mutual impedance of two coaxial circular turns over an iron core

The first mutual term can be expressed as follows:

$$M_1 = \mu_1 r_i a \int_{-\infty}^{+\infty} \overbrace{I_1(\beta r_i) K_1(\beta a)}^{\leftarrow r > a \rightarrow} e^{j\beta z} d\beta \quad \text{II. 5-14}$$

Where $\leftarrow r_i > a \rightarrow$ means the exchange of a and r when $r > a$, I_1 and K_1 are the modified Bessel functions of the first order evaluated at the arguments βx ($x = a, r_i$).

Then,

$$Z = j\omega M_1 + 2r_i a \int_0^{+\infty} \frac{K_1(\beta a) K_1(\beta r_i) I_1(\beta b)}{K_1(\beta b)} \times \left\{ \frac{f(\beta) - \frac{\mu_1}{\mu_2} f(\Gamma)}{g(\beta) + \frac{\mu_1}{\mu_2} f(\Gamma)} \right\} \cos(\beta z) d\beta \quad \text{II. 5-15}$$

where, $\Gamma = c\beta^2 + \gamma^2 = \beta^2 + j\omega\sigma_2\mu_2$, $f(x) = x \frac{I_0(xb)}{I_1(xb)}$ and $g(x) = x \frac{K_0(xb)}{K_1(xb)}$.

Note that Bessel equations are equally useful to define the induced currents in conductors (cf. §II.4). In fact, a very general solution of the induced currents can be extracted from the above results. The work of [13] in chapters 2 to 4 is particularly interesting to consider and compare with.

² The method used is a Fourier integral transformation of the field equations in the two different media by choosing β as the transformation parameter and transforming the electric field quantities with respect to the variable z ($E \rightarrow \hat{E}$), giving:
$$\begin{cases} \frac{\partial^2 \hat{E}_{\varphi 1}}{\partial r^2} + \frac{1}{r} \frac{\partial \hat{E}_{\varphi 1}}{\partial r} - \frac{\hat{E}_{\varphi 1}}{r^2} - \beta \hat{E}_{\varphi 1} = j\omega\mu_1 I_\varphi \delta(r - a) \\ \frac{\partial^2 \hat{E}_{\varphi 2}}{\partial r^2} + \frac{1}{r} \frac{\partial \hat{E}_{\varphi 2}}{\partial r} - \left(\frac{1}{r^2} + \Gamma\right) \hat{E}_{\varphi 2} = 0 \end{cases}$$
 and identifying to the Bessel equations.

As pointed out by the authors, equation (II.5-15) can only be evaluated by numerical computations. In very special cases, this equations can be reduced to more practical forms, and in our case, several hypotheses can be made to adapt to the abovementioned special cases.

Besides, this formulation is also valid for self-impedance calculations since it only takes to evaluate Z when $a = r + \alpha$ and $z = 0$, α being very small to represent the closeness of the turn to itself. Under these conditions, $Z \approx S$ where $S = j\omega L + R$ is the self-impedance.

5.3.2 Special Case 1: Air-cored inductor

In this case the relative permeability is considered to be 1. This makes $Z_c = 0$ and thus, Z is reduced to:

$$Z = j\omega M_1 \quad \text{II. 5-16}$$

The authors in [29] made a comparison between this equation and the Maxwell mutual inductance. It can actually be shown that (2) can be expressed as in [28]:

$$M_1 = \mu_1 \sqrt{r_i a} \frac{2}{k} \left[\left(1 - \frac{k^2}{2} \right) K(k) - E(k) \right] \quad \text{II. 5-17}$$

With

$$k = \sqrt{4 \frac{ar_i}{z^2 + (a + r_i)^2}} \quad \text{II. 5-18}$$

K and E being the complete elliptic integrals.

This result is interesting from the point of view of the numerical evaluation since no generalized integrals are to solve.

Since these are very well known and reliable formulations [27], they are helpful in determining the accuracy of other couplings such as capacitive couplings from an impedance plot measured from a winding over a non-ferromagnetic core. This is discussed in §II.0.

5.3.3 Special case 2: Zero penetration flux into the core

The case where frequency is considered to be high enough to have zero penetration of the flux into the core regardless of the value of the permeability which implies $|\Gamma| \rightarrow 0$. Thus,

$$Z_c = -j\omega M_2 \quad \text{II. 5-19}$$

Where,

$$M_2 = \mu_1 r_i a \int_0^{+\infty} \frac{K_1(\beta a) K_1(\beta r_i) I_1(\beta b)}{K_1(\beta b)} \cos(\beta z) d\beta \quad \text{II. 5-20}$$

Finally, the mutual impedance between the two turns in this configuration is $Z = j\omega(M_1 - M_2)$.

It is important to note that $Z = Im(Z)$ and that such formulation doesn't account for the losses in the core since no penetration is considered. If the assumption that the penetration depth isn't fairly valid, this formulation might not give good agreement for high frequency modelling.

5.4 ANALYSIS OF A SPECIFIC CASE OF CONCENTRATED WINDING

In order to demonstrate the impact of the variation of permeability on impedance and inductance, the mutual and self-inductances as well as the coupling coefficient are analyzed in the framework of the general case (§ II.5.3.1).

For the whole analysis of inductance in this thesis, a 70-point Gauss-Laguerre³ quadrature was successfully used and computation times are as low as few seconds with standard personal computer capabilities. The same case as in §III.4.3 is used to illustrate the dispersion of permeability and the effects on self and mutual inductance. The dimensions of the circular cross-section coil are resumed in Fig. II. 34 and Table II. 16.

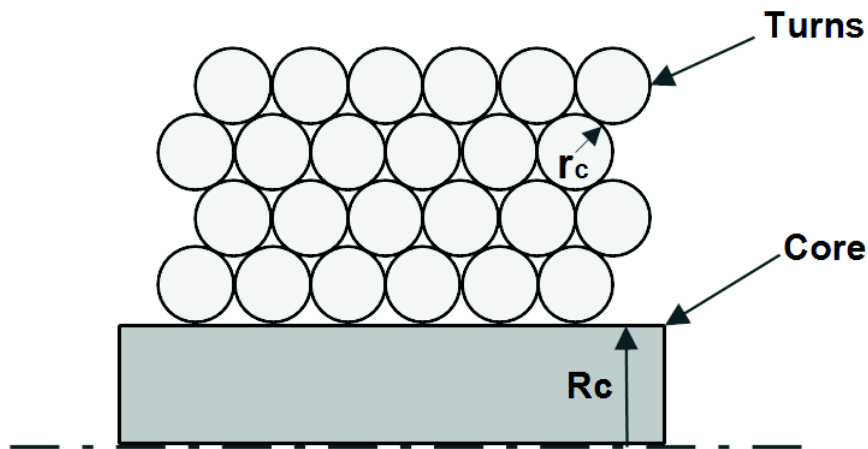


Fig. II. 34 – Layout of a particular winding for a case study

Table II. 16 – Winding characteristics

Dimension	Value
Core radius	8 mm
Copper wire diameter	0.35 mm
Turn diameter	39.5 mm
Number of turns per layer	12
Number of layers	4
Conductivity of copper	1.6e-8 Ωm
Relative permeability of copper	1
Relative permeability of air	1

Then, the characteristics of the core are resumed in Table II. 17.

Table II. 17 –Core physical properties

Property	Value
Relative permeability at 0 Hz	250
Relaxation frequency	3 kHz
Bulk conductivity of the core	3.57 kS

³ Gauss-Laguerre quadrature yields extremely good results even from only 10 point calculations.

The mean value of per-turn self-inductance against frequency is shown in Fig. II. 35. The mean value is obtained by calculating each of the 48 self-inductances of the winding and taking the average value. The purpose is to clearly show the magnetic behavior of the whole structure.

It can be pointed out that, the self-inductance mean value decreases as the magnetic dispersion appears.

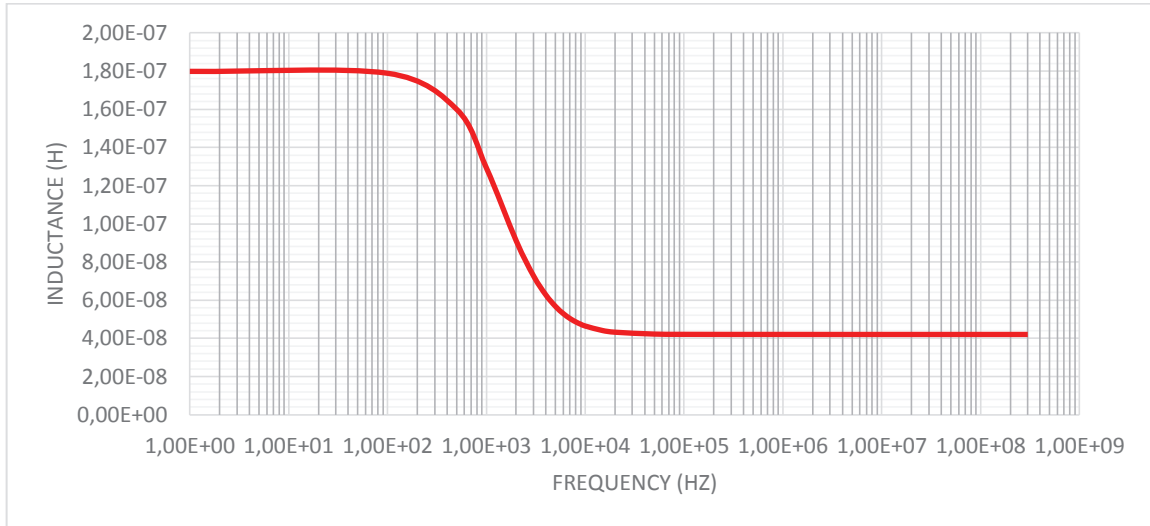


Fig. II. 35 – Mean value of the per-turn self-inductance against frequency

This same behaviour can be illustrated for the mean value of turn-to-turn mutual inductance in Fig. II. 36.

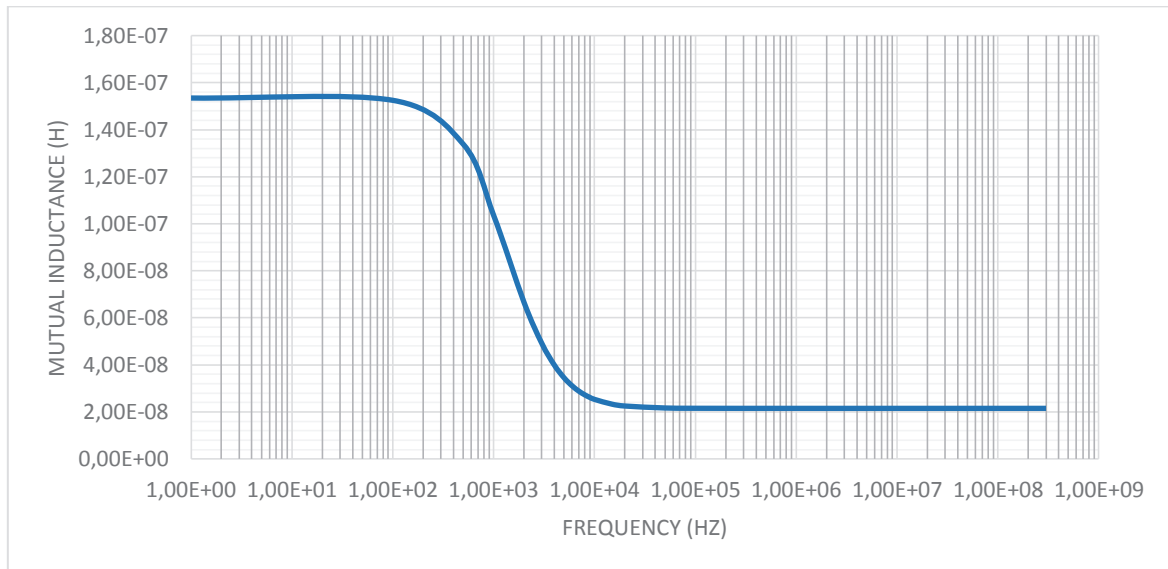


Fig. II. 36 - Mean value of the per-turn mutual inductances against frequency

Finally, the average value of the coupling coefficient between the turns also decreases as can be seen in Fig. II. 37.

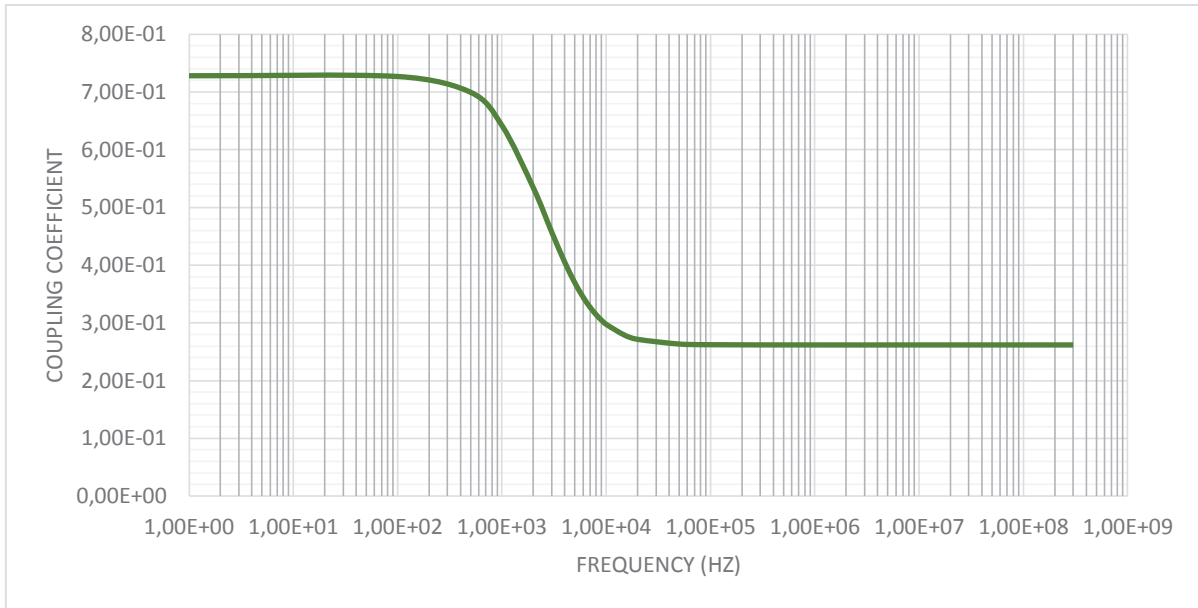


Fig. II. 37 - Mean value of the coupling coefficients against frequency

Consequently, the variation on the self-inductance of the coil, which involves the self-inductance of each turn and the coupling coefficient between each turn against the others, will vary not only because of the decrease in self-inductance, but also on the rate of decrease of the coupling between each turn. A double variation has then to be taken care of to account for the dispersion of the magnetic permeability of the core.

5.5 THE PROBLEM OF CORE LOSSES

Core losses have many inducing mechanisms at a mesoscopic level as detailed in [30], [31] among which eddy-current losses.

Since the term Z_c in eq.(II.5-13) is composed by a real and an imaginary part, it can be seen that $\text{Re}(Z_c)$ corresponds to $\text{Re}(Z)$. These dissipative element takes into account eddy-current losses. Eddy-current losses in the core in the form of resistive (real part) components, depend on the penetration of the electromagnetic field into the core which also depends on its permeability (and even the variations on conductivity which are not taken into account).

The problem of the penetration depth depending not only on frequency but also on permeability, is very complex because the losses depend directly on the penetration depth and frequency. As pointed out in § II.5, even for SMC materials, the penetration depths is as high as several millimeters even at 100 MHz.

However, contrary to the inductive case, core losses might be analyzed in the context of hypotheses:

- Low field intensity levels hypothesis

As stated in chapter I, the wide-band model built in this work concerns only low-level-wide-band excitations. The induced currents in the core are a function of the inducing field which is directly related to the excitation. Consequently, considering low excitation levels, eddy currents are here considered non-existent.

- Technological reality

Laminated materials or SMCs are generally used for drastically reducing the intensity of induced currents. Insulated laminations allow for current paths to be drastically reduced, thus reducing losses. In the case of SMCs, insulated grains of ferromagnetic materials have the same effect as laminations but in every direction and for very low grain sizes. Therefore, along with the above hypotheses, induced currents losses are neglected.

Considering the iron losses, levels are also field-intensity dependent and therefore, core losses are not taken into account in the frame of low-level signal excitation.

6 CIRCUIT REPRESENTATION OF THE ANALYTICAL MODELS

The analytical calculations carried out in the above paragraphs, are necessary for modelling the behavior of common and differential mode impedance in windings. But, in order to construct a more user-friendly full model for representing the above calculated impedances in the frequency and time domain, circuit simulators can be useful. Besides, implementing a circuit model of the windings allows system-level simulations to take into account the HF behavior of the actuator.

The circuit simulator used for the implementation of models is LTSpice IV [32]. It is a Spice based circuit simulator that includes schematic capture and waveform viewer created by Linear® semiconductors. It is a widely used free software for engineering design of complex electrical systems.

The purpose of the circuit implementation of the impedance models is to perform time and frequency domain simulations for analysis of the wound structure and the global mechatronic system as well.

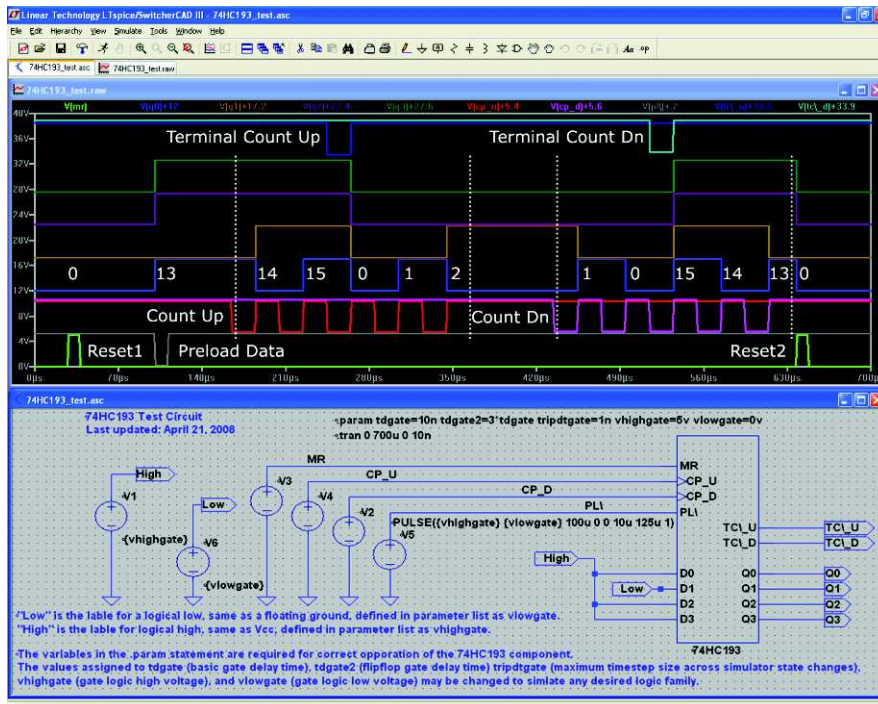


Fig. II. 38 - LTSpice screenshot

Note that all the previous modelling should be able to predict time and frequency domain impedance behaviors.

6.1 CAPACITANCE AND DIELECTRIC LOSSES IMPLEMENTATION

Along with the dielectric losses, the effective impedance brought by the turn-to-turn and core capacitances can be modelled in several ways. Moliton points out in [3] that in order to account for the evolution of permittivity and loss tangent as functions of frequency, that various equivalent circuits can represent the relaxation process. The author analyzes several topologies accounting for the diminishing permittivity and increasing losses, one of which is well adapted for our architecture: the parallel $C/(R+C)$ as shown in Fig. II. 39.

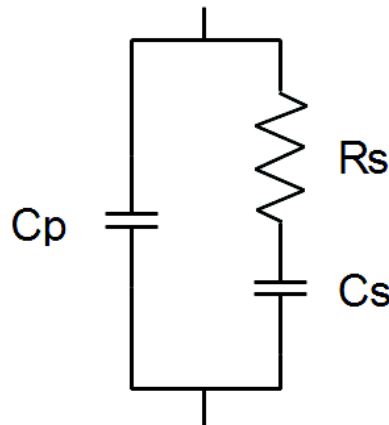


Fig. II. 39 - Common model for lossy dielectric materials

Although ϵ_r' and ϵ_r'' vary according to Debye relaxation model, this parallel topology, fails to handle the dissipation factor correctly.

A more complex model based on the previous topology was synthesized in [33]. It is composed of a parallel combination of a nominal capacitance C_0 N_{cap} branches of series R_k and C_k as shown in Fig. II. 40.

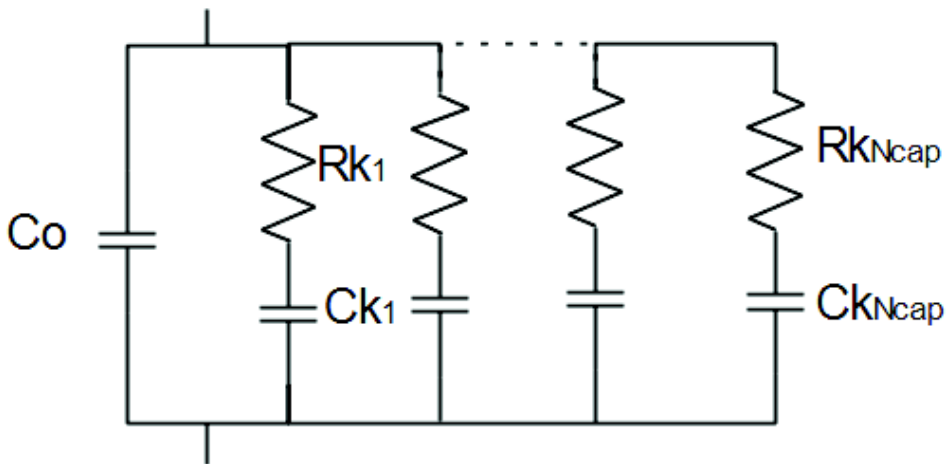


Fig. II. 40 - Several parallel branches model for lossy dielectrics modelling

For every branch, the pulsating frequency is written as $\omega_k = 2\pi f_k = \frac{1}{R_{pk} C_k}$ which yields an equivalent circuit admittance given by:

$$Y(\omega) = j\omega C_0 \left[1 + \sum_{k=1}^{N_{cap}} \frac{C_k/C_0}{1 + \left(\frac{\omega}{\omega_k}\right)^2} - j \times \sum_{k=1}^{N_{cap}} \frac{C_k/C_0}{\frac{\omega}{\omega_k} + \frac{\omega_k}{\omega}} \right] \quad II. 6-1$$

The equivalent parallel capacitance is then given by:

$$C_{eq} = C_0 \left(1 + \sum_{k=1}^{N_{cap}} \frac{C_k/C_0}{1 + \left(\frac{\omega}{\omega_k}\right)^2} \right) \quad II. 6-2$$

Although a more complex formulation of the dissipation factor is synthetized [33], for weak values of the dissipation factor (i.e. 10^{-4} to $1 \cdot 10^{-2}$), an approximation of the dissipation factor expression can be given by:

$$\tan\delta_{eq} \approx \sum_{k=1}^{N_{cap}} \frac{C_k/C_0}{\frac{\omega}{\omega_k} + \frac{\omega_k}{\omega}} \quad II. 6-3$$

Each contributing $\tan\delta_k$ contributes to the resulting mean value of the loss tangent as will be shown hereafter.

Equations (III.6-2) and (III.6-3) are sufficient to determine the dielectric behavior of a given material over the desired frequency range in a circuit simulator.

In order to precisely determine the values of (R_k, C_k) some intermediate calculations have to be performed.

First, for a given frequency range, a logarithmic distribution between $(k+1)^{th}$ and k^{th} frequencies is ensured by taking $\frac{\omega_{k+1}}{\omega_k} = \alpha = constant$. Besides, the series capacitances C_k are considered to be exactly the same (although some further work will be presented afterwards improving the behavior of the resulting model) thus making $C_k = C$.

Under this circumstances, it can be proven that,

$$\tan\delta_{eq_{max}} \approx \frac{C}{C_0} \sum_{k=1}^{N_{cap}} \frac{1}{\alpha^{j-k} + \alpha^{k-j}} \quad II. 6-4$$

$$\tan\delta_{eq_{min}} \approx \frac{C}{C_0} \sum_{k=1}^{N_{cap}} \frac{1}{\alpha^{j-k+1/2} + \alpha^{k-j-1/2}} \quad II. 6-5$$

If S_0 and S_1 are defined as:

$$S_0 = \sum_{-\infty}^{+\infty} \frac{1}{\alpha^k + \alpha^{-k}} \quad \text{II. 6-6}$$

$$S_1 = \sum_{-\infty}^{+\infty} \frac{1}{\alpha^{k-1/2} + \alpha^{1/2-k}} \quad \text{II. 6-7}$$

Then the equivalent loss tangent can be expressed as:

$$\tan\delta \approx \frac{C}{C_0} \times \frac{S_0 + S_1}{2} \quad \text{II. 6-8}$$

The error of the modelled loss tangent value $\tan\delta_{eq}$, compared to the real value $\tan\delta_D$ is given by

$$E \approx \frac{S_0 - S_1}{S_0 + S_1} \quad \text{II. 6-9}$$

Now, to determine the values of (R_k, C_k) for a maximum error E describing the value of $\tan\delta$ and the capacitance C_0 over a given frequency span, the quantities $\frac{C}{\tan\delta_{eq}C_0} = \frac{2}{S_0+S_1}$ and $E \approx \frac{S_0-S_1}{S_0+S_1}$ can be evaluated as a function of the logarithmic distribution α . In [34] are resumed some interesting values, allowing to evaluate the impact of the chosen parameter α in the error estimating $\tan\delta_D$ and the number of parallel branches needed to model the evolution of $\tan\delta_D$ over a chosen frequency range.

Table II. 18 - Resulting error for a given Ncap number of cells and maximum modelling frequency

α	$\frac{C}{\tan\delta C_0}$	E	Frequency span larger than 300 MHz	N_{cap}
5	1.024	1.5 %	1 to 1.22x10 ⁹ Hz	13
10	1.465	5.5 %	1 to 10 ⁹ Hz	9
20	1.906	15 %	1 to 10 ¹⁰ Hz	5

Thus, for a logarithmic distribution with $\alpha = 10$ (one decade per subsequent pulsating frequency), the error in approaching the real value of the loss tangent and the equivalent parallel capacitance values by the RC network is $E = 5.5 \%$.

Furthermore, the value of C is given by

$$C = 1.465 \times \tan\delta C_0 \quad \text{II. 6-10}$$

Finally, the series resistors are calculated from each of the N_{cap} pulsating frequencies:

$$R_k = \frac{1}{\omega_k C} \quad \text{II. 6-11}$$

It is important to acknowledge that, the more accuracy is sought, the more complex and harder to handle the whole circuit becomes. A relative small number of parallel branches should be considered.

The final conclusion about this circuit implementation is that, by taking a constant $C_k = C$, the equivalent permittivity is also kept constant over the whole frequency range. If the permittivity of the materials used were to see their permittivity to vary (especially at the higher end of the spectrum), this

hypothesis would have to be revised. But it wouldn't be complex since there is a linear relationship between the equivalent parallel capacitance and the permittivity. So for the higher frequencies this is not dealt with here.

For verification purposes, an arbitrary $N_{cap} = 13$ branches circuit network has been implemented with a value of $C_0 = 10 \text{ pF}$ and $\tan\delta = 0.008$.

Therefore, $C_k = C = 8.192 \times 10^{-14} \text{ F}$ and the calculated per-branch resistances are resumed in Table II. 19:

Table II. 19 - Resistance values calculated for a network of 13 branches

Series resistance per branch	Value (Ω)
<i>Rk1</i>	1,69E+11
<i>Rk2</i>	3,38E+10
<i>Rk3</i>	6,75E+09
<i>Rk4</i>	1,35E+09
<i>Rk5</i>	2,70E+08
<i>Rk6</i>	5,40E+07
<i>Rk7</i>	1,08E+07
<i>Rk8</i>	2,16E+06
<i>Rk9</i>	4,32E+05
<i>Rk10</i>	8,64E+04
<i>Rk11</i>	1,73E+04
<i>Rk12</i>	3,46E+03
<i>Rk13</i>	6,91E+02

The resulting response of the impedance seen at the leads of the hypothetical lossy capacitances implemented into the Spice simulator is presented here after (Fig. II. 41 and Fig. II. 42).

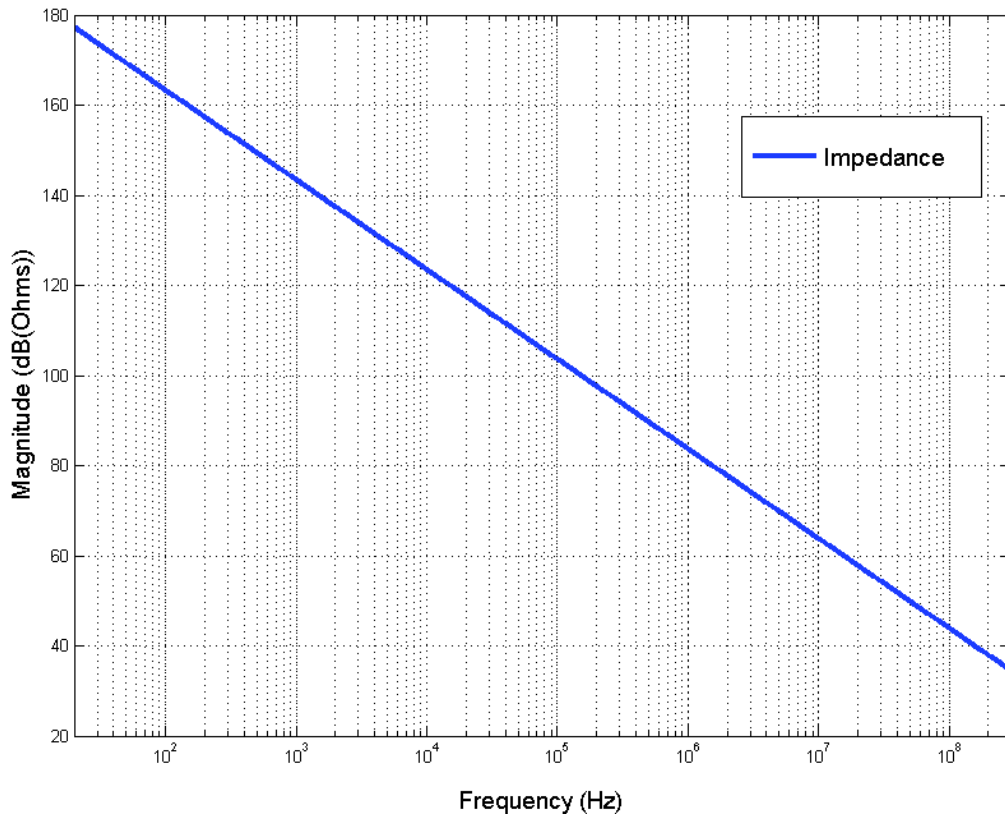


Fig. II. 41 – Impedance module of the dielectric network

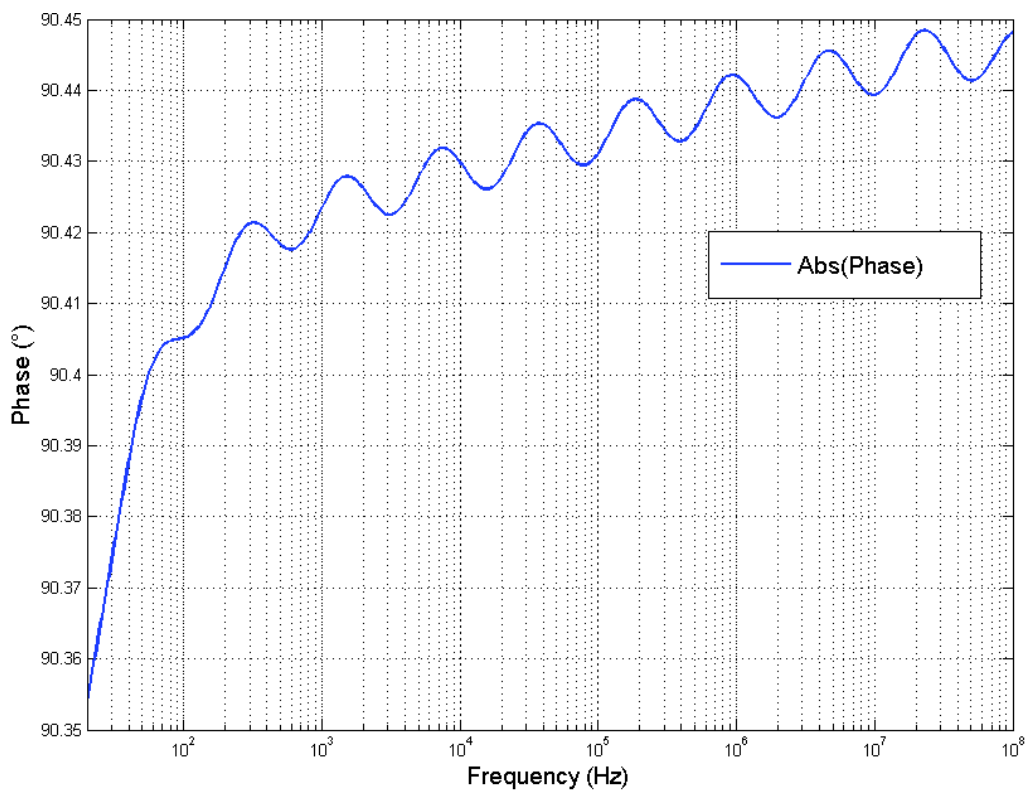


Fig. II. 42 – Absolute value of the phase of the impedance of the dielectric network

A 20 dB/dec decrease rate of the simulated impedance can be observed over the complete range of frequency. Besides, the phase plot shows a value slightly over 90°. The increase in phase is actually created by the losses integrated into the model as can be seen in Fig. II. 43.

To recall the definition of the loss tangent, let's observe that the permittivity can be analyzed in terms of real and imaginary part:

$$\tan\delta = \frac{\epsilon_r''}{\epsilon_r'} \tag{II. 6-12}$$

It can be shown, using the formulations (III.3-12) and (III.3-14) in section §II.3 of this chapter, that indeed, \underline{J}_T being the total complex current density through the capacitor:

$$\tan\delta = \frac{\epsilon_r''}{\epsilon_r'} = \frac{Re(\underline{J}_T)}{Im(\underline{J}_T)} = \frac{|I_R|}{|I_C|} \tag{II. 6-13}$$

If I_R and I_C are the resistive and capacitive currents delivered by the harmonic source, the resulting simulated dielectric loss factor is plotted in Fig. II. 44. The resulting modelled loss factor is slightly overestimated. Instead of 0.008, the mean value is about 0.0076. Besides, the value seems to increase with frequency, which shouldn't happen since it is considered that the loss tangent is constant up to 300 MHz but, the overall behavior can be considered to be acceptable if the large bandwidth is considered.

Although solutions for this have been analyzed, the resulting conclusions are not presented here. It can only be pointed out, that fitting the series resistances in the network is helpful and it actually can be a very useful tool for adjusting the variation of the loss tangent in real materials with frequency.

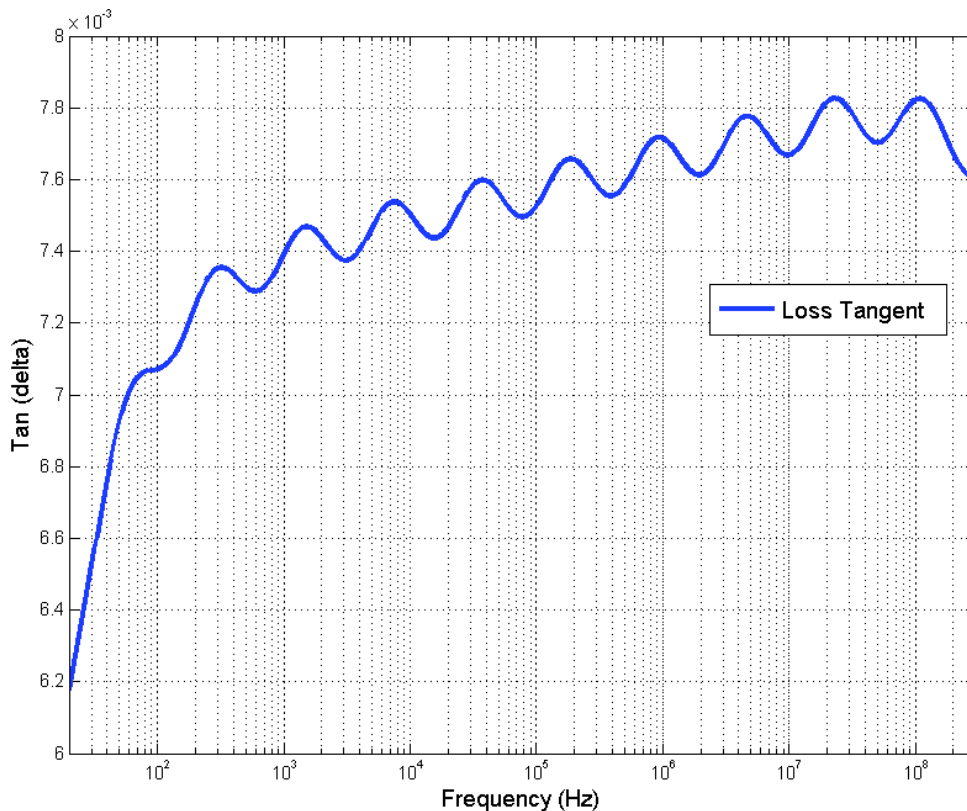


Fig. II. 43 - Dielectric loss factor of the modelled dielectric

Apart from the dielectric loss factor being slightly underestimated, the network synthesized seems to be accurate in the reproduction of the modelled dielectric behavior.

6.2 COPPER SKIN AND PROXIMITY EFFECT

6.2.1 Foster series Network Synthesis

Because of the inherent frequency dependence of impedance including eddy current effects, the circuit implementation of valid time- and frequency- domains of the above calculated values is not straight forward.

As for the loss models for electrostatic behavior, frequency dependent parameters have to be modelled by network synthesis for circuit implementation. The time-domain requirement, makes it extremely hard to use equation-implemented model used in frequency-domain simulations.

In this section, a Series Foster Network circuit is synthesized in order to implement time-domain and frequency-domain models of eddy current internal impedances of the winding turns for circuit simulation.

The *immittance* (impedance (R-L) or admittance (R-C)) representing a Series Foster Network is given by [34]:

$$F(j\omega) = jK_{\infty}\omega + K_0 + j\frac{K_i\omega}{j\omega + \sigma_i} + \dots \quad \text{II. 6-14}$$

Figure III.36 depicts a series Foster circuit that can be fitted to reproduce the frequency dependence of the impedance (increase of impedance with frequency) calculated with (II.4-15).

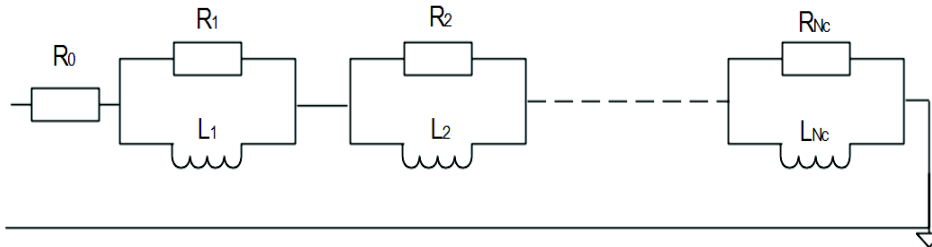


Fig. II. 44 - Foster series network

The equivalent impedance of that network is given by:

$$Z_f = R_0 + \sum_{i=1}^{N_c} \frac{jL_i R_i \omega}{R_i + jL_i \omega} \quad \text{II. 6-15}$$

The objective is thus to identify Z_f to the exactly calculated internal impedance Z_i .

In order for Z_f to reproduce exactly the behavior of Z_i , the condition $N \rightarrow \infty$ would have to be satisfied. This is not practical from a circuit simulation point of view. It is considered here that $N_c \in N^{\times}$.

In [10], the authors use a fixed point iteration to identify every R_i and L_i of the series. The equation (III.6-14) is evaluated at N_c frequencies to obtain the parameters of the circuit. Using the specified frequency ω_k , then

$$\frac{1}{R_k} - \frac{1}{jL_k\omega} = \frac{1}{Z_i(\omega_k) - R_{dc} + \sum_{\substack{i=1 \\ i \neq k}}^N \frac{jL_i R_i \omega_k}{R_i + jL_i \omega_k}} \quad \text{II. 6-16}$$

Since $N_c \in N^*$, errors between Z_f and Z_i exist except at the calculated ω_k , where $Z_f = Z_i$.

However, this process can be time consuming because it involves numerical loops in order to fit the values correctly (fixed point iteration). Instead, it can easily be noticed that (III.4-15) can be decomposed into partial fractions since the infinite series expansion of coth and csch yield:

$$\coth(x) = \frac{1}{x} + 2 \sum_{l=1}^{\infty} \frac{x}{\pi^2 l^2 + x^2} \quad \text{II. 6-17}$$

And

$$\operatorname{csch}(x) = \frac{1}{x} + 2 \sum_{l=1}^{\infty} \frac{(-1)^l x}{\pi^2 l^2 + x^2} \quad \text{II. 6-18}$$

Therefore, an equivalent expression of Z_i is:

$$Z_i = 2\pi R_{dc} \xi \left[v_1 \left(\frac{1}{\xi} + 2 \sum_{l=1}^{\infty} \frac{\xi}{\pi^2 l^2 + \xi^2} \right) - v_2 \left(\frac{1}{\xi} + 2 \sum_{l=1}^{\infty} \frac{(-1)^l \xi}{\pi^2 l^2 + \xi^2} \right) \right] \quad \text{II. 6-19}$$

Where

$$v_1 = (N - t + 1)^2 r_t + (N - t)^2 r_{t-1} \quad \text{II. 6-20}$$

And

$$v_2 = 2(N - t + 1)(N - t) \sqrt{r_t r_{t-1}} \quad \text{II. 6-21}$$

Then, by identifying (II.6-18) to (II.4-15) Z_i can be rewritten as follows:

$$Z_i = 2\pi R_{dc} (v_1 - v_2) + \sum_{l=1}^{\infty} \frac{16R_{dc}^2 v_2^2 \frac{\xi^2}{l^2}}{4\pi v R_{dc} + \frac{4\xi^2 v R_{dc}}{\pi l^2}} \quad \text{II. 6-22}$$

$$v = (v_1 - (-1)^l v_2) \quad \text{II. 6-23}$$

Since $\xi^2 = j\omega\sigma\mu d^2$ then,

$$Z_i = 2\pi R_{dc} (v_1 - v_2) + \sum_{l=1}^{\infty} \frac{16R_{dc}^2 v_2^2 \frac{j\omega\sigma\mu d^2}{l^2}}{4\pi v R_{dc} + \frac{4j\omega\sigma\mu d^2 v R_{dc}}{\pi l^2}} \quad \text{II. 6-24}$$

And consequently, (II.6-23) has exactly the same form as (II.4-15), provided that $N_c \rightarrow \infty$. Therefore, the N_c couples (R_l, L_l) are directly given by:

$$\begin{cases} R_l = 4\pi\nu R_{dc} \\ L_l = \frac{4\sigma\mu d^2\nu R_{dc}}{\pi l^2} \end{cases}$$

And the Foster network as:

$$Z_i = 2\pi R_{dc}(v_1 - v_2) + \sum_{l=1}^{\infty} \frac{jL_l R_l \omega}{R_l + jL_l \omega} \quad \text{II. 6-25}$$

The term $2\pi(v_1 - v_2)$ accounts for the increasing length of the turn as its radius increases.

6.2.2 Number of network cells for simulation

Now, the important aspect of this identification process is that for a circuit simulation to be manageable, the number of cells N_c has to be limited to a reasonable size.

This means that, the frequency span where the two expressions are equivalent for a finite number of cells has an impact on N_c . The larger the frequency range, the larger the number of cells. Besides, the number of cells increases exponentially with frequency.

To illustrate the importance of this stage, the example treated in §II.5.4 is used. In Fig. II. 45, the impedance module of the Foster network for different N_c is presented for $N_c = 25$, $N_c = 15$, $N_c = 10$, $N_c = 5$ and the module of the actual impedance up to 300 MHz.

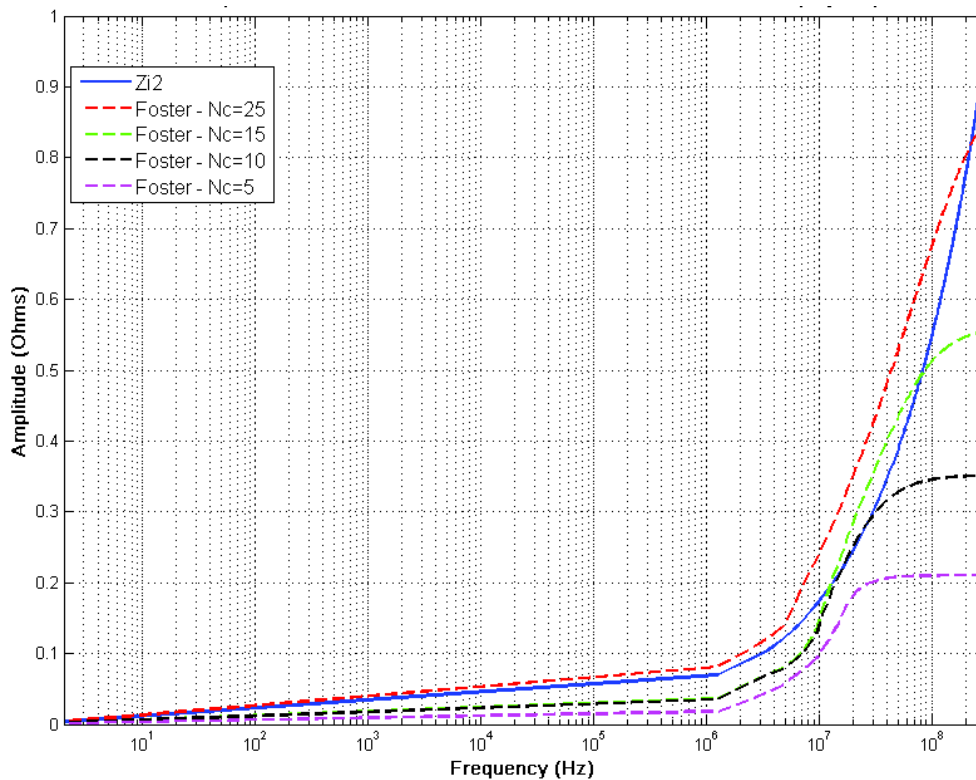


Fig. II. 45 - Foster series model for internal impedance compared to original impedance expression

Then in Fig. II. 46 are plotted the actual module of the internal impedance and the corresponding Foster module for $N_c = 25$ for different layers.

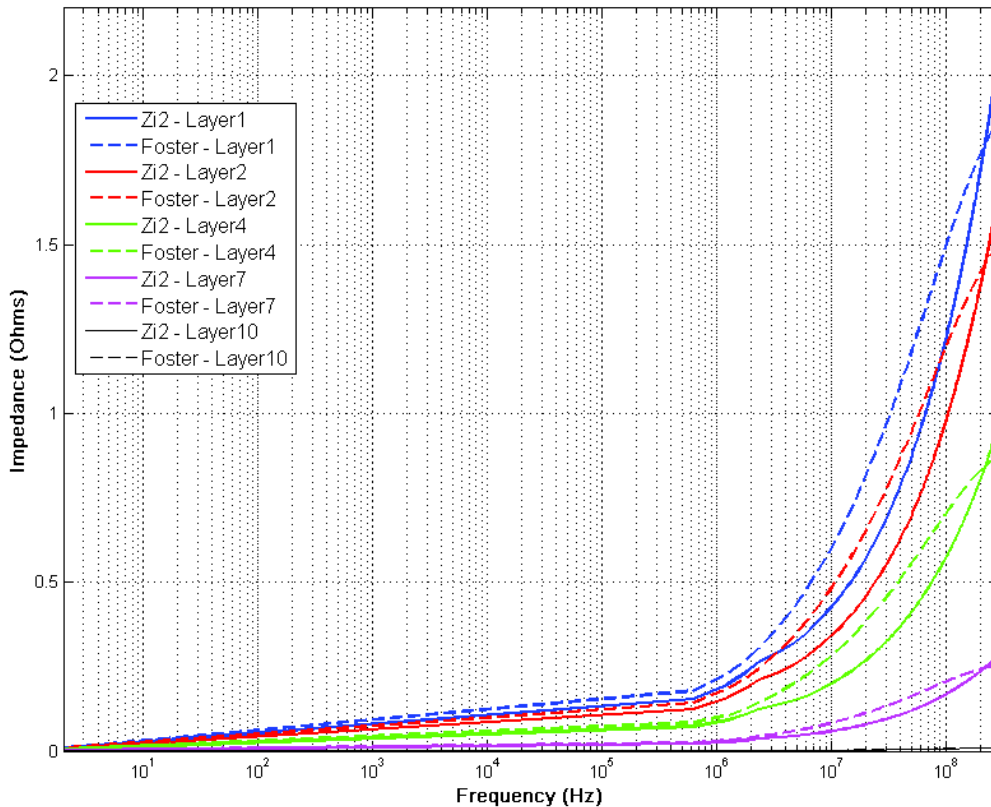


Fig. II. 46 - Foster model for different layers and $N_c = 25$

It can be seen from Fig. II. 46 that an elevated number of cells is needed to get good convergence between the actual and the Foster network impedance over the full frequency range.

Since wide band of the model is sought, a large number of cells would be needed. But, a limited number of cells is available since circuit simulation times, especially in time-domain, increases with large number of passive circuits.

The higher the frequency span, the higher the number of cells needed to have acceptable accuracy. In Table II. 20 are resumed some results on the necessary number of cells for the Foster network to yield acceptable results.

Table II. 20 - Resulting error at certain frequencies for different number of cells N_c

Relative error	$N_c = 25$	$N_c = 20$	$N_c = 15$
50 MHz	7.05 %	7.02 %	7.99 %
100 MHz	8.73 %	11 %	11.98 %
300 MHz	18.7 %	28 %	39.01 %

No rational analysis of the optimum N_c was made. Only a qualitative iterative analysis was carried out and the agreed number of cells is $N_c = 15$ since the largest error obtained at 300 MHz is 39 % whereas for $N_c = 20$, error is 28 %. To achieve a 20 % relative error, 25 cells would have been needed which is too expensive from a circuit simulation point of view.

6.3 INDUCTANCES AND CORE MODEL

This section is perhaps the most difficult to implement in the form of a circuit, since permeability dispersion plays a fundamental role in impedance behavior. This dispersion in combination with skin effect, is particularly hard to synthesize in a circuit network.

Each mutual inductance can then be represented by two self-inductances and a mutual coupling coefficient between them. For an inductor of N turns, $N(N - 1)/2$ coupling coefficients have to be calculated.

As stated before, from equation (II.5-13), a real and imaginary part can be extracted. The imaginary part $\text{Im}(Z)$ corresponds to the inductive coupling between turns and self-inductances from each turn.

Thus, the matrix M extracted from the imaginary part of Z can be transformed to a coupling coefficient matrix by calculating the self-impedances L and calculating the coupling matrix K by calculating each coupling coefficient of the t^{th} turn of the l^{th} layer and the u^{th} turn of the m^{th} layer as:

$$\kappa_{lt}^{mu} = \frac{(M_{lt}^{mu})^2}{L_{lt}L_{mu}} \quad \text{II. 6-26}$$

The matrix K (kappa), can then be directly imported into the circuit simulator along with the self-inductances of each turn.

But, although this process is straight-forward, each per-turn self-inductance, as seen in §II.5, varies with the penetration depth and the magnetic dispersion. The same goes for the coupling coefficient. In order to be able to simulate the behaviour of the motor windings over a wide frequency range, it would be necessary to take into account the inductive variations with frequency in the impedance analysis. In other words, impedance from inductive contribution can be written as follows:

$$Z_{ind} = j\omega.M(\omega)$$

With the natural variation of Z_{ind} with frequency and $M(\omega)$ representing the frequency-dependent behaviour of the inductance of the coil.

It would then be necessary to synthesize a network in an analogue manner as for the eddy-current induced impedance of the copper turns. A network representative of this behaviour would have the following characteristics:

- Decreasing impedance with frequency
- Constant impedance phase at $+90^\circ$ throughout the frequency range

This performance is not easily achievable, since decreasing impedances involves capacitive behaviors and positive phases involves inductive behaviors. The network would have to manage a very complex R-L-C structure to keep impedance within a certain range, while keeping the phase positive.

However, it is a very-time-consuming process to synthesize such a circuit and within the frame of this work, it couldn't be achieved. The frequency dependence of the permeability couldn't be taken into account in the circuit implementation. An extensive work would have to be overtaken to address this issue in future work.

A direct and major consequence of this problem, is that the circuit implemented has a constant value of inductance and coupling coefficient. Finally, the circuit is only valid for a small band around the frequency at which inductance values were calculated.

Therefore, the wideband behavior is not really taken into account in the circuit implementation since several simulations with different inductance and coupling coefficients have to be performed to simulate the whole frequency behavior.

A major improvement to this circuit model, would be the synthesis of a R-L-C network accounting for the magnetic dispersion and penetration depth into the core, to automatically simulate the frequency dependence of the core properties, as was made for the skin effect in conductors.

Nevertheless, it will be seen in the experimental results paragraph, that as much as 4 circuit simulations are enough to correctly predict the full frequency span of the impedance with ferromagnetic cores.

6.4 GLOBAL CIRCUIT MODEL OF A COMPLETE WINDING

6.4.1 One-turn circuit model

To start building the full concentrated winding model, a per-turn model is presented. A single turn (turn 1) in Fig. II. 47 is connected in series with a second turn (turn 2). In this model, the core is not represented.

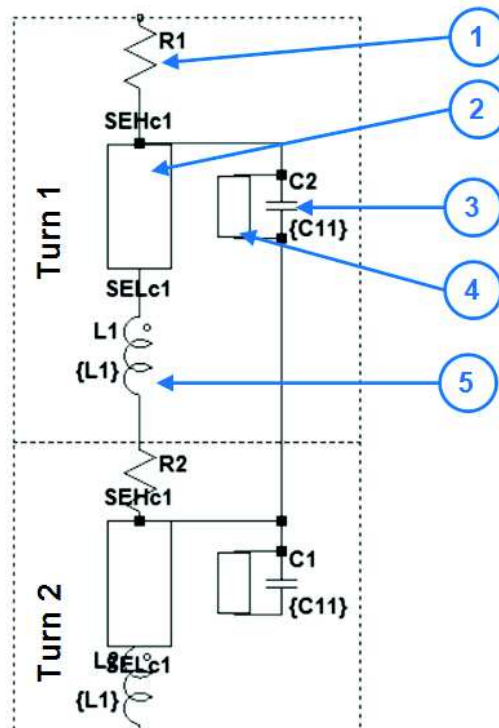


Fig. II. 47 - Single-turn circuit model

In Table II. 21 are described the elements composing the turn structure.

Table II. 21 - Elements composing the turn structure

Element	Description	Paragraph references
1	DC resistance of the turn	§II.4.4 and 6.2
2	Skin effect network (copper)	§II.4.4 and 6.2
3	Turn-to-turn capacitance C_o	§II.3.5 and 6.1
4	Dielectric losses network	§II.6.1
5	Self-inductance at single frequency	§II.5.3 and 6.3

The details of each element are here resumed:

1. DC resistance (straightforward)
2. Skin effect network synthesized per layer

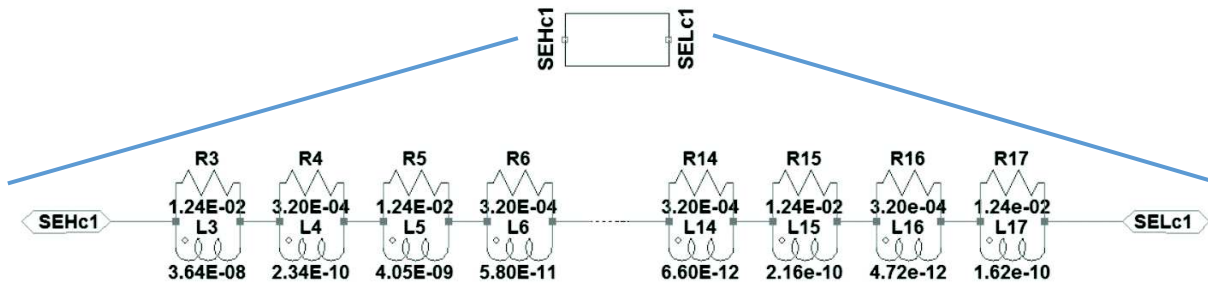


Fig. II. 48 - Foster network for copper skin effect

3. Parallel capacitance of the capacitive model for turn-to-turn mechanism (straightforward)
4. Dielectric loss network

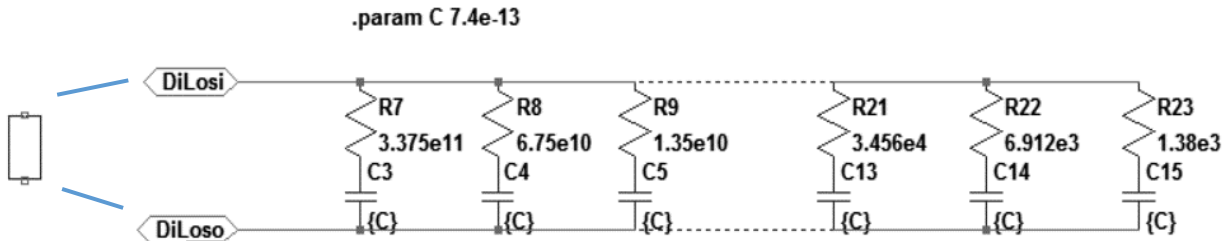


Fig. II. 49 - Dielectric network

Note that for the parallel capacitance (element n°4) and the dielectric loss network associated, the connection is done between the two series turns.

5. Self-inductance of the turn calculated at one frequency

6.4.2 Two turns of adjacent layers

For turns of two adjacent layers, capacitive couplings exist (cf. §II.3). The turn-to-turn capacitance between layers is represented in Fig. II. 50.

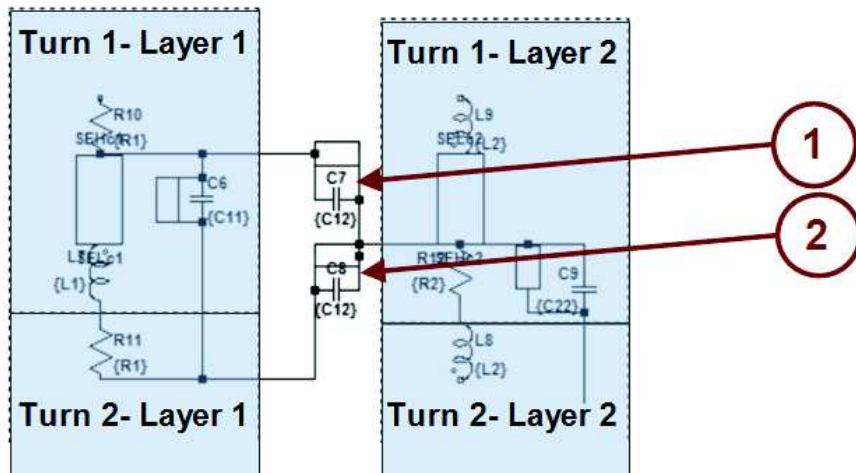


Fig. II. 50 - Couplings between turns of two adjacent layers

It can be seen, that because of the concentrated arrangement of turns, for one turn of a layer, two turns of the adjacent layer are concerned. Two turn-to-turn couplings exist between the turn of a layer and the other two adjacent turns of the adjacent layer.

The element one is the same as the element 2 of the figure. And these are the same capacitance and dielectric losses networks as for the above case. However, the values change according to §II.3.5.5.

6.4.3 Coupling to the core

If the core is non-conducting, no coupling exists to the core. If a conducting core is considered, the only coupling concerned is again a capacitive one as pictured here after:

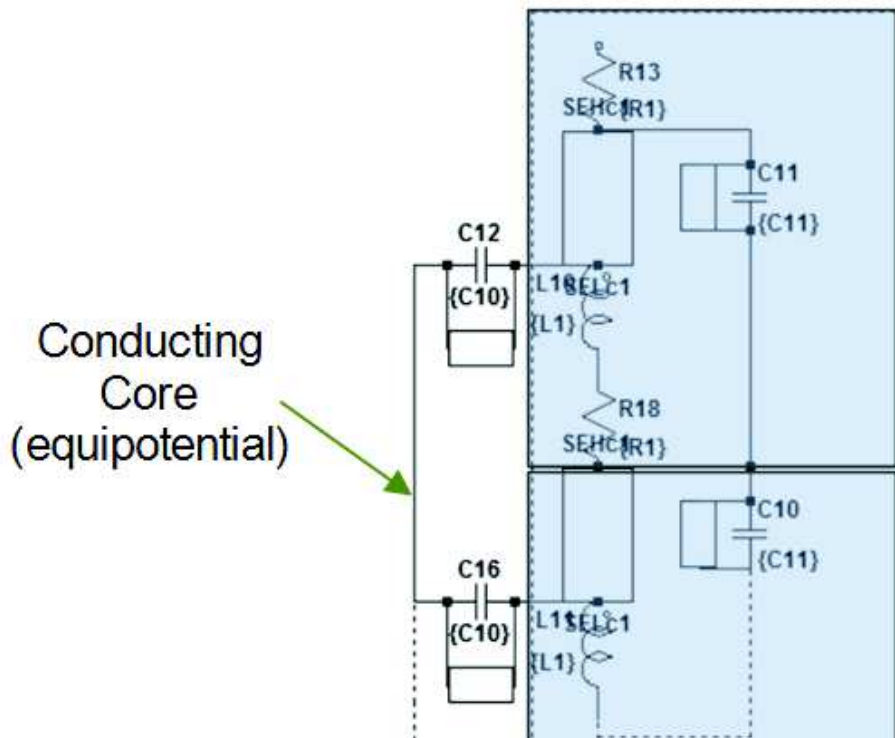


Fig. II. 51 - Couplings to the core

Capacitive couplings are also composed of a capacitance and the dielectric loss network.

6.4.4 Full model for a 4 layer cored winding (4 turns per layer)

An example of a 4 layer, 4 turns per layer cored concentrated winding is shown in Fig. II. 52. The coil is wound in a back and forth manner (last turn of the first layer is connected to the last turn of the second layer and so on) as indicated by the arrows in Fig. II. 52.

A ground connection of the core is enclosed in the figure, although the ground connection can be performed on either winding lead and/or a core depending on the real connection of the actual modeled winding. But for simulation purposes, a ground connection is necessary.

Layers are coupled to each other by the turn-to-turn capacitive couplings as described before.

With this circuit implementation of the calculated values with the analytical formulations, frequency- and time-domain analysis can be performed.

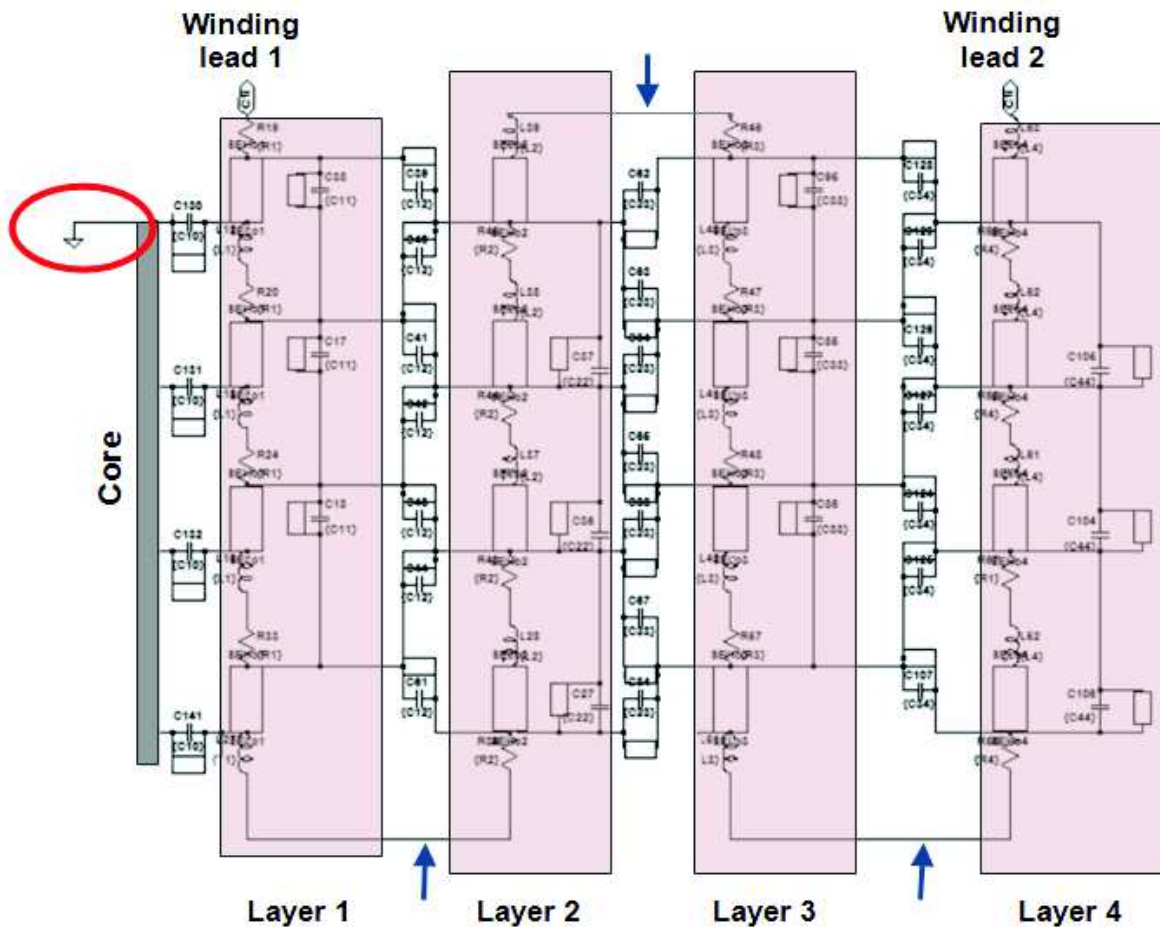


Fig. II. 52 – Circuit structure of a complete winding

In order to properly perform time-domain simulations, the frequency-dependent properties of the inductive couplings would be necessary since, as stated in (§II.6.3), without properly implementing the inductive variations with frequency, results are only valid for a range centered at the calculating frequency of inductive couplings.

7 EXPERIMENTAL AND SIMULATION RESULTS AND ANALYSIS

7.1 SPECIMENS USED FOR MODEL VALIDATION PURPOSES

In order to compare the results of frequency- and time-domain simulations with experimental measurements, several wound structures have been designed. The specimens are designed to test representative configurations of concentrated windings present in several types of electric motors. The specimens are here described and the materials used undergo a set of measurements in order to extract the needed information for modelling.

The structures are based on a circular cross-section core as represented in Fig. II. 53. Four layers of twelve turns each are then tightly wound over the core in a *back and forth* manner.

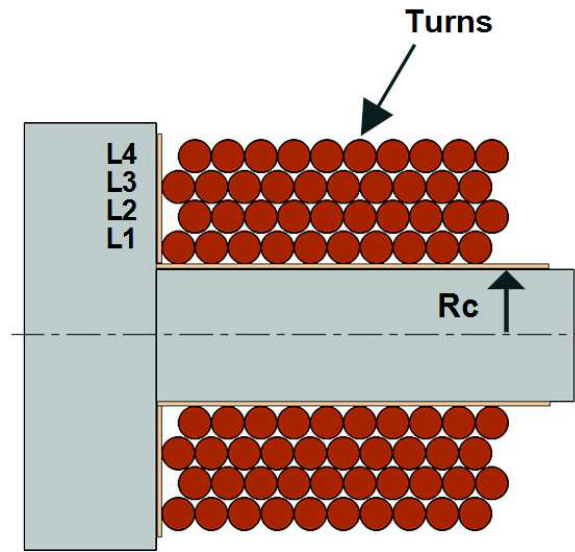


Fig. II. 53 - Schematic representation of the specimens for experimental comparison

The necessary dimensions for calculation purposes are resumed in Table II. 22.

Table II. 22 - Geometrical parameters of the samples

Dimension	Symbol	Value
Core radius	R_c	8 mm
Copper wire radius (bare copper)	r_c	0.355 mm
Enameling thickness (grade 1)	e	0.02 mm
Insulating film thickness (if existent)	i	0.05 mm

The shape of the cores are the same for the four specimens. However, substantial differences appear concerning the insulation and impregnation of the different test tubes as resumed in Table II. 23.

Table II. 23 - Specimens' materials and layout

Specimen	Name	Core material	Core insulation	Impregnation
A	Delrin	Delrin (polymer)	-	-
B	Bare Core	Soft Magnetic Compound	-	-
C	Insulated Core	Soft Magnetic Compound	Kapton® 50 μ m	-
D	Impregnated	Soft Magnetic Compound	-	Araldite F®

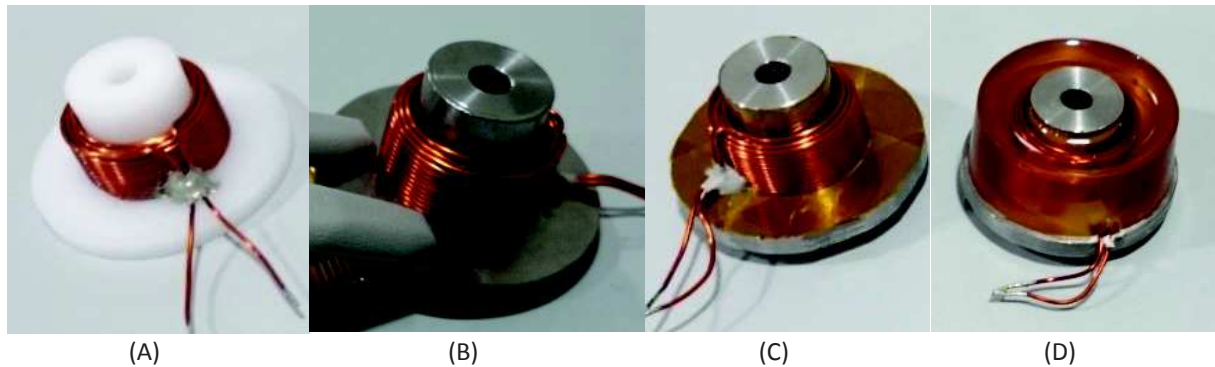


Fig. II. 54 - Different specimens for experimentation

The wire used is a diameter 0.71 mm grade 1, thermal class F wire, common in industrial applications for concentrated wound coils.

Other than the above described characteristics, the SMC cores are made with Höganäs® Somaloy™ Prototyping Material.

7.2 FREQUENCY-DOMAIN SIMULATION AND EXPERIMENTAL DATA COMPARISON

7.2.1 Experimental protocol for measurements

7.2.1.1 Test equipment

Two measurement instruments are used in this process:

- Keysight Precision Impedance Analyzer (PIA) E4990A for frequencies from 20 Hz to 1 MHz
- Keysight Vector Network Analyzer (VNA) E6051B for frequencies from 1MHz to 300 MHz

The reason for using two different equipment is that a single instrument cannot handle the measurement for the full frequency range of 20 Hz to 300 MHz.

In fact, although the PIA's upper limit is 120 MHz, the tests fixtures that were used were not all rated to be used up to 120 MHz.

On the other hand, the VNA can handle frequencies from 5 Hz to 3 GHz. However, because of the ESD protection on the ports and DC block protections, the lower limit of the VNA reduces to 300 kHz. It was decided that, for good quality measurements over the full frequency range, the two equipment should be used.

7.2.1.2 CM and DM measurements

Differential and common mode measurements were done on the four specimens. For differential-mode measurements, the two leads of the wound structures are left unsoldered as shown in Fig. II. 55. For common-mode, the two leads are soldered together, and the ferromagnetic core (polymer-cored winding is not concerned) is used as a second lead for measurement. This experimental data indicates through what impedance energy is being conveyed directly from the copper turns to the grounded ferromagnetic core.

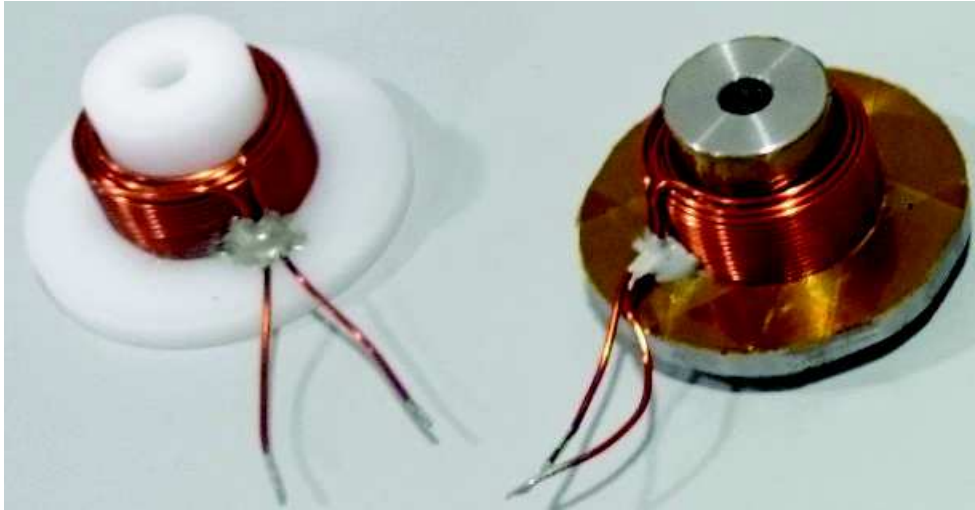


Fig. II. 55 - DM and CM connections on the DUTs

- Measurements with the impedance analyzer

The extraction of experimental data in the form of impedance is straight forward with the PIA. The two leads of the test terminals are used to connect a dipole and the PIA returns directly the impedance value and phase of the dipole over a selected frequency range.

The most useful test set used for these measurements was the E42942A terminal adapter for DM data. However, for CM data, a conductive gasket was used in order to ensure a good contact between the ferromagnetic core and one of the leads of the test instrument. The ferromagnetic core was scratched to rip-off the rust that accumulates over time.

- Measurements with the network analyzer

The extracted data is obtain in the form of Scattering Parameters (cf. Chapter I) which give equivalent information as impedance parameters. However, in this case, the winding is considered to be a 3-port device. Although the equivalent impedance between any of those ports is readily available, a specific test printed circuit board was manufactured as shown in Fig. II. 56.

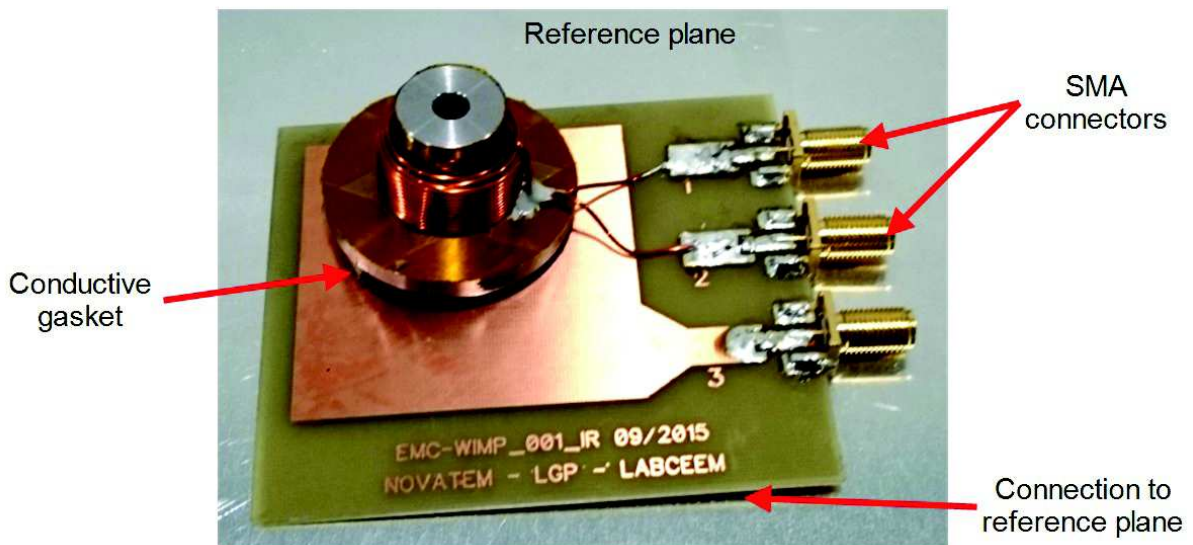


Fig. II. 56 - Specific fixturing of the samples for VNA measurements

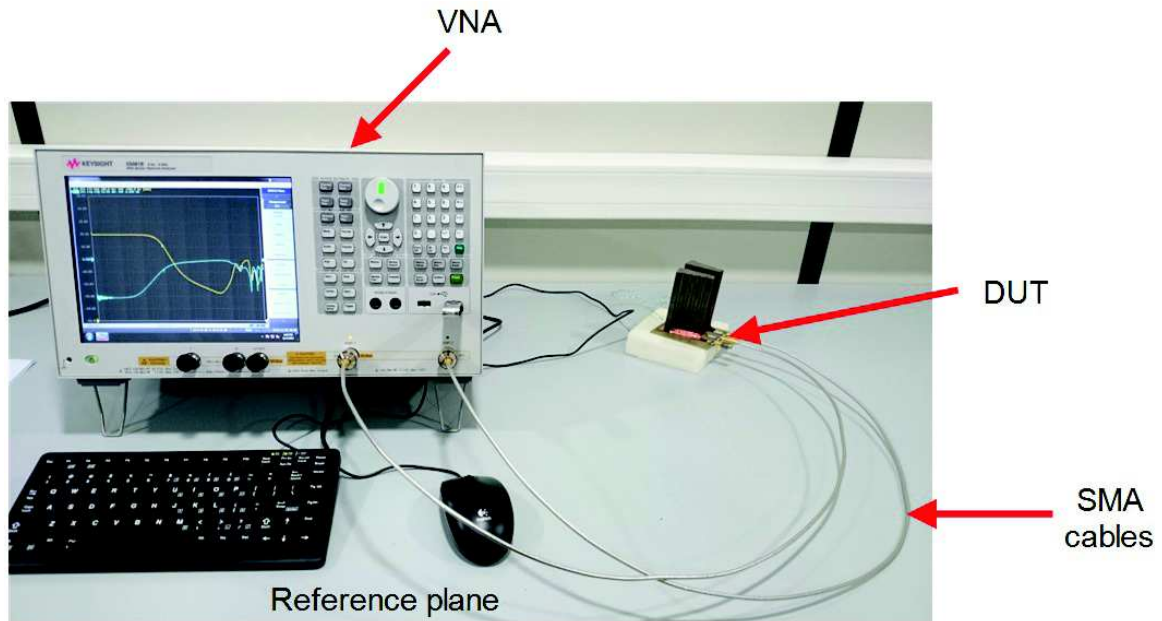


Fig. II. 57 - Test setup for S-parameters measurements on the samples

Common and differential-mode transformations were therefore done with S-parameters data obtained with the 9 element S-parameters matrix.

In order to show that the data from the two test instruments are concordant in the sub-120 MHz range, Fig. II. 58 presents the magnitude of a measured DM mode impedance of one of the test specimens.

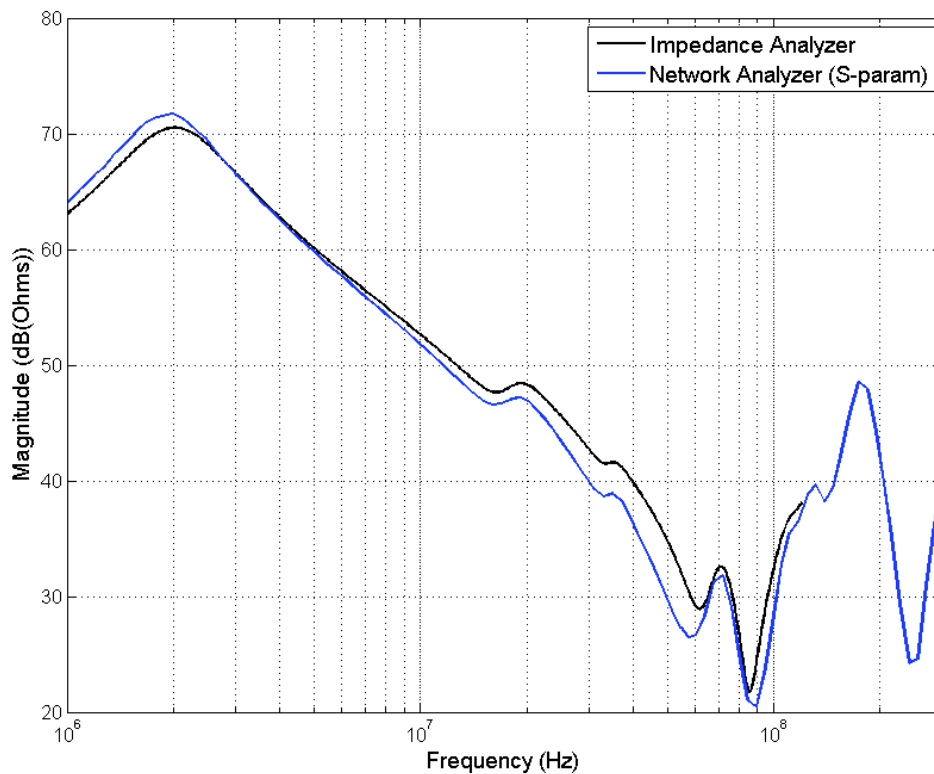


Fig. II. 58 - Impedance comparison with PIA and VNA measurements between 1 MHz and 120 MHz

Although for the phase plots, there seems to be a divergent tendency between 20 and 80 MHz, concordance in magnitude is **within 2.4 dB difference**. It is likely that calibration uncertainties for both instruments is the cause of the differences. These are two radically different experimental setups; impedance analysis is done directly at the leads of the fixture whilst for scattering parameters several different components are present. In subsequent measurements, a particular attention was put on calibration and neatness of the measurement setup.

7.2.2 Experimental and simulation results comparison

7.2.2.1 Non-ferromagnetic cored inductor specimen (specimen A)

The first validation stage was made with the non-ferromagnetic cored winding (air coil), since it allows to consider a predictable inductive behavior throughout the whole frequency range of the analysis.

It is obvious that only a DM impedance is relevant in this case, since no other metallic common conductor is present in the structure.

This stage is essential for the validation of the modelling process. The Maxwell formulation of mutual inductances in circular-shaped turns in the air, is outstandingly accurate. Once the calculations of the inductances and derived coupling coefficients were performed, a low-frequency measurement to validate the global inductance value of the coil.

Since the inductance is **sensibly** the same at the low end of the spectrum in question (eddy current effects that account for internal inductance decrease of the copper turns are negligible up to several kHz), a low-frequency measurement would validate the calculated value of the global inductance of the model. Now, the only hypothesis made here, is that it is being assumed that because the global value is accurately predicted, therefore, the per-turn inductance is also accurately predicted. This hypothesis is not verified, but it is assumed that the approximation is valid in order to verify the other phenomena modelling results. In Table II. 24, the calculated coil inductance and the low frequency inductance measurement are resumed.

Table II. 24 - Calculated vs. measured value of self-inductance of the non-ferromagnetic sample

Inductance of the <i>air</i> coil	
Calculated value	Measured value
2.475 μ H	2.418 μ H @ 20 Hz

As can be seen in Table II. 24, the error between measured and calculated value is 2.3 %. Taking this into account, it will be assumed that the calculated per-turn inductance is accurately predicted by the model.

Fig. II. 59 shows a comparison plot between the simulated model implemented in LTSpice and the measured DM impedance modulus. This first DM impedance plot was obtained only with the impedance analyzer.

Several annotations should be made in order to understand the differences between the two curves. First of all, a general appreciation can lead to several interesting points. Up to 80 MHz, the difference between the two impedance modulus is less than 10 dB. This can be considered a very high value for the purposes of constructing precise predictive methods. But between 1 kHz and 20 MHz, the difference is less than 5 dB.

Secondly, a more thorough analysis is necessary to understand the large differences especially at the higher end of the spectrum. A zone-driven analysis might be useful.

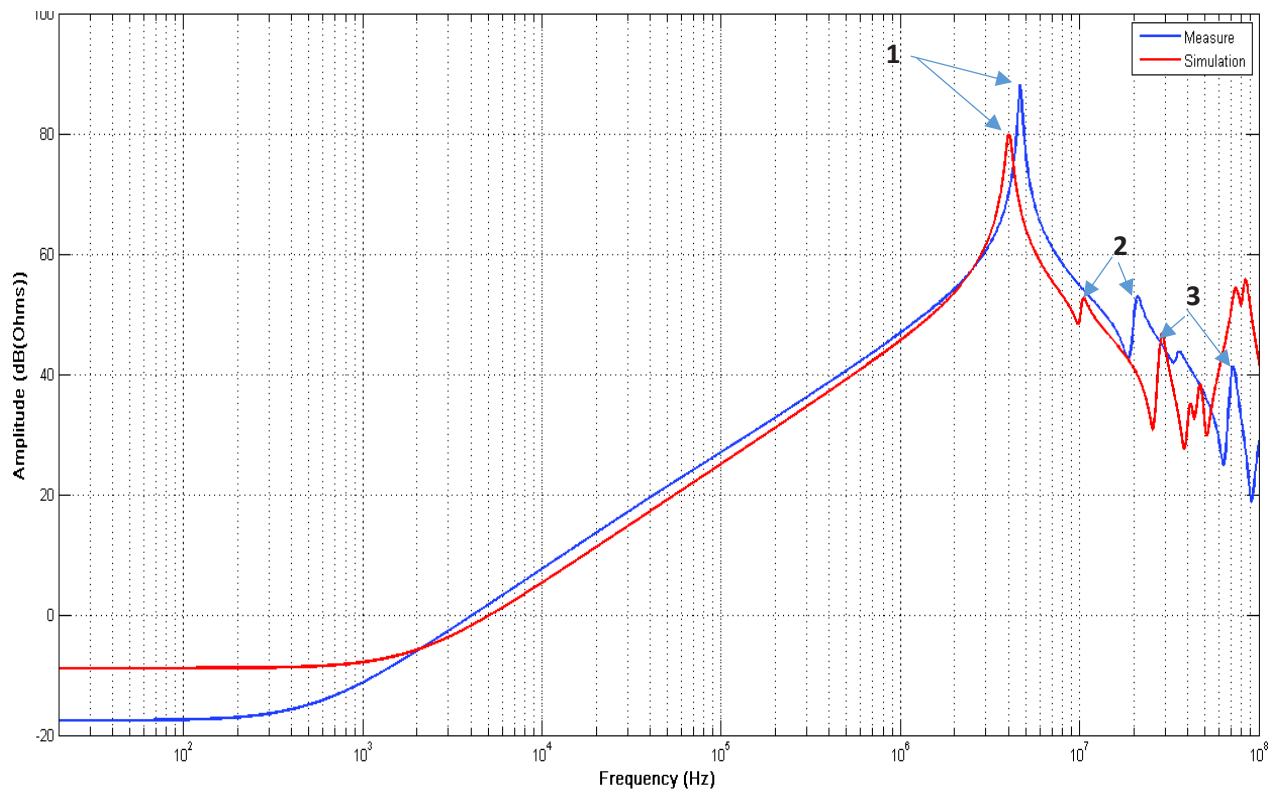


Fig. II. 59 - Resulting measured and simulated impedance module of the non-ferromagnetic core specimen

- Zone 1: 20 Hz to 1kHz

In this zone, an 8 dB difference is measured. This difference is strictly related to the implementation of synthesized networks in order to account for frequency-dependent phenomena. In this zone, a very high influence of the Foster network implemented for the eddy currents in the copper turns. As stated in [10], [34], this type of network introduces a low-frequency real value that increases with the number of cells of the network. In [10] the author goes through a very complete analysis and optimization to get rid of this low-frequency component. In this study, though, this parasitic value was deliberately ignored when the synthesis of the network was carried out.

The 8 dB difference corresponds to an increase of 2.5 times the measured impedance approximately, and the measured impedance at low frequency is 140 mΩ. In order to fairly criticize this value, an increase of the temperature of the whole winding would have a much larger impact than an increase of 350 mΩ. It should be pointed out, that this is not an offset value. It only affects the low frequency behavior of the synthesized Foster network.

To improve the model, a smaller number of cells, or an optimization as in [10], can be performed. But, given the very large band of frequency where the model is implemented, chances are that the reduction of the low frequency stray impedance will be limited.

Furthermore, as was stated in the modelling process, this eddy-current model is adapted for square conductors, not closely tightened round conductors as in our case. This also might be a reason for the difference.

- Zone 2: 1 kHz to first resonance

An inductive behavior is easily identified. Since it is assumed that the winding inductance is accurately predicted, it is possible to analyze the modelling of eddy current effects on copper turns which account for skin and proximity effect. Up to the resonance, the difference is extremely weak. The model predicts very well the eddy current effects. The hypothesis of the tightly packed squared-cross section copper turns seems to adapt sensibly well to the closely packed circular-cross section copper turns. This needs a lot more analysis, but it appears to be that as long as conductors are tightly packed together, the formulation yields good results. Be aware that because of the complex structure, fine conclusions are hard to establish on this particular issue since phenomena cannot be separated from one another in an impedance analysis.

- Zone 3: First resonance

At this point, capacitance value can be analyzed since at the resonance, a direct relationship between capacitance at the terminals and coil inductance appear. Again, a hypothesis has to be made: accurate calculation of global capacitance implies accurate modelling of turn-to-turn and core capacitance. However, at this point, and on behalf of the analysis of section §II.3.6 with FE analysis, a pretty accurate prediction of partial capacitances has been made for the modelling. The capacitance value extracted at resonance of the simulated impedance is given by

$$f_r = \frac{1}{2\pi\sqrt{LC_s}} = 4.03 \text{ MHz}$$

where f_r is the frequency at resonance, C_s the capacitance value across the coil, and L the above calculated (or measured) coil inductance. Therefore, the calculated capacitance is

$$C_s = 630 \text{ pF}$$

It is this capacitance value that is representative of the parasitic capacitance behavior of a winding and is useful for calculating the voltage spikes at the leads of any coil. The calculation of the capacitance with the measured data gives a smaller capacitance: $C_m = 482 \text{ pF}$. The difference is actually 23.1 % error which is a fairly elevated value.

- Zone 4: First resonance to 80 MHz

The model fails to accurately predict this part for now. In fact, it has been chosen to ignore the evolution of permittivity and loss tangent of the coating of turns with frequency throughout the frequency range in question. A constant ϵ_r of the coating directly induces a constant partial capacitance between turns. Nevertheless, if the permittivity was shown to decrease with frequency at frequencies well below the assumed ones (several hundreds of MHz), a consequence of such a behavior would be to decrease the equivalent capacitance.

To better understand the hypothesis of a faster dispersing permittivity, a calculation of resonances shows that (Table II. 25 - Calculation of self-inductance and capacitance at different resonance points) the decrease of resonant frequencies 2 and 3 on the plot gives:

Table II. 25 - Calculation of self-inductance and capacitance at different resonance points

Resonant point	Measured data		Simulated data		Ratio meas/sim
	$f r_m$	C_m	$f r_s$	C_s	
2	21.09 MHz	23 pF	10.40 MHz	96.8 pF	0.237
3	72.05 MHz	1.97pF	28.51 MHz	12.9 pF	0.153

The permittivity ratio encountered between the simulated and the measured data is highly likely to account for the permittivity dispersion with frequency in the dielectric materials. The hypothesis in which the permittivity was a constant value over the full frequency span creates a very divergent result.

If this hypotheses is validated, taking into account the permittivity dispersion with frequency could allow the third zone to present less differences with respect to the measured data. With lesser permittivity values, the capacitance at resonances is lower. This induces a frequency shift of the resonances which would make peaks to match in frequency but also to decrease the equivalent level of impedance at those peaks, which is necessary too.

The model seems to fail in achieving decent accuracy at high frequencies. However, when the upper frequency of the measurement is extended, interesting results appear to confirm the above hypothesis. This is discussed in the next subsection.

7.2.2.2 Ferromagnetic cored-coils: thorough analysis on Specimen (B)

Now that the validation of skin and proximity effect has been dealt with, an important step in understanding the core induced behavior into the model is undergone.

As stated in §II.5.4, the magnetic dispersion is not included into the circuit model. Therefore, comparison between measurement and simulation in this case, has to be dealt differently. The idea is to determine the flanking values of the simulated impedance when the simulations are performed with inductance and coupling coefficient values calculated at $f \in [1 \text{ Hz}, 300 \text{ MHz}]$.

As pictured in Fig. II. 60 and Fig. II. 61, simulated magnitude and phase of impedances for the case of specimen (B) are plotted. These plotted simulated impedances are obviously not valid throughout the full frequency range since the calculated inductances for the simulations are calculated at a fixed frequency. However, the plot allows to analyze the extreme values taken by the resulting impedance.

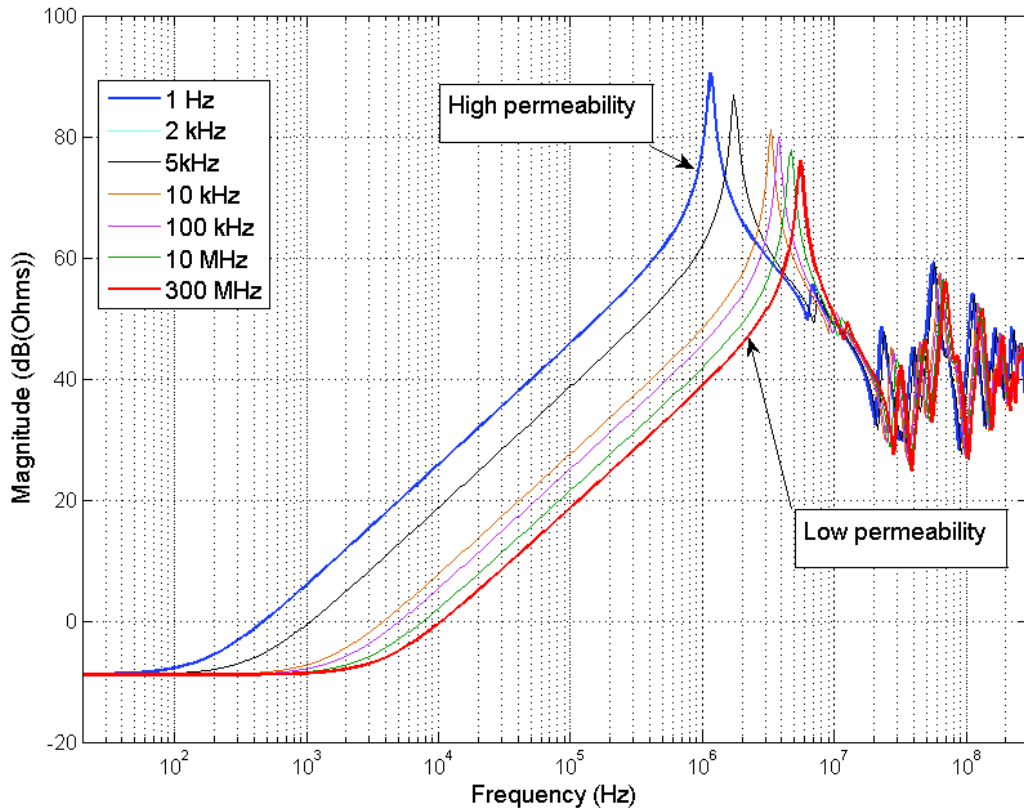


Fig. II. 60 – Simulated impedance magnitude with inductive parameters calculated at different frequencies

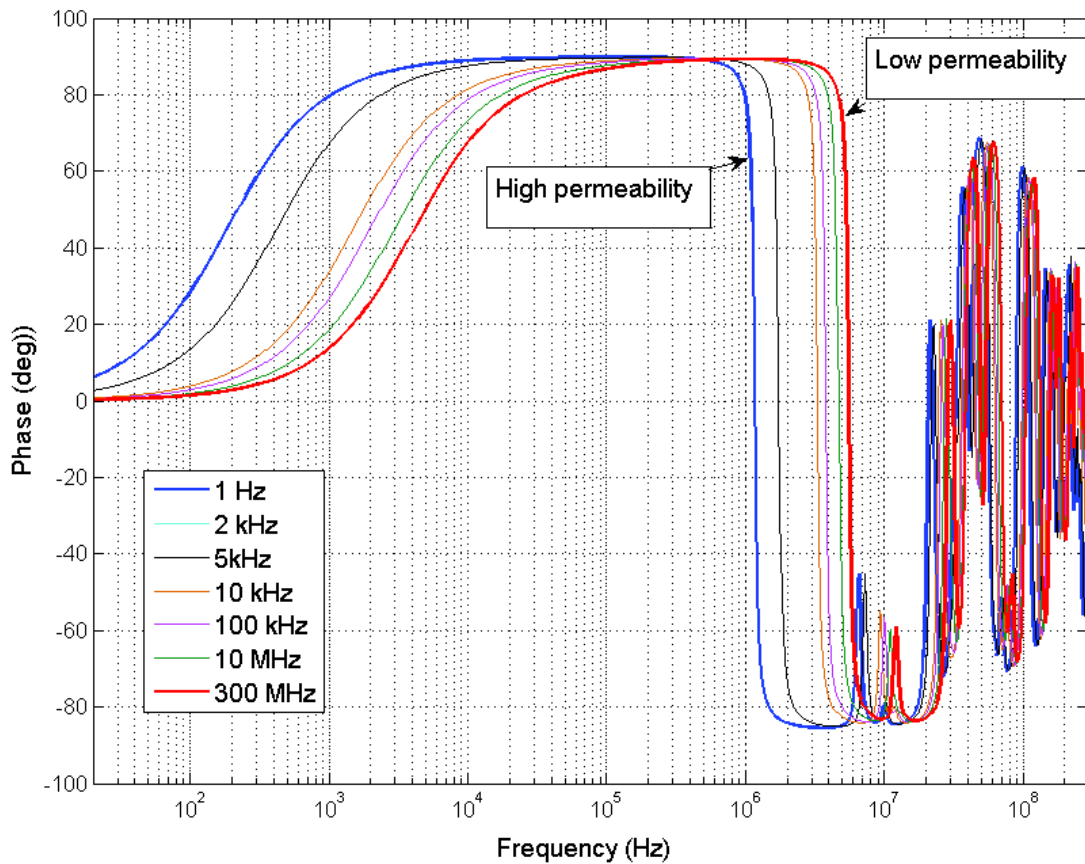


Fig. II. 61 - Simulated impedance phase with inductive parameters calculated at different frequencies

As measured before, the relaxation of the magnetic material used for the cores arrives at 6 kHz. But even between the cases 100 kHz and 300 MHz, differences exist showing the remains of higher-than-one relative permeability values even at several hundreds of kHz. In SMC (soft magnetic compounds) materials (cf. §II.5), relaxation processes are more moderate than in classic iron laminated materials usually used in motor technology. A remaining relative permeability value may be present at particularly high frequencies.

Another interesting characteristic, is that, the resonant point level varies with the dispersion of the permeability value and consequently, the higher the relative permeability of the material, the higher the difference in resonance magnitudes for the same material.

The measured impedance in the case of specimen (B) (bare core), is plotted in Fig. II. 62 to Fig. II. 63 along with the simulation results for the extreme cases of calculated inductance and coupling coefficients as shown above. As explained in the measurement protocol, two instruments had to be used for the full measurement frequency range could be covered. Thus, two plots corresponding to the two measurement ranges are shown separately.

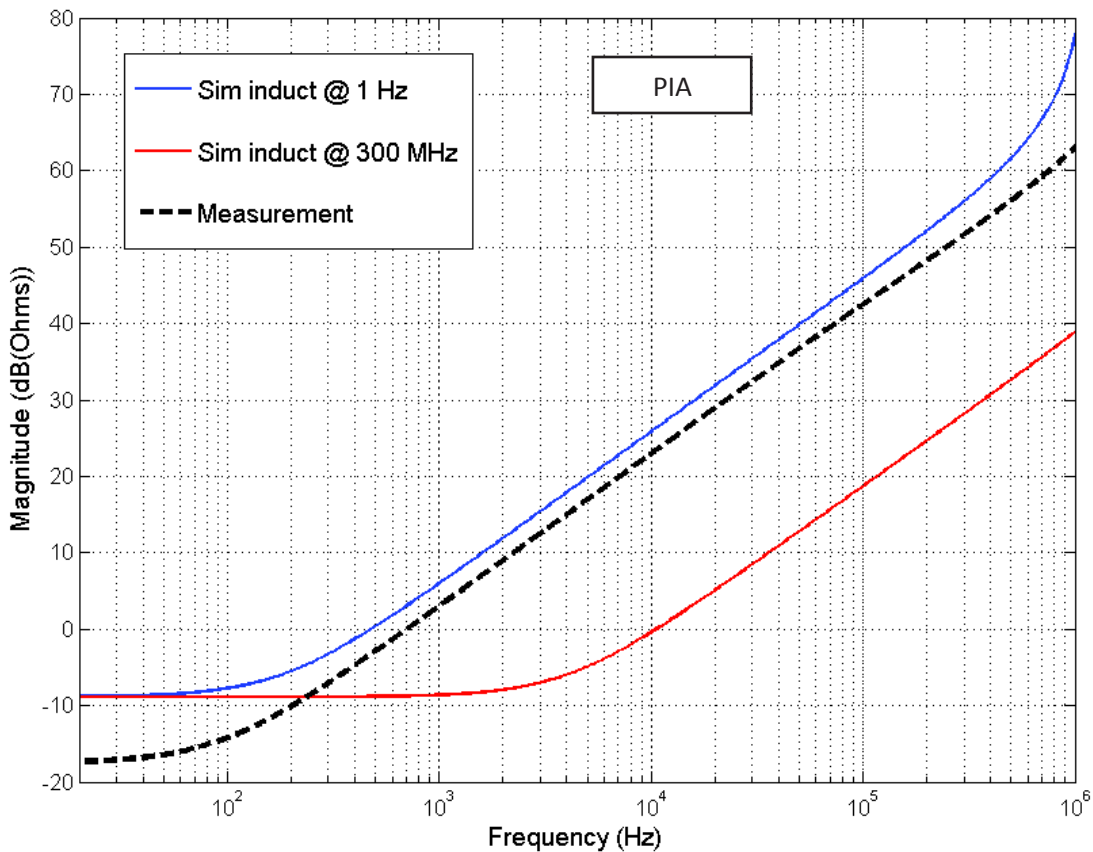


Fig. II. 62 – Measured DM impedance magnitude on Specimen (B) and comparison with extreme values up to 1 MHz (PIA measurement)

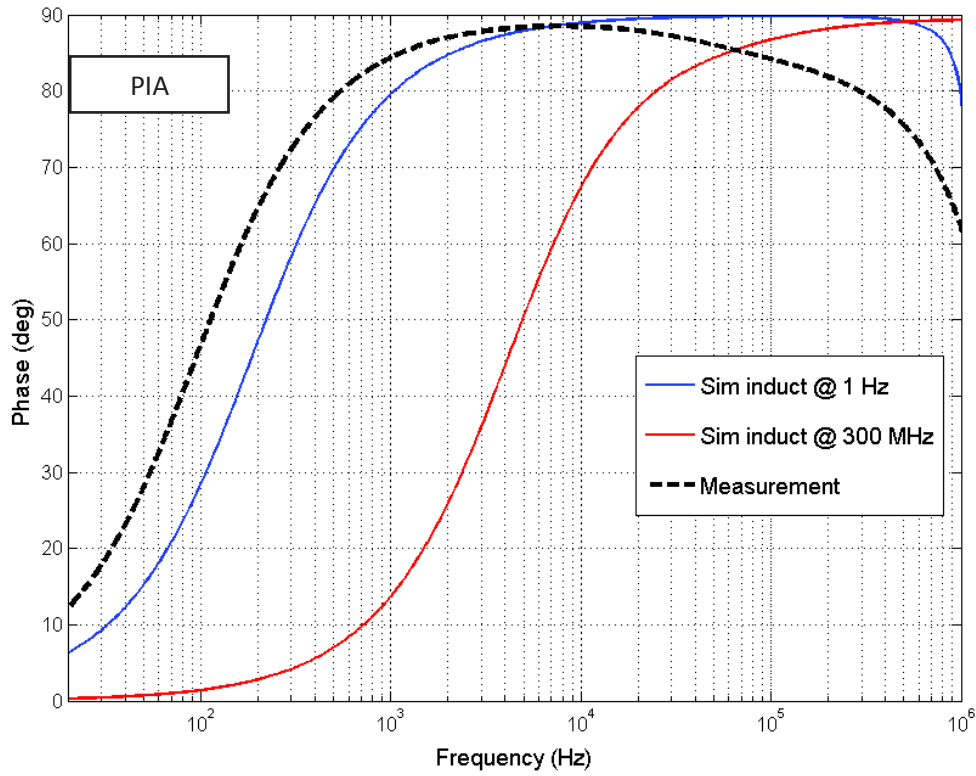


Fig. II. 63 - Measured DM impedance phase on Specimen (B) and comparison with extreme values up to 1 MHz (PIA measurement)

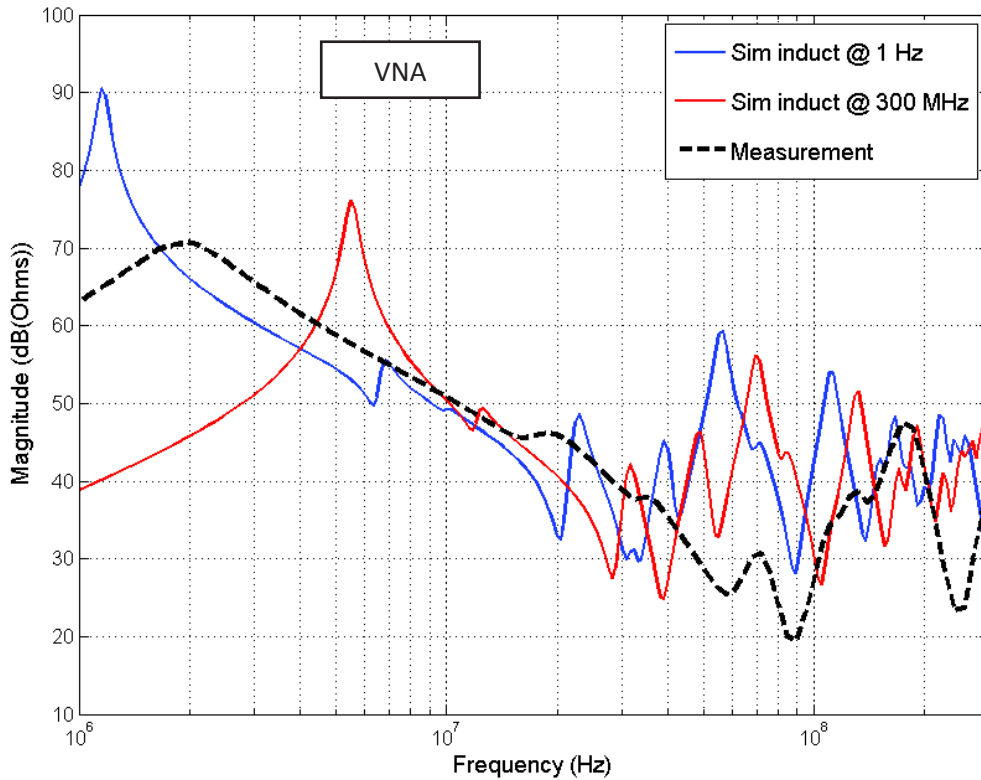


Fig. II. 64 - Measured DM impedance magnitude on Specimen (B) and comparison with extreme values up to 300 MHz (VNA measurement)

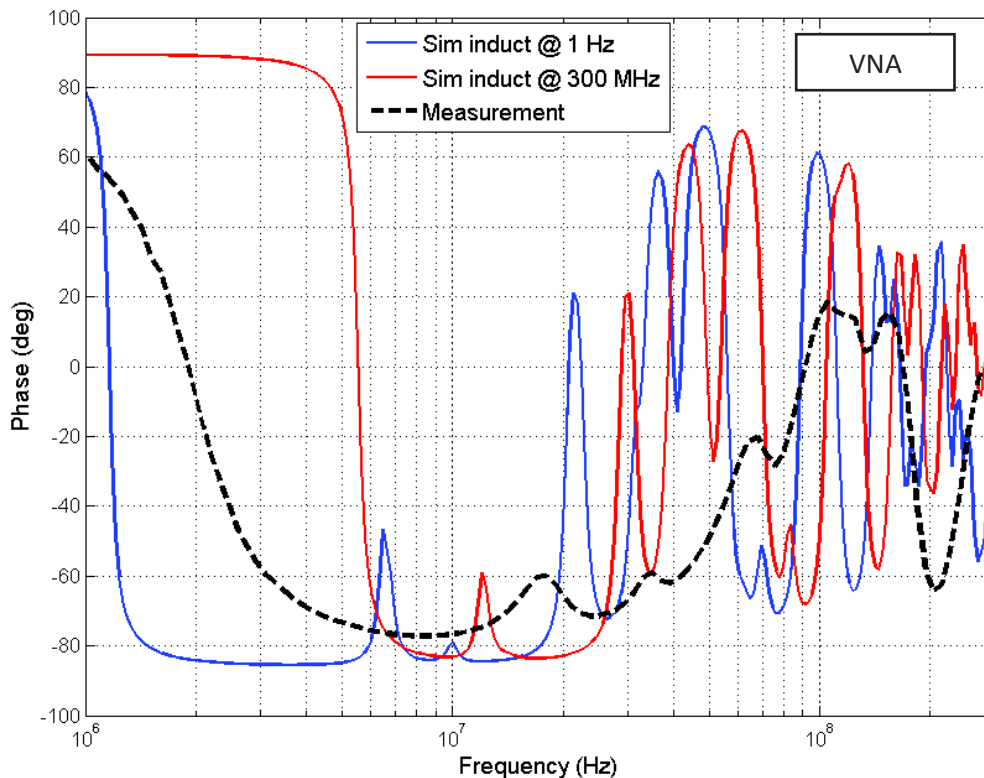


Fig. II. 65 – Measured DM impedance magnitude on Specimen (B) and comparison with extreme values up to 300 MHz (VNA measurement)

- 20 Hz to 1 MHz:

The effect of high permeability is clearly visible, since the simulated impedance (magnitude and phase) for inductive behavior modelled at low frequencies is closer to the measured value than the impedance with calculated inductances and coupling coefficients at 300 MHz.

Although the modelled impedance behavior allows to frame the measured value, large magnitude spans remain between the two extreme simulated values. This problem is accentuated for core materials with higher permeability values, since the difference between inductive couplings at low frequencies and couplings at frequencies above relaxation are directly impacted by the relative permeability value. However, it should be pointed out, that, for materials with high permeability values, relaxation appears at very low frequencies, and the dispersion mechanism is steeper than for low permeability materials (cf. II.5), narrowing the differences in magnitude at higher frequencies above relaxation.

Finally, let us analyze the first resonant point (towards 1 MHz). As can be seen from the phase plots, a decrease of phase in the inductive zone of measured impedance is observed to happen before the simulated impedance cases. This is an indication of dissipative behaviors reducing the quality factor of the winding at this resonant point. As was assumed in §II. 5, iron core losses are not taken into account in the modelling. But, it can be seen from measured plots, that iron losses are actually identifiable. Improving the circuit model could bring a better representation of simulated impedance.

- 1 MHz to 300 MHz:

Globally, the same conclusions than for the air-cored case can be drawn. The model predicts the *peaks and valleys* of impedance but with very different resonant frequencies. Again, the dispersion of dielectric permittivity and increase of dielectric losses can be causes for this behavior.

To better understand this, in Fig. II. 66 is plotted the simulated impedance magnitude (phase performance is also concordant as can be seen above) with calculated inductances at 300 MHz and the measured impedance for a narrower frequency span.

As outlined in this plot, resonances are well predicted with the analytically constructed circuit model. But, levels and frequencies are not.

The inductive behavior is not a parameter anymore for frequencies higher than 10 MHz since permeability is fully dispersed and the magnetic conduct of the winding is that of an air-cored one. This is fundamental to understand because it confirms the hypothesis that was stated for the air-cored winding that dielectric behavior is the main reason for the resonances and levels to mismatch to measurements. Inductances here are well predicted and constant, eddy-currents are well predicted at high frequencies but permittivity and dielectric losses are considered to be constant throughout the full spectrum and it is not.

To better model the winding behavior, a better understanding of dielectric behavior of insulating enamels is fundamental. This means that, the frequency dependence of permittivity, as for the permeability case, has to be included in the models, which is not an easy task.

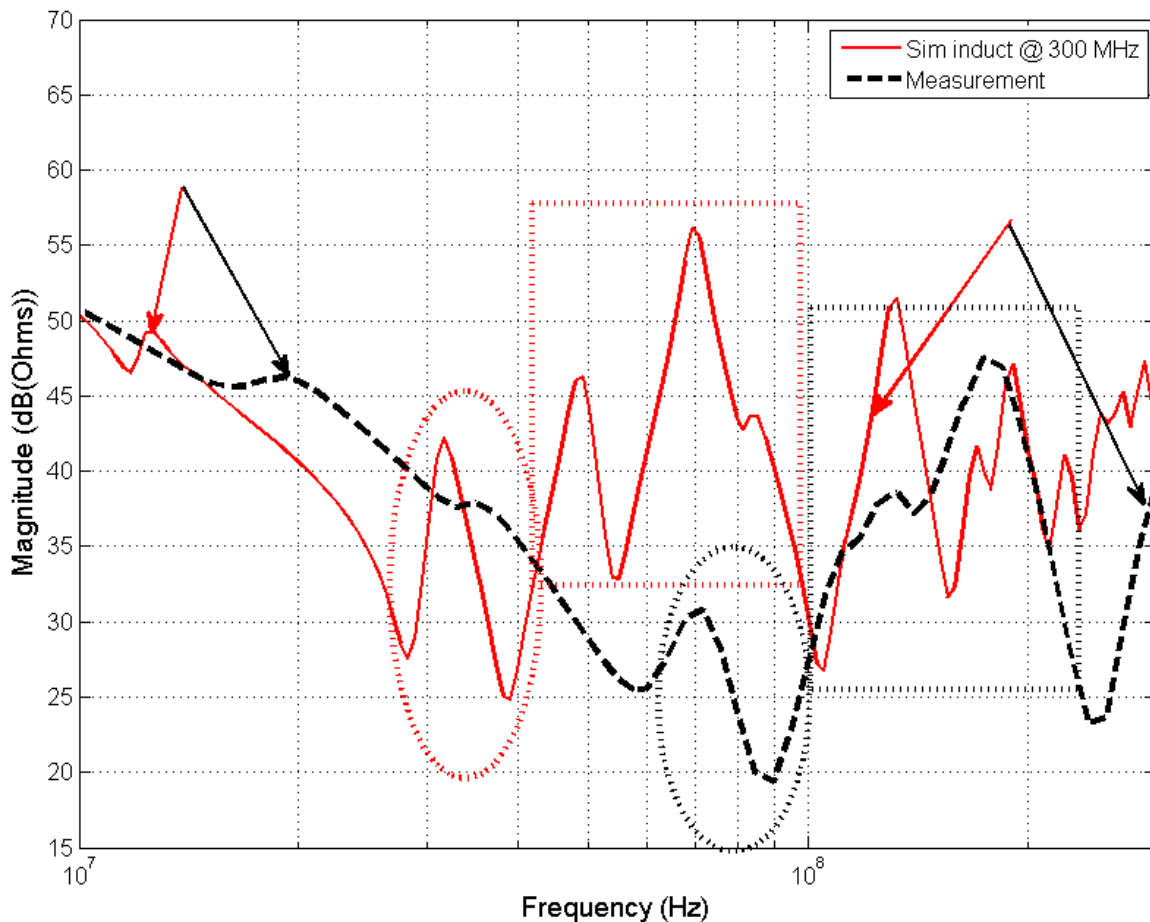


Fig. II. 66 - Resonances comparison between measured and simulated DM impedance

Now, the modelled common-mode impedance should be compared to measured results.

Fig. II. 67 depicts the plotted measured common-mode impedance of specimen (B) compared to simulated impedances for inductances and coupling coefficients calculated at different frequencies.

It is well known that capacitive couplings are a major contributor to common-mode impedance. This is verified here too. But this assumption is sometimes not valid for some frequency ranges, and as can be seen at the far end of the plotted spectrum, inductive-capacitive interactions exist too.

A difference of 7.5 dB between simulated and measured magnitude data is found. This difference is linked to two causes:

- Differences between calculated turn-to-turn and turn-to-core capacitance
- Parasitic resistance in the measurement lead of the instrument in contact with the core

The first cause is easily explained. Analytical models are naturally approximations of the reality. The second reason is related to the nature of the magnetic core. It is not a very easy surface to deal with and the connections to the measurement leads can be hard to ensure a good conductivity. Even though, common-mode impedance seems to be overestimated.

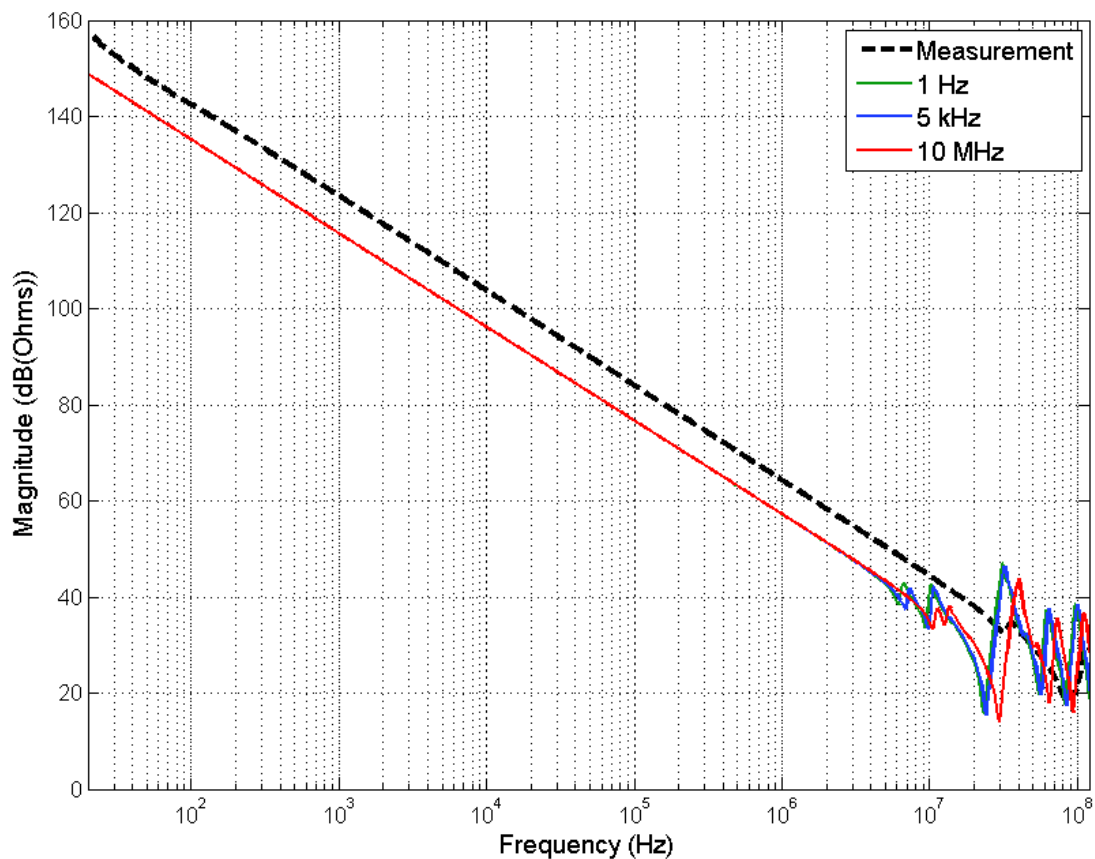


Fig. II. 67 - Common-mode impedance magnitude analysis on specimen (B)

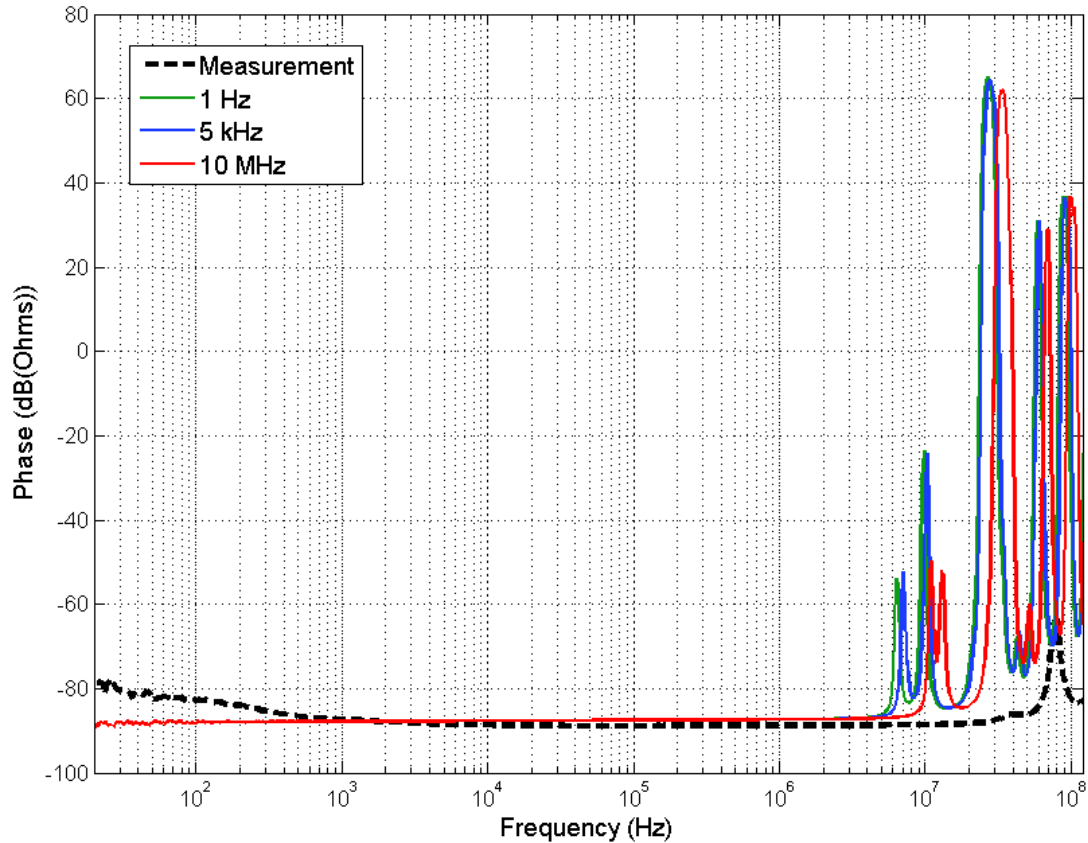


Fig. II. 68 - Common-mode impedance phase analysis on specimen (B)

7.2.2.3 Final analysis: specimens (B), (C) and (D) comparison for capacitive performance

The major difference in the constitution of the specimens are their capacitive behavior (for the cored samples). Fig. II. 69 shows that little-to-no difference between specimens (B) and (C) are recorded in measurement and that the same behavior is predicted by the simulation.

On the other hand, a significant difference is recorded between (B) and (C) and specimen (D). This is due to the impregnation treatment done on specimen (D), which increases its capacitive coupling in turn-to-turn and turn-to core mechanisms. However, very little difference is predicted by the simulation, at least at the lower end of the spectrum. Regardless, even for measured behaviors, the differences are so little that it is difficult to establish a conclusive statement on the performance of the model from this plot, which is somewhat deceiving.

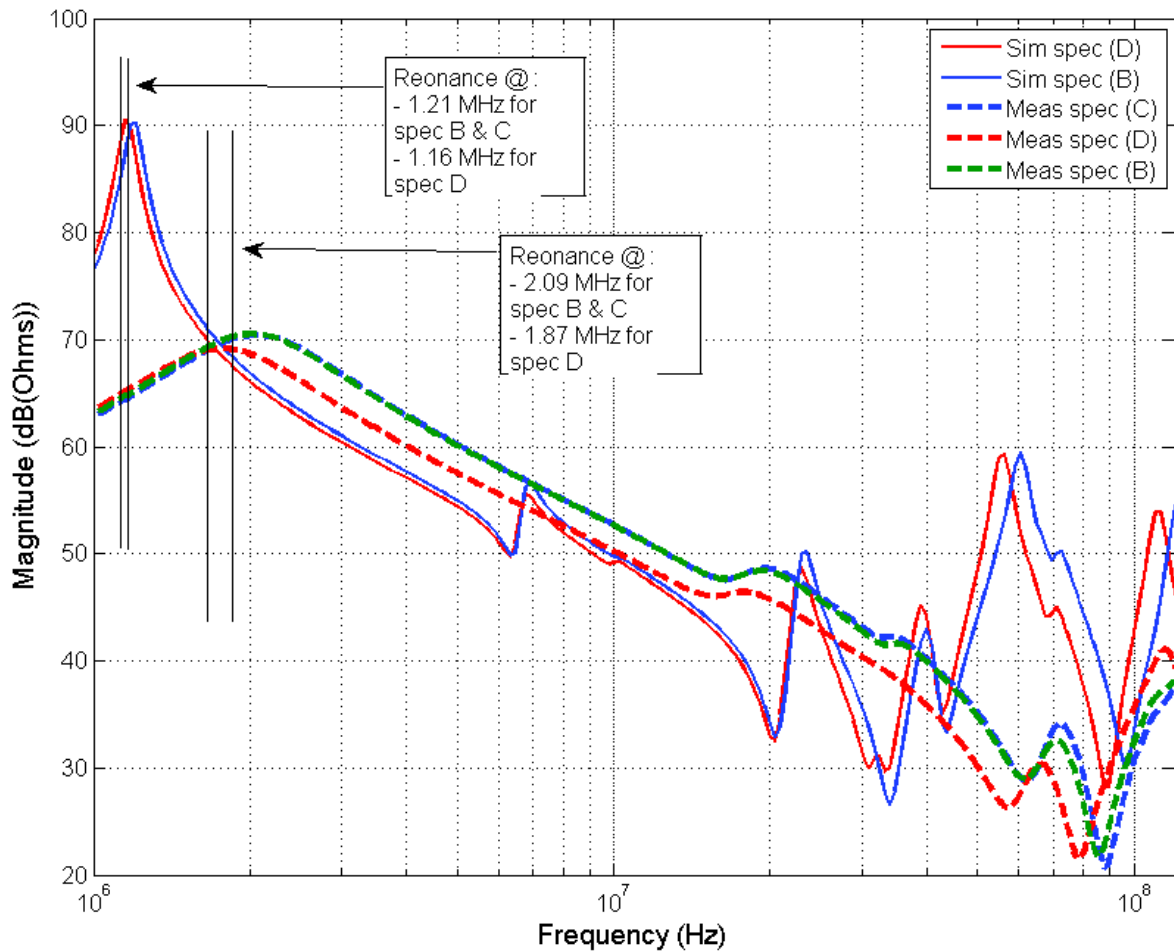


Fig. II. 69 - DM impedance comparison for specimens (B), (C) and (D) and resonance analysis

7.3 CONCLUSIONS ON EXPERIMENTAL VALIDATIONS

Above all, it should be considered the targeted frequency range of modelling is very large. And in light of the above observations, results are convincing from a point of view of the modelling process. The simulation results were confronted to experimental measurements and several points have to be made.

First, both differential- and common-mode impedance trends are very accurately described by the analytically constructed circuit model. All resonances present in the measured impedances happened to appear in the simulated impedances, both in magnitude and phase.

Then, even if the trends are accurately predicted, the models are very sensitive to analytical values alloted to the circuit parameters. Therefore, the more accuracy is conceded to analytical calculations, the more accurate the model will behave. The problem with this characteristic, is that, assumptions such as constant permittivity and dielectric losses have an enormous impact on resulting impedances.

Besides, the circuit model fails to account for the frequency-dependent permeability, which forces the analysis in terms of framing the impedance within extreme values, but for accuracy improvements, more narrow-band analysis are completely possible to achieve for frequencies surrounding that of the calculated inductances and coupling coefficients.

Overall, the analytical models are concordant with measurements, and most importantly, since the modelling and simulation process is physically based, to improve the model, the parameters that are lacking in this modelling can be identified and improved.

Bear in mind that, although the tested geometries are not those of machine windings, now, the model behaves outstandingly well for cored and concentrated windings. In the last chapter of this report, an application to a real motor winding is performed with excellent results.

8 CONCLUSION

An extended and fairly exhaustive analysis on the high frequency and wide-band behavior of cored-concentrated windings has been developed. The modelling is fundamentally rational and when compared to experimental results, very good concordance is achieved. The model implemented in terms of circuit simulation, allowing to have a more friendly interaction with it, is a predictive. This represents a fundamental difference with other models which use measured-based fitting parameters, since for mechatronic designers, motor and power electronics are designed in the same loop.

The main stages of the modelling can be summarized in a flowchart that can be considered to be a Virtual Experimentation (XVICE) process for winding design and characterization.

The analytical modeling process takes into account complex phenomena as frequency dependent parameters such as magnetic and dielectric dispersion. However, circuit implementation does not apart from eddy-current effects on copper. This is a major drawback of the tool presented here. Improvements should also account for losses in the magnetic cores to increase accuracy in predictions.

Finally, these results are here validated with circular-cross section cored coils, which are not used in motor winding design. The implementation of this modelling process is done on a real concentrated winding with ferromagnetic core from a vehicle traction motor in chapter IV.

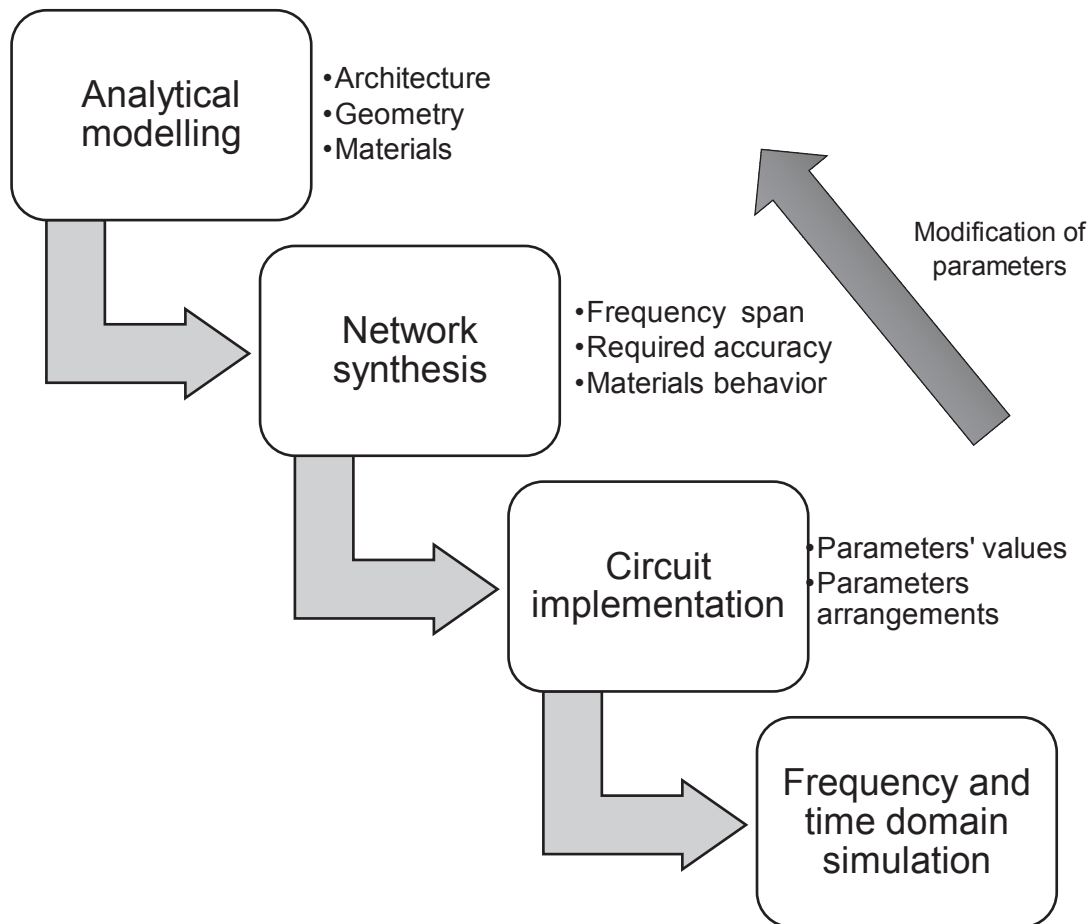


Fig. II. 70 - Flow chart of the modelling process presented here and Virtual Experimentation capabilities

9 REFERENCES

- [1] B. Nogarède and D. V. den Bossche, *Electrodynamique appliquée : Fondements et principes physiques de l'électrotechnique Cours et exercices corrigés*. Paris: Dunod, 2005.
- [2] L. D. Landau and E. M. Lifshits, *Electrodynamics of continuous media*. Pergamon, 1984.
- [3] A. Moliton, *Applied Electromagnetism and Materials*. Springer Science & Business Media, 2007.
- [4] "Synflex Elektro GmbH: Winding wires Enamelled copper wire," 02-Dec-2015. [Online]. Available: <http://www.synflex.com/en/produkte/?areaid=wickeldraehte>. [Accessed: 02-Dec-2015].
- [5] A. Massarini and M. K. Kazimierczuk, "Self-capacitance of inductors," *Power Electron. IEEE Trans. On*, vol. 12, no. 4, pp. 671–676, 1997.
- [6] A. Massarini, M. K. Kazimierczuk, and G. Grandi, "Lumped parameter models for single- and multiple-layer inductors," in *27th Annual IEEE Power Electronics Specialists Conference, 1996. PESC '96 Record, 1996*, vol. 1, pp. 295–301 vol.1.
- [7] F. Tourkhani and P. Viarouge, "Accurate analytical model of winding losses in round Litz wire windings," *Magn. IEEE Trans. On*, vol. 37, no. 1, pp. 538–543, 2001.

- [8] J. Lammeraner and M. Stafl, *Eddy Currents*. .
- [9] V. Mihaila, S. Duchesne, and D. Roger, "A simulation method to predict the turn-to-turn voltage spikes in a PWM fed motor winding," *Dielectr. Electr. Insul. IEEE Trans. On*, vol. 18, no. 5, pp. 1609–1615, 2011.
- [10] F. De Leon and A. Semlyen, "Time domain modeling of eddy current effects for transformer transients," *Power Deliv. IEEE Trans. On*, vol. 8, no. 1, pp. 271–280, 1993.
- [11] P. Holmberg, *Modelling the transient response of windings, laminated steel cores and electromagnetic power devices by means of lumped circuits: with special reference to windings with a coaxial insulation system*. Uppsala: Univ, 2000.
- [12] E. Hallen, *Electromagnetic Theory*, 1st U.S. Edition edition. Chapman and Hall, 1962.
- [13] R. L. Stoll, *The Analysis of eddy currents*. Oxford: Clarendon press, 1974.
- [14] X. Nan and C. R. Sullivan, "An improved calculation of proximity-effect loss in high-frequency windings of round conductors," in *Power Electronics Specialist Conference, 2003. PESC'03. 2003 IEEE 34th Annual*, 2003, vol. 2, pp. 853–860.
- [15] M. Magdowski, S. Kochetov, and M. Leone, "Modeling the skin effect in the time domain for the simulation of circuit interconnects," in *Electromagnetic Compatibility-EMC Europe, 2008 International Symposium on*, 2008, pp. 1–6.
- [16] C.-S. Yen, Z. Fazarinc, and R. L. Wheeler, "Time-domain skin-effect model for transient analysis of lossy transmission lines," *Proc. IEEE*, vol. 70, no. 7, pp. 750–757, 1982.
- [17] F. Dubreuil, *Expérimentation virtuelle pour la CEM: application aux perturbation issues de composants numériques*. Grenoble, France: ANRT, 2001.
- [18] Perry, *Low Frequency Electromagnetic Design*. CRC Press, 1985.
- [19] *Electrodynamics of Continuous Media, Second Edition: Volume 8*, 2 edition. Butterworth-Heinemann, 1984.
- [20] D. Stillman and G. Olhoeft, "Frequency and temperature dependence in electromagnetic properties of Martian analog minerals," *J. Geophys. Res. Planets*, vol. 113, no. E9, p. E09005, Sep. 2008.
- [21] J. Füzér, J. Füzérová, P. Kollár, M. Fáberová, and R. Bureš, "Iron Based Soft Magnetic Compacted Materials," *Acta Electrotech. Inform.*, vol. 13, no. 1, Jan. 2013.
- [22] M. I. Rosales, H. Montiel, and R. Valenzuela, "Magnetic Permeability and Relaxation Frequency in High Frequency Magnetic Materials," in *MRS Proceedings*, 2001, vol. 674, pp. U1–8.
- [23] N. Bowler and Yongqiang Huang, "Model-based characterization of homogeneous metal plates by four-point alternating current potential drop measurements," *IEEE Trans. Magn.*, vol. 41, no. 6, pp. 2102–2110, Jun. 2005.
- [24] V. A. Lebedev, W. Pellico, and Y. Tokpanov, "Measurements of Magnetic Permeability of Soft Steel at High Frequencies," *Conf.Proc.*, vol. C1205201, pp. 2711–2713, 2012.
- [25] C. Cyr, "Modélisation et caractérisation des matériaux magnétiques composites doux utilisés dans les machines électriques," UNIVERSITÉ LAVAL QUÉBEC, 2007.
- [26] É. Durand, *Magnétostatique*. Masson et Cie, 1968.
- [27] F. W. Grover, *Inductance Calculations: Working Formulas and Tables*. Courier Corporation, 2004.
- [28] J. C. Maxwell, *A Treatise on Electricity and Magnetism*. Clarendon Press, 1873.
- [29] M. C. D. J. Wilcox, "Calculation of self and mutual impedances for coils on ferromagnetic cores," *Phys. Sci. Meas. Instrum. Manag. Educ. - Rev. IEE Proc. A*, vol. 135, no. 7, pp. 470–476, 1988.
- [30] D. Eggers, S. Steentjes, and K. Hameyer, "Advanced Iron-Loss Estimation for Nonlinear Material Behavior," *IEEE Trans. Magn.*, vol. 48, no. 11, pp. 3021–3024, Nov. 2012.
- [31] J. Richter, A. Dollinger, and M. Doppelbauer, "Iron loss and parameter measurement of permanent magnet synchronous machines," presented at the Electrical Machines (ICEM), 2014 International Conference on, 2014, pp. 1635–1641.
- [32] G. Brocard, *The LTSpice Simulator: Manual, Methods and Applications*. Würth Elektronik, 2013.

- [33] B. Seguin, "Les pertes dans les condensateurs bobinés utilisés en électronique de puissance: mesure calorimétrique et modélisation," Institut National Polytechnique de Grenoble-INPG, 1997.
- [34] F. F. Kuo, *Network analysis and synthesis*, 2nd édition. New York: Wiley, 1966.

Chapter III

Extraction of Parasitic Parameters for Power Printed Circuit Boards

CONTENTS

Table of figures.....	134
Table index.....	134
1 Overview	135
2 The role of Printed Circuit Boards in the integrity of power converters.....	135
3 Parasitic parameters extraction of the PCB with 3D simulations	136
3.1 Purpose of the analysis.....	136
3.2 Parameters extraction	137
3.2.1 Circuit extraction from field solutions	137
3.2.2 Calculation of parameters at a fixed frequency and interpolation	139
3.3 Overview of the power converter supported by a multilayer PCB for this study	139
3.4 PCB modelling and hypotheses	141
3.5 Aluminum support of the PCB	145
4 Parameters extraction and equivalent circuit export	146
4.1 Net system definition and excitations	146
4.2 Solution setup.....	147
4.2.1 Partial capacitance calculations.....	147
4.2.2 AC resistance and inductance and computation frequencies.....	147
4.3 Output Data and Circuit analysis of extracted parameters (SPICE Netlists).....	148
5 Multiport scattering parameters calculation.....	149
5.1 Scattering Matrix analysis.....	149
5.2 Verification of interpolation precision from extracted equivalent circuits	150
6 Comparison and analysis of simulated and experimental data	151
6.1 Experimental setup for data comparison	151
6.2 Transmission and reflection parameters comparison by net	153
7 Conclusions	157
8 References.....	157

TABLE OF FIGURES

Fig III. 1 - Structure of a Power Distribution Network	135
Fig III. 2 - Resulting matrix systems from the extraction of the partial elements and synthesis of an equivalent circuit. System (a): partial resistances and resistive coupling coefficients. System (b): partial inductances and coupling coefficients. System (c) partial capacitances and coupling coefficients.....	137
Fig III. 3 - Two coupled microstrips with bending	138
Fig III. 4 - R, L and C matrixes containing the self-parameters and coupling coefficients	138
Fig III. 5 - Resulting equivalent circuit of the bent microstrip coupling	139
Fig III. 6 - Circuit description of the full bridge structure converter hold by the examined PPCB	140
Fig III. 7 - Power stage of the converter in full bridge configuration	141
Fig III. 8 - Internal structure of the PCB stack up	141
Fig III. 9 - Layout and routing of the PCB layers and description of the routed nets by layer	142
Fig III. 10 - Description of the process of electromagnetic analysis from the design data	143
Fig III. 11 - Modification of the 3D model for mesh size and resources reduction	144
Fig III. 12 - PCB layers final form without the FR4 substrate imported and modified in Q3D modeler	144
Fig III. 13 - Aluminum support with spacers and mounting elements	145
Fig III. 14 - Resulting complete 3D assembly ready for electromagnetic analysis.....	146
Fig III. 15 - Top view of the assembly for net excitations and sinks identification	147
Fig III. 16 - Flow chart of the computation process of Q3D®	148
Fig III. 17 - Equivalent Scattering Matrix of the PCB under analysis	149
Fig III. 18 - LTspice third-party model representing the netlist exported from Q3D and Identification of the connection spots of the Ports in the full bridge circuit	150
Fig III. 19 - Port identification in the PCB	150
Fig III. 20 - Comparison between reflection and transmission parameters for circuits extracted at different frequencies to validate the interpolation	151
Fig III. 21 - Instrumented bare PCB for measurements.....	152
Fig III. 22 - Schematic view of the experimental setup for power measurements.....	152
Fig III. 23 - Reflection and transmission of Bout1 net	154
Fig III. 24 - Reflection and transmission of Bout2 net	154
Fig III. 25 - Reflection and transmission of DCneg net	155
Fig III. 26 - Reflection and transmission of DCpos net	156
Fig III. 27 - Reflection and transmission of LEMph net	156

TABLE INDEX

Table III. 1 - Dimmensions of the elements for the coupled microstrip	138
Table III. 2 - Nets description and excitations.....	146
Table III. 3 - Ports and nets descriptions.....	149

1 OVERVIEW

For long, the development of EMI reduction techniques was primarily focused on modeling the switching behavior of components as MOSFETS and IGBTs as in [1], [2]. But increasing needed performance imposed more comprehensive analysis including interconnects, PCBs, advanced integration and surrounding architecture along with 3D electromagnetic and circuit analysis [3]. Apart from the analysis of EMI sources such as switching components, the architecture and layout of conducting parts connected to the power supply is a fundamental part in understanding the conducted and radiated emissions. Indeed, large conductors account for the majority of EMI and especially RFI issues [4], [5]. As analyzed in chapter I, increasing integration demands are development vectors of power converters architectures and consequently, main factor for EMI.

2 THE ROLE OF PRINTED CIRCUIT BOARDS IN THE INTEGRITY OF POWER CONVERTERS

Printed circuit boards (PCB) are core components of power converters, enabling the compact integration of functions surrounding switching devices. A wide range of architectures of power converters can be found in the industry. They are strongly dependent on parameters such as power density and type of application. But as a general trend, power converter PCBs are large structures with large power and ground planes because of the current handling capabilities needed for power applications. These large conductors tend to induce EMI and RFI issues. For instance, voltage drops on signal conductors can result in common-mode radiation as a result of driving two extended portions of the planes against each other [6]–[9].

Also, large planes in PCBs have been shown to form a dipole-antenna-like shape with their attached cables, while lumped RF sources are created by fast switching components. One part of the antenna is typically an attached cable, the other part of the antenna being a conducting enclosure or large PCB planes [9], [10].

For conducted EMI, voltage drops across large structures are also an issue for EMI. Switching noise and Simultaneous Switching Noise (SSN) in Power Distribution Networks (PDN), have been thoroughly analyzed for high speed applications[11]–[14]. PDNs are coplanar power bus PCB structures carrying the power from the Voltage Regulator Module (VRM) to the integrated circuits' (ICs) power pads. A PDN includes the VRM, ICs, decoupling capacitors and vias as schematized in Fig III. . Power and return current planes are large and often cover the whole PCB surface.

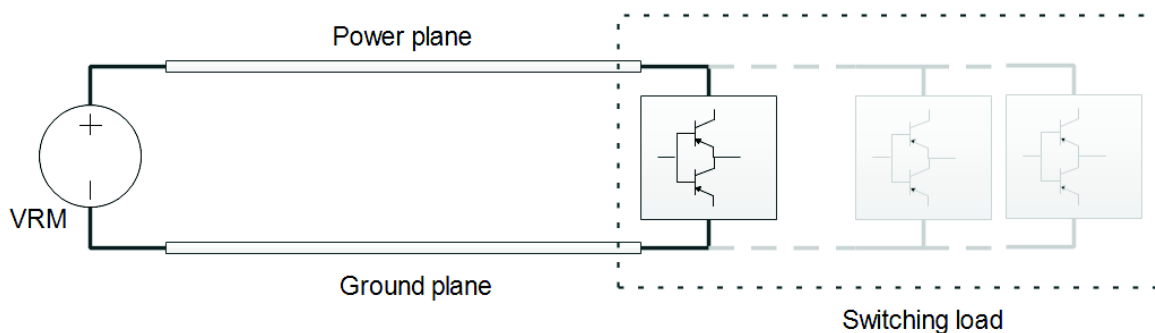


Fig III. 1 - Structure of a Power Distribution Network

As loads switch, interconnects' and board planes' impedance changes. This effect leads to increased voltage variations across the power and return planes. Finally, these voltage disturbances are source for SSN. In the case of digital circuitry, this problem is accentuated by the low threshold logic voltage levels [11].

For power applications, the problem can be transposed to signal integrity issues in the close control environment of the power switching devices, current and temperature measurements, or protection circuitry.

To model the behavior of PDNs under SSN, authors in [11] use Finite Difference Frequency Domain (FDFD) simulations including lumped elements. They specifically analyze the impact of decoupling capacitors on power integrity of PDNs. Then, in [12] authors model multilayer PDNs with segmentation techniques as well as resonant cavities theory [15]. The impact of vias is accurately modelled and the authors draw design implications of decoupling arrangements and board architecture. Finally, in [13], [14], authors analyze the impact of vias in power integrity of multilayered PDNs.

Common-mode coupling in PCB layers has also been analyzed [16]. Other studies examined the impact of interconnection of PCB ground planes to chassis to minimize radiated emissions through common-mode [17].

Finally, in [18], a rational analysis flowchart for multilayered power PCBs is addressed based on the coupling strength of the different conductors in a power PCB. For isolated strips, Transmission Line Method (TLM) or Thin Wire Method (TWM) can be used, whereas for strongly coupled strips, extraction of parameters through electromagnetic simulation methods as Partial Element Equivalent Circuit (PEEC) or Method of Moments (MoM) can be used.

In this chapter, the purpose is to investigate the response of large plane structures in complex multilayered PCBs of state-of-the-art power switched converters. The aim is to analyze the response and couplings of power buses and other signal planes in a rational and generic approach in order to integrate them into a larger scale circuit analysis.

The afore-described methods of analysis commonly used for PDNs and other multilayered PCBs are helpful in drawing design implications. However, for EMC/EMI verification and validation from a design point of view, more complete simulation methods can help to improve both power and signal integrity as well as EMI and RFI. For this matter, a more integral extraction and simulation process is used. Besides, the following described technique allows for including conductive structures surrounding the PCB which is helpful in predicting CM and DM coupling paths and taking into account parasitic inductive and capacitive coupling mechanisms from the PCB layers to conducting surrounding parts.

3 PARASITIC PARAMETERS EXTRACTION OF THE PCB WITH 3D SIMULATIONS

3.1 PURPOSE OF THE ANALYSIS

The aim of this study is to extract an equivalent circuit model of a multilayered PCB utilized in mechatronic applications. The circuit model should be valid both in time and frequency domain. For the latter, the frequency span sought in this analysis, is DC to 300 MHz.

The purpose of this model synthesis is to include it, as for the machine model, into a more global simulation including all the manufactured circuit models.

3.2 PARAMETERS EXTRACTION

3.2.1 Circuit extraction from field solutions

Ansoft's Q3D[®] is an electromagnetic computation software based on a hybrid Method of Moments (MoM) and Finite Element Method (FEM) analysis algorithms. Q3D[®] is a fixed frequency complete multi-material field analysis software taking into account geometrical and electrical layout of a structure. The electromagnetic field solutions of a given problem are interpreted in terms of current distribution or surface charge and, particularly, in terms of partial circuit elements [19], [20].

For a given problem, a set of conductors is defined as a system of nets. Each net is assigned with an input and output surface for the excitation current (harmonic). For a system of conductors, the unknown quantities then are the current density J in conductors and density of charges q on the surface of such conductors. In order to solve the system of equations derived from the given problem, current densities are discretized into volume cells, giving the overall current flow for each one of net volumes, in the three dimensional directions. As for the density of charges, they are defined on the conductor surface. Then, field solutions of the problem are thus interpreted in terms of capacitive, inductive and resistive voltage drops as $0 = v_R + v_C + v_L$, and thus, as circuit impedance partial elements.

Capacitance (C), Inductance (L) and Resistance (R) matrixes are then determined for a given system of nets as illustrated in Fig III. 2. For a system of nets forming a K –port network, these matrixes represent the main and parasitic coupling parameters within and between conductors of a multi-material problem. Each net is attributed with an input and output surface. Partial element matrixes can then be exported in a Spice netlist. The Netlist is imported into a circuit simulator as a sub circuit whose ports are functional conductors (nets) defined in the 3D model and connected to a complete circuit for larger circuit analysis [19].

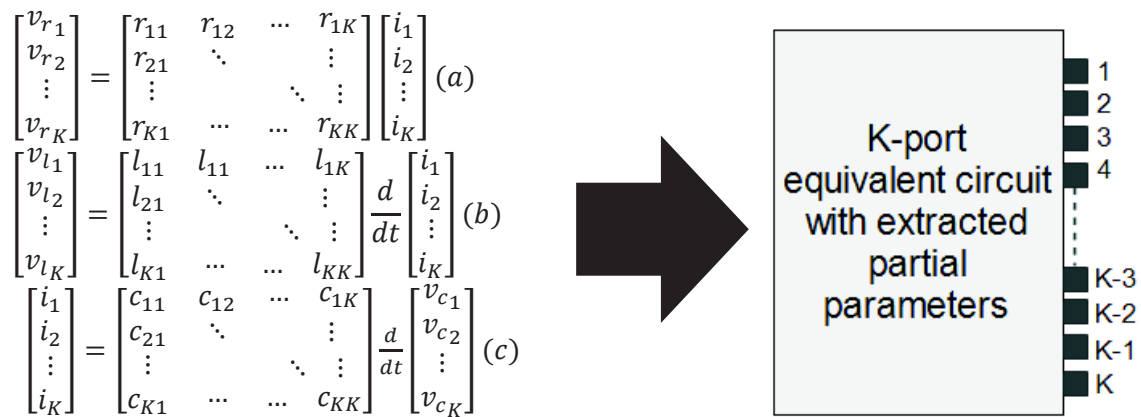


Fig III. 2 - Resulting matrix systems from the extraction of the partial elements and synthesis of an equivalent circuit. System (a): partial resistances and resistive coupling coefficients. System (b): partial inductances and coupling coefficients. System (c) partial capacitances and coupling coefficients

In order to illustrate the extraction process, let us take an example of two conductors. The example dealt with is a straight-to-bent microstrip line coupling analyzed in [21]. The two conductors over a ground plane form four ports as shown in Fig III. 3.

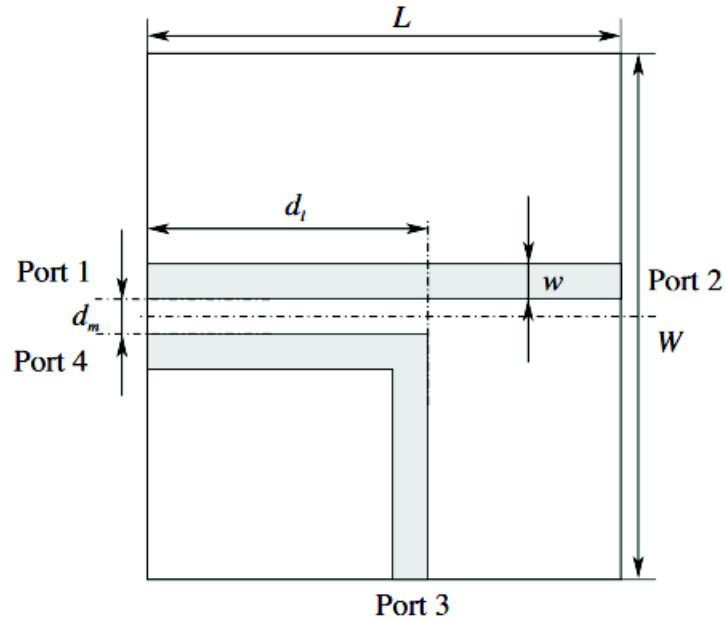


Fig III. 3 - Two coupled microstrips with bending

Description of the dimensions of the coupled microstrips is given in Table III. 1.

Table III. 1 - Dimensions of the elements for the coupled microstrip

Parameter	Description
L	Board length
W	Board width
h	Dielectric thickness
w	Strip width
t	Strip thickness
d_m	Separation between strips
d_l	Parallel section length

Three conductors are present in the problem: the two strips and the ground lane. Each strip forms a two-port network. The authors in [21] analytically synthesized the values of the parameters in the equivalent circuit. Strip 1 is named net 1, strip 2 is named net 2 and ground is named net 0. Dielectrics are considered to be perfect and resistive couplings between separate conductors neglected. Self-capacitances of the same conductors are also neglected. Thus, the 3 by 3 equivalent matrixes containing the circuit parameters shown above, are presented in Fig III. 4.

$$R_{problem} = \begin{bmatrix} R_1 & 0 & 0 \\ 0 & R_2 & 0 \\ 0 & 0 & R_0 \end{bmatrix}$$

$$L_{problem} = \begin{bmatrix} L_1 & L_{12} & L_{10} \\ L_{21} & L_2 & L_{20} \\ L_{01} & L_{02} & L_0 \end{bmatrix}$$

$$C_{problem} = \begin{bmatrix} 0 & C_0 & C_1 + C_2 \\ C_0 & 0 & C_3 + C_4 \\ C_1 + C_2 & C_3 + C_4 & 0 \end{bmatrix}$$

Fig III. 4 - R, L and C matrixes containing the self-parameters and coupling coefficients

Consequently, the equivalent circuit of the presented problem is shown in Fig III. 5.

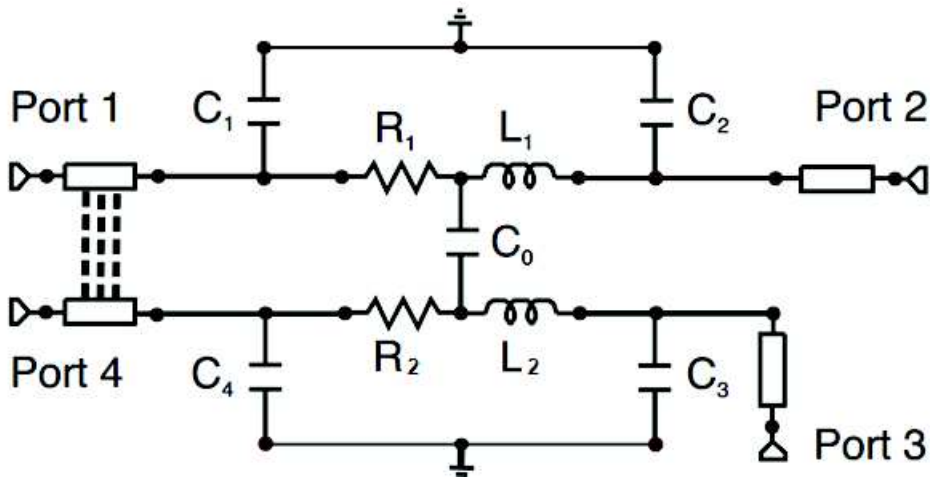


Fig III. 5 - Resulting equivalent circuit of the bent microstrip coupling

Instead of an analytical calculation of the circuit parameters, Ansoft Q3D® allows to compute the electromagnetic field solutions of the problem and directly interpret them in terms of circuit parameters in the form of matrixes.

3.2.2 Calculation of parameters at a fixed frequency and interpolation

It is essential to keep in mind that the calculation process of the field solutions of AC parameters is done at a specific frequency. This means that the solutions are only valid for a given frequency range. Interpolation for skin effect is nonetheless taken into account when exporting the circuit through non-linear current controlled sources, allowing the exported circuit to be representative over a wide range of frequencies.

However, calculation of AC parameters of a structure at a frequency $f_1 \neq f_0$ where f_0 is the frequency of a particular event such as skin effect occurrence in a cylindrical conductor, might induce divergence in the accuracy of predicting such an event. An agreement between frequency range and accuracy in predicting events has to be determined in order for the interpolation to be valid.

Moreover, a significant drawback of this method, is the increased memory requirements typical of method of moments techniques. Although MoM methods can accurately simulate power/ground plane structures, they are not suitable for fast simulation time nor for complex structures requirements [11].

3.3 Overview of the power converter supported by a multilayer PCB for this study

The converter used for the analysis in this part has been designed by Novatem to feed a single winding of a 20 kW fault-tolerant electric vehicle (EV) motor-generator. The multi-phase motor is designed to tolerate a partial loss of the winding structure. Since each winding is fed by an independent converter, the loss of a converter is also tolerated. More details on the EV drivetrain are given in chapter IV.

The power converter is composed of a 6-layer Power PCB (PPCB), a Microsemi SP1 Module in 4-IGBT Full-Bridge configuration (1 phase), an input capacitance stage and the close control elements (driver, diodes, decoupling capacitors, and rise/fall times resistors). In Fig III. 6 is schematized the electric architecture of the converter. The circuit diagram is divided in four main parts.

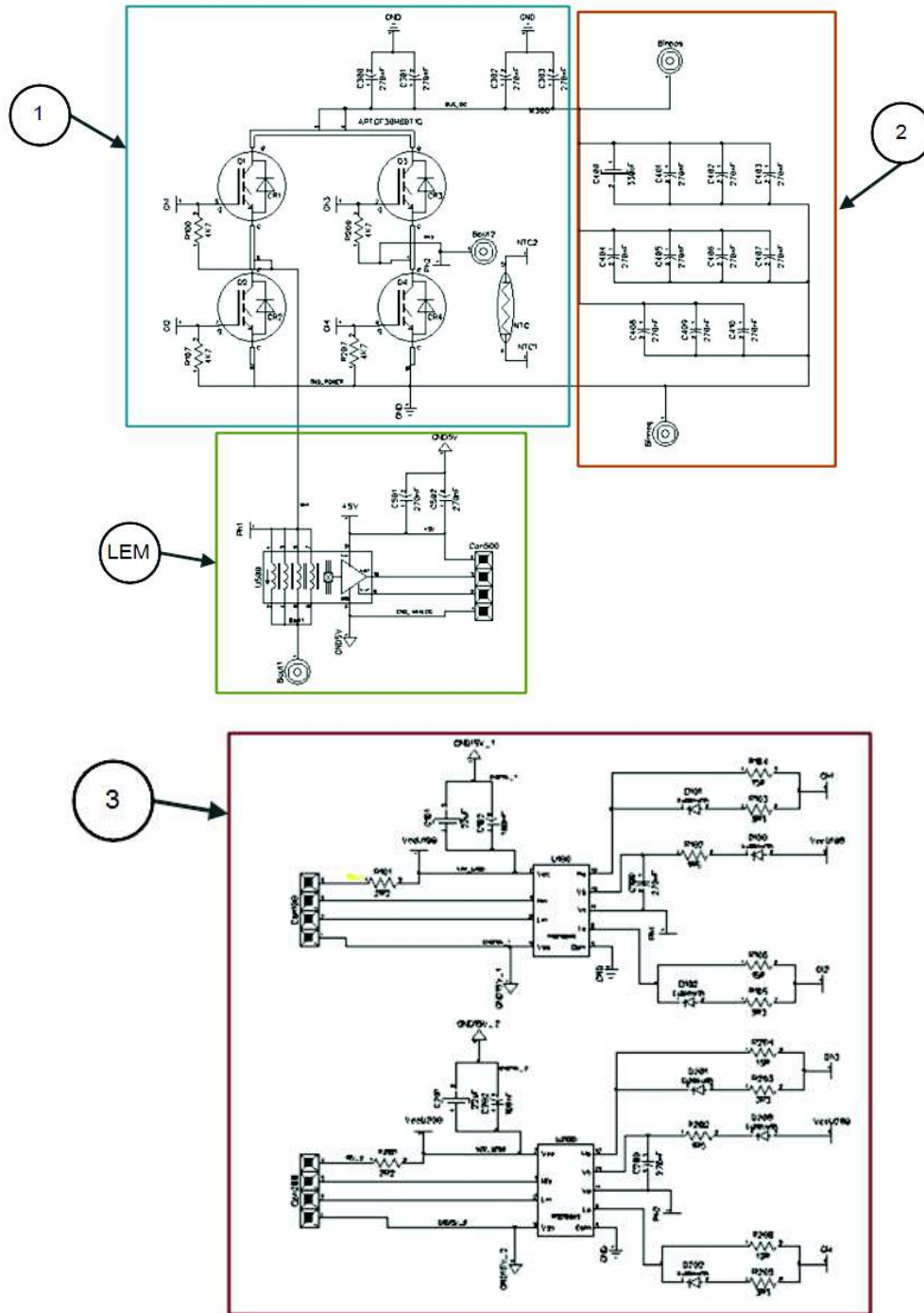


Fig III. 6 - Circuit description of the full bridge structure converter hold by the examined PPCB

- The high power stage including the full-bridge (1)
It is composed of one APTGF50H60T1G 1200V/60A from Microsemi® SP1 module with four IGBTs (numbered 1) in full-bridge configuration in a structure of a single-phase inverter, feeding each winding with alternate square-shaped currents. In Fig III. 7 is detailed the full bridge structure.

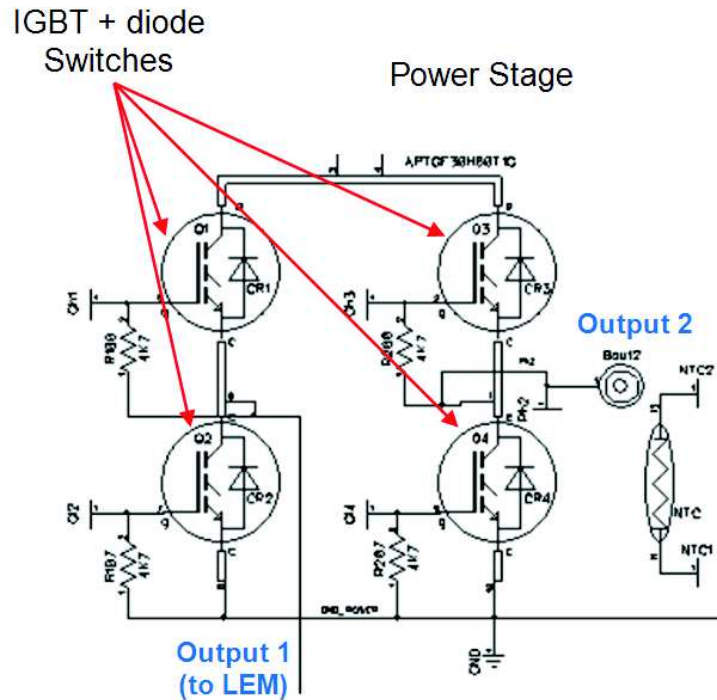


Fig III. 7 - Power stage of the converter in full bridge configuration

- The input capacitor stage (2)
- The phase (winding) current measurement probe (LEM)
- The drivers' stage (3)

This stage includes:

- Two gate driver circuits (high and low) for the four gates
- The Bootstrap circuits for the control of the upper side switches
- Gate rise/fall time circuits

3.4 PCB MODELLING AND HYPOTHESES

The stack up of 6 layers of the PCB is illustrated in Fig III. 8. The stack up is a standard WURTH ELEKTRONIK© 6-layer copper and FR4 epoxy board and the board dimensions are 125 mm long and 45 mm wide.

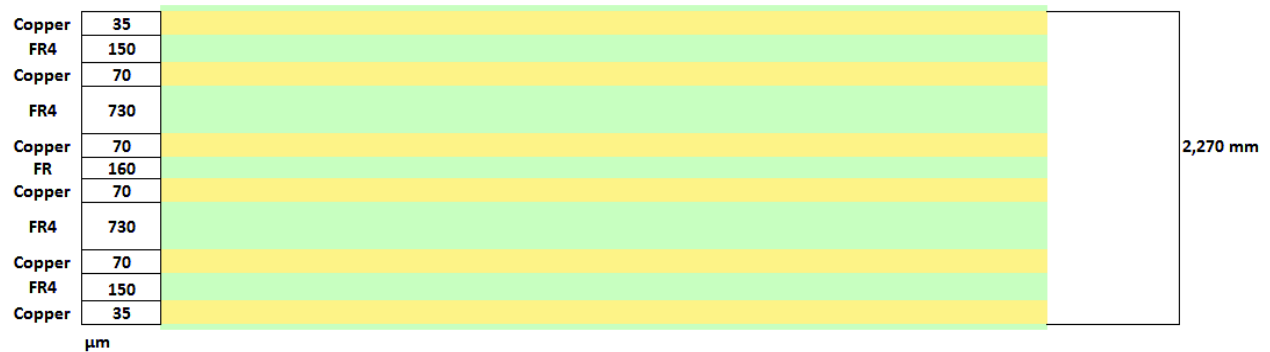


Fig III. 8 - Internal structure of the PCB stack up

For analysis of the specificity of the layout patterns, the layout of each layer is shown in Fig III. 9.

Note that very few traces are used for the routing. Most of the routing is done with large copper poured sections and planes.

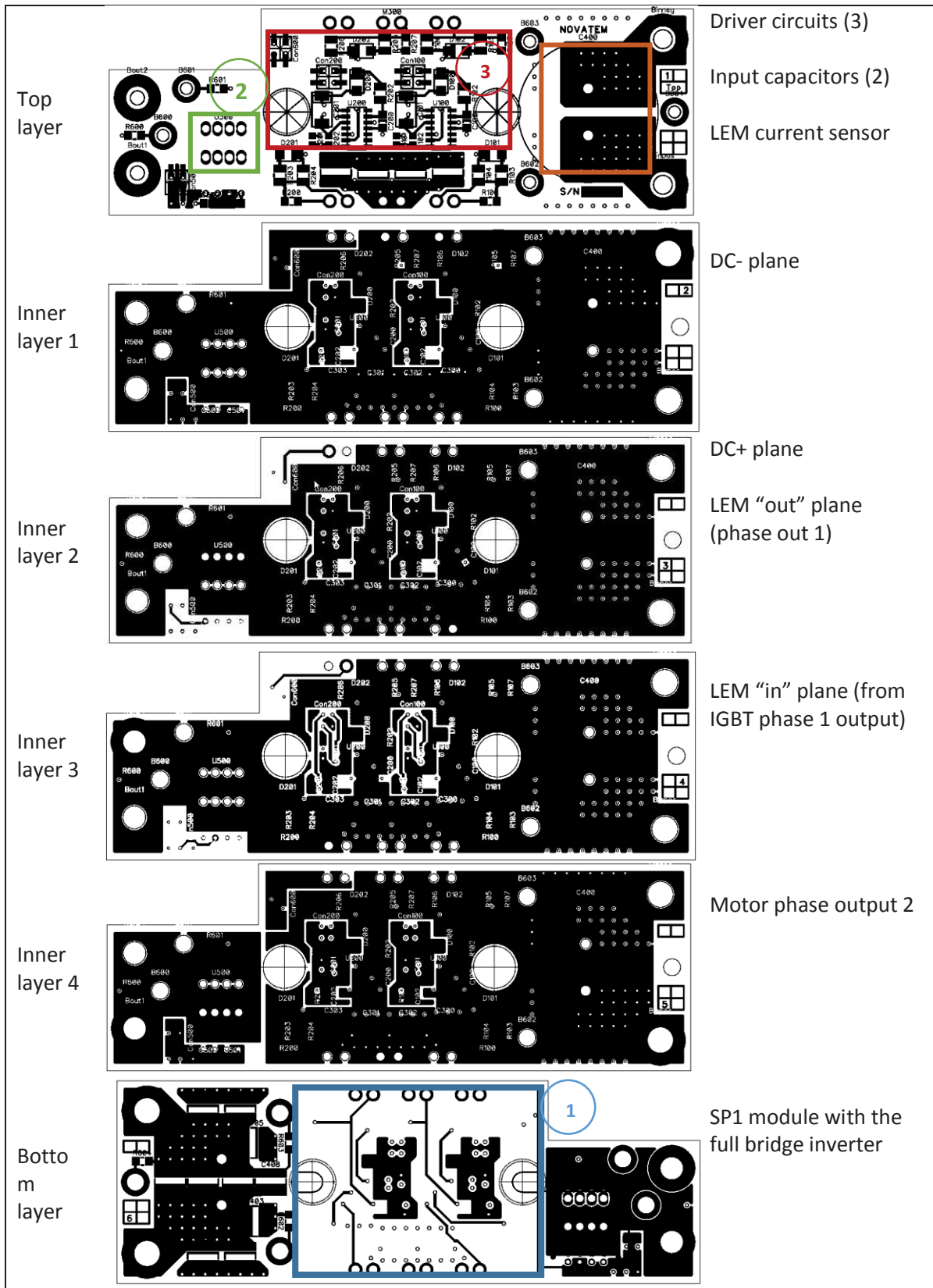


Fig III. 9 - Layout and routing of the PCB layers and description of the routed nets by layer

The basis of the method is to extract the layout information and to incorporate it into 3D geometries for electromagnetic analysis.

The extraction process is schematized in Fig III. 10. Once the routing process, named layout design, is done, an extraction of the layout is performed using an ODB+ format. Then, the ODB+ file is converted to STEP format in order it to be imported into a 3D modeler for further modifications.

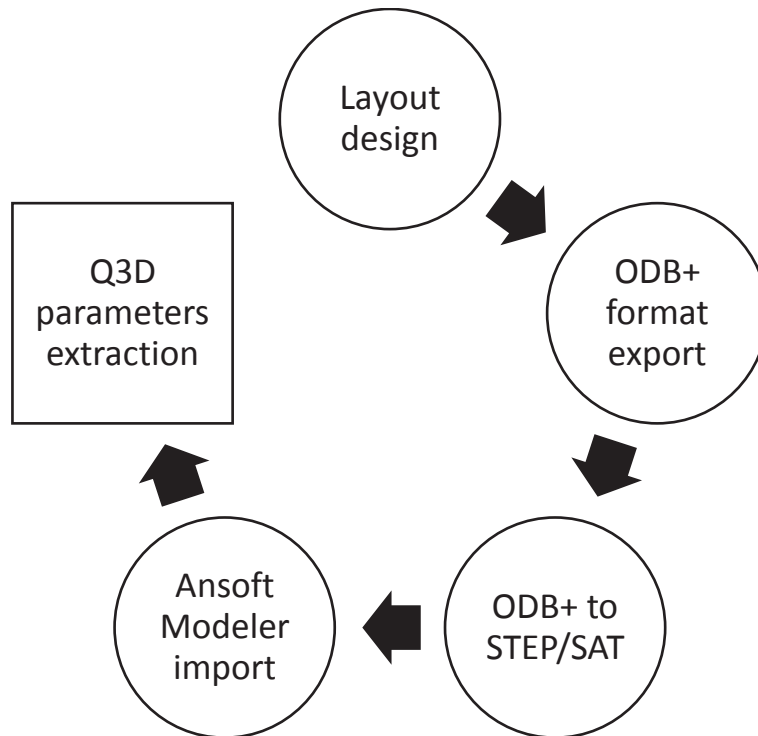


Fig III. 10 - Description of the process of electromagnetic analysis from the design data

This process allows to be extremely efficient when importing the 3D model of the desired structure. The most difficult part is the routing process done by the PCB designers. Once a preliminary layout is achieved, the exporting process to Q3D can be done in over a few minutes.

As can be seen in the Fig III. 11, few strip traces are present. These traces intervene in gate signal routing and signals from measurement of temperature and current. They are concentrated in the top and bottom layers and their electrical length are small compared to the highest frequency wavelength of 300 MHz. A significant hypothesis is then adopted: only the large planes are considered to be involved in large parasitic couplings both in differential and common-mode mechanisms. This means, that only large planes are kept for this analysis.

A direct consequence of this hypothesis is that small traces are therefore ignored in the parasitic parameters extraction. Traces are erased from the 3D model and the remaining free space was not replaced, leaving an empty space. Cross-talk between planes and pairs of traces is thus neglected, as well as potential couplings between traces carrying high speed signals from the drivers to surrounding metallic pieces potentially creating common-mode noise. Nevertheless, the functional modelling of such traces has been included in the next chapter.

Furthermore, through-hole vias across planes, were for most of them, replaced with solid cylinders of equivalent external surface as the number of vias they replace. For example, let us take the input

vias on the DC negative input net linking the top and bottom pads to an inner plane as shown in Fig III. 11.

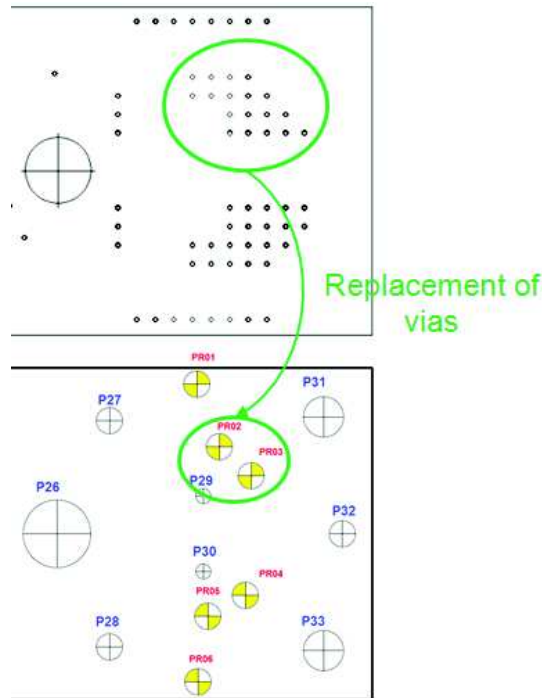


Fig III. 11 - Modification of the 3D model for mesh size and resources reduction

At 300 MHz, the skin depth in copper is around 5 μm . Therefore, instead of reasoning in terms of volume, an equivalent surface current must be kept and since the depth of the stack up is constant, this is transformed into an equivalent perimeter. The external perimeter of a via is 0.5 mm, thus for the total 18 vias shown in the above figure highlighted in green, the cumulated perimeter is 9 mm. Two cylinders of equivalent perimeter were therefore used to replace the 18 vias. This process allows a more simple meshing process and the computation times drastically reduced. A similar process was performed in [22] to replace wire bondings for spherical bumps or cylinders and cubes. The resulting modelled layers without the FR4 substrate is shown in Fig III. 12. With these modifications done, 5 conductors (nets) can be identified for the PCB itself.

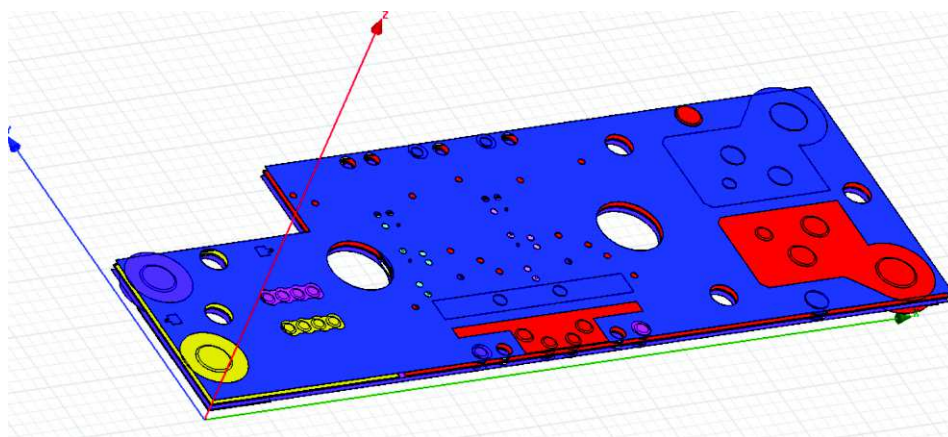


Fig III. 12 - PCB layers final form without the FR4 substrate imported and modified in Q3D modeler

3.5 ALUMINUM SUPPORT OF THE PCB

Since IGBTs need to be cooled, the PCB needs to be in contact with an aluminum support serving as heatsink as depicted in Fig III. 13. This aluminum support has two main purposes: mechanical support of the PCB and heatsink for IGBTs cooling.

As stated before, the main common-mode couplings in power applications are generated from functional traces to nearby metallic components through parasitic couplings. By including the model of the aluminum support to the parameters extraction, these parasitic couplings to the grounded support can be accounted for.

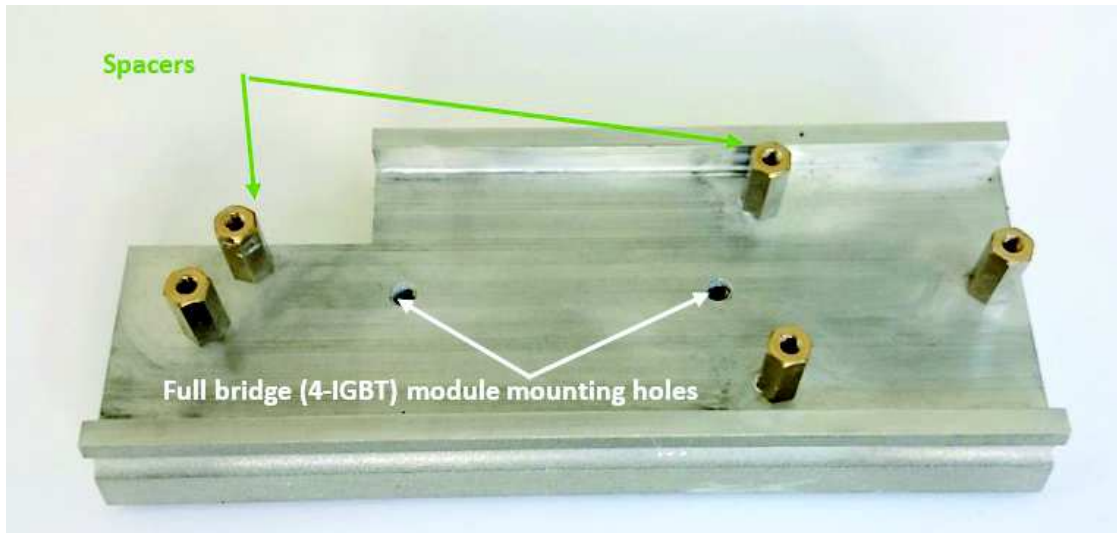


Fig III. 13 - Aluminum support with spacers and mounting elements

The aluminum support is considered as a sixth net (cf. Table III. 2). However, since it is a grounded conductor, the calculation of electromagnetic fields will also be done considering a grounded net for the aluminum support. This implies that no equivalent circuit of the metal piece is extracted, but only the capacitive couplings between the support and its spacers (including the fixation screws) and the planes of the PCB. This is particularly interesting for capacitive coupling paths to common-mode analysis as will be shown later.

The resulting modelled assembly is described in Fig III. 14.

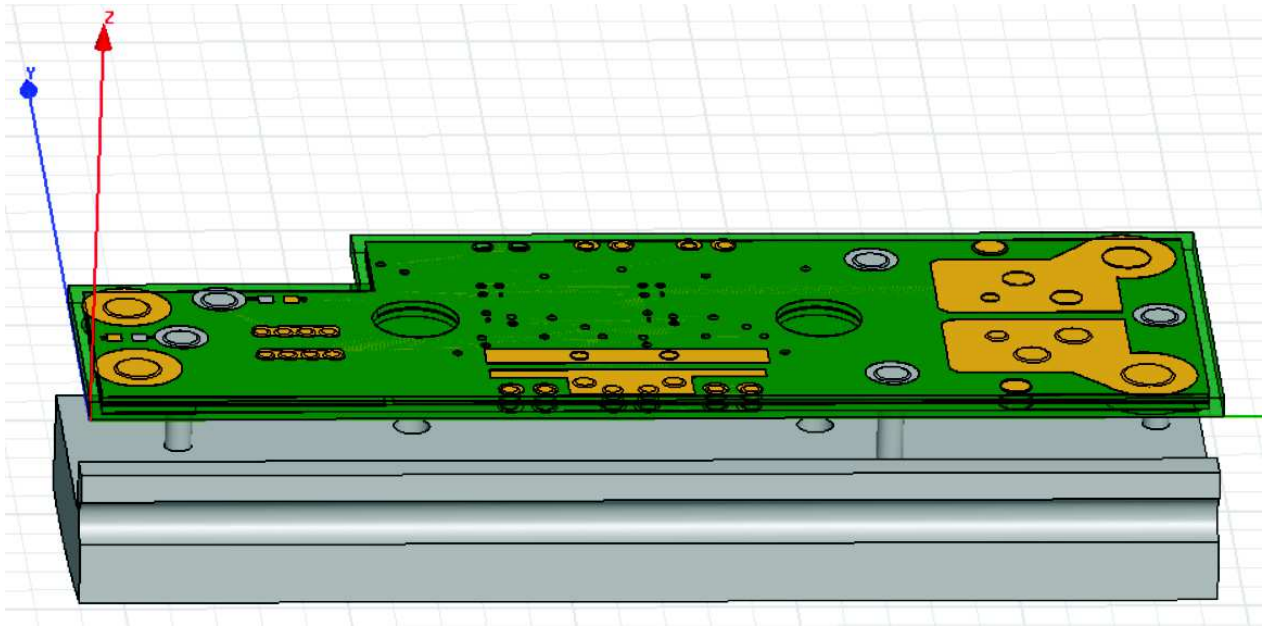


Fig III. 14 - Resulting complete 3D assembly ready for electromagnetic analysis

4 PARAMETERS EXTRACTION AND EQUIVALENT CIRCUIT EXPORT

4.1 NET SYSTEM DEFINITION AND EXCITATIONS

Once the geometry is dealt with, the excitation ports have to be integrated into the model. The excitation ports for the 5 nets (the aluminum support is a grounded net) are described hereafter. Indeed, each conductor (net) needs a source (I-x) and a sink (O-x) to allow the current to flow through as described in Table III. 2 and Fig III. 15. These sinks and sources are defined as excitation ports.

Table III. 2 - Nets description and excitations

Net	Description	Color	Excitation	
DC_Pos	High DC input	Red	I-a	O-a
DC_Neg	Low DC input	Blue	I-b	O-b
Bout1	Phase out 1	Yellow	I-c	O-c
Bout2	Phase out 2	Purple	I-d	O-d
LEM_Ph	Phase 1 IGBT to LEM	Pink	I-e	O-e
Support	Aluminium base	Gray (not displayed)	Grounded	

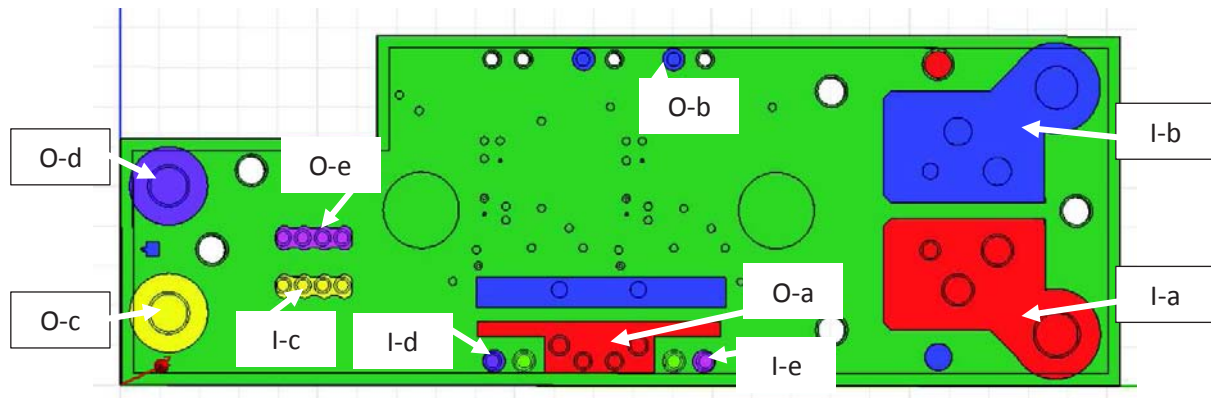


Fig III. 15 - Top view of the assembly for net excitations and sinks identification

With this setup, the resulting exported spice circuit is composed of 5 nets forming 10 ports; grounded nets are not accessible.

Once the Nets and Excitations are determined, the solution setup may be defined.

4.2 SOLUTION SETUP

4.2.1 Partial capacitance calculations

Partial capacitances between nets as well as a self-capacitance for each net are calculated. The numerical computation specifications for the extraction are the default parameters:

- The threshold of capacitance error between two mesh refinement passes inducing the stop of the computation : 1 %
- The mesh refinement ratio between passes : 30 %
- The maximum number of passes : 10

4.2.2 AC resistance and inductance and computation frequencies

For AC resistance and inductance calculations, a fixed frequency has to be specified. It is at this frequency that the partial parameters will be calculated taking into account frequency dependent phenomena such as proximity and skin effect. This can have an impact in the validity of solutions since a conductor carrying a current containing high and low frequency harmonics will appear to be equally resistive for either switching harmonics. But interpolation performed by Q3D[®] can overcome this problem as will be analyzed later.

Since a very wide frequency band has been defined for the extraction, three cases will be compared:

- Low frequency extraction at 100 Hz
- Medium frequency extraction at 30 MHz
- High frequency extraction at 150 MHz

The aforementioned cases are meant to verify that the interpolation taken into account in the three different exported circuits are consistent over the whole frequency span.

And for each one of these cases, the solution setup is kept as follows:

- The threshold of resistance error between two mesh refinement passes inducing the stop of the computation : 5 % (due to limited memory resources)
- The mesh refinement ratio between passes : 30 %

- The maximum number of passes : 10

The results of the different frequency setups will be discussed in §III.6. The algorithm of general solution is described in Fig III. 16.

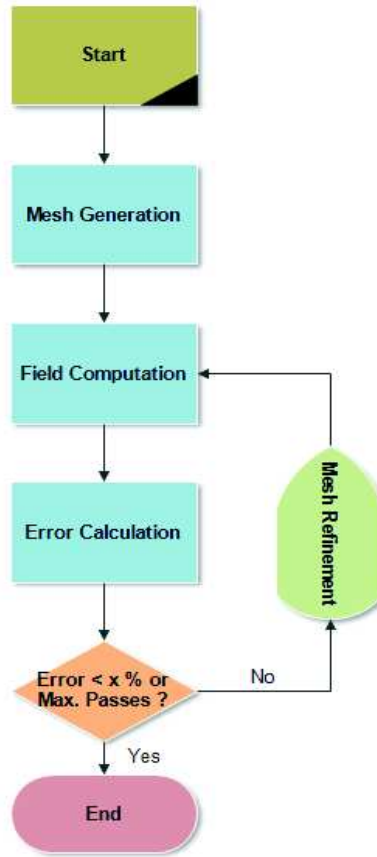


Fig III. 16 - Flow chart of the computation process of Q3D®

4.3 OUTPUT DATA AND CIRCUIT ANALYSIS OF EXTRACTED PARAMETERS (SPICE NETLISTS)

As stated before, the desired data are equivalent circuits containing the partial elements of the structure. Q3D® offers the capabilities of directly exporting the matrixes and coupling coefficients as a Spice Netlist. Equivalent circuits are therefore exported.

The circuit is then imported into LT Spice® [23] (cf. Chapter II for machine modelling) for circuit analysis in time and frequency domain.

When exporting the circuit, depending on the frequency range sought, a number of “cells” can be defined to improve propagation behavior. The number of cells, as for a transmission line model, takes into account the phase shift of a wave traveling in an electrically long transmission line. An elementary cell describes the behavior of the transmission line in a circuit model, and series connection of elementary cells describes also the propagation effects [4].

Propagation velocity in FR4 material is inferior to vacuum propagation velocity. Assuming an average propagation velocity of $v_{FR4} = 1.8 \times 10^8 m/s$ in the material, the wavelength at $f = 300 MHz$ is given by

$$\lambda = \frac{v_{FR4}}{f} = 0.6 m$$

From Fig. III.8 it can be seen that the largest dimension of the PCB is 0.125 m, i.e. nearly 5 times smaller than the smallest wavelength. Since propagation effects start to be noticeable at around dimensions 4 to 5 times smaller than the wavelength, only one cell is exported.

5 MULTIPOINT SCATTERING PARAMETERS CALCULATION

5.1 SCATTERING MATRIX ANALYSIS

Impedance simulation is a useful way to analyze the extracted circuit and to compare it to measured data. Because of the large frequency range of analysis and the elevated number of ports, scattering parameters (S-parameters) are used. Scattering parameters can easily be measured using a Vector Network Analyzer (VNA).

Although a direct equivalence from scattering parameters to impedance exists [15], the comparison of simulated data to readily measured S-parameters is straightforward.

Fig III. 17 shows the scattering matrix relevant to the 10-port network extracted from the PCB.

$$S_{PCB} = \begin{bmatrix} S_{11} & S_{12} & & \cdot & \cdot & \cdot & & & & S_{19} & S_{110} \\ S_{21} & S_{22} & & & & & & & & & S_{210} \\ & & S_{33} & & & & & & & & \\ \cdot & & & S_{44} & & & & & & \cdot & \\ \cdot & & & & S_{55} & & & & & \cdot & \\ \cdot & & & & & S_{66} & & & & \cdot & \\ & & & & & & S_{77} & & & & \\ & & & & & & & S_{88} & & & \\ S_{91} & & & & & & & & S_{99} & S_{910} \\ S_{101} & S_{102} & & \cdot & \cdot & \cdot & & & S_{109} & S_{1010} \end{bmatrix}$$

Fig III. 17 - Equivalent Scattering Matrix of the PCB under analysis

The 10-port system formed by the 5 nets' input/output ports referred to the ground, are calculated from the extracted equivalent circuit containing the partial elements. Then, the simulated data is compared to S-parameters measured data. The ports description and 10-port S-parameters matrix is presented in Table III. 3 and Fig III. 18.

Table III. 3 - Ports and nets descriptions

Port n°	Port name	Net name
1	Ph1_LEM_out	Bout1
2	Ph1_Bout1	
3	Ph2_IGBT	Bout2
4	Ph2_Bout2	
5	DC_neg_IN	DC_neg
6	DC_neg_IGBT	
7	DC_pos_IN	DC_pos
8	DC_pos_IGBT	
9	Ph1_IGBT	LEM_Phase
10	Ph1_LEM_in	

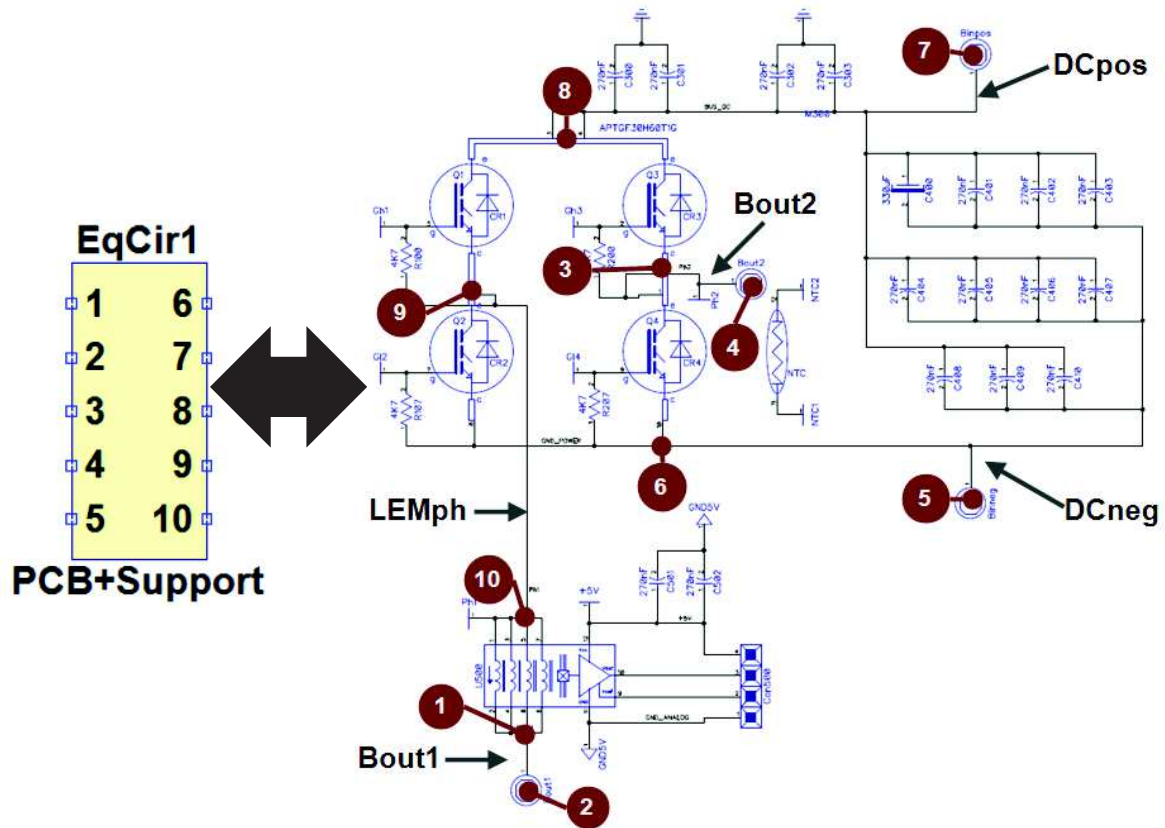


Fig III. 18 - LTspice third-party model representing the netlist exported from Q3D and Identification of the connection spots of the Ports in the full bridge circuit

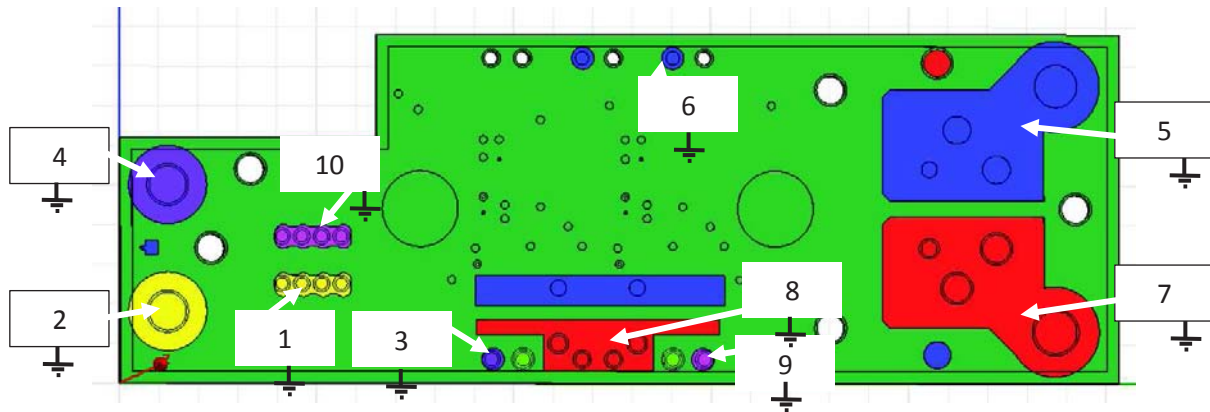


Fig III. 19 - Port identification in the PCB

5.2 VERIFICATION OF INTERPOLATION PRECISION FROM EXTRACTED EQUIVALENT CIRCUITS

As explained in §3.4 and §4.2.2 AC parameters are extracted at three different frequencies (i.e. 100 Hz, 30 MHz and 150 MHz) in order to verify that the interpolation of behaviors of frequency dependent parameters is properly handled by the exported circuit. Fig III. 19 shows the plotted data of reflection and transmission parameters for the models extracted at different frequencies. No difference at all is spotted between reflection parameters for different frequencies. The same conclusion is drawn for transmission parameters. This is the case for every other ports in the system.

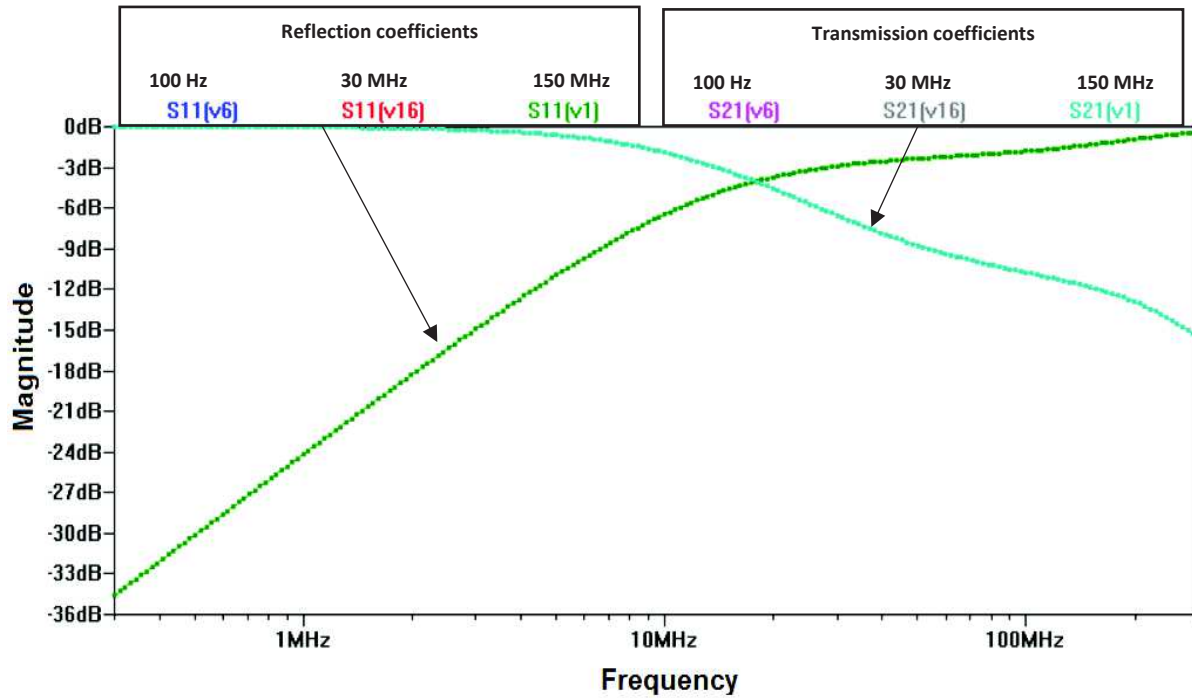


Fig III. 20 - Comparison between reflection and transmission parameters for circuits extracted at different frequencies to validate the interpolation

There is no difference at all for the different equivalent circuits exported from extracted parameters at different frequencies. The interpolation is correctly handled in the circuit. It seems that, although the interpolation is correctly handled for DC-300 MHz it doesn't mean that the same circuits would behave in the same manner at much higher frequencies. Anyhow, for the purposes of our modelling, the extraction at any frequency between the selected three would bring the same results.

6 COMPARISON AND ANALYSIS OF SIMULATED AND EXPERIMENTAL DATA

The extracted R-L-C-G parameters by numerical computation are directly integrated into a Netlist and exported by Q3D®. The 10-port netlist representing the PCB is then imported into the circuit simulator for Scattering Parameters (S-parameters) simulation and analysis. Simulated S-parameters are compared to measured data. The experimental 10-port S-parameters matrix is completed with several measurements done with the E6051B Vector Network Analyzer [24] from 300 kHz to 300 MHz.

6.1 EXPERIMENTAL SETUP FOR DATA COMPARISON

For the experimental measurement of the response of the PCB in the frequency domain, the PCB has been fitted with HF connectors allowing to create accessible ports between the excitation points of the conductors and the ground. In Fig III. 21 is pictured the PCB with attached SMA (Sub-Miniature type A) connectors at the locations of simulated excitation ports. The experimental setup is schematized in Fig III. 22.

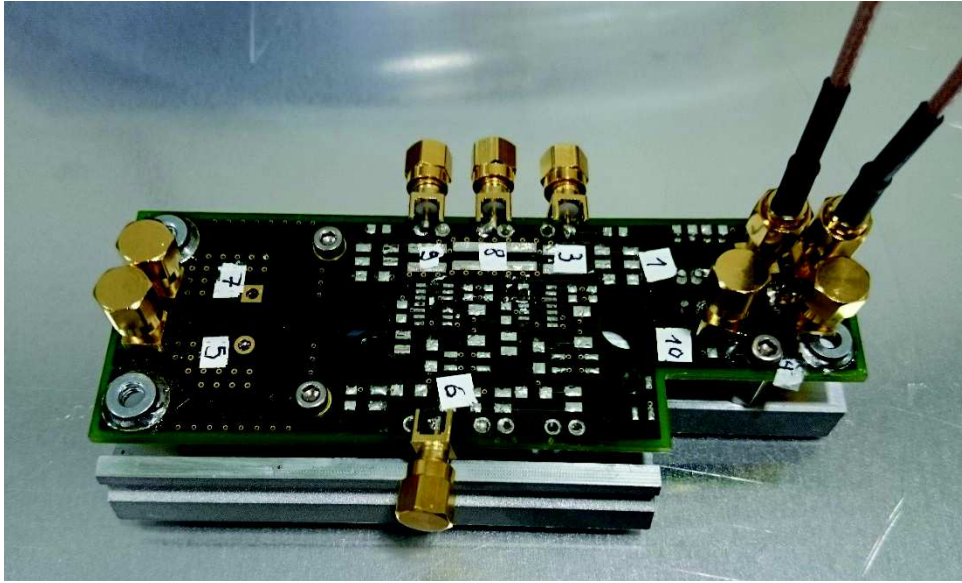


Fig III. 21 - Instrumented bare PCB for measurements

The SMA connectors, terminations and cables were chosen because they allow to minimize the insertion effects of the measuring fixtures over more than the needed frequency span used in the measurements. The connections to ground are close to the center conductor, therefore minimizing parasitic loops.

As seen in §I.5.2.2, a total number of 100 parameter measurements would be needed to fill the 10-port matrix. Indeed, in general, the number of measurements needed to fill a 10-port linear, passive and reciprocal matrix with a VNA capable of measuring forward and reverse parameters in one measurement is given by (n being the number of ports) [25]:

$$N_{meas} = \frac{n(n-1)}{2} = \frac{10(10-1)}{2} = 45$$

Although a total of 45 measurement have to be performed, the measurement process takes less than one hour to complete with modern VNAs.

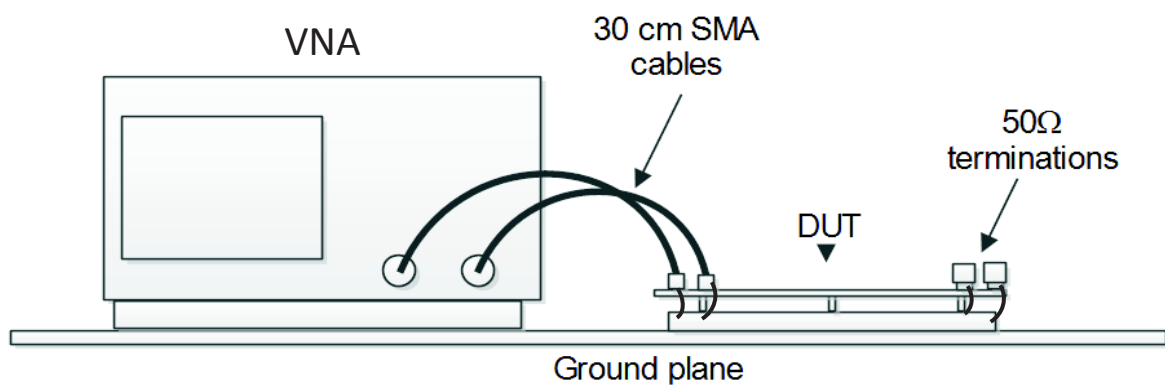


Fig III. 22 - Schematic view of the experimental setup for power measurements

The 50 ohm terminations allow for the S parameters to be measured in a constant normalized impedance environment thus easing the direct construction of the matrix without mathematical transformations.

All nets are considered to be single-ended lines, since it is assumed that no pair of lines are strongly coupled. This means that even for the power input (DCpos) and output (DCneg) pair, single-ended considerations are adopted.

6.2 TRANSMISSION AND REFLECTION PARAMETERS COMPARISON BY NET

Resulting differences between simulated and measured data have been taken from 300 kHz up to 300 MHz. The reason to start at 300 kHz is that protection equipment used for the VNA has an operational bandwidth from 300 kHz up to 3 GHz. Nevertheless, for transmission parameters, little to no effects of parasitic couplings are observed at low frequencies as can be seen in Fig III. 23 to Fig III. 27. In fact, a 0 dB magnitude is steadily observed from lower frequencies inferior to 2 MHz. For reflection coefficients, a steady increase in magnitude is also observed from low frequencies and for some, the noise floor is almost reached even at 300 kHz.

Globally, resulting predictions are within 5 dB for most of the spectra but several zones, especially for frequencies superior to 200 MHz present an increasing error of about 10 dB.

In this comparative study, discrepancies are thoroughly analyzed. The first plotted data corresponds to transmission and reflection parameters for each one of the planes under test. Other S parameters are also analyzed afterwards. Since the nets are weakly coupled, only transmission and reflection parameters by net are compared. In fact, weakly coupled nets present a high return loss and very low (close to the noise floor) transmission.

Since the PCB is a symmetrical, passive and reciprocal network, input and output insertion loss coefficients as well as reflection coefficients are the same, therefore $S_{ij} = S_{ji}$ and $S_{ii} = S_{jj}$ [15]. Only one insertion loss coefficient and one return loss coefficient are included in the plotted data.

In Fig III. 23 can be observed that the largest error between simulated and measured data is found below 4 MHz for the reflection parameters for Bout1 net. A maximum of 12.6 dB difference is found at these frequencies.

For the transmission coefficients, error is lower throughout the full frequency range with a maximum error of 8 dB at 300 MHz.

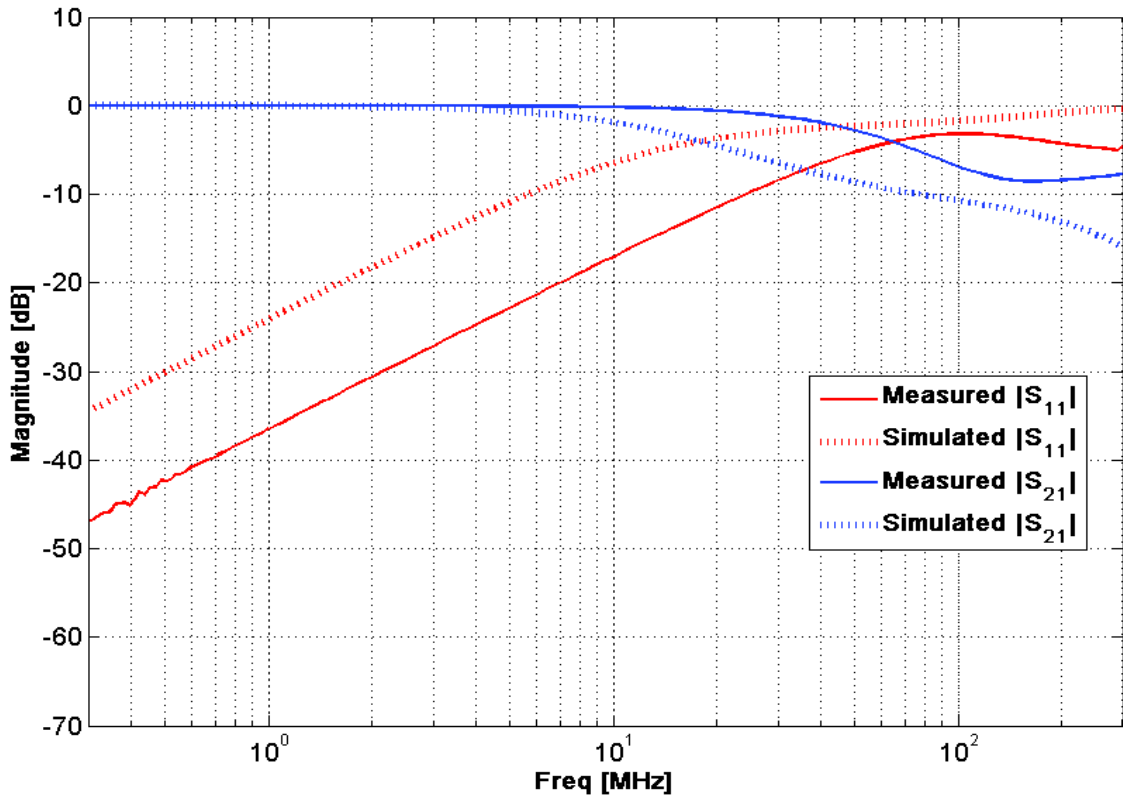


Fig III. 23 - Reflection and transmission of Bout1 net

The problem with the modelling of the return loss at low frequencies is uncertain especially when comparing to the outstandingly good concordance for other cases presented hereafter.

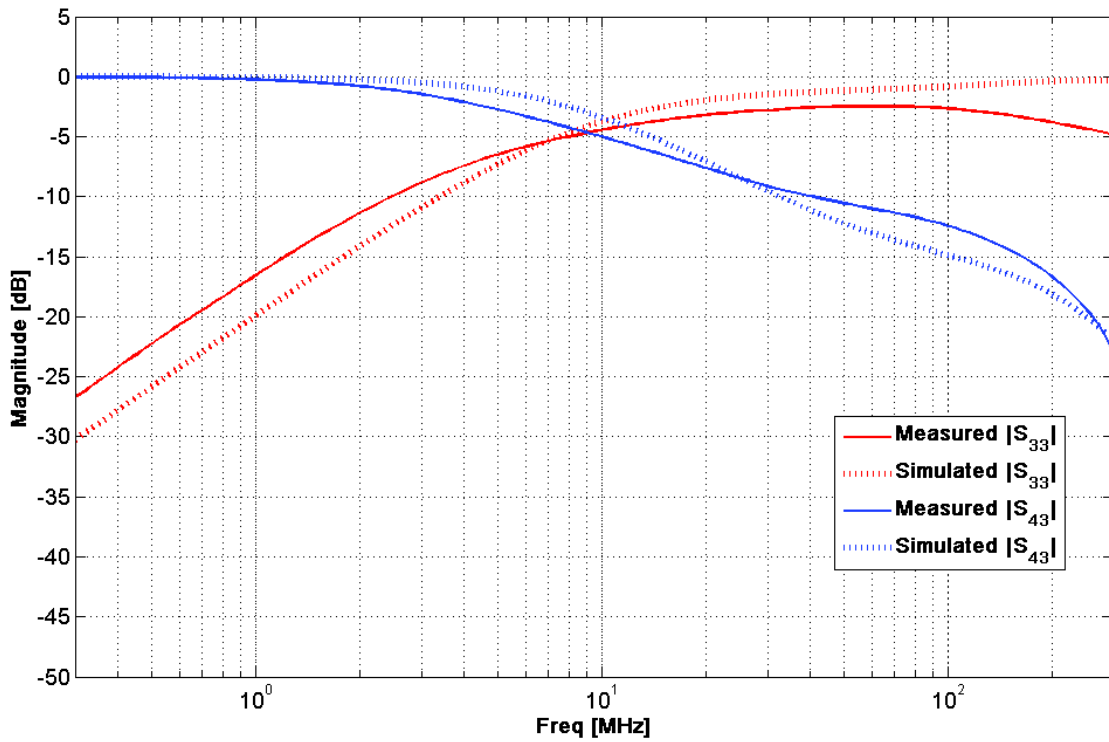


Fig III. 24 - Reflection and transmission of Bout2 net

For Bout2 net, scattering parameters magnitudes are presented in Fig III. 24. Concordance between simulated data from the extraction process and the measured data is very good. A 5 dB difference is found at 300 MHz for return loss. It is interesting to point out that contrary to the plane Bout1 which is shorter in length than Bout2, the transmission is noticeably degraded at fairly low frequencies. Starting at 1 MHz, the attenuation is higher than 10 dB and at 300 MHz, attenuation reaches -22 dB. Besides, return loss is higher for frequencies below 1MHz although a 30 dB attenuation is found at 300 kHz. This means that high frequency harmonics and switching-induced spectra are attenuated between the phase output of the full bridge and one of the motor leads. However, return loss shows a less impendent path to high frequency spectra to common-mode from around 1 MHz.

For the power DCpos and DCneg, simulation results are also concordant with experimental measurements as presented in Fig III. 25 and Fig III. 26. The main important aspect to conclude is the divergence appearing at the high end of the modelled spectra. Since these are planes covering the full surface of the board, propagation effects might start to be noticeable. Since simulation doesn't take into account propagation effects, divergence is found when compared with experimental data. However, at 300 MHz, this divergence is of 11 dB for DCneg net. A possible verification of this hypothesis could be done by exporting the Netlist from Q3D® with more than one cell as established in §III.4.3, and account for improvements in the simulated data.

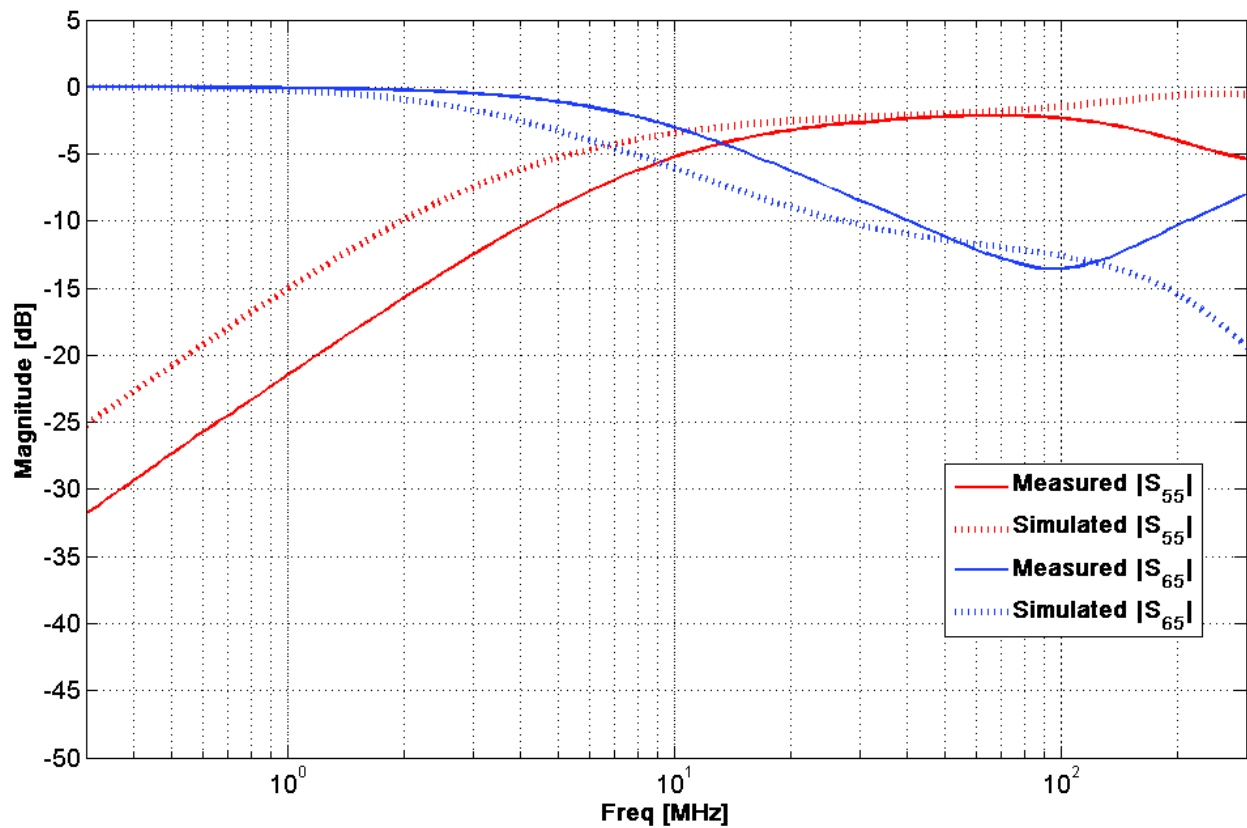


Fig III. 25 - Reflection and transmission of DCneg net

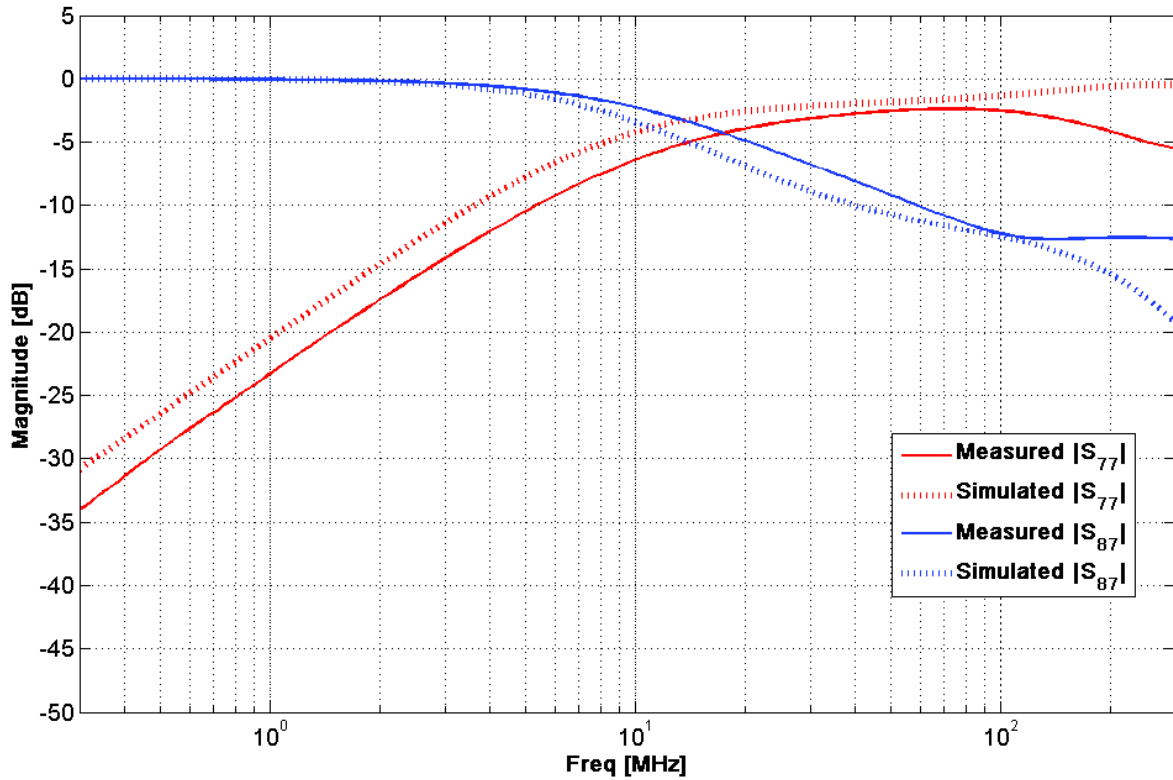


Fig III. 26 - Reflection and transmission of DCpos net

Finally, comparison between simulated and measured data for the LEM net rouses very low errors. Only a 5 dB difference is found at 300 MHz for return loss as shown in Fig III. 27.

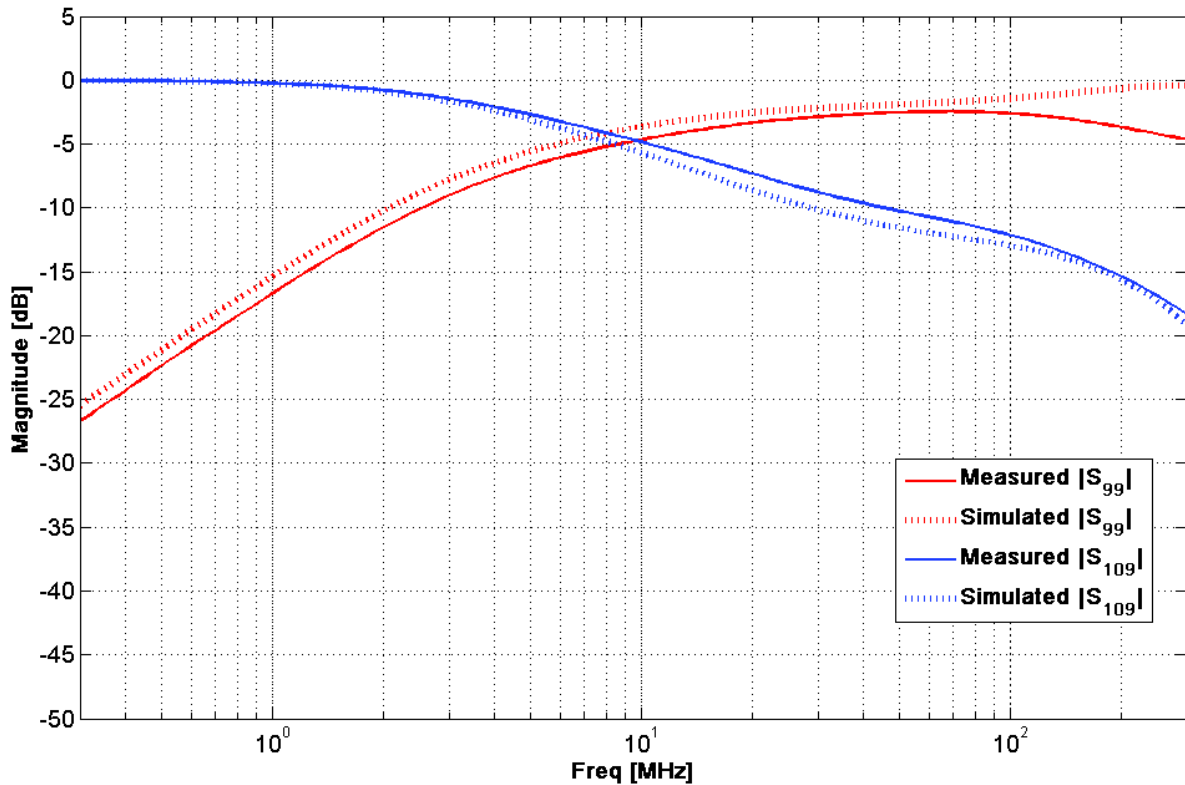


Fig III. 27 - Reflection and transmission of LEMph net

Good agreement between simulation results and measured data is conclusive regarding the equivalent circuit extraction from multilayered power PCB, especially from a predictive point of view. Although measurements could be performed to compare with simulations, extracting the partial circuit elements from electromagnetic simulations is proven to be an efficient way of virtually experimenting and characterizing such a structure.

7 CONCLUSIONS

In this chapter, a rational method allowing to characterize a multilayered power PCB from the computer aided layout has been presented. The method shows the standard procedure to obtain 3D data from the layout files, importing the files into an electromagnetic computation solver, extracting the equivalent circuits and exporting the circuits into a circuit simulator. Several adaptations of the 3D geometry have to be accounted for in order to narrow complex geometries down to manageable computation times and file sizes. The resulting extracted circuits are an image of the projected PCB. Indeed, the simulation for EMC/EMI analysis can be used for predicting emissions without the need for the PCB to actually be manufactured. If unacceptable behavior is then detected, modifications to the PCB layout and architecture can therefore be done before prototyping.

Although good knowledge of the architecture is needed to properly achieve such an analysis, the method is straightforward.

The circuit analysis can either be done by plotting scattering or impedance parameters equivalently. Anyhow, the above analysis shows a great concordance between simulated and measured data thus validating the overall procedure for virtually characterizing a power PCB.

In the next and last chapter, a system level analysis involving this PPCB and a winding structure modelling is carried out. A virtual experimentation process is done for a real system composed of a full bridge converter driving a winding of a fault-tolerant motor for vehicle traction designed by Novatem.

8 REFERENCES

- [1] Y. Hamieh, "Caractérisation et modélisation du transistor JFET en SiC à haute température," phdthesis, INSA de Lyon, 2011.
- [2] M. Bareille, "Contribution à l'analyse des problèmes de compatibilité électromagnétique dans les circuits de l'électronique de puissance : la cellule de commutation IGBT + diode et son environnement," Toulouse, INSA, 2001.
- [3] Dolente, Andrea <1976>, "Analysis of the heatsink influence on conducted and radiated electromagnetic interference in power electronic converters," 2007.
- [4] C. R. Paul, *Introduction to Electromagnetic Compatibility*. John Wiley & Sons, 2006.
- [5] M. Mardiguian, *Controlling Radiated Emissions by Design*. Springer Science & Business Media, 2001.
- [6] M. Radojicic and G. Costache, "A model to predict radiated emissions from electronic circuits," in , *IEEE 1991 International Symposium on Electromagnetic Compatibility, 1991. Symposium Record*, 1991, pp. 54–57.
- [7] R. W. Dockey and R. F. German, "New techniques for reducing printed circuit board common-mode radiation," in , *1993 IEEE International Symposium on Electromagnetic Compatibility, 1993. Symposium Record*, 1993, pp. 334–339.
- [8] J. L. Drewniak, T. H. Hubing, and T. P. V. Doren, "Investigation of fundamental mechanisms of common-mode radiation from printed circuit boards with attached cables," in , *IEEE*

- International Symposium on Electromagnetic Compatibility, 1994. Symposium Record. Compatibility in the Loop*, 1994, pp. 110–115.
- [9] D. M. Hockanson, J. L. Drewniak, T. H. Hubing, T. P. V. Doren, F. Sha, and M. J. Wilhelm, “Investigation of fundamental EMI source mechanisms driving common-mode radiation from printed circuit boards with attached cables,” *IEEE Transactions on Electromagnetic Compatibility*, vol. 38, no. 4, pp. 557–566, Nov. 1996.
- [10] K. B. Hardin and C. R. Paul, “Decomposition of radiating structures using the ideal structure extraction methods (ISEM),” *IEEE Transactions on Electromagnetic Compatibility*, vol. 35, no. 2, pp. 264–273, May 1993.
- [11] O. M. Ramahi, V. Subramanian, and B. Archambeault, “A simple finite-difference frequency-domain (FDFD) algorithm for analysis of switching noise in printed circuit boards and packages,” *IEEE Transactions on Advanced Packaging*, vol. 26, no. 2, pp. 191–198, May 2003.
- [12] G. Feng and J. Fan, “Analysis of Simultaneous Switching Noise Coupling in Multilayer Power/Ground Planes With Segmentation Method and Cavity Model,” *IEEE Transactions on Electromagnetic Compatibility*, vol. 52, no. 3, pp. 699–711, Aug. 2010.
- [13] G. Heinrich and S. Dickmann, “Interactions between Vias and the PCB Power-Bus,” in *Electromagnetic Compatibility, 2009 20th International Zurich Symposium on*, 2009, pp. 257–260.
- [14] A. Abou-Alfotouh, M. Orabi, and A. Ghahary, “PCB layout vias effect on power supply performance,” in *Applied Power Electronics Conference and Exposition, 2008. APEC 2008. Twenty-Third Annual IEEE*, 2008, pp. 339–345.
- [15] D. M. Pozar, *Microwave Engineering, 4th Edition*. Wiley, 2011.
- [16] M. Hampe and S. Dickmann, “Generation of common-mode currents on PCB power-bus structures,” in *Electromagnetic Compatibility, 2006. EMC-Zurich 2006. 17th International Zurich Symposium on*, 2006, pp. 320–323.
- [17] D. Moongilan, “Method for direct interconnection of PCB power layer to chassis to minimize radiated emissions,” in *Electromagnetic Compatibility (EMC), 2011 IEEE International Symposium on*, 2011, pp. 173–178.
- [18] A. Guena, F. Costa, and C. Labarre, “Hybrid Modeling Techniques for Multilayered Printed Circuit Board in Power Electronics: Association of Electromagnetic Methods,” *IEEE Transactions on Electromagnetic Compatibility*, vol. 46, no. 4, pp. 559–570, Nov. 2004.
- [19] E. Batista, “Nouvelles structures électroniques pour le transport électrique : impacts des nouvelles contraintes d’intégration sur les interférences électromagnétiques et moyens de prévision de la compatibilité électromagnétique,” phd, Université de Toulouse, Université Toulouse III - Paul Sabatier, 2009.
- [20] “Q3D Technical Notes, Maxwell 3D Technical Notes.” ANSOFT, 2001.
- [21] P. Bernardi, R. Cicchetti, G. Pelosi, A. Reatti, S. Selleri, and M. Tatini, “An Equivalent Circuit for EMI Prediction in Printed Circuit Boards Featuring a Straight - to - Bent Microstrip Line Coupling,” *Progress In Electromagnetics Research B*, vol. 5, pp. 107–118, 2008.
- [22] G. Lourdel, “Méthodologie et outils de calcul numérique pour la prise en compte de la compatibilité électromagnétique des nouveaux prototypes de circuits intégrés de puissance,” Toulouse 3, 2005.
- [23] G. Brocard, *The LTSpice Simulator: Manual, Methods and Applications*. Würth Elektronik, 2013.
- [24] “E5061B ENA Series Network Analyzer | Keysight (Agilent).” 11-Apr-2016.
- [25] J. C. Tippet and R. A. Speciale, “A Rigorous Technique for Measuring the Scattering Matrix of a Multiport Device with a 2-Port Network Analyzer,” *IEEE Transactions on Microwave Theory and Techniques*, vol. 30, no. 5, pp. 661–666, May 1982.

Chapter IV
EMC Investigation Method for Power
Mechatronic Assemblies and Virtual
Experimentation

CONTENTS

Table of figures.....	164
List of tables	165
1 Introduction and objectives	166
2 Modelling and analysis of a Flyback converter	167
2.1 System architecture.....	167
2.2 General strategy of Common-Mode-Currents induced Radiated Emissions prediction	168
2.3 Part1: Circuit Modelling of the converter	169
2.3.1 Structure.....	169
2.3.2 Mosfet -SPICE smulation file (circuit).....	170
2.3.3 Modelling of the Flyback transformer	170
2.3.4 Modelling of other components and simulation	177
2.4 Part 2: Assessment of preponderant parasitic couplings resulting in CM currents	177
2.4.1 Common-mode termination load for the converter’s modelling.....	177
2.4.2 Examination of couplings between the Mosfet and the Heatsink	178
2.5 Part 3: Extraction of CM currents from the circuit simulation	181
2.5.1 Line Impedance Stabilization Network (LISN)	181
2.5.2 Plotting of CM currents and Export	183
2.6 Part 4: Assessment of radiated emissions with the CM currents retrieved from the simulation.....	183
2.6.1 Structure’s 3D model, currents import and simulation	184
2.6.2 Comparison to experimental results.....	184
3 EMOD analysis and rational predictive models inclusion	187
3.1 EMOD: Fault-tolerant traction system.....	187
3.2 Motor winding.....	189
3.3 Power Converter	190
4 Modelling and circuit simulation of EMOD.....	193
4.1 Circuit model of the winding	193
4.2 Power converter circuit model and SPICE files	194
4.2.1 Full bridge IGBT module	194
4.2.2 Drivers and gate circuit fast diodes.....	195
4.2.3 LEM current transducer and voltage probe	195
4.3 Resulting global circuit	195
5 Virtual Experimentation on EMOD	195
5.1 Example of some functional signals.....	196

5.2 Non-functional signals examples 199

5.3 Common-mode currents from capacitive couplings between the winding and the core ... 200

6 Conclusions 202

7 References 203

TABLE OF FIGURES

Fig. IV. 1 - Schematic drawing of servo-motor assembly and its electronic control elements..... 167

Fig. IV. 2 – Generic structure of a Flyback converter 169

Fig. IV. 3 - Custom-made Flyback converter 170

Fig. IV. 4 - Excerpt from the WE Midcom transformer datasheet..... 171

Fig. IV. 5 - Simulation circuit model including transformer and Mosfet models..... 172

Fig. IV. 6– Comparison between the Drain – Source tension simulation with the time measurement and its frequency equivalent 172

Fig. IV. 7 - Comparison between the secondary voltage simulation with the time measurement and its frequency equivalent 173

Fig. IV. 8 - Different connections of the transformer to the VNA ports in order to obtain the S parameters 174

Fig. IV. 9 - PCB made for measuring the S parameters 174

Fig. IV. 10 - Time response of the circuit model with S parameters extracted between 100 kHz and 200 MHz 175

Fig. IV. 11 - Impedances calculated from the extracted S parameters 175

Fig. IV. 12– Simple model equivalent to the transformer’s low frequency behavior 176

Fig. IV. 13 - Extrapolated Impedances by means of low and high frequency concatenation 176

Fig. IV. 14 - Global circuit with common-mode load 177

Fig. IV. 15 - Capacitive couplings between the Drain and its environment 179

Fig. IV. 16 - Spectrum of common-mode currents flowing through the power cord 179

Fig. IV. 17 - Zoom to the high-end frequency spectrum 180

Fig. IV. 18 - 3D model for the parameters' extraction with Q3D® 180

Fig. IV. 19 - Line impedance Stabilization Network (LISN) schematics 182

Fig. IV. 20 - Equivalent LISN circuit model 182

Fig. IV. 21 - Flyback fed through a LISN 183

Fig. IV. 22 – Approach to predict radiated emissions of the Flyback’s power supply cable 184

Fig. IV. 23 - Experimental protocol for the measurement of radiated emissions 185

Fig. IV. 24 – Physical setup for experimental measurements of radiated emissions 185

Fig. IV. 25 - Setup for the common-mode current measurement in semi-anechoic chamber 186

Fig. IV. 26 - Comparison of the radiated emissions by measurement and by simulation 186

Fig. IV. 27 - EMOD motor 188

Fig. IV. 28 – Stator of EMOD motor with magnetic modules and their attached power electronics .. 188

Fig. IV. 29 - Single module and power converter for 1 phase 188

Fig. IV. 30 - Cross-sectional view of the winding 189

Fig. IV. 31 - Main characteristics of Microsemi IGBTs 190

Fig. IV. 32 – Power stage of the converter 191

Fig. IV. 33 - Main characteristics of Infineon Mosfet gate driver 191

Fig. IV. 34 - Close control stage of the converter 192

Fig. IV. 35 - Measured and simulated differential-mode impedance of an EMOD winding.....193
Fig. IV. 36 - Measured DM impedance and simulated impedance extracted at 1 Hz194
Fig. IV. 37 - Global circuit model of an EMOD phase195
Fig. IV. 38 - Output voltage with and without the PCB model197
Fig. IV. 39 - Differences at switching of output voltage with and without PCB model197
Fig. IV. 40 - Load current with and without PCB model198
Fig. IV. 41 - Differences of the two load currents at switching198
Fig. IV. 42 - FFT of the currents plotted with and without the PCB model199
Fig. IV. 43 - Voltage across the LEM current sensor199
Fig. IV. 44 - Zoom of the voltage across the LEM at switching.....200
Fig. IV. 45 - Common-mode currents between some turns and the core of the winding.....201
Fig. IV. 46 - Zoom on the common-mode currents at the winding level201
Fig. IV. 47 - FFT of the common-mode currents with and without PCB model.....202

LIST OF TABLES

Table IV. 1 - Components of the servo drive with equivalent operation frequencies168
Table IV. 2 - Estimated parasitic capacitances.....178
Table IV. 3 -EMOD winding and core parameters189
Table IV. 4 - Functional parameters of the power converter.....192
Table IV. 5 - Dynamic characteristics of both IGBT technologies.....194
Table IV. 6 - Turn-to-core capacitances and their position in the winding structure200

1 INTRODUCTION AND OBJECTIVES

This chapter is divided in two different studies. The first study deals with the EMC / EMI analysis of a portion of a marketed servo-drive system. The second study deals with the implementation of the techniques and methods developed in this work to complement the first study.

The first study, which is referred as the “Flyback analysis”, addresses the problem of EMC and EMI from a modelling point of view. The Flyback analysis establishes a standard procedure for evaluation of common-mode-induced radiated emissions (RE) of a power system. A complete method, starting from circuit simulation to radiated emissions predictions is constructed.

Although the Flyback converter is not considered as a Mechatronic system, the procedure established here can help to the evaluation of radiated emissions in any mechatronic system RE.

As for the process of modelling of the Flyback converter, during the modelling of functional components forming it, a customized PCB with very specific and well-known features is manufactured and the transformer modelled by measuring its S-parameters. Thereby, changing one of these constituents would induce manufacturing and measuring again their characteristics to include them in the modelling process for the general method to work.

The second study, referred as “EMOD analysis”, is aimed to include the modelling techniques addressed in the work presented in Chapter II and III in the procedure presented in the Flyback study. It is applied to a module of a 20 kW motor designed by Novatem, used for Electric Vehicle (EV) traction. In the EMOD analysis, the predictive models of the PCB and winding are performed. Instead of measured based component models, analytical based models for the winding and parameters extraction for the PCB are used to complete the simulation.

Consequently, both techniques are decidedly complementary. With the EMOD analysis, it is shown that common-mode currents generated in the system can be accessed without the need of measurement and therefore, prototyping. By changing the measurement-based modelling used in the Flyback analysis, the whole method becomes fully predictive.

The Flyback analysis was elaborated during a 3-month collaboration between the Laboratoire Génie de Production and the Electromagnetic Compatibility Laboratory (EMCLab) of the Missouri Science and Technology University based in Rolla, Missouri, United States co-funded by Ecole des Docteurs de l’Université Fédérale de Toulouse, Institut National Polytechnique de Toulouse and Novatem.

Participants in this collaboration were:

- From EMCLab : Dr. David Pommerenke, and Satyajeet Shinde, Ph.D. student
- From Panasonic, Japan : Dr. Kohei Masuda
- From Laboratoire Génie de Production : José Ioav Ramos Chavez, Ph.D. student, Pr. Jean-Marc Dienot, Dr. Paul-Etienne Vidal
- From Novatem : Dr. Christophe Viguiet

2 MODELLING AND ANALYSIS OF A FLYBACK CONVERTER

2.1 SYSTEM ARCHITECTURE

This project deals with the study of a marketed Panasonic™ system and made available by its manufacturer, for the purpose of developing new analysis methods and EMC models for a well-known system for application in new products.

The system consists of a mechanical 200 W servo-motor powered by a power electronics supply assembly and a control stage. Fig. IV. 1 presents a schematic view of the servo-motor architecture and its structural components.

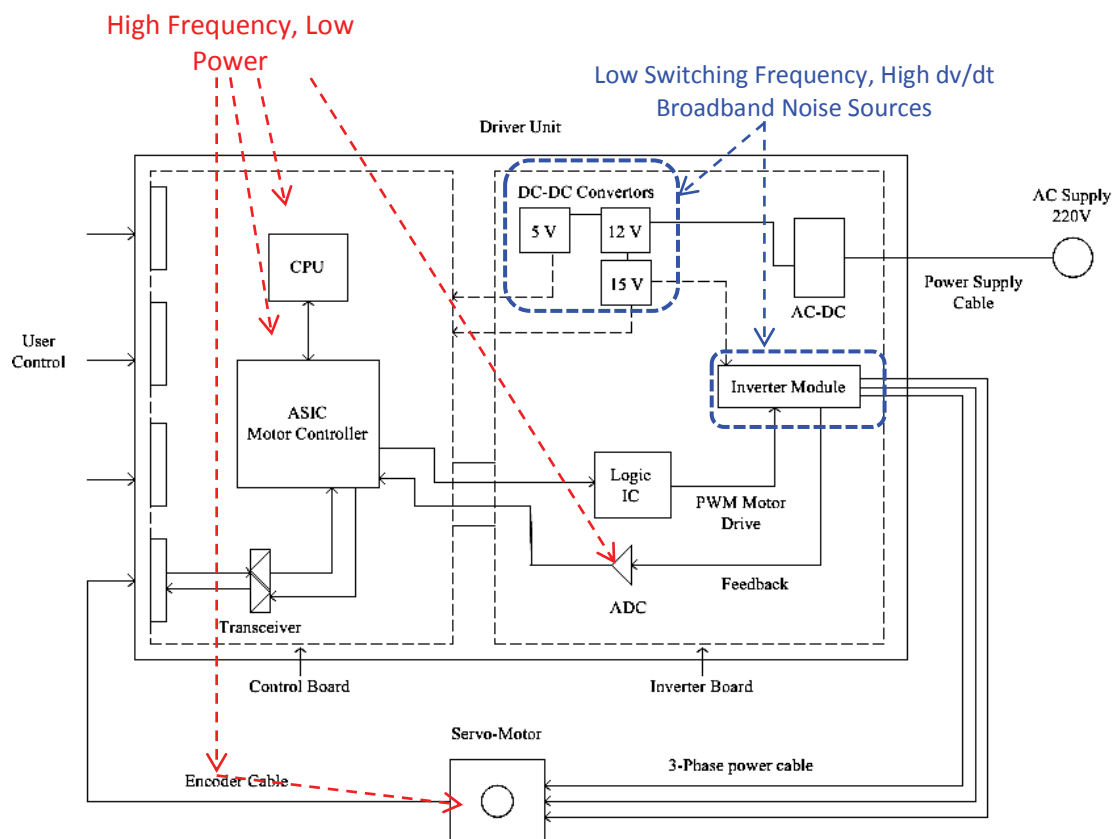


Fig. IV. 1 - Schematic drawing of servo-motor assembly and its electronic control elements

The power electronics converters elements located on the inverter board, such as rectifiers, stepdown Flyback converter and motor inverter are controlled by analog and digital electronic elements located on the control board.

A preliminary analysis was carried out to determine the type of radiation sources, as well as the characteristic times and frequencies of each part of system: inverter board and digital board. Table IV. 1 shows the results of these preliminary analyses.

The entire system being complex, the analysis focuses only on the « Flyback» converter. The purpose is to allow the **prediction of radiated emissions through the power cable of the converter under the different configurations** provided in the electromagnetic emission standards, FCC part 15 and CISPR-25.

Table IV. 1 - Components of the servo drive with equivalent operation frequencies

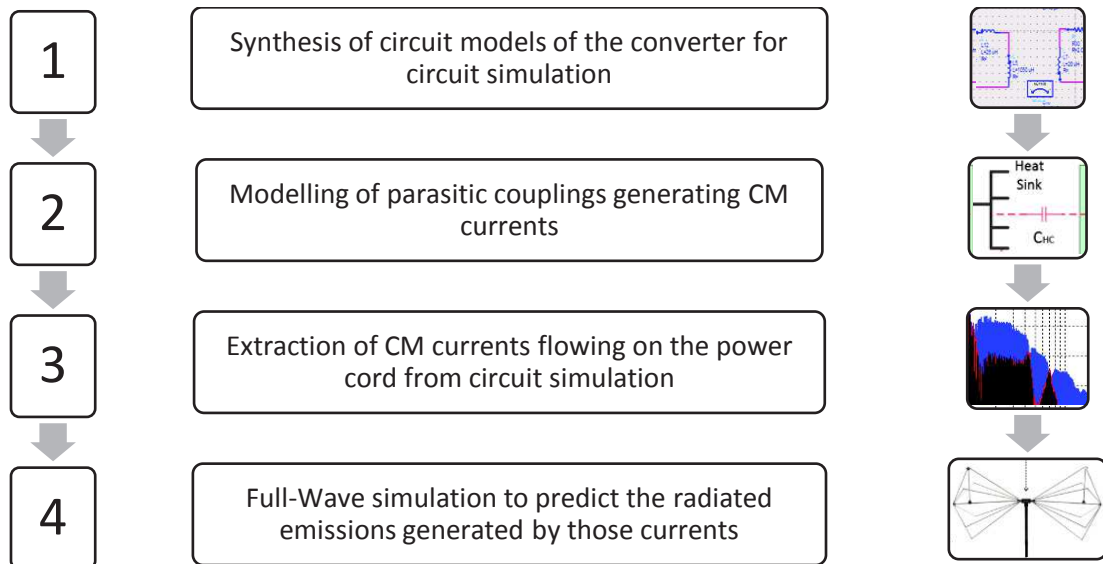
Main Components	Switching period/ Frequency	Active mode of servo- motor	Spectrum measured in far field
Inverter at IGBT	12 kHz	Servo-Lock	30 MHz – 100 MHz
Flyback Converter (250V – 12 V)	42 kHz	Plugged-In, Servo-Lock	30 MHz – 100 MHz
ADC - (SPI-Serial Data)	2 MHz	Plugged-In, Servo-lock	30 MHz - 550 MHz
IC513 (ADC-Clock)	10 MHz	Servo-Lock	30 MHz – 1 GHz
ASIC : Encoder Data	2.5 MHz	Plugged-In, Servo lock	30 MHz – 220 MHz

2.2 GENERAL STRATEGY OF COMMON-MODE-CURRENTS INDUCED RADIATED EMISSIONS PREDICTION

The global, strategy of study of the entire system is founded upon precise circuit simulation of the functional system and the parasitic couplings leading to common-mode currents. This part involves two aspects:

- Modelling each of the components constituting the converter
- Modelling every coupling generating common-mode currents possibly flowing through long conductors (efficient antennas)

It is these CM currents that are mainly responsible of radiated emissions. This is why, this is a fundamental stage in the prediction method. Once the simulation completed, the extraction of common-mode currents in a Netlist file can be performed. The idea is to be able to import this file into the Full-Wave simulation software, in order to use it as excitation current for the cable. This allows to simulate the near- and far-field radiation from the cable excited by the simulated common-mode currents. This can be synthetized as follows :

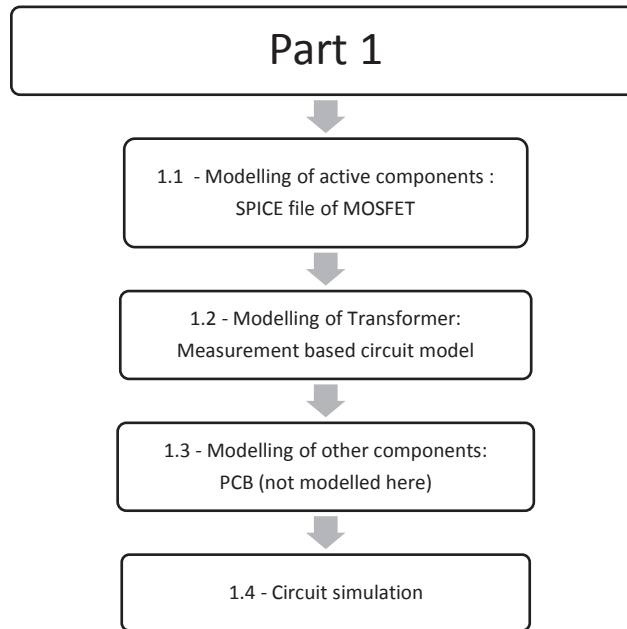


Special attention will be granted to the modeling of the converter’s components. This is because it is in this part of the analysis that the two aforementioned studies are complementary. Indeed, very specific techniques were used in order to model the Flyback transformer. As will be seen in subsequent

sections, the modelling techniques used in the Flyback analysis are not predictive, and thus, the complete method depends on the existence of certain components to be valid.

2.3 PART1: CIRCUIT MODELLING OF THE CONVERTER

This part concerns the first stage of the radiated emissions prediction method. The process is done as follows:



2.3.1 Structure

The Flyback converter ensures low-level power supply to the servo motor control parts. It is used to supply power to the close control functions such as the inverter’s IGBT drivers. It transforms 200 VDC into 12 VDC that can be used by other less powerful converters feeding the control circuits themselves. Fig. IV. 2 is a schematic drawing of a generic Flyback structure.

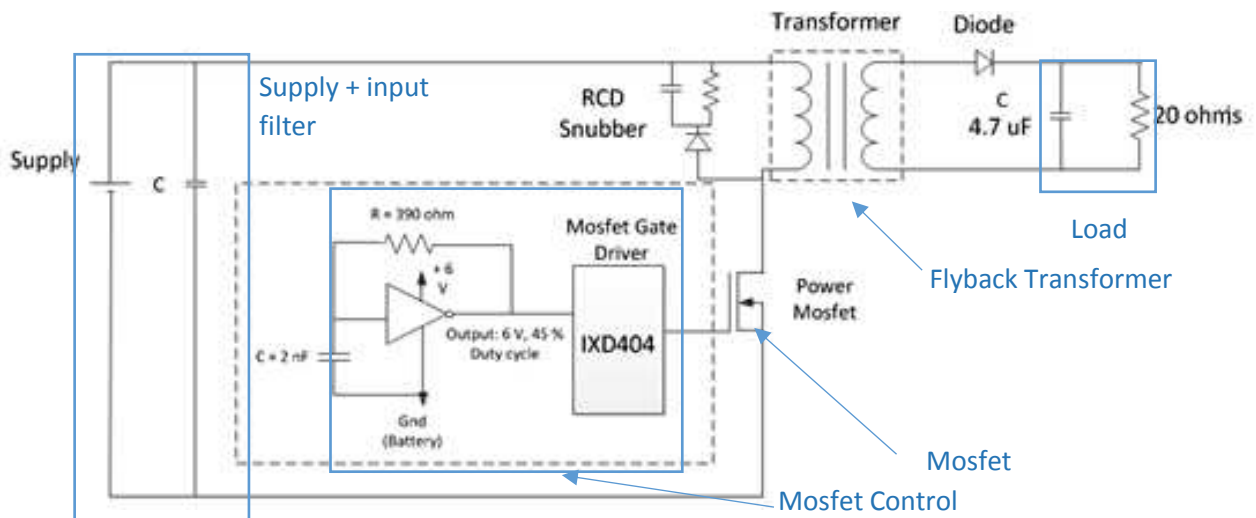


Fig. IV. 2 – Generic structure of a Flyback converter

The fundamental problem encountered with the analysis of the Flyback converter, is that it cannot be driven autonomously from the rest of the system. **Therefore, a completely different and customized converter was made to precisely identify the noise generated by Flyback topologies, and to analyze the impact of the power supply cables on radiated emissions.** The industrial Power PCB originally designed to support such converter was discarded. A simpler, minimalistic PCB was manufactured for the analysis and is shown in Fig. IV. 3.

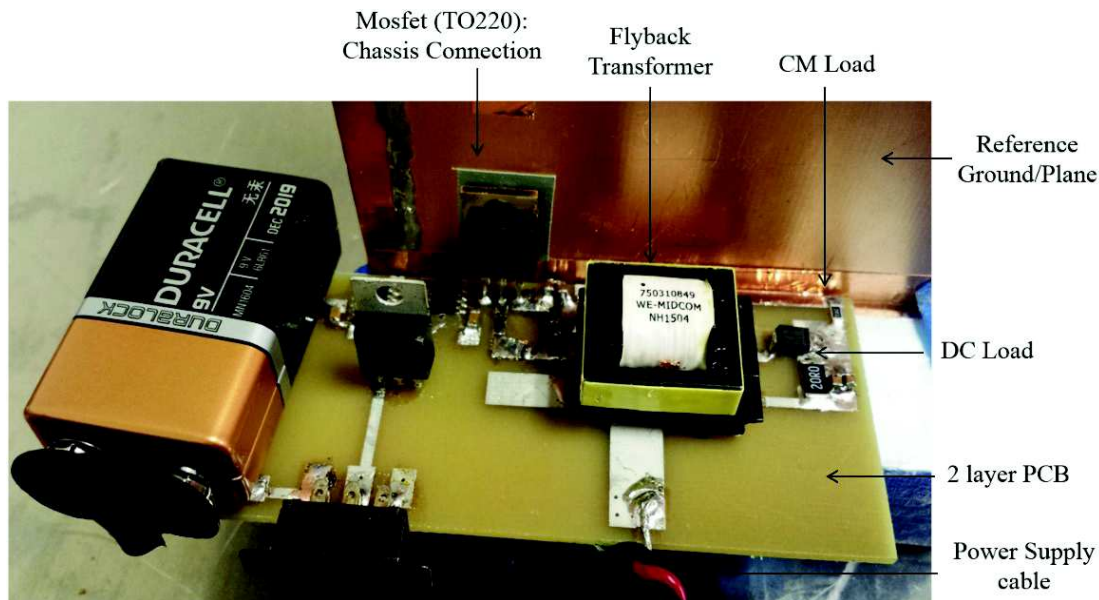


Fig. IV. 3 - Custom-made Flyback converter

2.3.2 Mosfet -SPICE smulation file (circuit)

The Mosfet International Rectifier reference is IRL4310. A SPICE simulation file was made available by International Rectifier. The simulation results were experimentally validated for up to 100 MHz and, as a matter of fact, it was anticipated for the study described herein that the results obtained would be of up to 120 MHz, as a minimum. As for time and efficacy concerns, the assumption was that the simulation results with this SPICE file would be applicable up to 120 MHz. However, validation of this hypothesis, although very probably verifiable, remains pending.

2.3.3 Modelling of the Flyback transformer

Modelling of the Flyback transformer was one of the most critical areas of the study.

In order to achieve an accurate model of the transformer's behavior up to the hundreds of MHz level, it is necessary to take into account the parasitic couplings that form the structure's geometry: leakage inductances, inter-turn capacitances, inter-winding capacitances and every other parasitic coupling present in the structure. Several methods were assessed. We only obtained partial results from the analytic modelling of inter-turn and inter-winding capacitive couplings. Indeed, the lack of information on the transformer's configuration and its exact geometry prevented us from achieving a correct modelling of these elements. Consequently, the team chose a tuning approach.

2.3.3.1 Simulation with tuning strategy

Tuning consists of adding branches containing resistances, inductances and capacitances branches (RLC branches) in series and/or in parallel depending on the resonances to be modelled. The values are then modified or tuned to obtain the impedance levels and frequencies for the various desired resonances.

The transformer’s functional model is constituted by primary and secondary inductances coupled to one another by a coupling coefficient K . Fig. IV. 4 shows a summary of all the corresponding datasheet information.

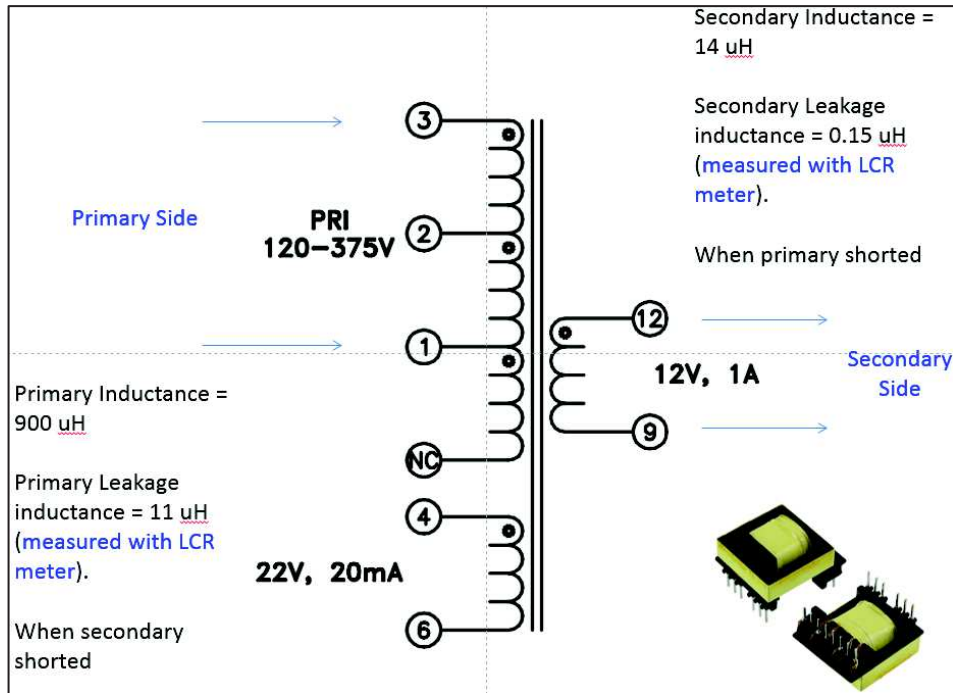


Fig. IV. 4 - Excerpt from the WE Midcom transformer datasheet

The coupling coefficient is estimated here at $K = 1$ since the ferromagnetic structure is considered to be perfect and with no flux leakage. It is evident that this is not true. But, it is difficult to guess what could be the level of leakage of flux without geometry and architecture information.

The main problem with tuning is that a measurement reference must exist in order to be able to adjust the values of the RLC branches. This is not a predictive method. Without the actual transformer, measurements cannot be performed, and circuit models cannot be tuned.

But, even when the transformer is present, as in this case, tuning proves to be difficult since RLC branches interact with each other at different frequencies throughout the frequency span. Therefore, a more rational approach was used to include the transformer model into the global circuit simulation of the Flyback converter.

In order to compare the simulation results with the experimental measurements, we decided to analyze the Mosfet’s drain-source voltage and the secondary voltage in the time and frequency domain. There is a good consistency in the results between simulation and measurement up to 20 MHz (Fig. IV. 6 and Fig. IV. 7).

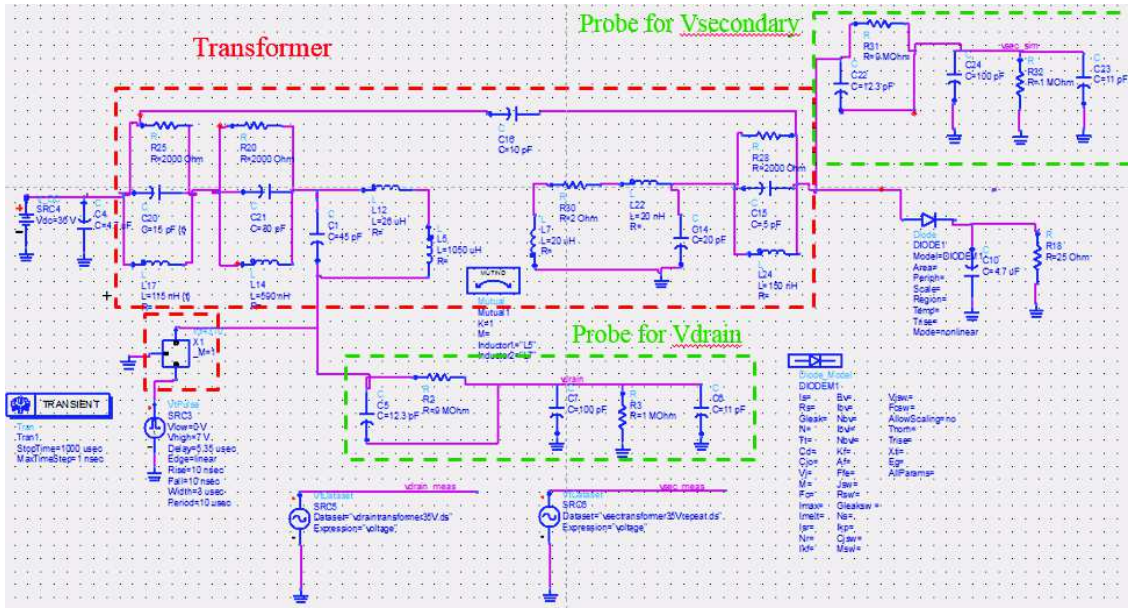


Fig. IV. 5 - Simulation circuit model including transformer and Mosfet models

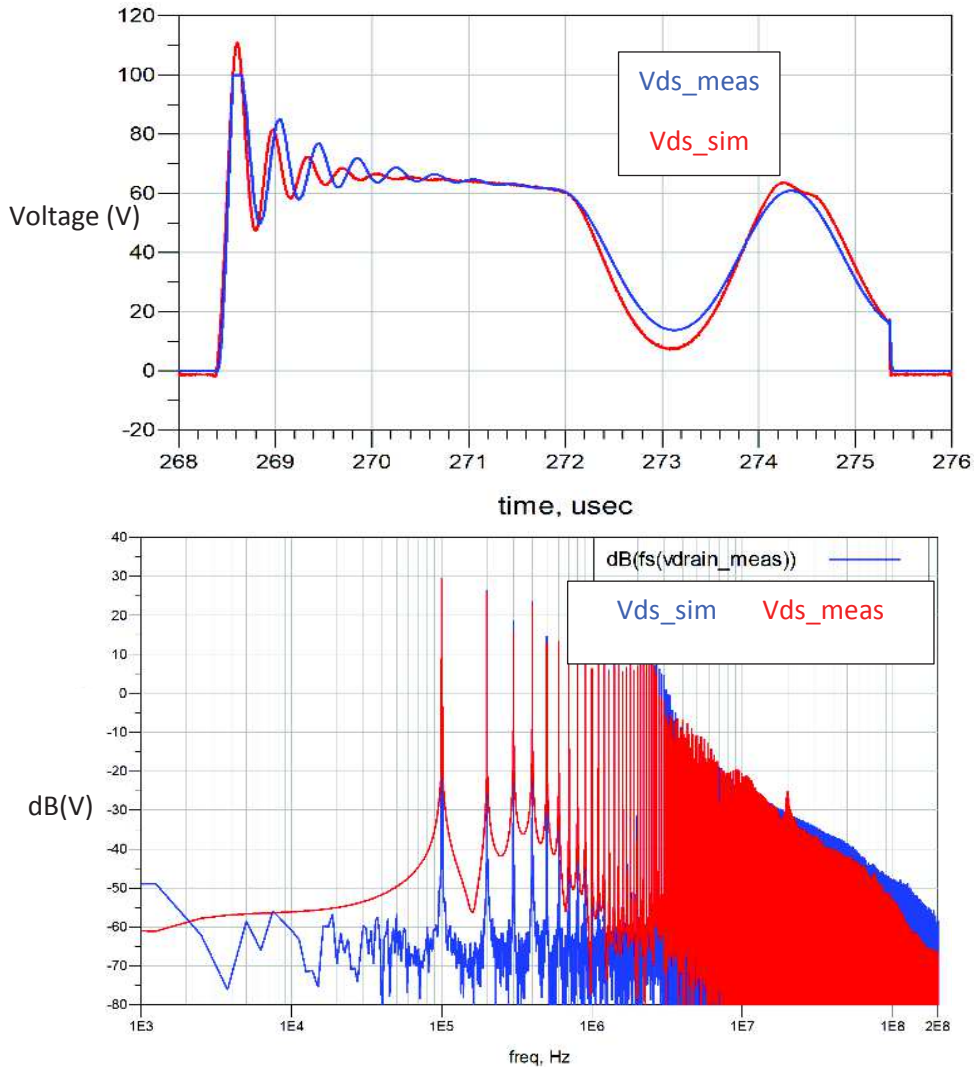


Fig. IV. 6– Comparison between the Drain – Source tension simulation with the time measurement and its frequency equivalent

Beyond 20 MHz, the simulation no longer matches the experiment. Therefore, the modelling objective of up to 200 MHz is not achieved.

To solve this issue, we decided on a radical change in the transformer’s modelling strategy, which is by far the most complex element and the most difficult to model. We chose to undertake measurements of the S parameters on various connection configurations between 100 kHz (VNA low threshold) and 200 MHz.

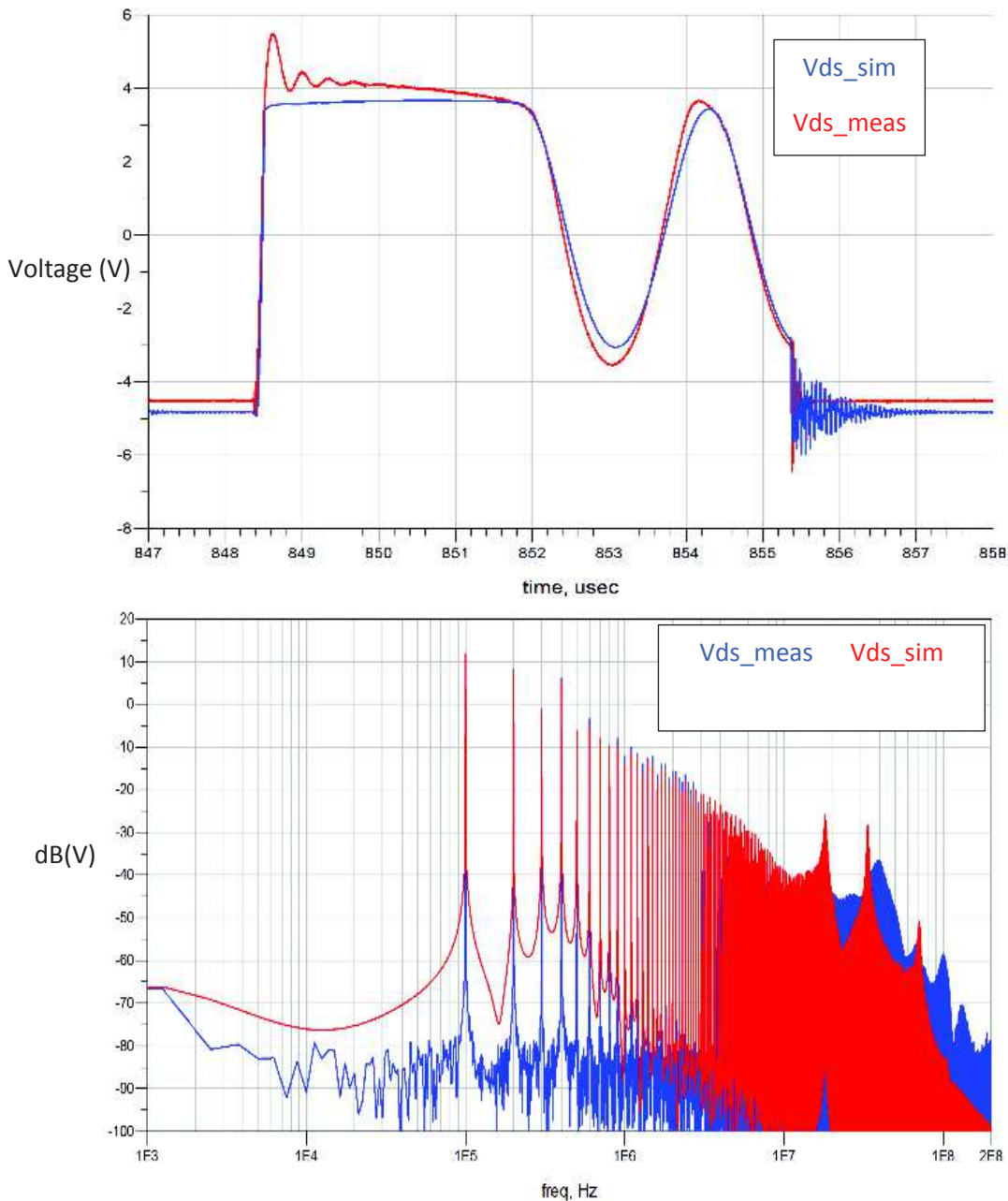


Fig. IV. 7 - Comparison between the secondary voltage simulation with the time measurement and its frequency equivalent

2.3.3.2 Simulation model using the transformer’s measured S-matrix

Since no detailed information on the transformer is available, a solution to include the transformer into the modeling effort, is to extract measured data and include the experimental data into the simulation. To do this, a 2-port Vector Network Analyzer (VNA) is used. Six 2-port measurements are

necessary to complete the 4-port matrix (16 elements) representing the transformer (cf. Chapter III). Fig. IV. 8 explains the method used.

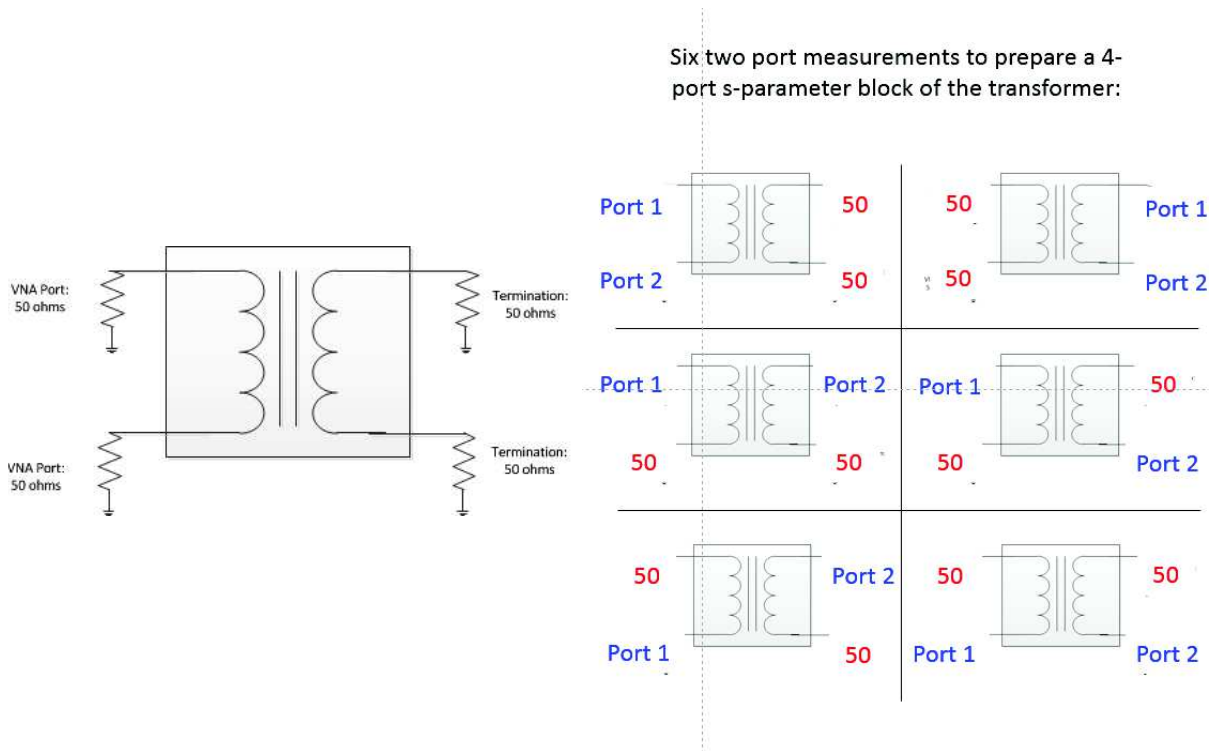


Fig. IV. 8 - Different connections of the transformer to the VNA ports in order to obtain the S parameters

A specific PCB was conceived for measuring all S parameters (Fig. IV. 9).

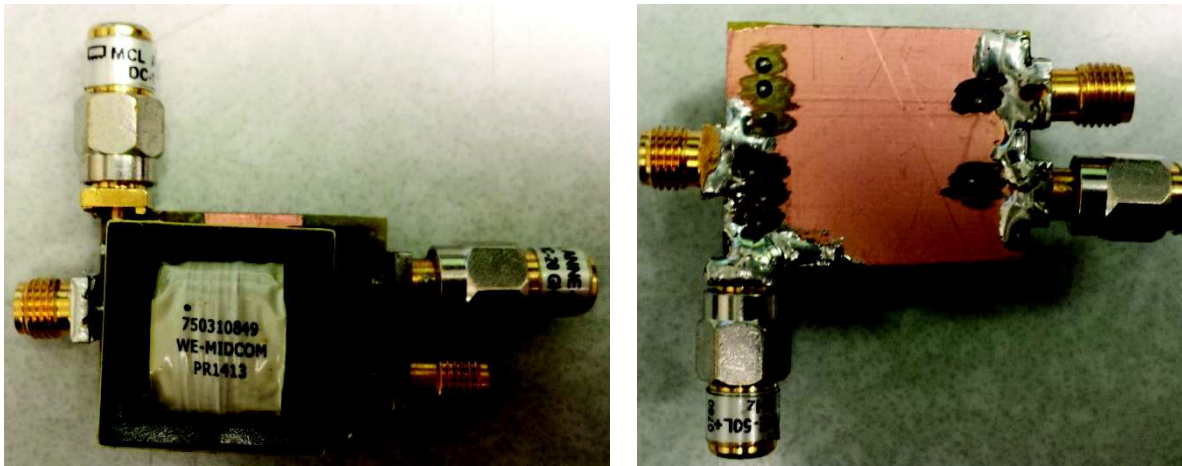


Fig. IV. 9 - PCB made for measuring the S parameters

The VNA at our disposal for these measurements is a 2-port VNA with a low measuring frequency of 100 kHz. **Therefore, the use of this method for modelling the low frequency behavior will not be feasible.** To include low-frequency data into the simulation process, the idea is to perform a concatenation of low-frequency simulated data done with the datasheet information up to 100 kHz, and the data from the experimental matrix extracted with the VNA.

With regards to extrapolation to low frequencies, when observing the model's behavior between 100 kHz and 200 MHz, in terms of time domain, the low frequency behavior is not well modelled (Fig.

IV. 10). V_{ds} (drain source voltage) shows a discontinuous conduction response, which was not the case of measured voltage.

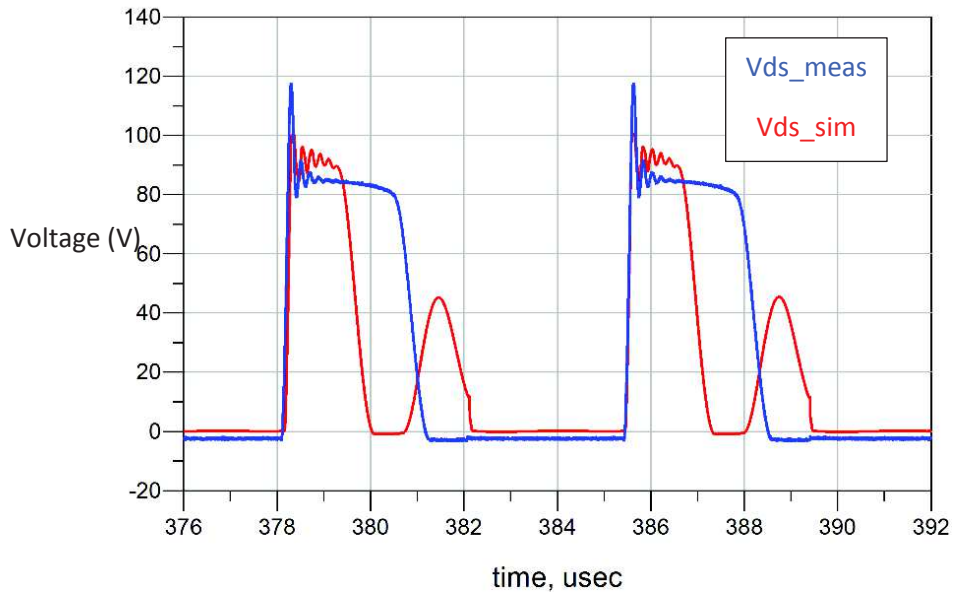


Fig. IV. 10 - Time response of the circuit model with S parameters extracted between 100 kHz and 200 MHz

If the VNA did not have a low threshold in frequency, this low frequency behavior would have been directly considered by the measurement. However, the low threshold is of 100 kHz, thus the need of extrapolation (Fig. IV. 11). A discontinuous conduction behavior was found because the transformer that participates towards the load is modelled in low frequency with an impedance taken at 100 kHz (weaker), instead of a DC inductance as shown below:

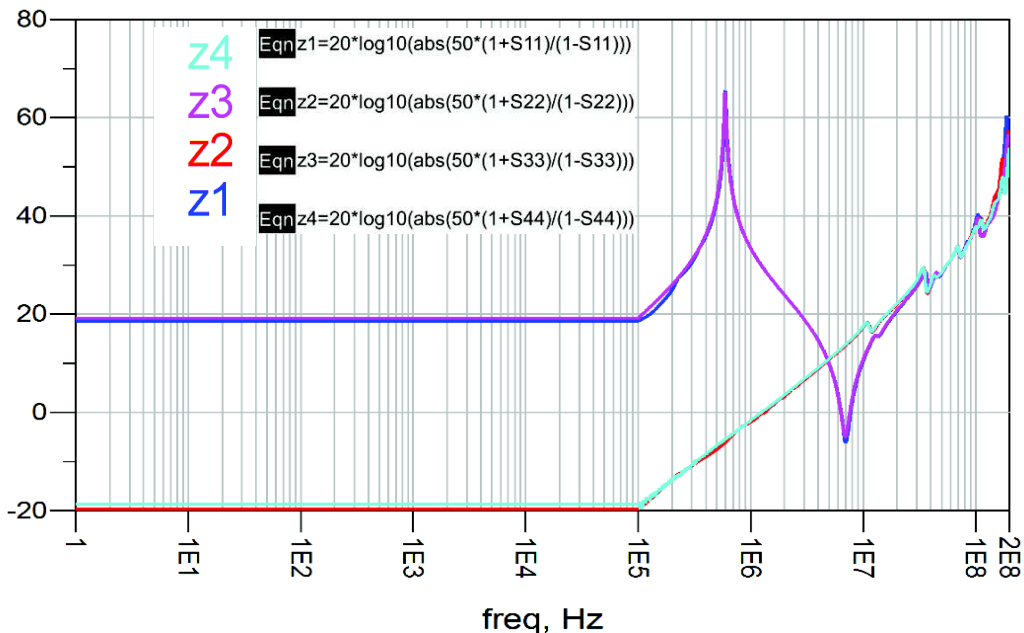


Fig. IV. 11 - Impedances calculated from the extracted S parameters

To do this, we used the transformer's simple circuit model with data obtained from previous tests and datasheet:

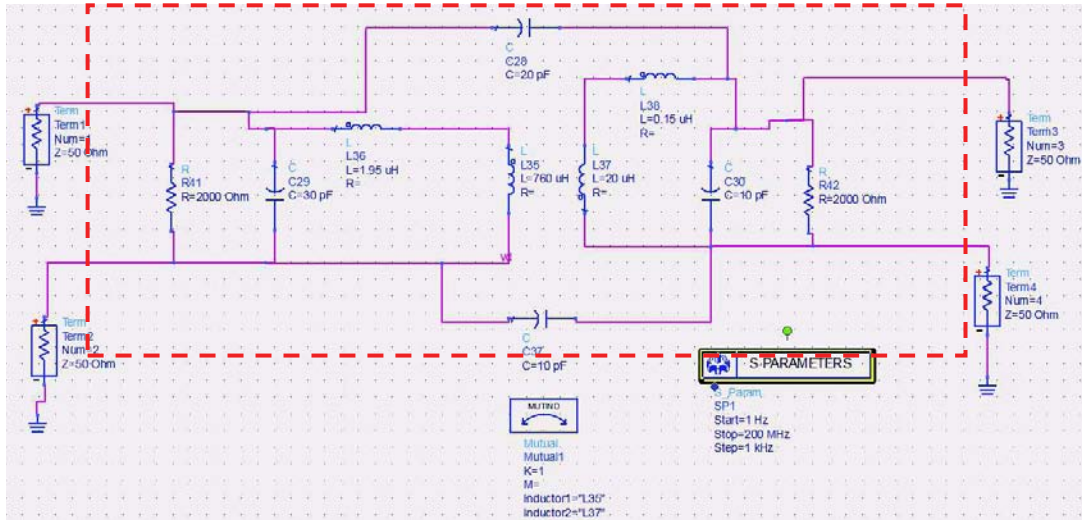


Fig. IV. 12– Simple model equivalent to the transformer’s low frequency behavior

The S parameters in this structure were simulated and extracted in the form of a 4-port S matrix. We verified that the behavior between DC and 100 kHz was consistent with the measurement. In this manner, we were then able to concatenate both matrices: the one coming from the measurement between 100 kHz and 200 MHz and the one simulated with a simple circuit (Fig. IV. 13).

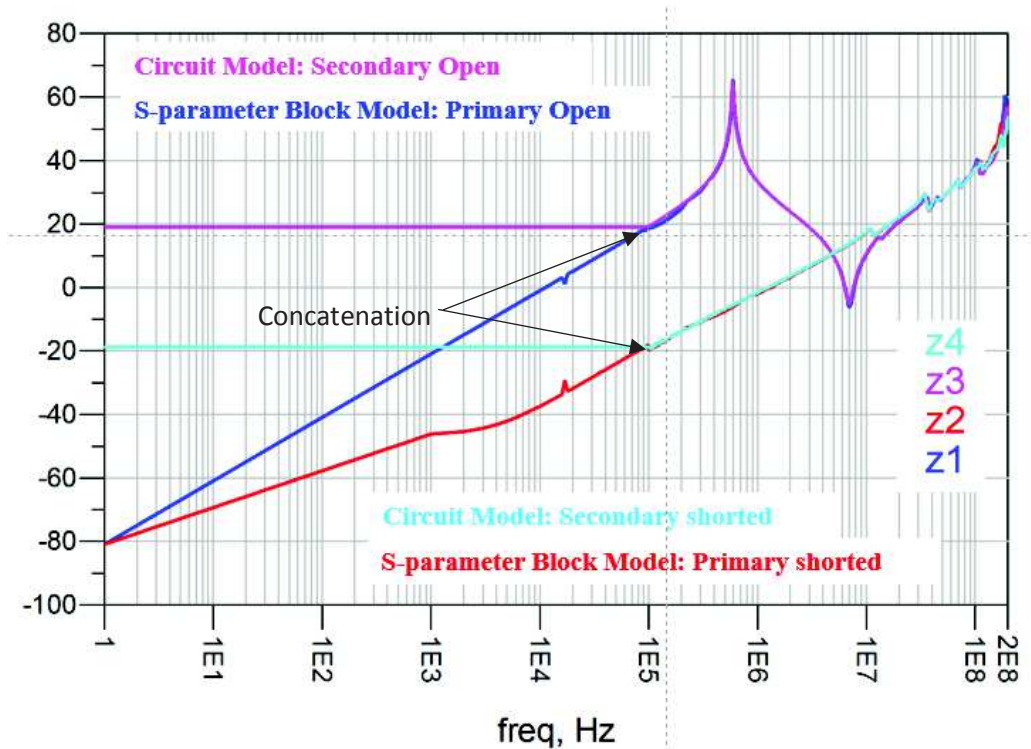


Fig. IV. 13 - Extrapolated Impedances by means of low and high frequency concatenation

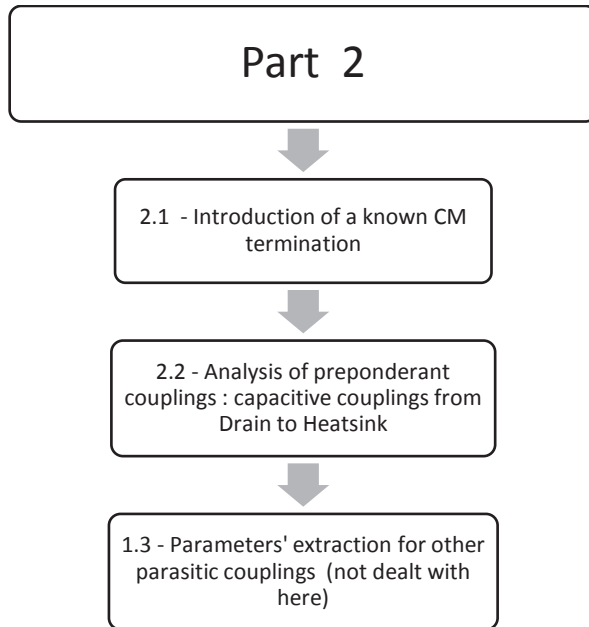
The circuit simulation result including the transformer’s model with the concatenation is compared to the measurement, in terms of time- and frequency- domain. The results proved conclusive. The model can be used in the DC range at 200 MHz. For different loads, the behavior in discontinuous conduction that was found in the HF model is no longer found.

2.3.4 Modelling of other components and simulation

Since the PCB is a custom-made design, it is assumed that its parasitics are kept at a minimum. Therefore, it was decided that no modelling was required for the PCB.

2.4 PART 2: ASSESSMENT OF PREPONDERANT PARASITIC COUPLINGS RESULTING IN CM CURRENTS

The parasitic couplings analysis is performed as follows:



2.4.1 Common-mode termination load for the converter’s modelling

Fig. IV. 14 shows the electrical, functional schematic diagram in use for this study.

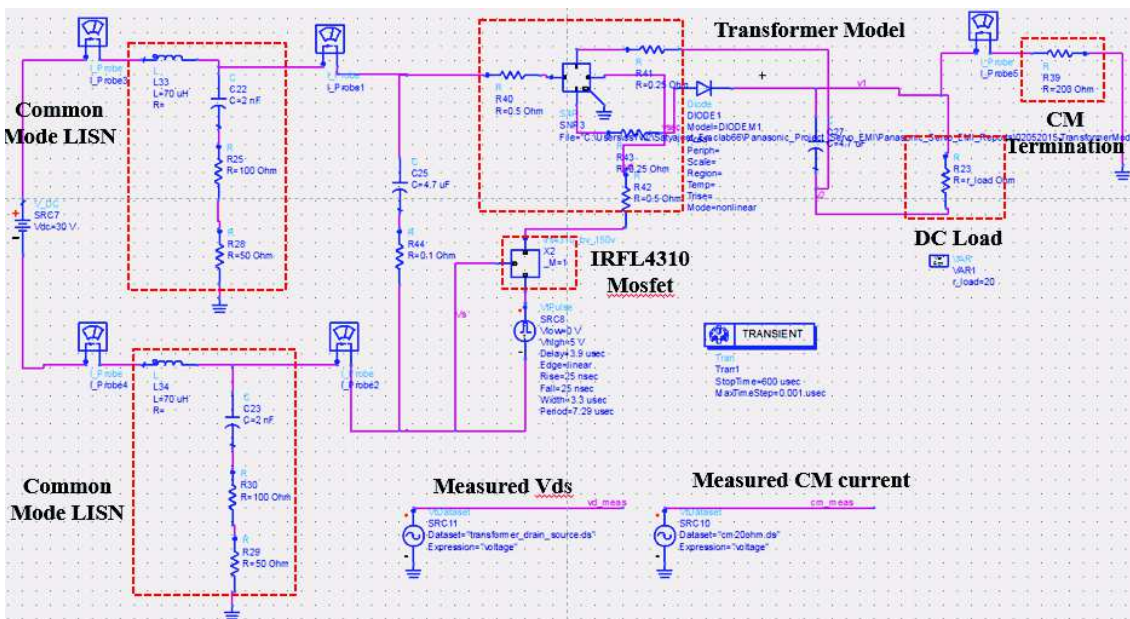


Fig. IV. 14 - Global circuit with common-mode load

Before being able to adequately determine and develop the model for the different parasitic couplings in the custom Flyback board responsible for the creation of common-mode currents, it was

necessary to establish an emulation of a dominant coupling path to ground. A known impedance was inserted into the board and integrated into the circuit simulations, in order to create a preponderant coupling path compared with the real parasitic effects that actually exist in the PCB.

As shown in Fig. IV. 14, the impedance, called **CM Termination** inserted is a 200 Ω resistance. Since this charge allows permits « easy » passage of common-mode currents, it is a well-known fact that the majority of these currents are due to this charge. An impedance value that is too high does not guarantee the preponderance of common-mode path with respect to the other couplings. On the other hand, a too-low impedance value induces a load that modifies the behavior of the actual functional circuit.

This charge is not part of the actual Panasonic converter. However, this step has permitted validation of the models without caring about the true parasitic couplings, making possible to carry out the validation of models through experimentation.

Besides, this resistance provides a well-defined trajectory, which facilitates access for measurement purposes. Otherwise, the evaluation of common-mode currents would have been difficult to achieve and, although this path serves as a point of comparison for simulation, it is not unique. That is why its preponderance is of such importance.

Once the transformer model and the Mosfet have been validated, this type of charge is not necessary.

2.4.2 Examination of couplings between the Mosfet and the Heatsink

Since the drain carries the high dV/dt variations, any parasitic coupling leading to the heatsinks may lead to EMI performance degradation in the system. The heatsink influence has been amply analyzed and discussed in [1] [2], [3].

In order to evaluate the impact of coupling between the Drain and its environment, three configurations were contemplated (Fig. IV. 15).

The approach in use consisted of assessing the parasitic capacitances that could cause *leakage* currents to the ground or to 0 V main power. Whenever possible, these capacitance values were precisely calculable and the results were implemented directly in the stimulation. However, if the values were not easily calculable, we had two options: the estimation based upon experience and the « tuning » on the circuit model, or the retrieval of parameters by Q3D® Extractor (Fig. IV. 18).

In Table IV. 3 are summarized the results of the estimations and/or calculations of parasitic capacitances found in all the different configurations.

Table IV. 2 - Estimated parasitic capacitances

Parasitic Element	Case 1	Case 2	Case 3
C (Drain to Heat sink)	Direct connection	4 pF – 18 pF	4 pF – 18 pF
C (Heat sink to Source)	1 pF	Direct connection	1 pF
C (Heat sink to Chassis)	4 pF – 18 pF	4 pF – 18 pF	Direct connection

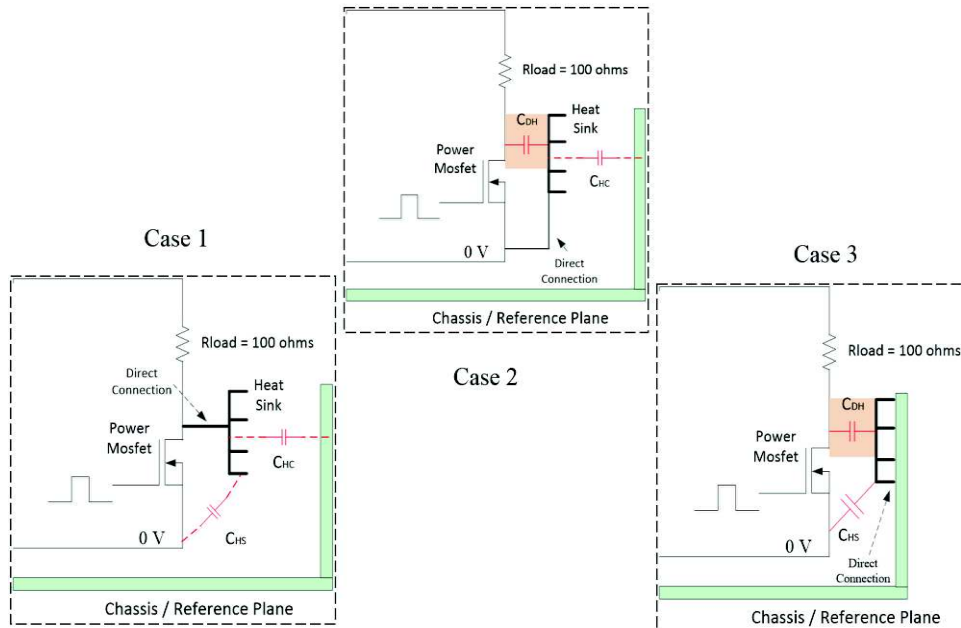


Fig. IV. 15 - Capacitive couplings between the Drain and its environment

With the previous estimates, three circuit stimulations were conducted. Since this was the worst-case estimate, a capacitance of 18pF between the radiator and the ground was retained. A common-mode charge was used, but its value was increased to prevent the charge from being more preponderant than the capacitance effects between the drain and its environment. However, this charge was eliminated after the first results due the fact that the condition of preponderance is no longer met, as shown in the following results.

In order to assess the effects of parasitic capacitances, we simulated the common-mode on the power cable right at the exit of RISL. The length of the cable was kept short to avoid the need to simulate the cable through the method of transmission lines.

Case number 1 was not included, since it's considered to be a rare case where the radiator is set at a potential different than 0. Case 0 is the case of reference, without taking in consideration its parasitic capacitances and with a common-mode charge of 500 Ω. Results are shown in Fig. IV. 16.

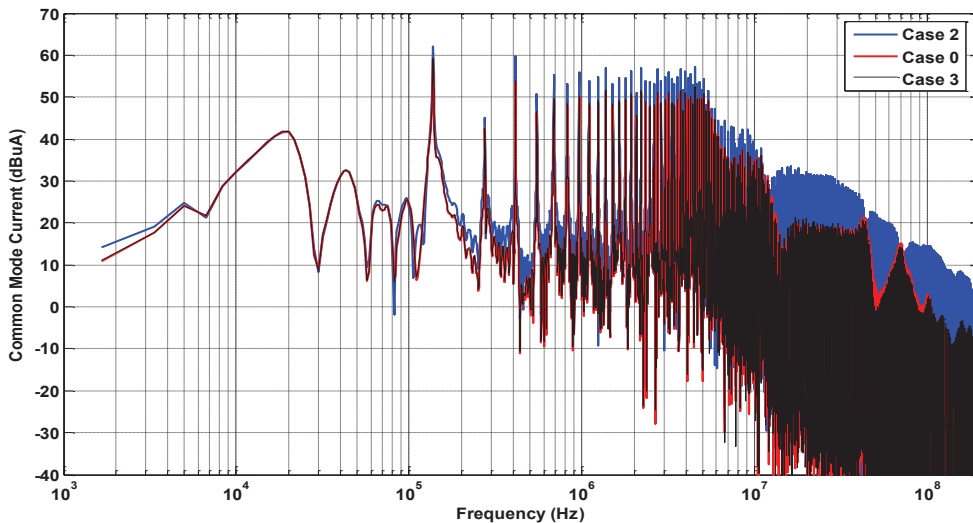


Fig. IV. 16 - Spectrum of common-mode currents flowing through the power cord

A close-up to the results of the simulation between 30 and 200 MHz allows us to appreciate the scale of the effects on the frequency of radiated emissions (Fig. IV. 17). The capacitance effect of the drain-source is marginal compared to the capacitance effect between the drain and the radiator connected to the chassis/ground. An increase of at least 15 dB on most of this frequency range was induced by this capacitance.

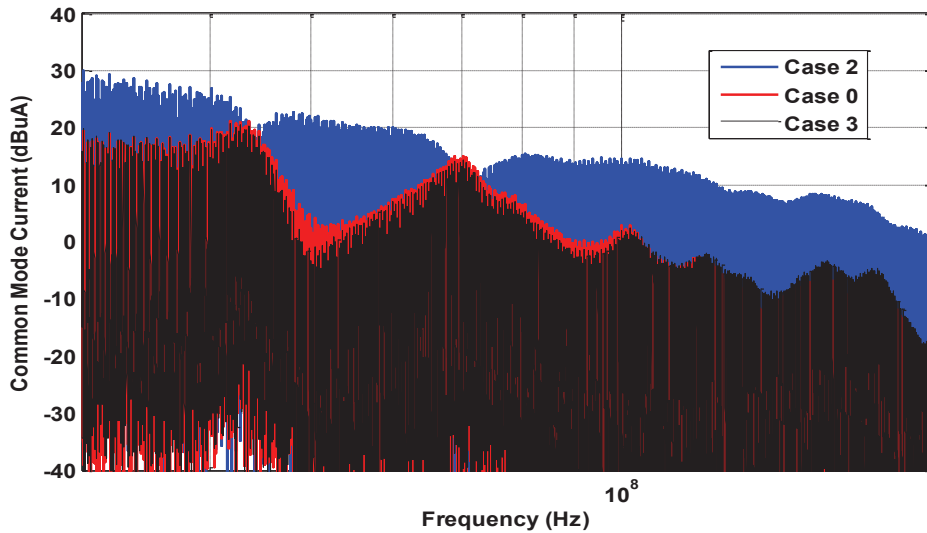


Fig. IV. 17 - Zoom to the high-end frequency spectrum

Model validation through experimentation was performed on the board. We made sure that we controlled the value of capacitance between the radiator and the drain to maintain a capacitance of 14 pF. This value was updated on the circuit model, and the results were similar. However, a lag between certain resonances was observed.

Due to lack of time, the studies on this matter were suspended at this stage.

Furthermore, some preliminary results on the extraction of parameters with Q3D[®] confirmed the estimated values to an approximate of a 20 % relative difference. Fig. IV. 18 shows a 3D model for the parasitic capacitances' extraction done in Q3D[®] modeler.

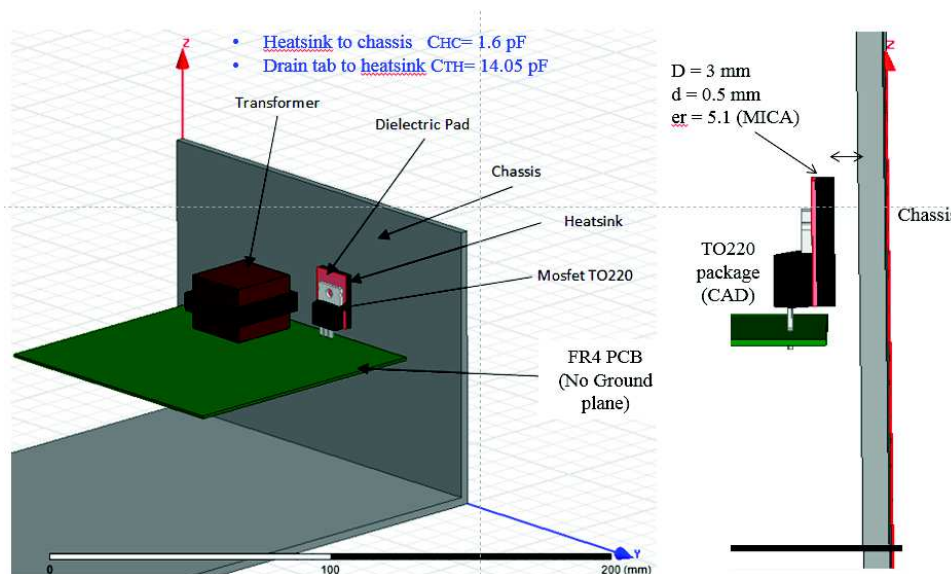
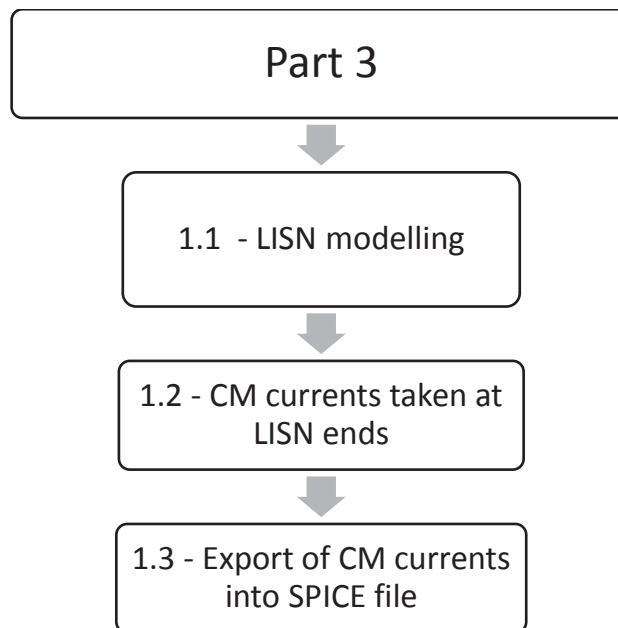


Fig. IV. 18 - 3D model for the parameters' extraction with Q3D[®]

Overall, the circuit model created based on different models of the converter components was validated through the measurement of common-mode currents with a short power supply cable between a Line Impedance Stabilization Network (LISN) and the converter. The simulated common-mode currents at that time were supplied to a cable ranging between 1 and 3 meters between the LISN and the converter.

2.5 PART 3: EXTRACTION OF CM CURRENTS FROM THE CIRCUIT SIMULATION

Here, the extraction of the common-mode currents is done as follows:



2.5.1 Line Impedance Stabilization Network (LISN)

A LISN (Line Impedance Stabilization Network) is connected between the power supply and the converter's input filter. The LISN is a passive impedance network with three main functions (Fig. IV. 19):

- To provide impedance of reference between the ground and test circuit (DUT) (here 150 Ω) equivalent to a port for the analysis of the DUT of RF. It is due to this impedance of reference that the emissions conducted from the DUT may be analyzed using measurement devices such as specter analyzers.
- To create a low-pass filter to eliminate conducted HF emissions from the power supply to the DUT.

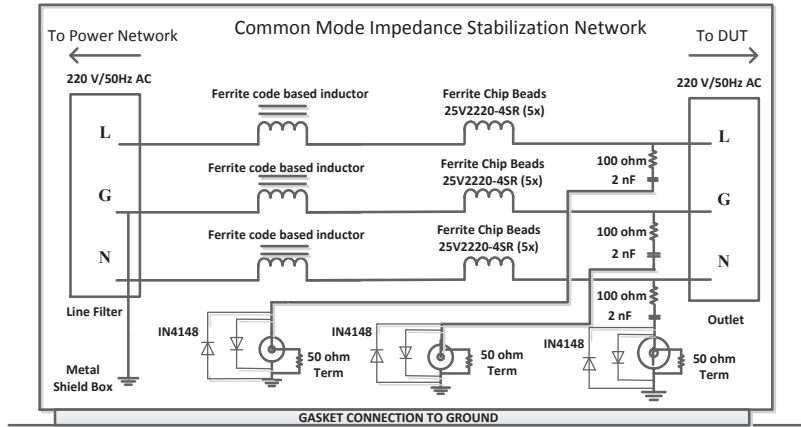


Fig. IV. 19 - Line impedance Stabilization Network (LISN) schematics

The equivalent model is presented in Fig. IV. 20

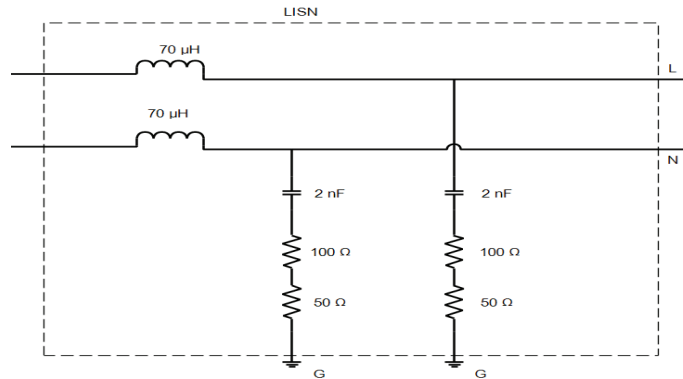


Fig. IV. 20 - Equivalent LISN circuit model

Fig. IV. 21 presents the schematic drawing of the principles of a Flyback converter whose power supply comes from a continuous source through the impedance stabilization network (equivalent model). This set up will remain in use throughout the whole study. It is quite a different model from the one implanted in the servo motor system. However, the results that are obtained with this model will also be applicable to the original Flyback study, thus enabling use to analyze the validity of the methods used for the entire system.

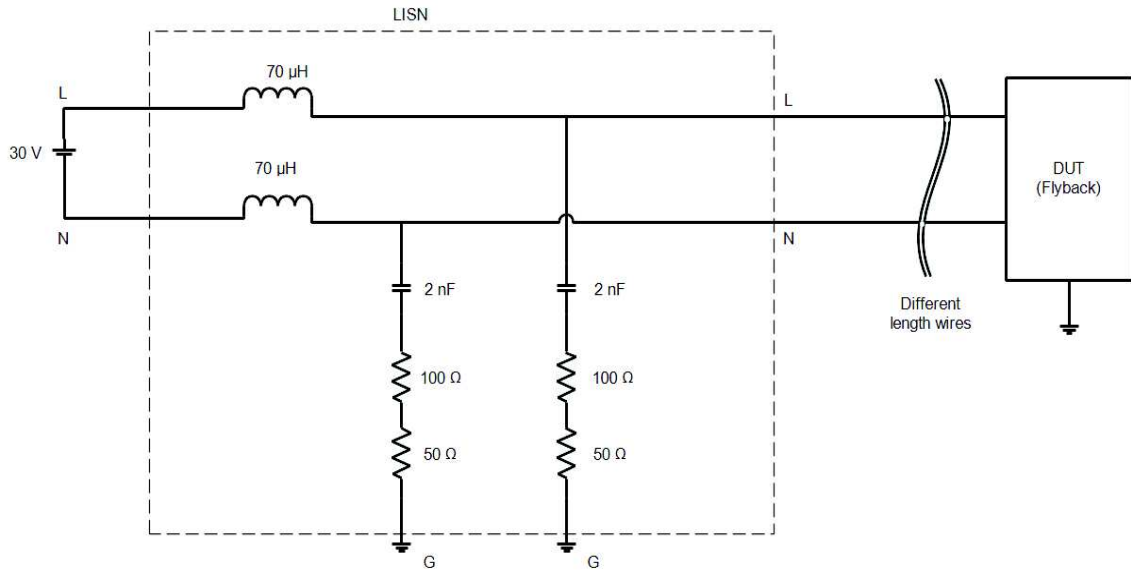


Fig. IV. 21 - Flyback fed through a LISN

The equivalent impedance of reference introduced through LISN is 150 Ω. Hence, the normalized DUT impedance is 150 Ω.

2.5.2 Plotting of CM currents and Export

It is at the LISN ends *L* and *N* that the common-mode currents are observed. Within the simulation, the currents flowing through *L* and the currents flowing through *N* are plotted as follows:

$$I_{CM} = \frac{I_L + I_N}{2}$$

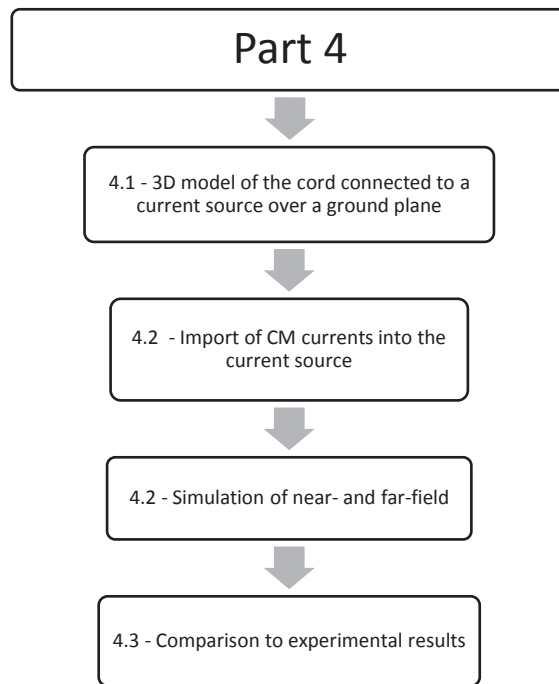
The resulting currents are plotted against frequency and the vector exported as a SPICE-like file. These are the currents responsible for the CM-induced radiated emissions of the power cord.

2.6 PART 4: ASSESSMENT OF RADIATED EMISSIONS WITH THE CM CURRENTS RETRIEVED FROM THE SIMULATION

There are analytical methods to predict the maximum radiation for cables under very specific configurations [4]. However, restrictive conditions, such as the impossibility to have a cable in a random position or the need to have a ground plane underneath the cable, have fostered the use of full-wave simulation.

Full-wave simulation may be performed through finite elements in the frequency domain (FEFD) such as in the case of Ansoft® HFSS Finite Difference Time Domain (FDTD) in the case of CST® Microwave Studio [5], [6].

The procedure is as follows:



2.6.1 Structure’s 3D model, currents import and simulation

The structure consists of a cable over a ground plane in a CISPR-25 configuration. The current source attached to the end of the cable is assigned with the CM file imported from the circuit simulation. This is not further detailed.

In this case study we chose to use CST as the full-wave field calculation software. The approach for analysis was as described in Fig. IV. 23.

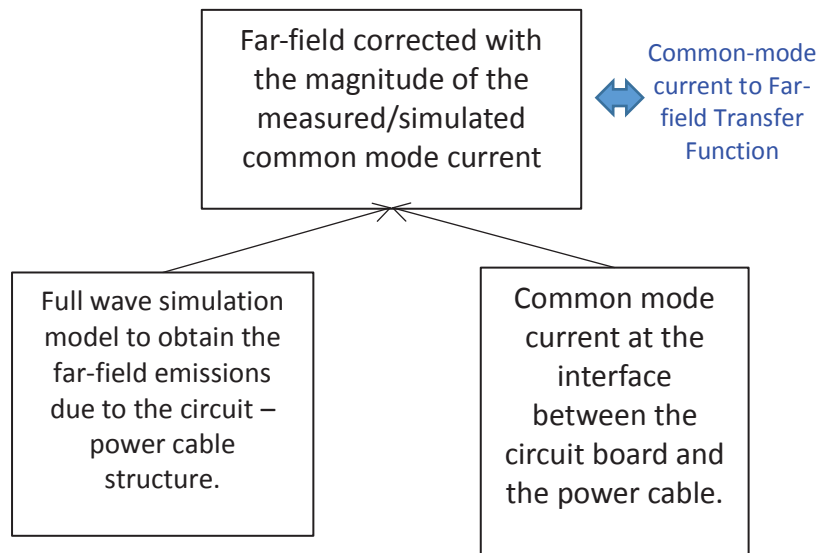


Fig. IV. 22 – Approach to predict radiated emissions of the Flyback’s power supply cable

2.6.2 Comparison to experimental results

The experimental configuration is described in Fig. IV. 23.

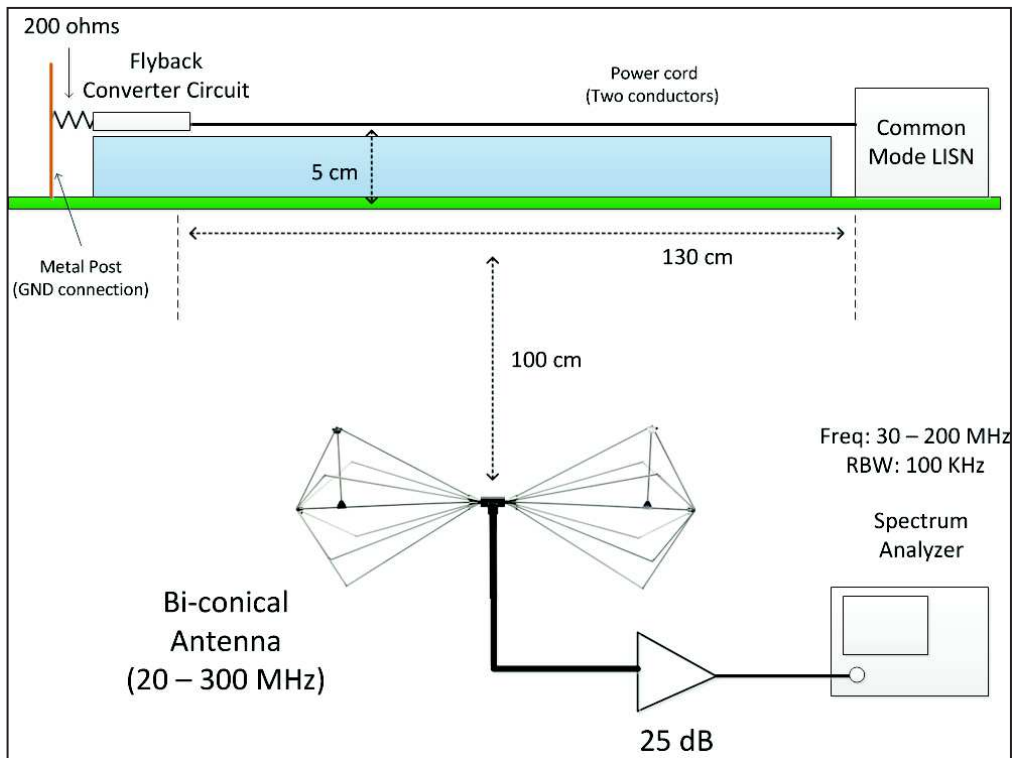


Fig. IV. 23 - Experimental protocol for the measurement of radiated emissions

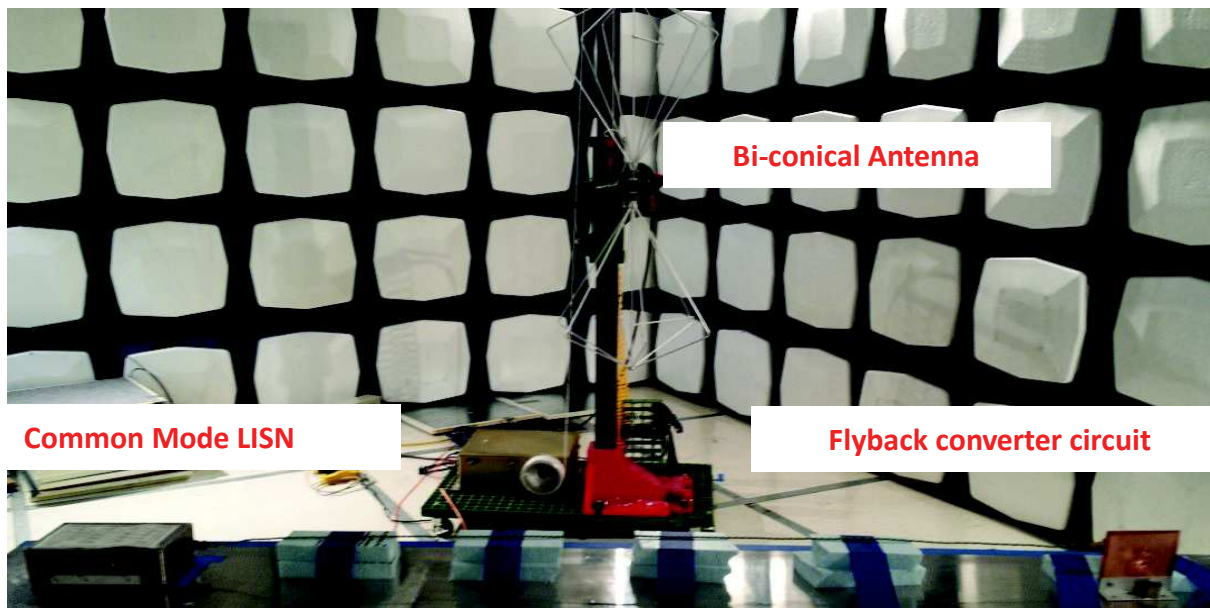


Fig. IV. 24 – Physical setup for experimental measurements of radiated emissions

The configuration is very similar to the one imposed by CISPR-25 standards.

The first stage of this analysis was to validate the model for the full-wave simulation. In order to do this, we did not use the simulated currents but the measured currents.

The common-mode current measurement (Fig. IV. 25), was performed along a twisted pair with a length of 1.5 in intervals of approximately 30 cm.

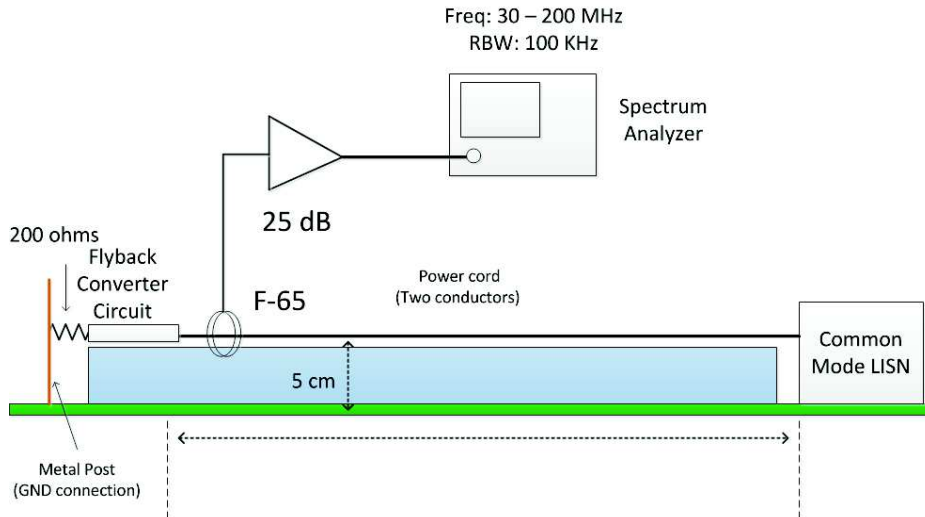


Fig. IV. 25 - Setup for the common-mode current measurement in semi-anechoic chamber

For all the experimental stages of this study (validation of included models, parts 1 and 2), the Resolution Bandwidth (RBW) for current measurement was kept at 100 kHz because the CISPR-25 norm anticipates this RBW for the radiated field measurements. Thus, the measured currents to be used for the validation of the full-wave model have constantly had the same resolution bandwidth.

The validation results for the full-wave model are summarized in Fig. IV. 26. The error between the simulation and the observed measurement between 40 and 60 MHz with the antenna in a vertical position could be related to currents flowing on the vertical wall of the LISN and on the plate representing the chassis due to the common-mode charge, but this hypothesis was not validated due to lack of time. The distance of measurement is 1 m.

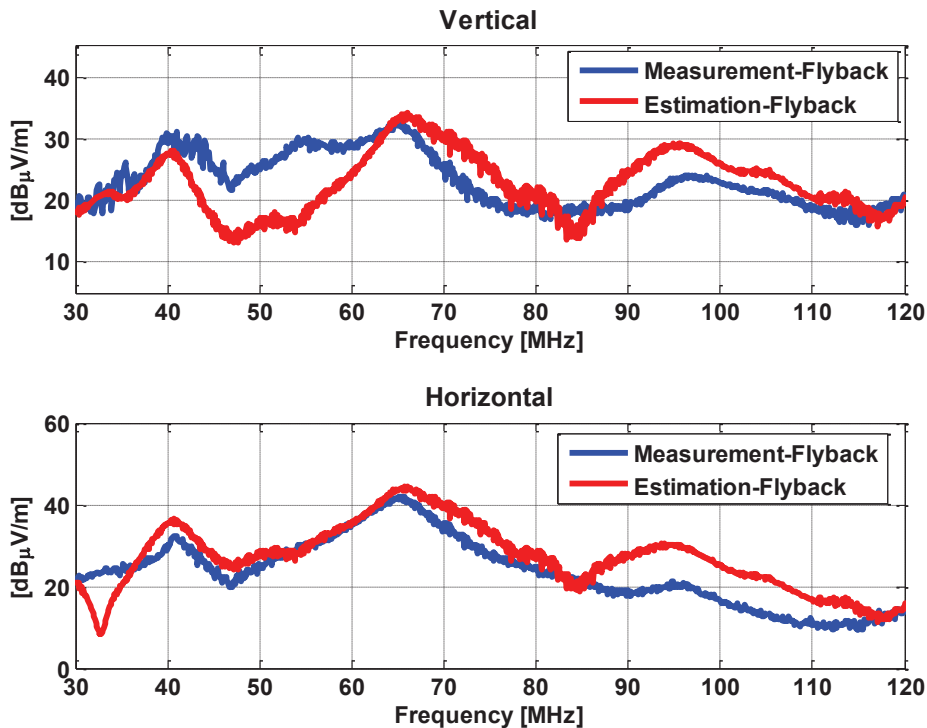


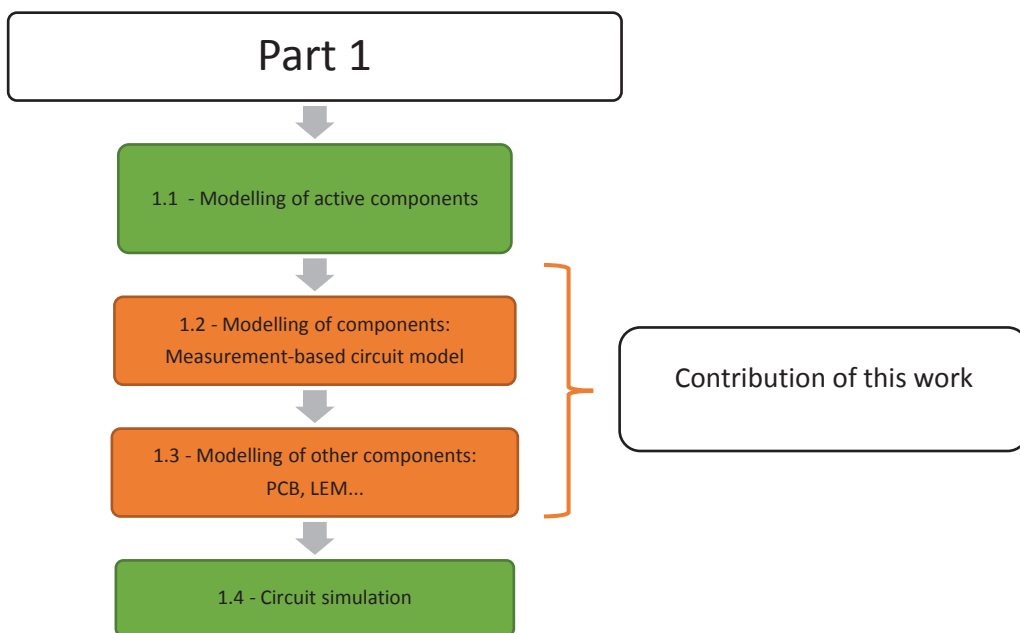
Fig. IV. 26 - Comparison of the radiated emissions by measurement and by simulation

Since the full-wave model is validated, although some details are still to be refined, we can assume that the prediction regarding the radiated emissions with the simulated currents will correspond to reality.

3 EMOD ANALYSIS AND RATIONAL PREDICTIVE MODELS INCLUSION

As could be seen in the first paragraph of this chapter, full-scale validation techniques exist to study EMC and EMI on power systems. It is divided in 4 parts.

However, improvements can be achieved by including the techniques presented in Chapters II and III of this thesis. More specifically, the improvements can be applied to achieve a fully predictive set of methods and techniques for EMC/EMI prediction. The contributions made by this work is highlighted hereafter:



The above studied Flyback converter used measured-built models to perform circuit simulations on the transformer. Also, the Flyback converter was purposely built on a custom PCB for its analysis.

The idea in this part is to include the predictive tools synthetized in Chapters II and III into the same philosophy of analysis of EMC and EMI as for the Flyback.

3.1 EMOD: FAULT-TOLERANT TRACTION SYSTEM

The system under consideration is a fault-tolerant multiphase Switched Reluctance Motor (SRM) machine composed of several magnetically and electrically independent modules **designed and patented by NOVATEM**. Each magnetic module is fed by an independent power converter. The system is presented in Fig. IV. 27. The 20 kW, 14 krpm motor is designed for vehicle traction.

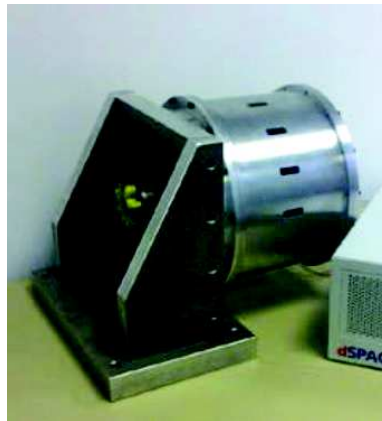


Fig. IV. 27 - EMOD motor

In Fig. IV. 28 is depicted the stator of the considered system. It can be seen that every magnetic module is mechanically and electrically independent of each other.

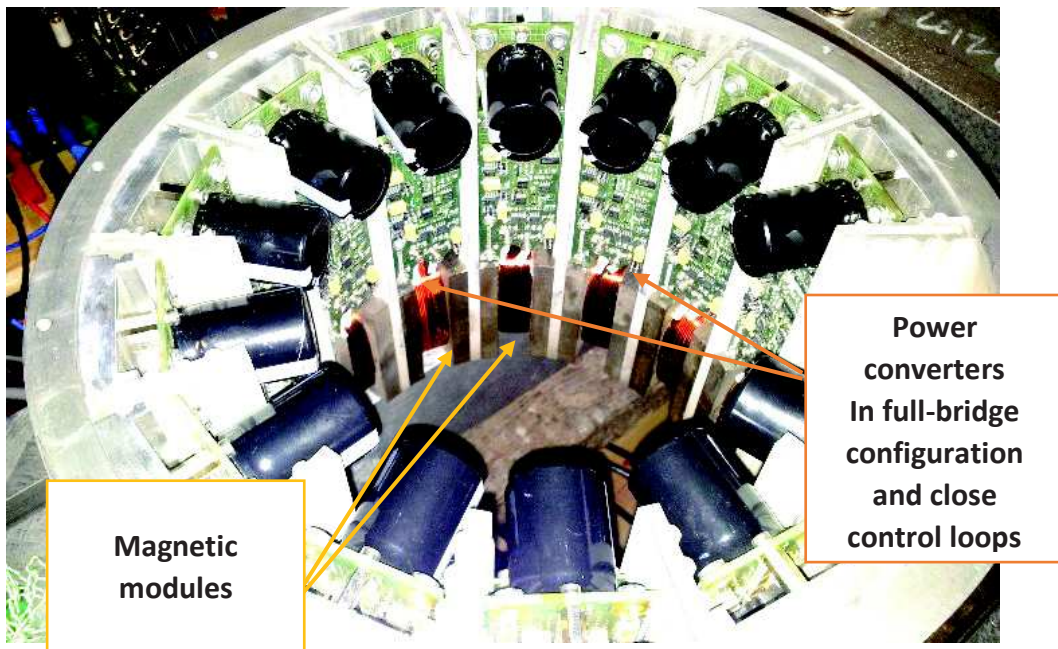


Fig. IV. 28 – Stator of EMOD motor with magnetic modules and their attached power electronics

A single module is pictured in Fig. IV. 29. It is accolated to its power converter and DC power cables.

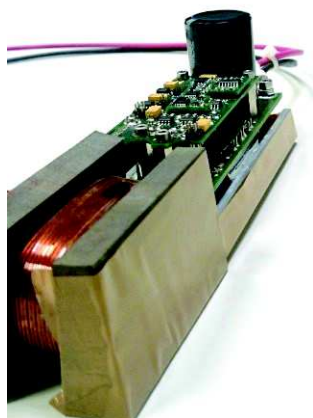


Fig. IV. 29 - Single module and power converter for 1 phase

3.2 MOTOR WINDING

The magnetic module creates the magnetic field necessary to the machine to create the torque. The converter element feeds the winding (concentric coil) of the magnetic element with a specific current form and amplitude according to the position of the rotor and the demanded torque and speed conditions.

The winding is a 7-layer and 14 turns per layer winding over a Soft Magnetic Compound (SMC) core (cf.II.5.1). The winding was made in a “two in hand” manner. This means that two parallel wires were used to make the turns, thus creating two parallel turns every time. Therefore, the magnetic behavior of the module corresponds to a 7-layer and 7 turns per layer coil in parallel with another 7-layer and 7 turns per layer coil.

Fig. IV. 30 shows the wires wound in a regular way around the pole. Physical parameters of the winding are presented in Table IV. 3. The center of the pole supporting the winding has a rectangular cross section with rounded corners, which differs from the circular shape used in previous parts of the work. Besides, the pole has a particular shape causing the external turns of each layer to be adjacent to the core. However, with similar hypotheses as for the analytical calculations, we can show that the only changing factor is the turn length and for the external turns of each layer in contact of the core over a certain length, we consider the same behavior of turn-to-core capacitance as for the inner turns against the central core. Symmetries and invariances are conserved so hypotheses are the same.

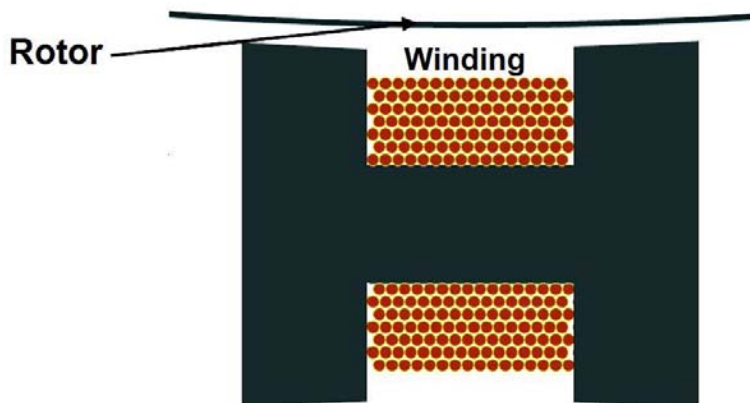


Fig. IV. 30 - Cross-sectional view of the winding

Table IV. 3 -EMOD winding and core parameters

Parameter	Symbol	Value	Unit
Number of layers	N_l	7	-
Number of turns per layer	N_t	14	-
Copper wire diameter	D_c	1	mm
Coating thickness	e	0.08	mm
External wire diameter	D_0	1.16	mm
Ferromagnetic core length	L	52	mm
Ferromagnetic core width	l	18	mm
Ferromagnetic core height	h	17	mm
Coating relative permittivity	ϵ	3.5	-
Core relative permeability	μ	75	-
Copper resistivity	ρ	1.67e-8	$\Omega.m$

3.3 POWER CONVERTER

The power converter feeding the winding current converter was partially presented in §III.3.3. Indeed, the PPCB that served for the partial parameters extraction is the actual PPCB of this application. Therefore, no more details on the PCB modelling will be treated. Only the details on the electronic components are here discussed.

In Fig. IV. 32 is recalled the power converter circuit and its components. It is composed of an integrated module APTGF30H60T1G containing 4 IGBT switches arranged in full bridge configuration [7]. It is manufactured by Microsemi® and is based in Non-Punch Through IGBT NPT-IGBT technology. NPT-IGBTs are the fastest switching Silicon IGBTs commercially available. The main characteristics of the module are presented in an extract of its datasheet in Fig. IV. 31.

Absolute maximum ratings

<i>Symbol</i>	<i>Parameter</i>		<i>Max ratings</i>	<i>Unit</i>
V_{CES}	Collector - Emitter Breakdown Voltage		600	V
I_C	Continuous Collector Current	$T_C = 25^\circ C$	42	A
		$T_C = 80^\circ C$	30	
I_{CM}	Pulsed Collector Current	$T_C = 25^\circ C$	100	
V_{GE}	Gate – Emitter Voltage		± 20	V
P_D	Maximum Power Dissipation	$T_C = 25^\circ C$	140	W
RBSOA	Reverse Bias Safe Operating Area	$T_j = 125^\circ C$	60A@500V	

Fig. IV. 31 - Main characteristics of Microsemi IGBTs

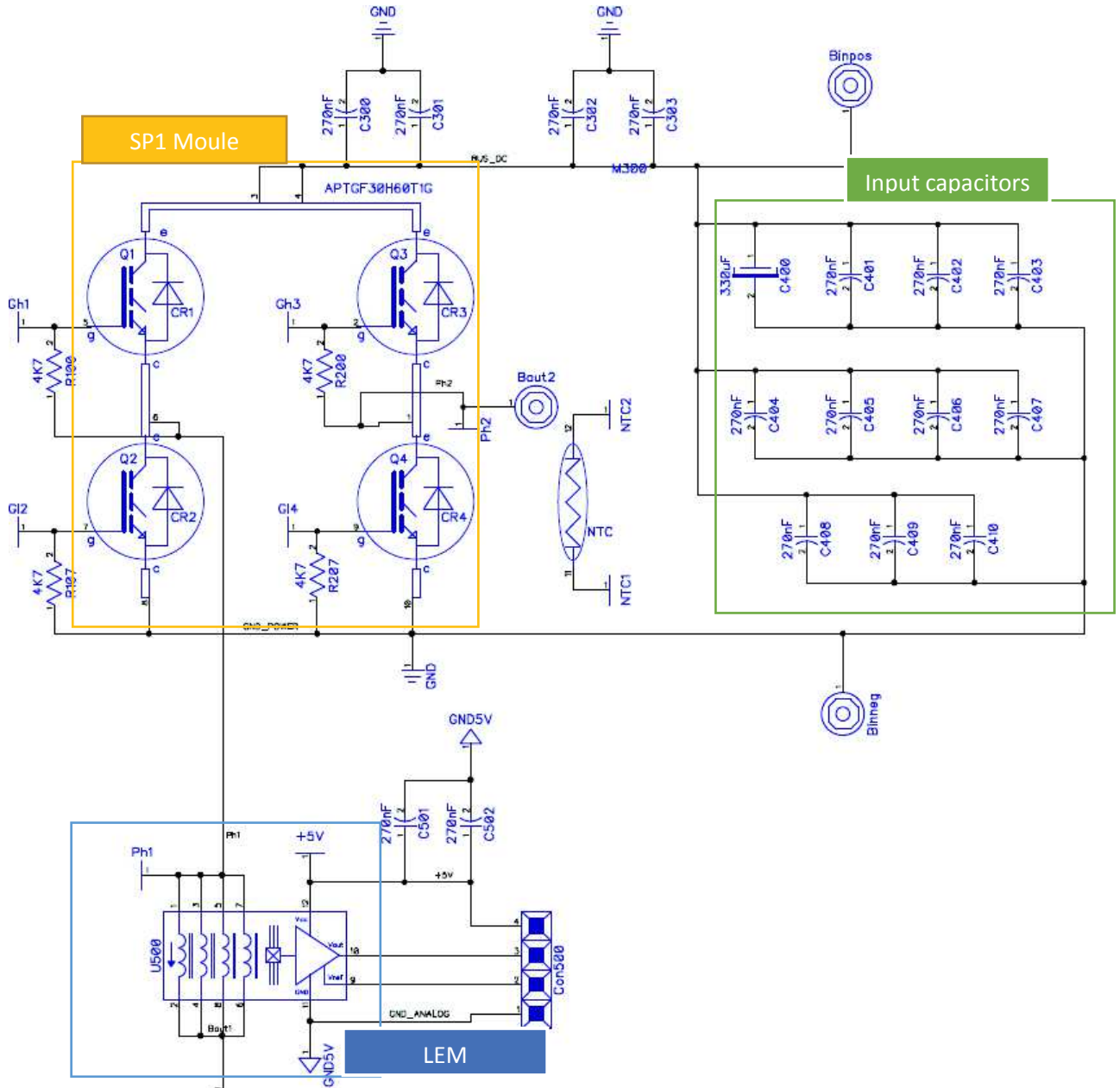


Fig. IV. 32 – Power stage of the converter

The drivers used here are two Infineon® IRS21864S Mosfet drivers with bootstrap capabilities for High and Low operation. Its main characteristics are resumed in Fig. IV. 33.

Symbol	Definition	Min.	Max.	Units
V_B	High-side floating supply absolute voltage	$V_S + 10$	$V_S + 20$	V
V_S	High-side floating supply offset voltage	COM -8 (Note 2)	600	
V_{St}	Transient high-side floating supply offset voltage	-50 (Note 3)	600	
V_{HO}	High-side floating output voltage	V_S	V_B	
V_{CC}	Low-side and logic fixed supply voltage	10	20	
V_{LO}	Low-side output voltage	0	V_{CC}	
V_{IN}	Logic input voltage (IN & SD)	V_{SS}	V_{CC}	
DT	Programmable deadtime pin voltage (IRS21844 only)	V_{SS}	V_{CC}	
V_{SS}	Logic ground (IRS21844 only)	-5	5	°C
T_A	Ambient temperature	-40	125	

Fig. IV. 33 - Main characteristics of Infineon Mosfet gate driver

The driving circuit is detailed in Fig. IV. 34.

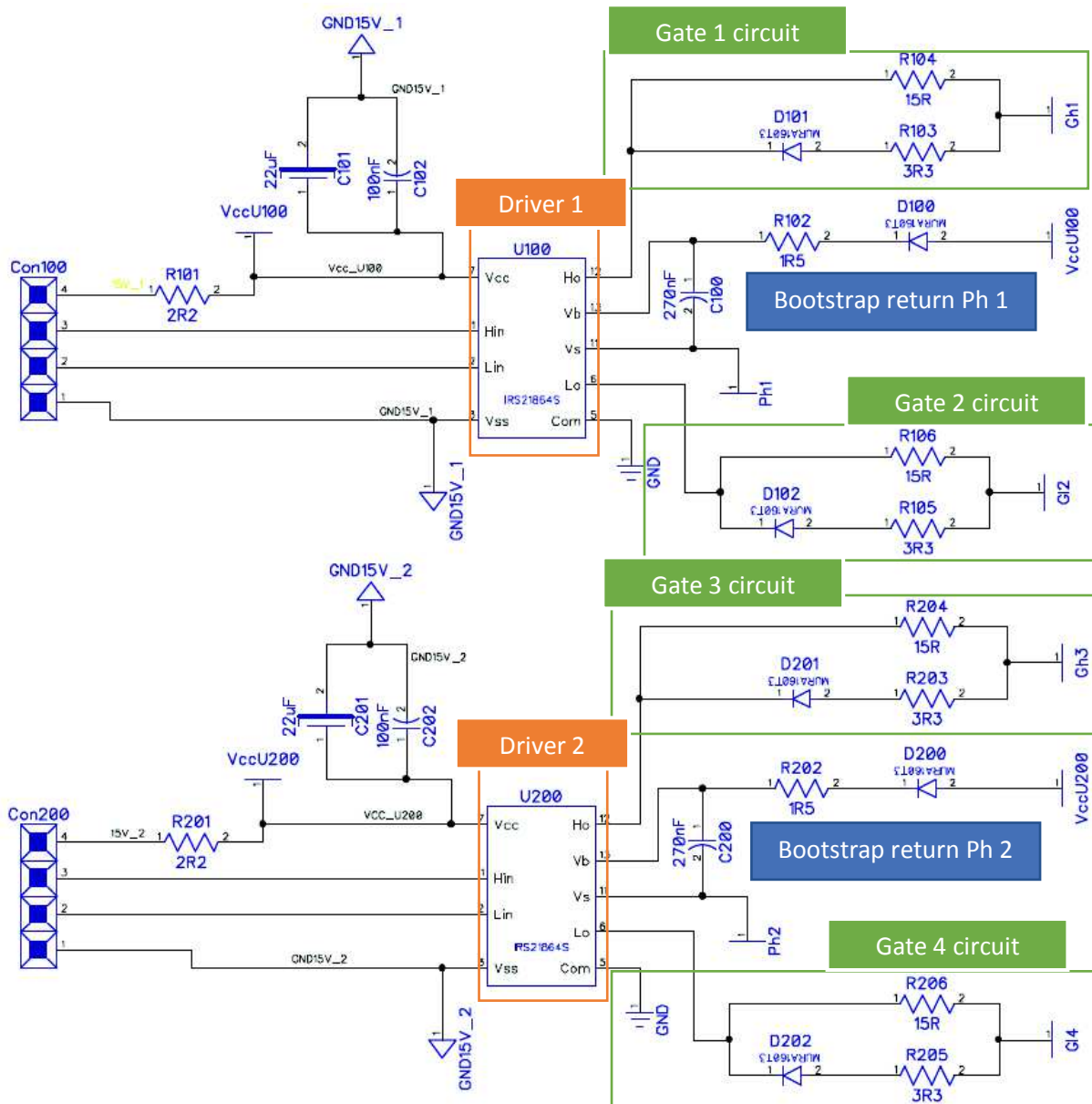


Fig. IV. 34 - Close control stage of the converter

The functional parameters of the power converter are resumed in Table IV. 4.

Table IV. 4 - Functional parameters of the power converter

Function	Max equivalent frequency
Driver rise/fall slopes (18-20ns)	17-20 MHz
Driver/IGBT switching frequency (PWM freq)	33 kHz
IGBT rise/fall slopes (200-300 ns)	1.5-2 MHz
DC Voltage	300 V

4 MODELLING AND CIRCUIT SIMULATION OF EMOD

4.1 CIRCUIT MODEL OF THE WINDING

As described in Chapter II, the modelling procedure was applied to the magnetic module of the present application.

The differential-mode impedance is pictured in Fig. IV. 35. Again, different values of inductance were calculated at several frequencies.

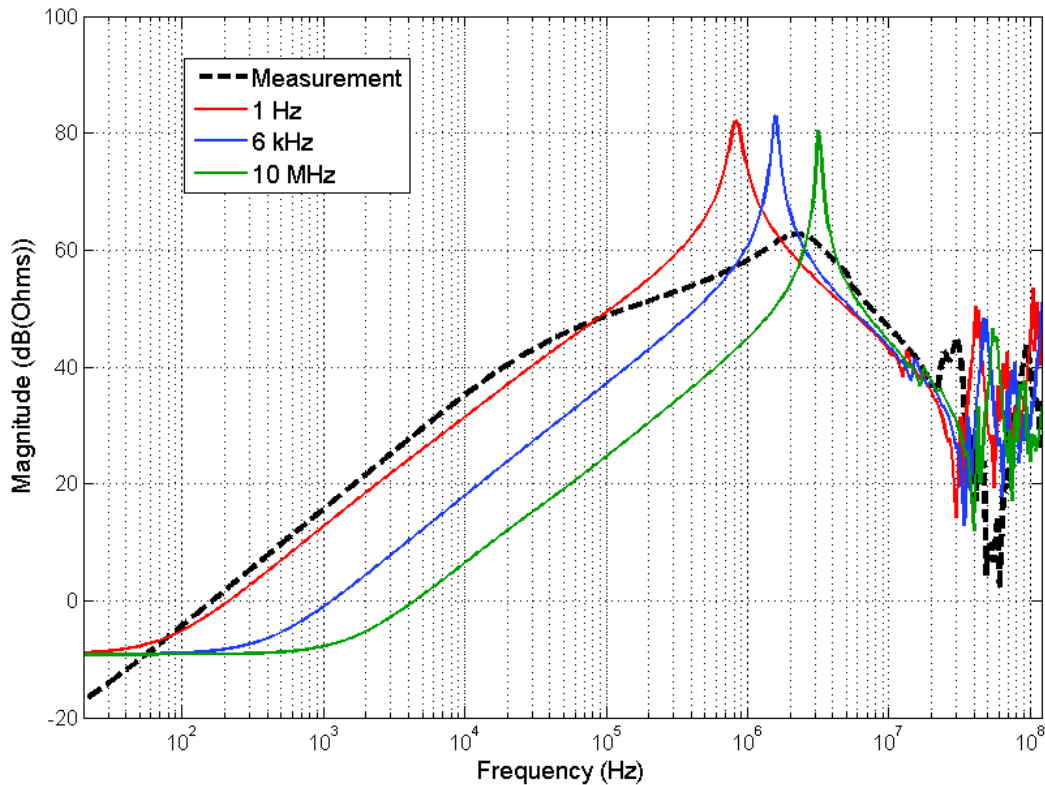


Fig. IV. 35 - Measured and simulated differential-mode impedance of an EMOD winding

Not being able to include frequency dependence of permeability is a fundamental problem to solve for circuit simulation.

For the purposes of this analysis, it will be assumed that, the closest simulated impedance behavior to the measured one will be representative of the full frequency and time domain behavior of the module. As can be seen in Fig. IV. 35, the simulated impedance with inductances calculated at 1 Hz is the closest to the measured one. Thus, this model at 1 Hz will be kept to the global simulation.

Ideally, the circuit model of the winding should include dispersion for permeability and permittivity. But it is not possible for now. For the demonstration purposes, it is therefore assumed that the model established with inductive parameters at 1 Hz is representative of the full frequency behavior. The impedance is again plotted in Fig. IV. 36 to show the resulting comparison.

Now, considering that several parameters are not taken into account, such as iron losses, this model is only valid for low-level signals. This allows to ignore core losses, and saturation effects. As mentioned in Chapter II, a lot can be improved in this modelling technique. But for now, let us consider that the real behavior is well represented.

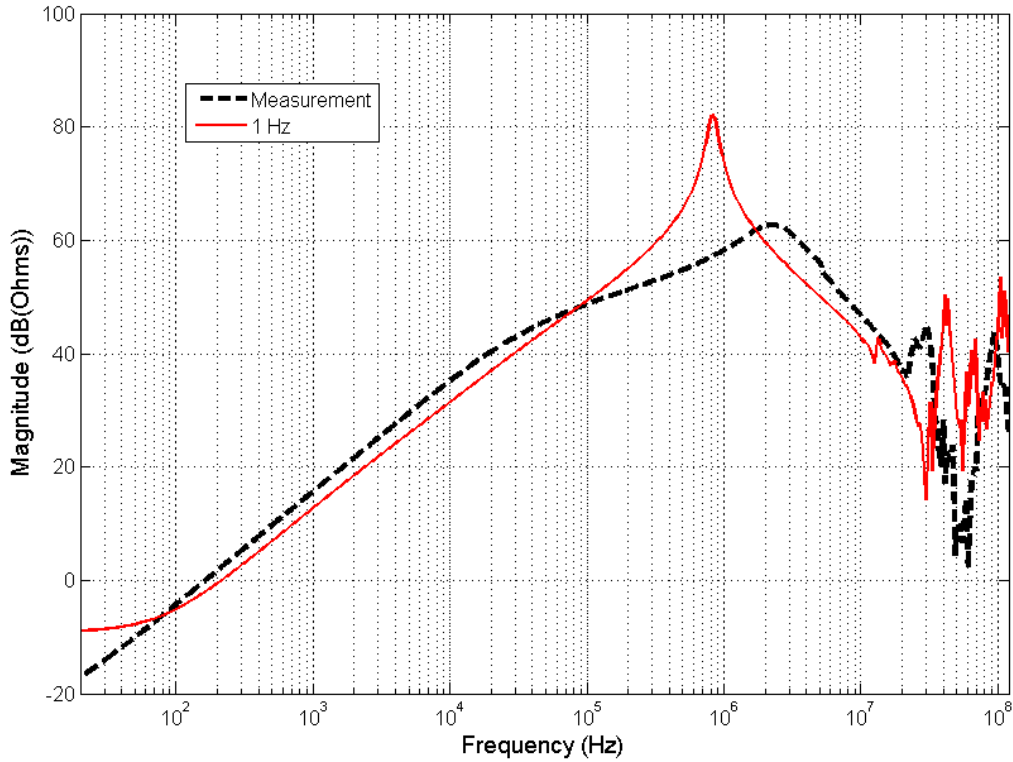


Fig. IV. 36 - Measured DM impedance and simulated impedance extracted at 1 Hz

4.2 POWER CONVERTER CIRCUIT MODEL AND SPICE FILES

The global simulation is performed in LTSpice.

In order to simulate the active components and fast diodes, manufacturer-made SPICE files were used in the circuit simulation.

4.2.1 Full bridge IGBT module

Unfortunately, Microsemi® doesn't provide a SPICE simulation file for the APTGF30H60T1G. However, Infineon provides SPICE simulation files for various NPT-IGBTs. The strategy is then to modify the SPICE file of a similar NPT-IGBT from Infineon. The reason why this can somewhat easily be done, is that SPICE files from Infineon IGBT files are physical models based in Kraus models [8]. The NPT-IGBT file from Infineon is the SKW30N60HS.

The main characteristics of both technologies are compared and are virtually the same as can be seen in their respective datasheets [7], [9].

The main parameters modified in the Infineon file are the dynamic characteristics, and especially, the Gate charge, since the gate charge is responsible for the turn-on and turn-off times. To compare both technologies, Table IV. 5 resumes the dynamic characteristics of Microsemi and Infineon IGBTs.

Table IV. 5 - Dynamic characteristics of both IGBT technologies

Parameter	Microsemi APTGF30H60T1G	Infineon SKW30N60HS
Input capacitance	1350 pF	1500 pF
Output capacitance	193 pF	203 pF
Reverse transfer capacitance	120 pF	92 pF
Total gate charge	99 nC	141 nC

Once the SKW30N60HS SPICE file modified, 4 IGBT models were included into the global circuit model.

4.2.2 Drivers and gate circuit fast diodes

For the Infineon driver, SPICE models exist. Also, the SPICE file of the MURA16 diode is available from ON® semiconductor’s website.

4.2.3 LEM current transducer and voltage probe

The LEM sensor HSX 50 uses on a combination of Hall Effect and a current transformer to build the image of the phase current flowing through the winding and producing a voltage proportional to the measured current. The resulting voltage can be measured for control and protection purposes. But the transformer induces a voltage drop corresponding to its impedance which is modeled by series 25 nH inductance and 20 μΩ resistance given by the manufacturer.

The model of the voltage probe was also included into the global circuit simulation so its parasitic contributions can also be accounted for.

4.3 RESULTING GLOBAL CIRCUIT

The PCB with the extracted parameters from Chapter III is then used for the global circuit simulation.

The resulting global circuit is presented in Fig. IV. 37.

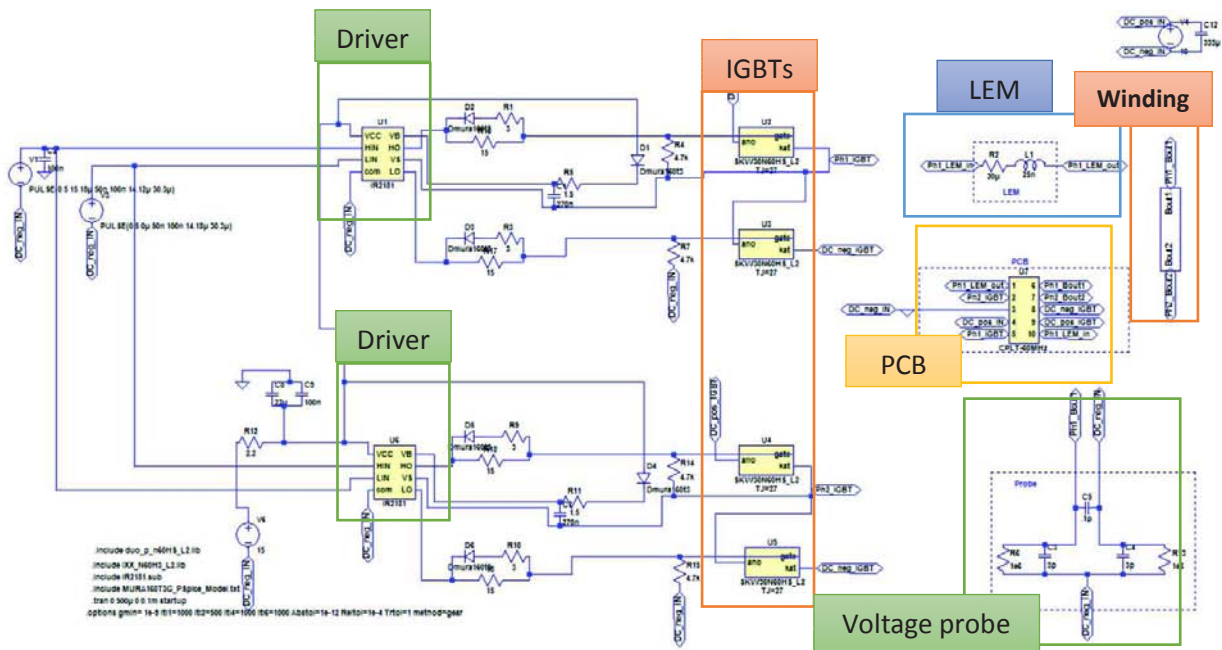


Fig. IV. 37 - Global circuit model of an EMOD phase

5 VIRTUAL EXPERIMENTATION ON EMOD

The leading idea for the virtual experimentation on the EMOD magnetic module and its power converter is that every voltage and current can be virtually accessed and analyzed. Thus, the common-mode currents that could be needed to evaluate radiated emissions from the power cord, could be directly obtained without the need of measured-based models nor custom-made PCBs as for the Flyback converter.

It is essential to keep in mind that the setup for the below simulations is set taking the experimental setup in mind:

- For this analysis, the input DC voltage is kept at 10 V in order to allow for HF instruments in experimental tests to correctly handle the signals magnitude and to keep the low-level signal conditions for the magnetic module valid;
- PWM switching frequency is set to 33 kHz;
- The duty cycle of the converter is kept constant and close to 50 %. This is to limit the current fed into the magnetic circuit and therefore, the current drawn from the DC source through the IGBTs;
- The control signals (PWM signals) are generated with a signal generator, allowing us to isolate the close control and the power from the control stage. The control signals are simulated to behave as the real signals coming from digital optocouplers. Rise and fall times coming from the optocouplers were independently measured and their value estimated at 60 to 80 ns. These signals are the input signals into the drivers. In the simulation they are represented by switched sources.

Although measurements were performed, the experimental results are not presented here. The reason is that some measurements were not well performed and problems with the utilization of the LISN made measurements to introduce a great amount of uncertainty. These problems have to be corrected before comparing again with simulations and draw conclusions on simulation performance. The experimental data is essential to validate the modelling and simulation tools from a real-life application point of view. Efforts need to be done to perform these experimental validations, but keep in mind that, the validation of partial models of the PCB and winding has been carried out in the above sections of this work.

Nevertheless, the virtual experimentation is shown in order to illustrate the capabilities of the rational method of modelling and integration into the circuit simulator. Besides, this method completes the already performant RE predictions method described in the first part of this chapter.

By assuming that the validation of all the partial components can be equivalent to the validation of the global model, the analysis can be sustained. Of course, this can be questionable, but the demonstration can then be completed. Hopefully, the experimental validation would be done in the future.

5.1 EXAMPLE OF SOME FUNCTIONAL SIGNALS

The output voltage (phase voltage) and the load current flowing through the winding are here analyzed in two configurations: in one case, the global model includes the PCB model, and in the second case, the PCB model is ignored. The output voltage of the converter is virtually measured with a voltage probe at the leads of the winding. The comparison in time-domain is presented in Fig. IV. 38 and Fig. IV. 39.

It can be seen that the low voltage used for this setup affects the delivery of a proper squared-shaped voltage to the load. A small step is seen at the top of each voltage square. However, this disappears with increasing DC voltage.

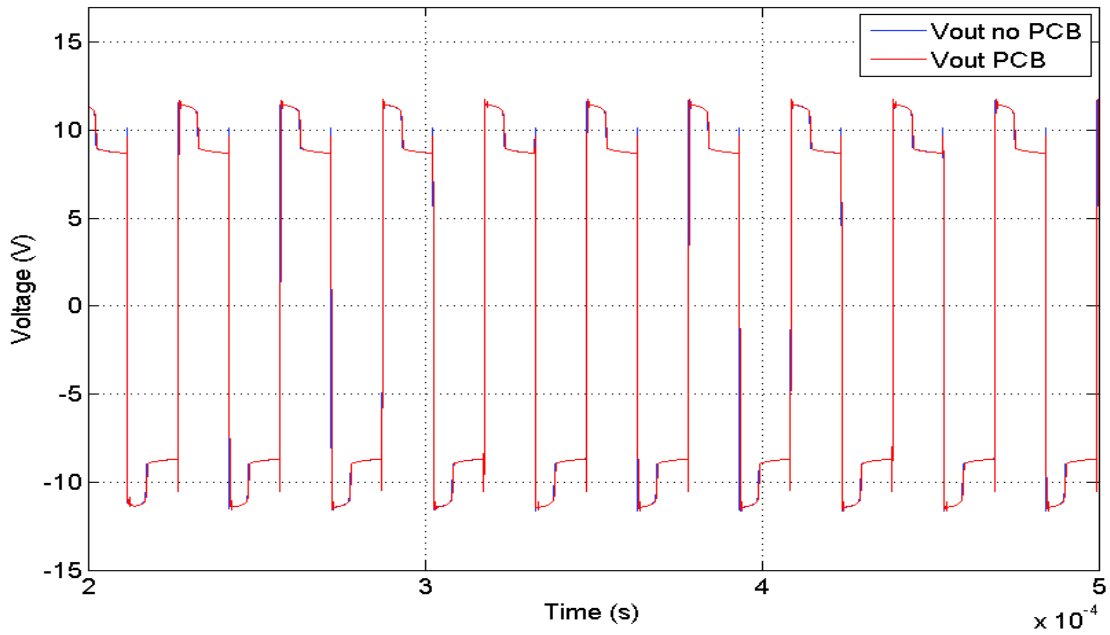


Fig. IV. 38 - Output voltage with and without the PCB model

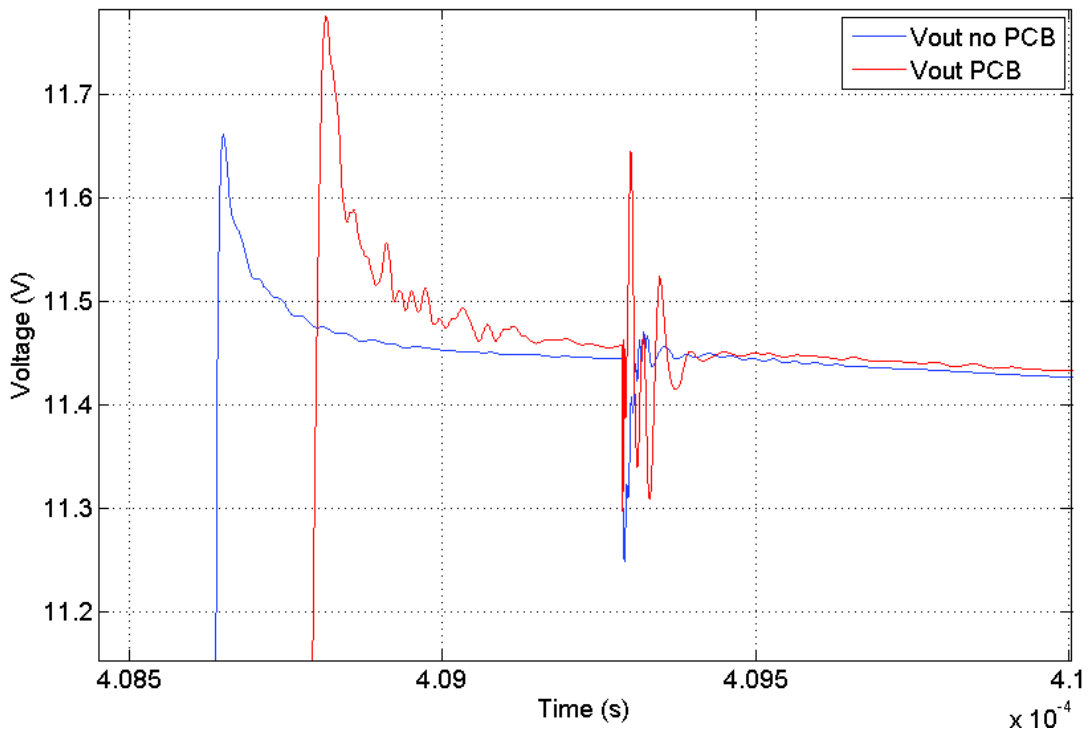


Fig. IV. 39 - Differences at switching of output voltage with and without PCB model

It can be observed that the inclusion of the PCB into the simulation modifies the response of the output voltage. Parasitic elements as plane inductance and capacitance between the power planes induce resonances in the impedance seen by the load.

The load current is also plotted in Fig. IV. 40 and Fig. IV. 41.

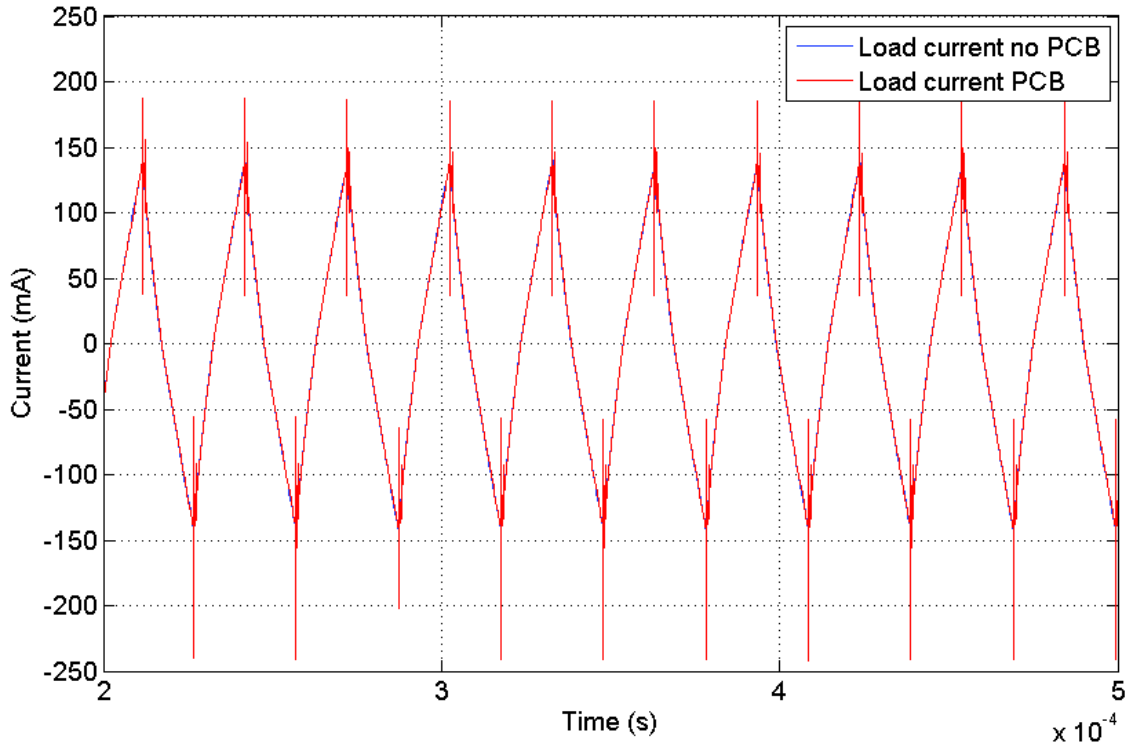


Fig. IV. 40 - Load current with and without PCB model

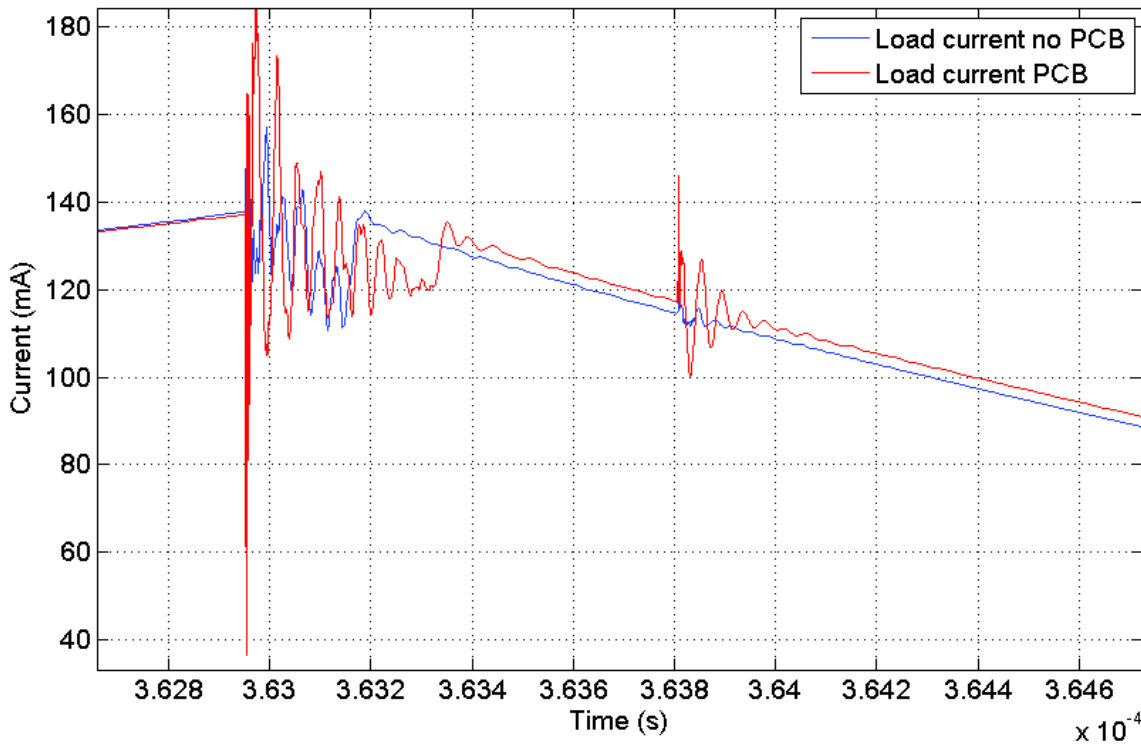


Fig. IV. 41 - Differences of the two load currents at switching

Although the impact of the PCB traces and planes involved in the delivery of V_{out} and the load current is very low, the difference show that each parasitic parameter in the system modifies the general behaviour. This difference can also be found in the FFT of the two load currents is presented in Fig. IV. 42.

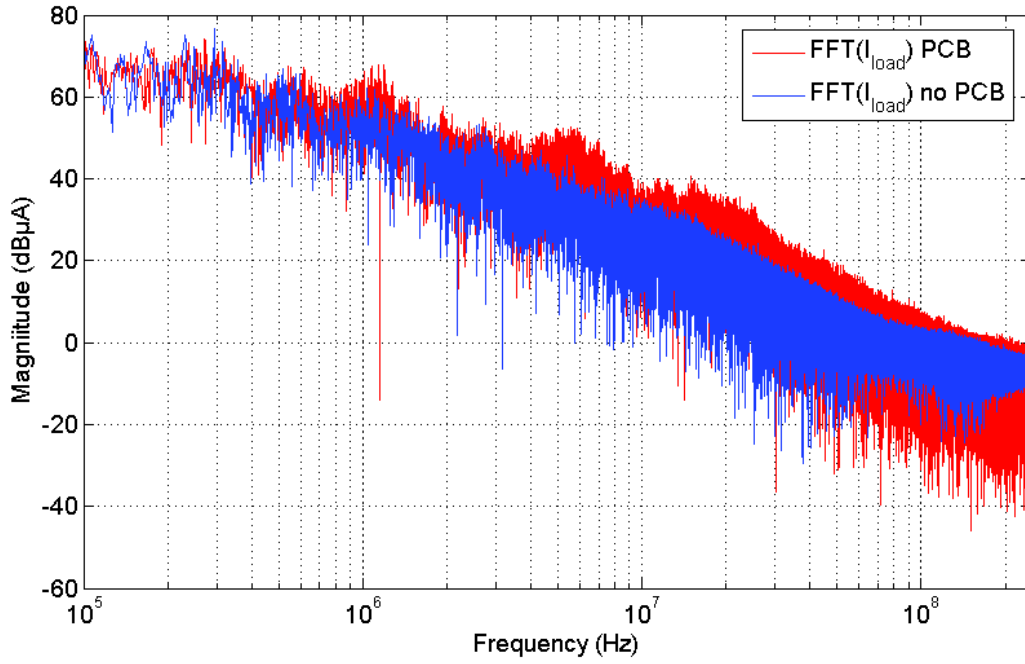


Fig. IV. 42 - FFT of the currents plotted with and without the PCB model

5.2 NON-FUNCTIONAL SIGNALS EXAMPLES

The voltage across the equivalent LEM impedance can be seen in Fig. IV. 43 and Fig. IV. 44.

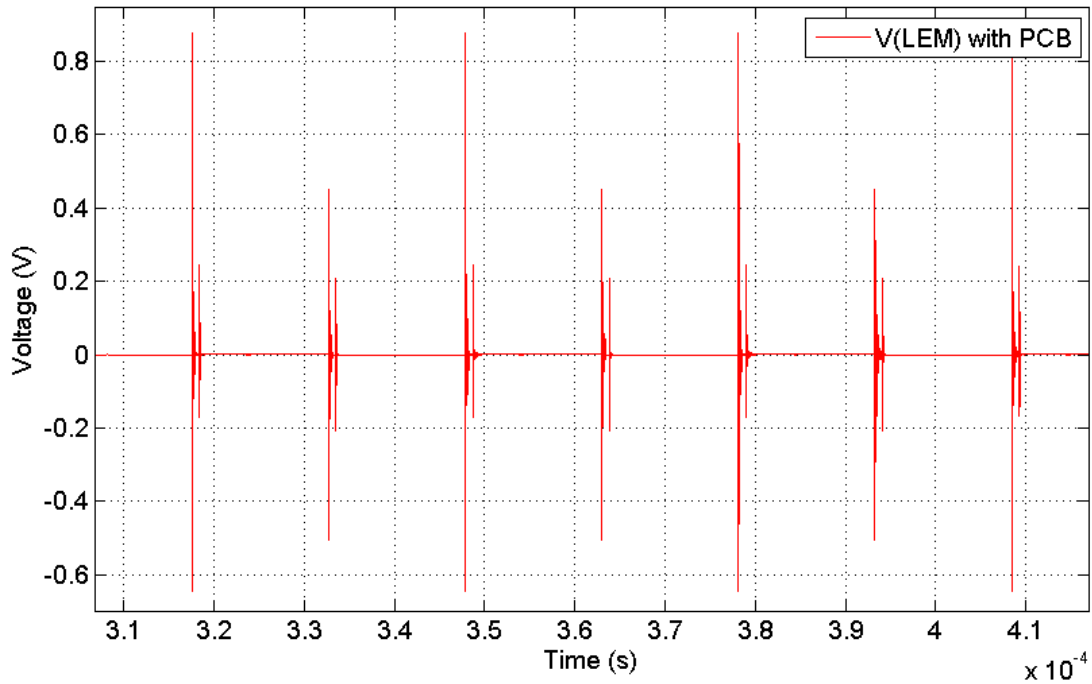


Fig. IV. 43 - Voltage across the LEM current sensor

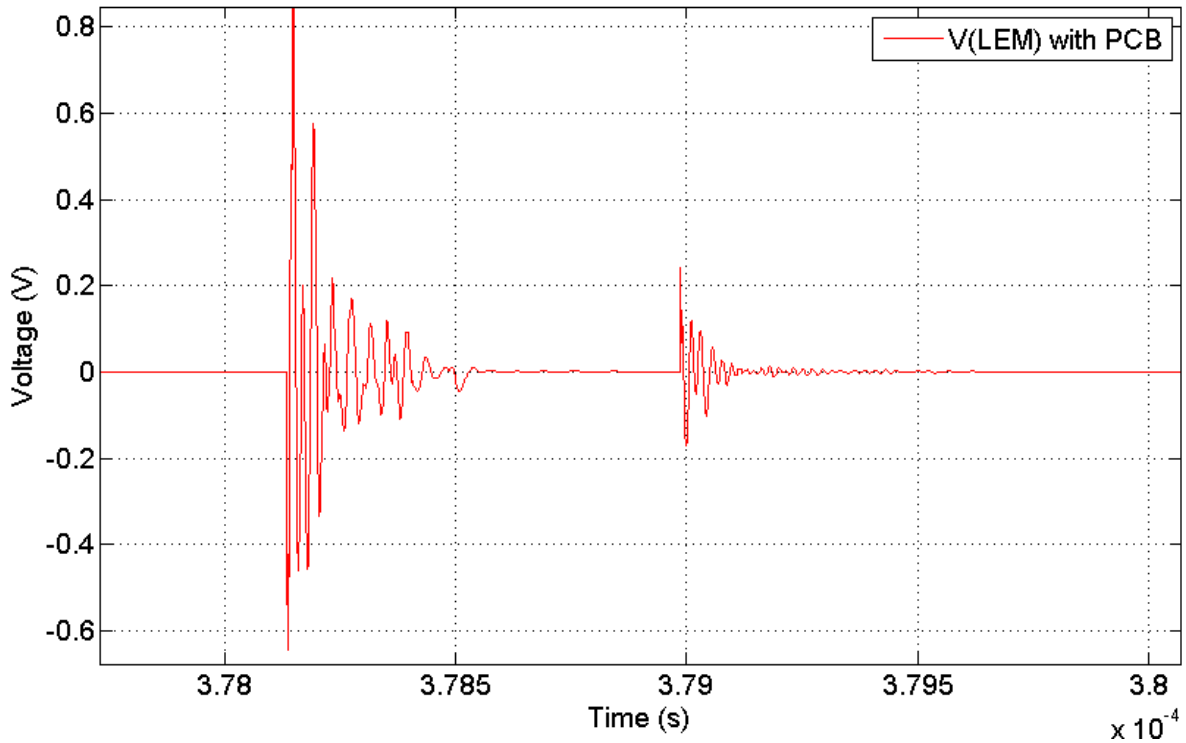


Fig. IV. 44 - Zoom of the voltage across the LEM at switching

The Virtual Experimentation allows for the exploration of the various signals involved in the delivery of power to the winding. Indeed, the LEM is an essential component of the converter, since it measures the phase current for control and protection purposes. The impact of the LEM on the whole structure can therefore virtually analysed from the design phase.

5.3 COMMON-MODE CURRENTS FROM CAPACITIVE COUPLINGS BETWEEN THE WINDING AND THE CORE

Perhaps, this is the most interesting analysis from the point of view of motor modelling. The currents generated between each turn can be observed, and therefore, every current from the turns to the core can be evaluated.

As would be expected, the voltage across the turns is different depending on the “electrical position” of the turn. Some currents corresponding to different turns are plotted in Fig. IV. 45 and Fig. IV. 46. The corresponding positions are described in Table IV. 6.

Table IV. 6 - Turn-to-core capacitances and their position in the winding structure

Capacitance name	Layer location	Turn position
C114	Layer 1 “first turn of the winding”	1
C271	Layer 7 “last turn of the winding” (lateral contact to core)	14
C272	Layer 2 (lateral contact to core)	14

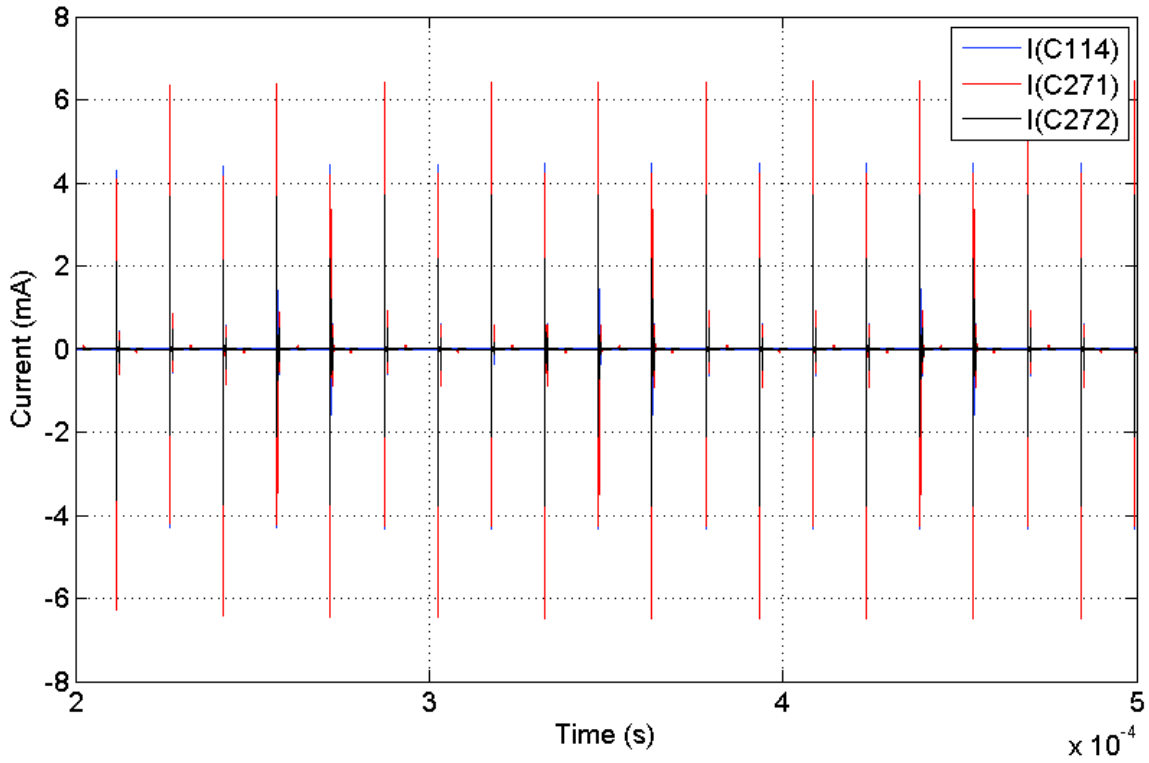


Fig. IV. 45 - Common-mode currents between some turns and the core of the winding

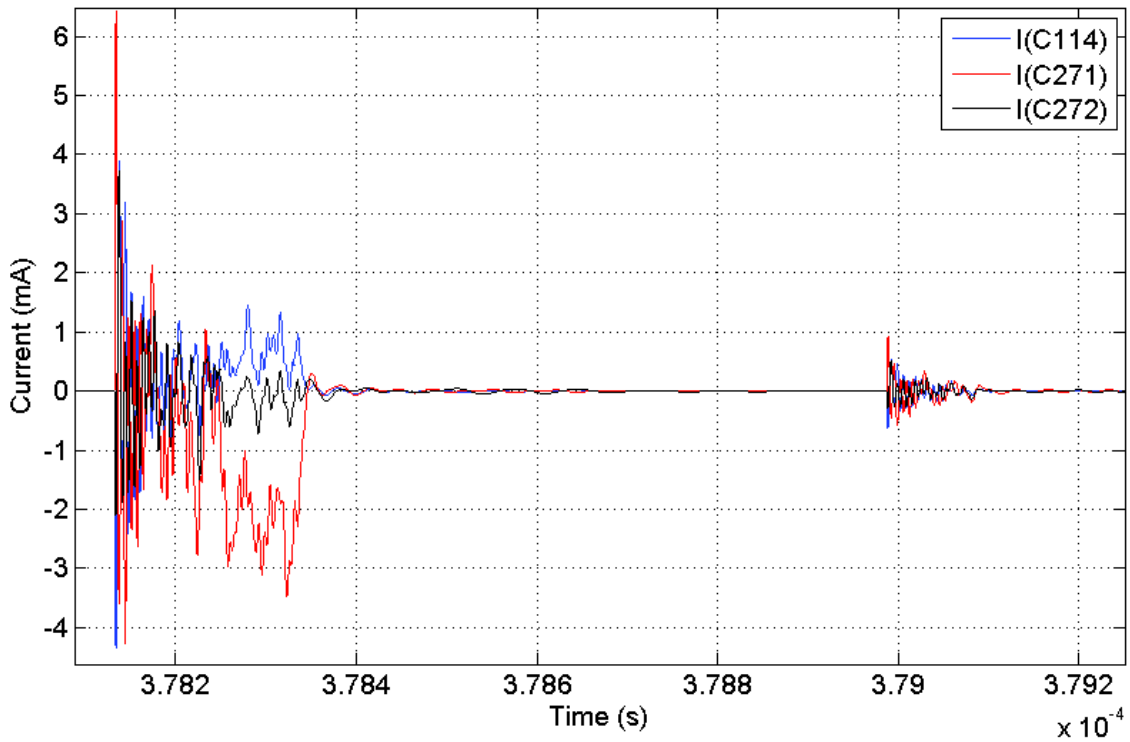


Fig. IV. 46 - Zoom on the common-mode currents at the winding level

The effects of the PCB can also be seen in the common-mode currents at the winding level. In Fig. IV. 47, are plotted two currents corresponding to the same turn, the first one with the influence of the PCB and the second, with no PCB included into the global simulation. Ringing behaviors between the motor’s partial capacitances and the PCB’s traces’ inductances appear at high frequencies, and this

behavior has an impact in common-mode currents through the couplings between turns and motor core.

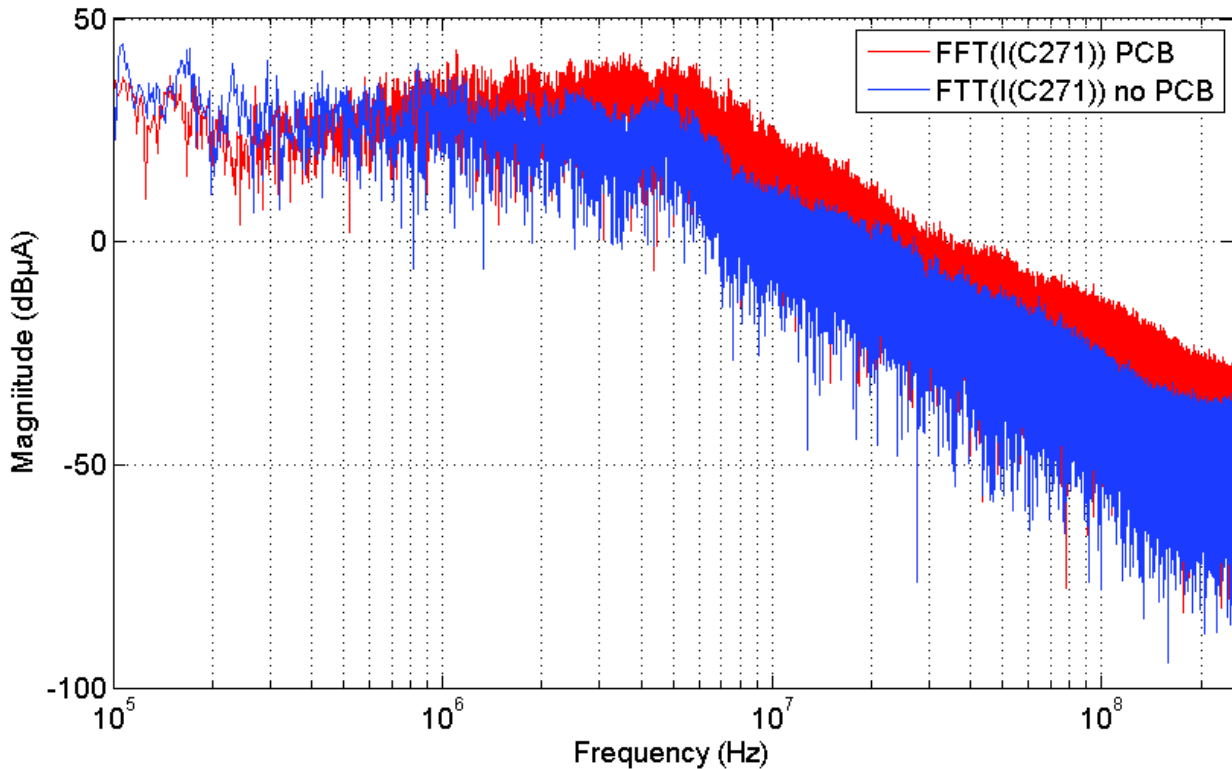


Fig. IV. 47 - FFT of the common-mode currents with and without PCB model

Not all currents were extracted here. But the process is the same for other parts of the circuit. A significant advantage of the rational method here proposed is that every single current can be accessed. The designer can make virtual modifications to improve the RE performance of the assembly. For example, modifying the thickness of insulating materials over the core of the winding has an effect in reducing the equivalent capacitance as seen in Chapter II. Therefore, the equivalent impedance seen by the common-mode currents flowing directly from the winding would be increased. The effects of such modifications could be explored without a major guess in the process.

Likewise, modifying the PCB layout might modify the levels of radiated emissions by better decoupling planes from one another. Even the modification of materials and media properties can be evaluated with this method.

The possibilities are vast, and give an infinite number of degrees of freedom to the designer to improve EMC performance.

6 CONCLUSIONS

The analysis of a Flyback converter helped to establish the techniques that can help to predict radiated emissions from the knowledge of the common-mode currents flowing through the power cable from the DC source to the converter. The procurement of the common-mode in the Flyback converter was done by manufacturing a very specific PCB with a simplified structure, and by measuring the parameters of the transformer and including them into a Netlist for circuit simulation purposes. Very good results were obtained, and radiated emissions could be validated up to 120 MHz.

In a second part of this work, a contribution regarding the prediction of the common-mode currents from a predictive perspective is presented. A global simulation was established with purely physical and thus, predictive models. This technique allows for a Virtual Experimentation that showed how a large number of parameters and signal can be explored. The impact of simple elements as the LEM current sensor and the influence of the PCB impedance were observed.

Maybe the most important aspect that can be explored with these predictive tools from the motor design perspective, is the common-mode currents that are generated between the turns and the core. This shows, how the fact that every component inserted into a mechatronic system modifies its high frequency behavior. The common-mode currents flowing directly from the windings are ultimately going to flow up to the power cord to return to the DC source. The impact of these currents on the radiated emissions fatally carry the signature of the PCB, and vice-versa. Ignoring one component on the chain can lead to prediction errors and certification rejection.

The predictive tool allowing to estimate the radiated emissions created by common-mode currents established in collaboration with the EMClab in Rolla, is thus completed with a very thorough tool of common-mode currents prediction.

The Virtual Experimentation process can represent a very useful tool for motor and converter designers, since it can allow to modify significant components of the model without the need of prototyping.

7 REFERENCES

- [1] Dolente, Andrea, "Analysis of the heatsink influence on conducted and radiated electromagnetic interference in power electronic converters", Ph.D., University of Bologna, Italy, 2007.
- [2] N. J. Ryan, B. Chambers, and D. A. Stone, "FDTD modeling of heatsink RF characteristics for EMC mitigation," *IEEE Transactions on Electromagnetic Compatibility*, vol. 44, no. 3, pp. 458–465, Aug. 2002.
- [3] T. Williams, "Characterisation of emissions due to power electronics heatsinks," presented at the Electromagnetic Compatibility (EMC EUROPE), 2013 International Symposium on, 2013, pp. 616–621.
- [4] S. Deng, T. Hubing, and D. Beetner, "Estimating Maximum Radiated Emissions From Printed Circuit Boards With an Attached Cable," *IEEE Transactions on Electromagnetic Compatibility*, vol. 50, no. 1, pp. 215–218, Feb. 2008.
- [5] "ANSYS HFSS," www.ansys.com/Products/Electronics/ANSYS-HFSS.
- [6] "CST Microwave Studio," www.cst.com/products/cstmws.
- [7] "APTGF30H60T1G Microsemi," www.microsemi.com/existing-parts/parts/61104.
- [8] R. Kraus, P. Turkes, and J. Sigg, "Physics-based models of power semiconductor devices for the circuit simulator SPICE," in *Power Electronics Specialists Conference, 1998. PESC 98 Record. 29th Annual IEEE*, 1998, vol. 2, pp. 1726–1731.
- [9] "Infineon IRS21864 Mosfet Gate Driver," www.infineon.com/cms/en/product/power/motor-control-and-gate-driver-ics/non-isolated-gate-driver-ics-and-controllers/general-purpose-gate-driver-ics-industrial/IRS21864.

General Conclusion and Perspectives

General Conclusion and Perspectives

General Conclusion and Perspectives

The work presented in this thesis is led by the need for rational predictive tools to be established for the analysis of high frequency behavior of power mechatronic systems. The tools and methods of modeling presented in four chapters deal with the physical properties of the constitutive elements present in mechatronic structures.

To begin the work, a literature review was done in order to put into context the development of the tools here presented. The integration pressure put on the assembly of motors and their power converters has brought a wide range of techniques to increase the power density. Increasing switching frequencies and decreasing switching times have become the preferred vectors of development of power converters, thus drastically reducing the volumes of integrated systems. The literature review showed that this tendency has yet to be intensified in the next decades. Besides, the introduction of wide band gap SiC and GaN based switches has also brought new perspectives for the integration of mechatronic systems by further pushing the reduction in switching times and the increase of their working temperature. The impact of the fast switching has to be thoroughly analyzed since parasitic behavior further manifests in the mechatronic systems with increasing equivalent switching-related frequencies. Resulting EMC and EMI concerns in mechatronic design might be grasped by establishing predictive tools that allow the designer to estimate the emissions before the prototyping phase.

Based on these conclusions drawn from the current research, it was noticed that a profound lack of predictive models exist for high frequency motor modeling. The impact of the association of the motors and converters has been widely studied but not with a predictive perspective.

It is with these observations that in the second chapter, analytical expressions of the impedance in concentrated windings of electrical motors are established taking into account physical and structural parameters of the components of the winding. The synthesized models are purely predictive and no measured-based models are considered. The modeling frequency span objective was set to DC to 300 MHz because of several observations made during the literature review.

The parameters taken into account range from constitutive properties of materials such as relative permittivity and permeability, to frequency dependence of parameters such as skin effect and magnetic and dielectric dispersion. The analytical expressions were then used to create time-domain and frequency-domain circuit models of concentrated windings. The drawn circuit models were then used for analyzing the common-mode and differential-mode impedances of the motor windings. The circuit representation was in fact used because of the large capabilities of circuit simulation when handling very large models. Each partial parameter established analytically, was introduced into the circuit model of the winding.

Although the analytical expressions take into account the dispersion of the permittivity of the insulating materials and the permeability of the core, the inclusion of the resulting calculated parameters into the circuit models couldn't handle these frequency dependence behavior. Indeed, the network synthesis theory was not helpful in solving this problem because of the very specific phase and magnitude behavior of these dispersion phenomena. Therefore, a mismatch between the analytical predictions and the circuit representation of the winding was pointed out. When confronted to experimental data, the analytically-based circuit models predict impedance resonances at frequencies lower than in measured data. And although there is a frequency shift, the predictive purpose of the models is fulfilled. The shift appears because dielectric dispersion is not handled correctly by the model. The same problem appears with the dispersion of the magnetic permeability. Only maximum and minimum values of inductive couplings analytically calculated can be used in the circuit model.

General Conclusion and Perspectives

Albeit, models give precious information on general frequency behavior of the winding impedance up to hundreds of MHz. To improve the models, investigations on the dispersion of dielectric permittivity over large frequency spans could give precious information on the behavior of the established models. Indeed, estimations of the dispersion were assumed but not verified. It would be of great value to get more detailed information of the dielectric behavior of insulating materials commonly used in electromechanical converters.

Furthermore, although the models give excellent results for small magnitude excitations, an interesting work is yet to be performed to include saturation effects on the magnetic core model. Besides, the core losses are not included in the modelling. Since small signals are used for the excitation of the global circuit, the impact of such absence of iron losses is small.

A third chapter deals with the numerical electromagnetic simulations for the extraction of parameters in Power Printed Circuit Boards (PPCBs). In this analysis an industrialized multilayer PPCB was used as a support to the 3D computation of electromagnetic fields. The resulting calculations were then interpreted in terms of circuit models that can be used for time- and frequency-domain impedance simulations.

Again, the leading idea of this analysis was that rational tools for establishing predictive models should be created. This way, an infinite number of PCB configurations can rationally be studied without the need of building custom-made prototypes in a process that would be time consuming.

The input parameters of the model are the 3D model, the materials' properties and the identification of the concerned conductors, traces and planes. Each conductor then, is assigned an electrical source and sink allowing the excitation of each conductor. The resulting electromagnetic field solutions are thus numerically interpreted in terms of a Netlist that can then be exported into a circuit simulator. Once in the circuit simulator, a Scattering parameters analysis could be performed between DC and 300 MHz.

The simulation results were confronted to experimental measurements performed with a Vector Network Analyzer. Each conductor was considered to be a two-port network along with the ground plane. SMA connectors and fixtures were used to measure the 2-port S-parameters and to complete the 10-port S matrix representing the modelled PCB. The simulated S-parameters performed with a SPICE simulator were within 10 dB difference for the worst case scenario. Considering that not a single measured parameter was used to complete the simulated data, results were considered to be acceptable from a predictive logic.

But, although results were encouraging, accuracy can still be improved. And an idea worth exploring is the inclusion of more than one TLM cell per conductor when exporting the extracted parameters into a Netlist. This would transform a lumped circuit into a distributed circuit allowing for propagation to be accounted for in the circuit simulation.

Finally, in the last chapter, system-level analysis is performed. This chapter is composed of two perfectly complementary methods of analysis of EMC and EMI.

The first study is the outcome of a collaboration between the teams in Laboratoire Génie de Production and Labceem in Tarbes, France and the EMCLab in The University of Science and Technology of Missouri, in Rolla, MO, USA. The established method aims to predict common-mode radiated emissions from the power cord from a Flyback converter. The analysis process is decomposed in three main stages: components modelling and measured-based circuit models, circuit simulation and extraction of common-mode currents and finally, full-wave simulation for prediction of radiated

General Conclusion and Perspectives

emissions. The delicate part of this process was the modelling of the Flyback transformer since no more information beyond that of its datasheet was available. The idea then was to build a measurement based model by extracting the S-parameters data with a VNA and integrating them into a circuit simulator. Once the transformer model was established, the circuit simulation allowed to extract the CM currents and use them in a full-wave simulation. The results were then compared to measured data in a semi-anechoic chamber for far-field radiated tests. The results were validated up to 120 MHz.

The second study, deals with the establishment of a fully predictive method for extracting the common-mode currents without the need for measured-based circuit models, making the two methods fully complementary. By building fully predictive models of the constitutive elements of the mechatronic assembly, the circuit simulation and CM currents extraction can be directly performed. Thus, from the design phase, the designer can build a model without prototyping and be able to estimate the radiated emissions only by simulation.

Based on the modeling process established in Chapters II and III of this work, a real-life partial mechatronic system was modeled and served as a support for simulation and currents and voltages extraction. The support used for this study was a 20 kW motor module. The module is composed of a concentrated winding and a 1-phase power converter. The winding was modelled according to the techniques crafted in this work, and the power converter was also built upon the already modelled PPCB analyzed in Chapter III.

The most interesting part of this latter study is the capacity for the designer to include every single component into the global simulation. A virtual experimentation was performed by simulating the converter and winding with and without the PCB response. The results were compared and analyzed. Finally, the CM currents at the winding level could be visualized turn by turn. This is only possible because of the modeling process which takes into account physical and structural parameters to build the circuit simulation.

This work is still to be validated with those experimental tests in the future.

So to conclude, a lot of work has still to be overcome. Not all motors have concentrated windings, and modeling distributed windings might not be easily done. Besides, important aspects of winding modelling have still to be detailed. Indeed, important parameters as core losses are still not included in this modelling, and although the models are used for small signal, simulation with more realistic signals can be achieved. Then, although this work is very generalizable, building physical models can sometimes be a time-consuming process at the beginning. But mathematical models used here can easily be integrated in a single mathematical or matrix code.

Other aspects that have to be explored are the parametrical influence of materials and other variables such as geometrical aspects. A thorough knowledge of physical parameters is essential to building sound models.

Finally, a global experimental validation of the radiated emissions of the analyzed system in chapter IV would be extremely reassuring from an engineering perspective.

This is decidedly only a very small step in the contribution to understand the challenging constraints' effects that power systems will face in the future. But, the physics-based models can be a definitive answer to the need of designers to better understand the technological choices they are faced with. This work has been constructed with the objective of getting closer to rational and generalizable methods that enable more efficient and trustworthy engineering design processes.

* * * *

General Conclusion and Perspectives

General Conclusion and Perspectives

Author: José Ioav Ramos Chávez

Thesis Advisers: Pr. Jean-Marc Dienot, Dr. Paul-Etienne Vidal and Dr. Christophe Viguier

Thesis Financing: Novatem SAS¹

Research Lab and Associated Platforms: Laboratoire Génie de Production²; Labceem³; PRIMES⁴

Date of Thesis Defense: November 21, 2016 at Ecole Nationale d'Ingénieurs de Tarbes, France.

¹ Novatem SAS, 3 rue, Merlin de Thionville 11110 Coursan, France www.novatem-sas.com

² Laboratoire Génie de Production at Ecole Nationale d'Ingénieurs de Tarbes INP-ENIT

³ Labceem EMC Research Platform, Tarbes Institute of Technology labceem.iut-tarbes.fr

⁴ PRIMES Research Platform www.primes-innovation.com

General Conclusion and Perspectives